THE EFFECT OF INTERFACE STRUCTURE ON ALL-ORGANIC THIN FILM GROWTH MORPHOLOGY: A COMPUTATIONAL ANALYSIS OF C_{60} ON PENTACENE

A Dissertation

Presented to the Faculty of the Graduate School

of Cornell University

in Partial Fulfillment of the Requirements for the Degree of

Doctor of Philosophy

by

Rebecca Ann Cantrell

August 2011

THE EFFECT OF INTERFACE STRUCTURE ON ALL-ORGANIC THIN FILM GROWTH MORPHOLOGY: A COMPUTATIONAL ANALYSIS OF C_{60} ON PENTACENE

Rebecca Ann Cantrell, Ph.D.

Cornell University 2011

The C_{60}/pentacene heterojunction is of considerable interest for organic electronic devices (especially for photovoltaic applications), yet its nature, particularly its structural morphology, is not well characterized at the molecular level. With that in mind, this work presents the results of both fully atomistic Molecular Dynamics and kinetic Monte Carlo approaches to elucidate the behavior of C_{60} molecules on a variety of different pentacene polymorphs. The diffusion characteristics of C_{60} molecules on the surfaces of "thin film" and "bulk" phases of pentacene (upright polymorphs) are analyzed in detail. The results highlight surprising differences between the two polymorphs, with lower diffusion coefficients (by one half) and anisotropic diffusion behavior, sometimes non-Arrhenian, of C_{60} on bulk phase pentacene, compared to the thin film phase. An extensive catalog of energetic barriers for diffusion created from the Molecular Dynamics simulations was used as the sole input into a kinetic Monte Carlo simulation in order to follow the evolution of multiple layers of C_{60} on pentacene for time scales approaching a millisecond that are unattainable using Molecular Dynamics alone. A novel kinetic Monte Carlo algorithm was developed for this purpose, featuring a multi-lattice set-up to capture the behavior of singleton and non-singleton C_{60} molecules diffusing, clustering and reorganizing as monolayers on the surface. For recumbent pentacene polymorphs, in which

the molecules are essentially lying almost flat on an underlying silicon surface, Molecular Dynamics was revisited to elucidate the tendency for C_{60} nanowires to persist in the crevasses formed by these tilted pentacene structures. We find that the likelihood for C_{60} nanowires to be formed and to persist depends sensitively on the angle that the recumbent pentacene makes with the surface normal, the amount of initial tensile strain applied to the nanowire, and the presence of surface step edges. The most compelling finding was that pentacene step edges, which would result from any appreciable surface roughness and will be a common experimental occurrence, strongly enhances the likelihood of nanowire formation due to the strong binding energy of C_{60} molecules to step edges.

BIOGRAPHICAL SKETCH

Rebecca Ann Cantrell was born in Houston, Texas on February 11th, 1984. From 1998 to 2002, she attended middle and high school at St. John's School, a coeducational independent school in the Upper Kirby district of Houston. It was in high school that her love of math and science really grew strong; engineering seemed a logical choice of career path. She then attended Northwestern University in Evanston, Illinois and received a B.S. degree in chemical engineering in June 2006. During the summer of 2006, between college and graduate school, Rebecca received her private pilot's license for single engine land at KYEQ Weiser airport in Houston, and has flown occasionally at the East Hill Flying club in Ithaca, NY. Other diversionary activities in Ithaca included triathlons, half marathons, and volunteering at the Tompkins Country SPCA. For the past five years, she has been performing research on organic heterojunction materials in the Department of Chemical and Biomolecular Engineering at Cornell University.

This work is dedicated to my Mom, Dad, and sister Emily for their support.

May this work reward their patience as I complete my 22nd year as a student.

ACKNOWLEDGEMENTS

First and foremost I want to thank my advisor Paulette Clancy. She has been an inspiration to me as a great researcher and successful woman in the field of nanoscience. Throughout my graduate career, her positive and open-minded attitude toward complex problems taught me be resilient in the face of adversity. Her ability to frame complex problems allowed me to see issues in a new light, which enabled me to not only solve the problems at hand, but inspire new interest in my research. Finally and most importantly, she has always patiently guided me to find the right questions to ask. No amount of words could ever truly express the gratitude I feel towards Professor Clancy, but in the end I can wholeheartedly say that I could not have done it without her.

I would also like to thank my committee members, Donald Koch (Chemical Engineering) and Michael Thompson (Material Science and Engineering). Professor Koch helped me view things from an entirely different perspective than I had been used to in my research. He opened my eyes to many issues that I had not thought about before, and in the end, strengthened my research. Professor Thompson was my main channel to the experimental world, a world which would be completely foreign to me without him. His seemingly limitless knowledge of materials properties and their connection to electronic devices proved extremely useful. I would also like to mention George Malliaras, a former professor in Material Science in Engineering, who gave me some very useful ideas early in my graduate career. Finally, I would like thank my collaborators Dr. Daniel Dougherty (National Institute of Standards and Technology) and Bradley Conrad (University of Maryland) who performed experiments on closely related work to my own simulations; I found discussions with them to be enlightening and inspiring.

I must also mention the Paulette Clancy group members who have been there for me throughout my five years at Cornell. From oldest to youngest, I was so glad to know and befriend the following PhD students: Leonard Harris ('09), Joseph Goose ('10), Krishna Iyengar, Ananth Kaushik, Alexandra Cooper, Brian Koo, and Vikram Thapar. These students and Professor Clancy provided me with unending emotional support, camaraderie, entertainment, and caring, for which I cannot thank them enough.

Finally, I would like to acknowledge the funding sources throughout my time at Cornell. These consisted of an IGERT Fellowship from the National Science Foundation and MRSEC funds administered by Cornells Center for Materials Research (CCMR).

TABLE OF CONTENTS

LIST OF TABLES

LIST OF FIGURES

CHAPTER 1

INTRODUCTION

1.1 Organic electronic devices

Organic semiconductor materials are a key component in the growing field of organic electronics, covering electronic devices such as organic light-emitting diodes (OLEDs), organic thin film transistors (OTFTs), and organic photovoltaic cells (OPVs). The drive for the development of organic semiconductor materials has been their potential to offer lower cost and larger-scale (roll-to-roll) processing than traditional inorganic semiconductors as well as the inherent flexibility that organic substrates offer.[4,5] Organic electronic devices usually involve some form of a *p*-*n* junction, just like their inorganic counterparts, where a semiconducting material with electron-donating capabilities (*n*-type) and one with electron-accepting capabilities (*p*-type) are placed in contact. In a solar cell, as light is incident on the device, an exciton (electron-hole pair) can form on either side of the junction. This exciton then diffuses to the region of the junction, where a built-in electrostatic field to drive the electrons and holes apart to their respective electrodes. Figure 1.1 shows a schematic of a generic *p*-*n* junction, and illustrates how the charge carriers flow under illumination.

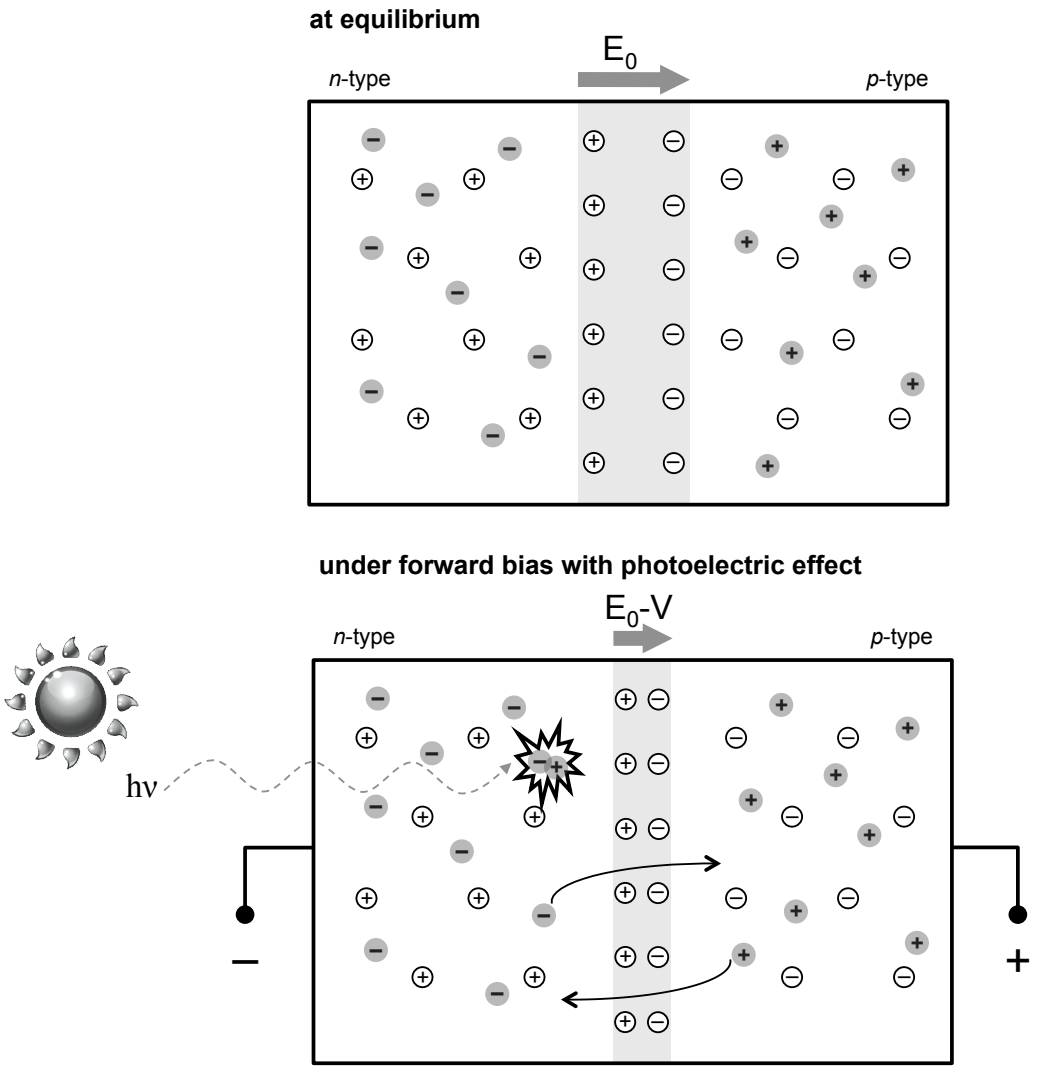

Figure 1.1: Diagram of a generic *p*-*n* junction at equilibrium (top) and under illumination (bottom). Circular particles with a shaded background are free charge carriers, and those with a white background are local charges, fixed by the structure of the material. At equilibrium, a built-in electric field (E_0) develops as particle diffusion and electric drift balance. Sunlight stimulates the creation of excitons, which diffuse toward the interface, split, and diffuse toward their respective electrodes (electrons (−) toward the positive electrode and holes (+) toward the negative electrode).

Simple organic solar cells can be fabricated by layering thin films of organic semiconductors between electrodes with different work functions. High photocurrent quantum efficiencies are achieved in heterojunction systems that include both good electron-donating and electron-accepting layers.[6] Unfortunately, the performance of current organic photovoltaics is hampered by poor charge transport, structural instabilities, and large band gaps (resulting in little to no red absorption). This is largely the reason that the photovoltaic market is still dominated by devices made from crystalline silicon. Although inorganic semiconductor materials generally have much higher charge carrier mobilities, recent progress has resulted in the development of *p*-type aromatic hydrocarbon materials, especially pentacene, which show comparable hole mobilities to those of amorphous silicon ($\geq$1 $cm^2/V\ s$).[7,8] For organic *n*-type semiconductors, such as C_{60}, reported electron mobilities can be as high as 0.65 $cm^2/V\ s$.[9] This thesis focuses on the particular material combination, C_{60} and pentacene, which is a prototypical combination for an organic semiconducting device suitable for a solar cell; this material choice will be described further in Section 1.2. More background on previous studies of C_{60}/pentacene and similar systems will follow in Section 1.3 and will illustrate the need for computational studies to characterize this interface.

1.2 Background on material choice

One of the more common organic semiconductor heterojunctions studied experimentally involves the interface between the fullerene, C_{60}, and the small crystalline organic molecule, pentacene, both of which have relatively large charge carrier mobilities.[10–20] This combination of materials has been studied experi-

mentally for OTFTs[13,18] and especially for OPV devices,[10,11,15,19] exploiting the absorbance properties of the system for use in photovoltaic devices. However, there are challenges in controlling molecular order at the C_{60}/pentacene interface due to the delicate balance of interactions.[21–23] As such, this thesis focuses on the impact of the dissimilar interactions between *p*-type pentacene and *n*-type C_{60} as an exemplar for a *p*-*n* heterojunction in an organic semiconductor system.

An ideal heterojunction is assumed to be one in which either both of the organic components forming the interface exist in as orderly and planar a form as possible (planar heterojunction), or one which maximizes the surface contact area between the two materials (bulk heterojunction) hence facilitating exciton splitting. Generally maximizing heterojunction surface area comes at the expense of material order and *vice versa*, but for the planar systems studied in this work, we are considering the maximum order and minimum contact surface. The desire for order is often interpreted to imply a need to use highly crystalline materials. Order in the bulk and at the interface is associated with very little charge scattering, which can otherwise lead to the undesirable result of electron-hole recombination. Despite this commonly acknowledged need to create a highly ordered interface, there has been little experimental work to probe the detailed nature of the C_{60}/pentacene interface and even fewer computational studies. The relevant works that *do* touch on the C_{60}/pentacene interfacial nature are discussed in Section 1.3. Before that, we provide more background in Sections 1.2.1 and 1.2.2, discussing specific material properties of the individual C_{60} and pentacene molecules. Then, Section 1.2.3 discusses the different types of organic heterojunction morphologies, and the possibilities that exist for the C_{60}/pentacene system.

1.2.1 C_{60}

C_{60} is an organic molecule with sixty carbon atoms arranged in an interlocked series of 20 hexagons and 12 pentagons, resulting in a truncated icosahedron as shown in Figure 1.2. At room temperature and ambient pressure, single-crystal X-ray diffraction experiments have shown that bulk C_{60} molecules prefer a rotationally disordered face-centered cubic (fcc) crystal structure bound by weak van der Waals forces and having a lattice constant of 14.2 Å.[24–26] It has also been shown that C_{60} rotates quite freely about its center when in its fcc crystal configuration at ambient temperatures.[27] The molecular diameter of C_{60} is 7.1 Å and equilibrium center-to-center intermolecular distance is 10.0 Å.[24] C_{60} thin film lattice parameters do not vary with the lattice parameters of the substrate, in contrast to the epitaxial growth habit of most van der Waals crystals.[28–30]

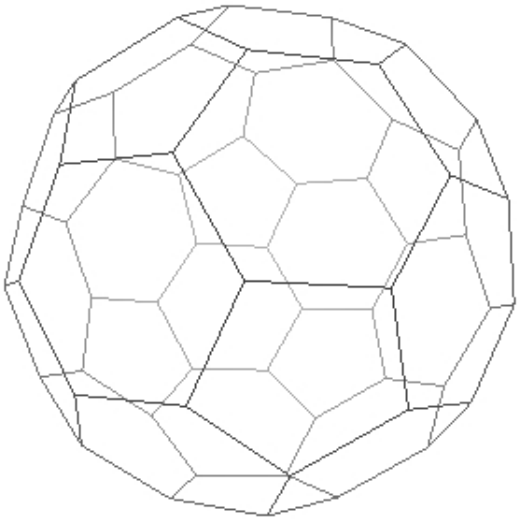

Figure 1.2: Wire frame structure of the truncated icosahedron shape of C_{60}.

1.2.2 Pentacene

Pentacene adopts more complex morphology than C_{60} due to its anisotropic shape and electrostatic forces. It is a planar molecule that is about 14 Å long and 5 Å wide (see Figure 1.3). The fused benzene rings that make up the pentacene body create π-electron clouds along the faces of the benzene rings. Due to the propensity for electrons to be shared, pentacene often tries to arrange itself such that the π-π stacking is balanced among neighboring molecules. This balancing act leads to the polymorphisms that exist for pentacene.

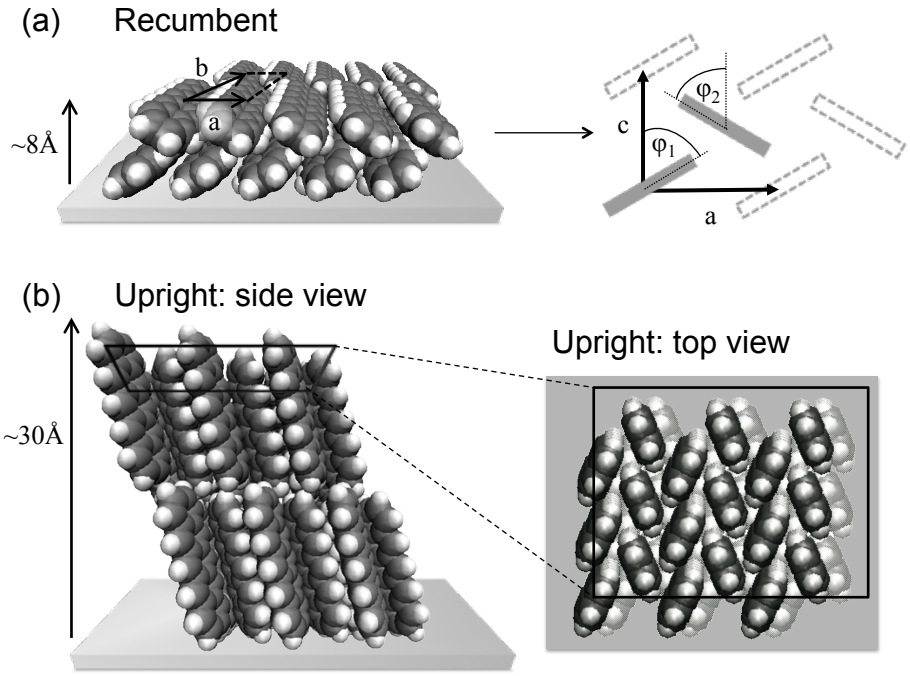

Figure 1.3: Schematic diagrams to illustrate the molecular disposition in (a) recumbent and (b) upright phases of pentacene. Lattice parameters a and b, whether for upright or recumbent, are always in the plane parallel to the substrate. For recumbent pentacene, the parameter ϕ is used to describe the degree of tilt of the pentacene short axis off the surface normal, and the subscript on ϕ denotes to which molecular layer it is referring.

It is important at this point to establish our "vocabulary" to describe these polymorphisms in an unambiguous way. The literature contains a mixture of terminologies to describe the orientation of pentacene molecules on a surface, using words such as parallel, perpendicular, co-facial, upright, flat, lying-side, *etc.* There appears to be no commonly adopted terminology, and often no schematics are provided in papers that explain precisely how these terms are intended to be interpreted. We define two main classes of pentacene structures—upright and recumbent—as shown in Figure 1.3. Upright pentacene encompasses the well-known, thermodynamically stable, "thin film" and "bulk" phases of pentacene, in which the long axis of the molecule is roughly perpendicular to the underlying surface, though tilted off-normal by 8.6° for the thin film phase and by 22.6° for the bulk phase. Although this thesis only covers these two phases, there are other thermodynamically stable and metastable phases of upright pentacene known.[31,32] In contrast, recumbent pentacene implies molecules lying with their long axis parallel to the surface, but perhaps tilted somewhat off the horizontal by a rotation involving their short axis. The thermodynamic stability of recumbent pentacene "phases" has not been established, largely because they typically exist for only one or two monolayers and hence it is unclear whether this can be referred to as a "phase."

The upright bulk and the thin film phases appear when growing pentacene on electrically insulating substrates such as SiO_2 or Al_2O_3 using either low-pressure organic vapor phase deposition[33] or vacuum thermal evaporation.[34] As its name suggests, the thin film phase occurs during the first few monolayers of growth (at least). The ratio of bulk phase to thin film phase pentacene increases with deposition temperature, deposition pressure (for vapor phase deposition) and film thickness.[34–36] Unfortunately, most experimental methods

produce a mixture of thin film and bulk phases. While it is not critical to produce one phase over the other, it would be preferable to have just one phase present. Recently, it was demonstrated how to use a laser-induced structural transition that experimentally produces just the bulk phase of pentacene.[37]

Both bulk and thin film pentacene phases consist of a triclinic unit cell, with two molecules per unit arranged in a herringbone configuration.[38] The (001) plane, as outlined in Figure 1.3(b), is the lowest energy surface.[39] The intermolecular bonding of the pentacene molecules is a result of dipole-dipole and weak van der Waals interactions.[39,40] The bulk phase has the well-accepted triclinic lattice parameters of $a = 7.90$ Å, $b = 6.06$ Å, $c = 16.01$ Å, $\alpha = 101.9°$, $\beta = 112.6°$ and $\gamma = 85.8°$, reported by Northrup *et al.*[39] based on X-ray diffraction results from Campbell *et al.*[41] The thin film phase has the triclinic lattice parameters of $a = 7.56$ Å, $b = 5.93$ Å, $c = 15.65$ Å, $\alpha = 93.3°$, $\beta = 98.6°$ and $\gamma = 89.8°$, reported by Yoshida *et al.*[42] based on X-ray diffraction reciprocal space mapping.

As for the recumbent pentacene structures, there is no accepted thermodynamic "phase" in the literature. Pentacene molecules grown on non-electrically insulating materials, primarily metals[43–46] and silicon,[47,48] where opportunities to share electrons are more facile, lie down on the surface in a recumbent fashion to an extent determined by the nature of the substrate. Once sufficient monolayers of pentacene have been deposited, the material will transition to an upright phase (thin film or bulk). The onset of this transition is not well established in experiments; it may occur as early as the second or third monolayer, though other papers and other processing approaches seem to delay or thwart this transition. There have been more than fifty papers published to describe experimental studies of pentacene growth on different noble metal substrates. However,

there has been no prior examination of all these results taken as a whole, and inspection of these papers shows that authors rarely, if ever, compare their findings to other similar studies. That being the case, we have collected together this body of experimental results and looked for a link between choice of metal, experimental conditions and resultant tilt angle, largely without success. Papers that quoted a tilt angle mostly used NEXAFS, which is a reasonably sensitive tool with a commonly quoted uncertainty of about ±5°.

There are many techniques and experimental variables that have been used to determine the structural characteristics of monolayer(s) of recumbent pentacene molecules: Different deposition methods (*e.g.*, solution-based, Physical Vapor Deposition, *etc.*) have been used, as well as different deposition rates, substrate temperatures, and applied potentials. We have summarized the recumbent pentacene structures reported in the literature for gold (Table 1.1, silver (Table 1.2), and copper (Table 1.3). In these tables, "success" is equated with achieving periodic, ordered growth of recumbent pentacene monolayers.

This body of experimental work on the behavior of pentacene on metals has conclusively established that the first monolayer (ML) of pentacene lies recumbent on conducting surfaces like the noble metals—Au, Ag, and Cu. This is primarily due to the favorable interaction between the pentacene π clouds and the empty d-orbitals of the metal. A second monolayer of pentacene deposited on such metals is largely reminiscent of a recumbent position, but one in which the short-axis of the pentacene molecules is tilted up and away from the underlying first monolayer (see Figure 1.3(a)).

Table 1.1: Summary of literature results for recumbent pentacene growth on Au metals. Data missing were either not provided by the authors or were unclear. Only results for close to full monolayer (ML) coverage were noted. PVD = physical vapor deposition; MBE = molecular beam epitaxy. *The ordered layer(s) are shown to be commensurate with the substrate's lattice plane. **Inferred value. ¶Author denotes as "modeled". †A second, coexisting phase. §Corresponding to the 2nd ML or higher.

Reference	Substrate	Method	Deposition rate (nm/min)	Substrate temperature (K)	Ordered 1st ML?	Successful recumbent multilayer growth?	Lattice parameters			Angles made by substrate normal
							a (Å)	b (Å)	γ (°)	ϕ(°)
Corradini *et al.*[49]	Au(110)-(1×2)	PVD (MBE)	~0.1	80 300 370	N Y Y	N Y (≤12nm) Y (≤12nm)				
Guaino *et al.*[50]	Au(110)-(1×2)	PVD		~300	Y*	Y (≤12nm)	8.3±0.7	24.9±1	90	
Floreano *et al.*[51]	Au(110)-(1×2)	PVD (MBE)	~0.14	280 370 420 470	N Y* Y* Y*	N N N N	17.3	32.6	~90	
Bavdek *et al.*[52]	Au(110)				Y*		8.65	24.47	~90	90±5

Table 1.1: Continued. Key as in Table 1.1.

Reference	Substrate	Method	Deposition rate (nm/min)	Substrate temperature (K)	Ordered 1st ML?	Successful recumbent multilayer growth?	Lattice parameters			Angles made by substrate normal
							a (Å)	b (Å)	γ (°)	ϕ(°)
McDonald *et al.*[53]	Au(100)	PVD		~300, 373	Y*	Y (≤~1nm)	7.4±0.4	15.5±0.8	85.5±2.5	
France *et al.*[54]	Au(111)-($23\times\sqrt{3}$)	PVD	0.4	~300	Y		6±1 5.76¶ 6±1† 5.76¶†	15±1 15.3¶ 15±1† 16.0¶†	79±3 79.1¶ 75±3† 69¶†	
Suzuki *et al.*[55]	Au(111)-($22\times\sqrt{3}$)		0.1–0.2	~300	Y					77
Beernink *et al.*[56]	Au(111)	PVD (MBE)	0.05–0.3	200, 300	Y	N				>85
Hu *et al.*[57]	Au(111)	PVD	6	~300	Y	Y (≤100nm)				

Table 1.1: Continued. Key as in Table 1.1.

Reference	Substrate	Method	Deposition rate (nm/min)	Substrate temperature (K)	Ordered 1st ML?	Successful recumbent multilayer growth?	Lattice parameters			Angles made by substrate normal
							a (Å)	b (Å)	γ (°)	ϕ(°)
Kang *et al.*[58]	Au(111)-(22× $\sqrt{3}$)	PVD (MBE)	0.1–1.6	293	Y	Y (≤~6nm)	6.6±0.5 6.4±0.5†	15.5±0.5 15.5±0.5†	75±2 82±2†	
Käfer *et al.*[59]	Au(111)	PVD (MBE)	0.1–20	300 330	Y Y	Y (≤110nm) Y (≤110nm)	5.7±0.3	~16**		77 (<ML) 59§ (20nm) 58§ (110nm)
Yang *et al.*[60]	Au(111)	Solution			Y		10.4±0.1 8±0.2†	16.1±0.1 17.5±0.5†		
Pong *et al.*[61]	Au(111)-(22× $\sqrt{3}$)	Solution		298	Y	N	8.2 7.8§	16.4 15.7§		

Table 1.2: Summary of literature results for recumbent pentacene growth on Ag metals. Key as in Table 1.1.

Reference	Substrate	Method	Deposition rate (nm/min)	Substrate temperature (K)	Ordered 1st ML?	Successful recumbent multilayer growth?	Lattice parameters			Angles made by substrate normal
							a (Å)	b (Å)	γ (°)	ϕ(°)
Wang *et al.*[44]	Ag(110)	PVD (MBE)	~0.34	~300	Y		9.58	13.55**	90**	90
Danişman *et al.*[62]	Ag(111) miscut = 0.56°	PVD (MBE)		200	Y*	Y	8.67 6.1±0.1§	17.6 16.5±0.6§	68 68§	90 70§
Eremtchenko *et al.*[63]	Ag(111)	PVD (MBE)	~0.03	~300	N	Y*(≤~1nm)	8±1§	18±1§	~78§	
Käfer *et al.*[64]	Ag(111)	PVD (MBE)		~300	Y	Y (≤30nm)				77 56§
Pedio *et al.*[65]	Ag(111)	PVD		~300	Y					80±5
Dougherty *et al.*[66]	Ag(111)	PVD		~300	Y	Y		~16.5**		56–62§
Mete *et al.*[67]	Ag(111)	DFT			Y*	Y*				90 72 (2 ML) 73 (3 ML) 75 (4 ML)

Table 1.3: Summary of literature results for recumbent pentacene growth on Cu metals. Key as in Table 1.1.

Reference	Substrate	Method	Deposition rate (nm/min)	Substrate temperature (K)	Ordered 1st ML?	Successful recumbent multilayer growth?	Lattice parameters			Angles made by substrate normal
							a (Å)	b (Å)	γ (°)	ϕ(°)
Gavioli *et al.*[68]	Cu(119)	PVD (MBE)	0.1	~300 373	N Y*		11	22		
Betti *et al.*[69]	Cu(001) Cu(119)	PVD	~1	300	Y Y					
Baldacchini *et al.*[70]	Cu(119)	PVD (MBE)	0.1	~370	Y*					
Schuerlein *et al.*[71]	Cu(100)	PVD (MBE)	~0.06	373	Y		9.7	15.5	66.8	
Satta *et al.*[43]	Cu(100)	MD		0	Y*	Y (≤~3nm)			90	90 65–70§
Chen *et al.*[72]	Cu(110)	PVD	~0.07	~300, 400	Y*		7.2**	21.7**	90	90
Söhnchen *et al.*[73]	Cu(110)	PVD (MBE)	0.05–0.5	450, 300	Y*	Y (≤~2nm)	7.7±0.1 6.9§	14.7±0.1 15.3**§	72 71.5**§	90 62±5§
Götzen *et al.*[74]	Cu(221)	PVD (MBE)	0.05–0.1	~300, 400	Y*	N	8±0.5	17±1	90	

Rules governing the orientation of pentacene molecules were difficult to extract from this compilation of literature results. On Au, for example, there is no consensus concerning the number of monolayers at which the pentacene transitions from a recumbent to an upright morphology. For pentacene on Au(111), Beernik *et al.* state that this transition occurs around 4 nm,[56] whereas Käfer *et al.*[59] and Hu *et al.*[57] find that pentacene films remain recumbent even at thicknesses around 100 nm. There seems to be no clear reason for this discrepancy based on the temperature or deposition rate used.

The effect of temperature on the recumbent pentacene structures is also unclear from the literature. For pentacene on Au(110), Corradini *et al.* found that a higher substrate temperature (370 K) improved long-range ordering of recumbent pentacene up to 12 nm.[49] For pentacene on Au(111), Kang *et al.* also found that raising the temperature from room temperature to 353 K allowed the second recumbent monolayer to grow more readily at sub-monolayer densities and with larger multi-layer domain sizes.[58] Beernick *et al.*, on the other hand, found that raising the temperature from 200 K to 300 K gave rise to three-dimensional upright structures of pentacene on Au(111).[56] There appears to be a competition at work: Raising the temperature increases the molecular diffusion length of recumbent pentacene molecules, but it also increases the probability of the transition from recumbent to upright, which is undesirable in this context.

Finally, we note the significant, but expected, effect of the choice of orientation of the fcc metal surface plane on the resulting structure of the first pentacene monolayer and subsequent multi-layer growth. For example, pentacene molecules readily line up against the atomic structure of Au(110)-(1×2),[50] but not on Au(111)-(23× $\sqrt{3}$)[54] or Au(111)-(22× $\sqrt{3}$).[58] Similar results hold for silver:

Danisman *et al.* found that Ag(111) with a miscut angle of 0.6° caused pentacene molecules to line up at the metal terraces, whereas Ag(111) with a miscut angle of <0.1° (lower step density) gave rise to differently oriented recumbent pentacene grains. The formation of ordered multilayers in this case were only found for the Ag(111) with a higher step density, implying that the corrugation of the metal surface provides a template for long-range multilayer order. On the other hand, this templating prerequisite for multilayer growth on Ag(111) was not seen by Eremtchenko *et al.*. They showed that ordered recumbent monolayers can form on top of a disordered first monolayer on Ag(111),[63] which is surprising and provides hope that ordered multilayers are not completely dependent upon pentacene-on-metal templating. It is as yet unresolved as to whether the monolayer crystallizes as a result of bilayer nucleation. Dougherty *et al.* show weak evidence for ordering of recumbent pentacene beneath a bilayer on Ag(111) at low temperatures.[75]

While some of the differences among these reported results may be attributable to details of the experimental approach taken, the net result is that it is difficult to extract any underlying guiding physico-chemical principles that link tilt angle to the nature of the underlying metal substrate. Experimental results to date have not provided a clear picture of the conditions that give rise to predictable pentacene morphology. Finally, despite the large number of systems studied to date, the results for noble metals shows only a narrow range of pentacene tilt angles that can readily be obtained, and thus only a limited sampling of the available "parameter space" for recumbent pentacene growth on metal substrates.

1.2.3 Heterojunction classifications

Unlike many inorganic *p*-*n* junctions, organic *p*-*n* junctions carry charges by a localized hopping mechanism, which is generally assumed to be responsible for the lower charge carrier mobilities. Correspondingly, there are fundamental differences in the exciton behavior between organic and inorganic materials. Organic photovoltaic materials have a relatively strong exciton binding energy (~1 eV) compared to inorganic semiconductor materials ($<kT$), making the charge splitting more difficult.[76] Also, the diffusion length of an exciton in organic photovoltaic devices is much lower, which only allows the excitons to split if they are formed very near, or at, the *p*-*n* junction interface. Thus, knowing the atomic-scale details of the interface between the *p*- and *n*-type materials is very important for understanding the performance of organic semiconductor materials.

The C_{60}/pentacene studies presented in this thesis describe mainly what is referred to as a "planar heterojunction," rather than a "bulk heterojunction;" the distinction being that the bulk heterojunction involves an interpenetrating blend of donor and acceptor molecules in an attempt to reduce the distance that an exciton has to travel to dissociate. Figure 1.4 shows schematics of example types of *p*-*n* heterojunctions. The planar heterojunction, as its name implies, assumes a planar, non-interpenetrating interface. It has been found that bulk C_{60}/pentacene heterojunctions have a slightly higher open-circuit voltage than planar heterojunction devices; however, their short-circuit current density and thus power conversion efficiency are approximately six times lower than those of planar C_{60}/pentacene heterojunctions.[17,20] Not only do bulk C_{60}/pentacene heterojunctions tend to phase-separate and short-circuit, but there is also a large

charge recombination rate due to the C_{60} molecules being positioned directly against the benzene-ringed "face" of a pentacene molecule, facilitating hopping.[77] This configuration occurs much less often in planar heterojunctions because C_{60} lies in the "crevices" between the pentacene molecules, interacting with the end or edge of the molecule, not its "face." For these reasons, we focus solely on the planar C_{60}/pentacene heterojunction.

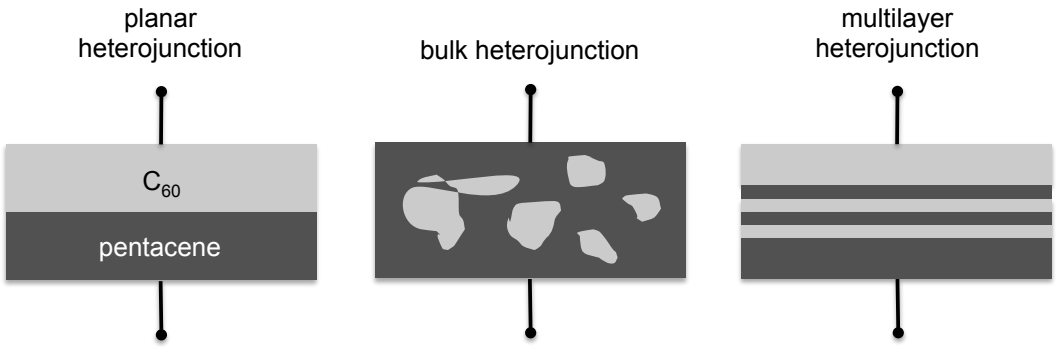

Figure 1.4: Example *p-n* heterojunction types. The black lines at the top and bottom represent the electrodes, and the two shades of gray represent C_{60} (lighter) and pentacene (darker).

Even within the category of planar heterojunctions, many different C_{60}/pentacene interface geometries can exist. Depending on growth conditions, the pentacene molecules can arrange themselves in different orientations with respect to the planar interface. This is important because the orientation of pentacene's quadrupole moment, determined by the molecular orientation relative to the plane of the interface, dominates interface energetics.[78] Since C_{60} has no quadrupole, the discontinuity of the quadrupole field at the interface leads to permanent interface dipoles, which is partly what makes this material effective at separating electrons from holes. Engineering the pentacene orientation (and thus interface energetics) can lead to device optimization. In this thesis, many different pentacene orientations are analyzed, covering a wide range of C_{60}/pentacene interface geometries.

1.3 C_{60} growth on pentacene: previous studies

1.3.1 Experimental studies of C_{60} on upright pentacene phases

Studies of C_{60}/pentacene device properties usually focus on the electronic properties (*e.g.* current-voltage curves and power conversion efficiencies).[13–16,18,19] However, there are a couple of previous studies which focus on the submonolayer growth of C_{60} on thin film pentacene: Highly ordered pentacene films can be fabricated in the laboratory using a variety of techniques,[34,79,80] but the ability to grow the desired ordered layers of C_{60} on top of a pentacene surface in an ideal layer-by-layer manner is not straightforward. Two-dimensional C_{60} growth is preferred based on a rubric that links increased structural order to

higher electron and hole mobilities.

There is some inconsistency in experimental observations regarding whether C_{60} "wets" or "dewets" a thin film pentacene surface, the former outcome being a much preferred outcome. The ability of a particle to wet a surface refers to its ability to maintain contact with the surface *via* adhesive forces overcoming cohesive forces. Itaka *et al.*[81] suggested that C_{60} wets a thin film layer of pentacene on Al_2O_3, whereas Conrad *et al.*[22] showed that C_{60} on a thin film layer of pentacene on SiO_2 does not wet the surface. Itaka *et al.* grew 20 nm-thick C_{60} films on Al_2O_3 and found that C_{60} formed crystalline grains as large as 600 nm with very smooth surfaces. Conrad *et al.* grew up to 0.25 ML of C_{60} on 1.6 ML of thin film pentacene on SiO_2 and found that C_{60} forms small three-dimensional "roughly spherical" clusters several nanometers tall. Thus, the Conrad *et al.* paper shows C_{60} dewetting the surface. Superficially, these contradictory observations could be ascribed to the difference in substrates used by the two groups, but this seems unlikely since the dielectric surfaces in each case are at least 20 Å away from the center of the C_{60} molecules (*i.e.* out of the range of influence even without a screening pentacene layer). A more likely cause is that Itaka *et al.* used a deposition rate twice as slow as that of Conrad *et al.* If the deposition rate is very high, the C_{60} molecules may not have as much chance to diffuse before they encounter another deposited molecule, thus causing a higher density of smaller islands. In order to theorize further about the growth mode of C_{60} on pentacene, by a continuum reaction diffusion theory, for example, the details of the C_{60}/pentacene kinetics (*e.g.*, energy barriers and diffusion coefficients) will need to be known. This aspect is addressed in Section 5.6.

1.3.2 Experimental studies of C_{60} on recumbent pentacene

Although nearly all of the literature on C_{60}/pentacene systems deals with upright phases of pentacene, there are a couple of references to C_{60} growth on recumbent morphologies of pentacene (refer to Figure 1.3 for pentacene structural schematics). It has been shown that one can direct the growth of C_{60} molecules into one-dimensional structures, specifically nanowires.[66] We define a C_{60} "nanowire" to be one in which the molecules are arranged linearly and spaced apart by their van der Waals diameter (~1 nm), so as to be close enough to facilitate one-dimensional charge transport. As we have defined them, nanowires have been made successfully on metals several times, but only once on an organic material—pentacene—by Dougherty *et al.*. They found C_{60} nanowires to exist on two layers of recumbent (*i.e.*, face down) pentacene on Ag(111). Chapter 6 is dedicated to the study of such a system, so the Dougherty *et al.* paper will be referenced frequently there.

Other than Dougherty *et al.*,[66] there has only been one other experimental study of C_{60} on recumbent pentacene on metal, by Yang *et al.*[60] Their studies of the near-monolayer structure of C_{60} on one monolayer of pentacene on Au,[60] suggested that the C_{60} structure on bare Au is the same as that on pentacene-modified Au, implying that pentacene molecules do not influence the C_{60} arrangement. However, this observation is due to the high C_{60} coverage which did not allow the formation of C_{60} nanowires; Dougherty *et al.* also found that higher C_{60} coverage replaces the C_{60} nanowires by larger domains of disordered C_{60} molecules. The focus in Chapter 6 is on lower coverage of C_{60} molecules, where the assembly of C_{60} nanowires is possible.

In general, research in organic electronic devices has seen an increasing fo-

cus on designing molecularly scaled materials. This has been driven by the exploitation of quantum size confinement effects of nanoparticles, nanotubes and nanowires that lead to different electronic, optical and other properties.[82–84] Nanowires, the focus of Chapter 6, have been studied for over a decade as optoelectronic devices, but the majority of those studies involved inorganic materials, ranging from Si and Ge, to II/VI and III/V materials.[85–90] Papers describing organic nanowires were considerably less common until quite recently, despite the fact that self-assembling nanowires from small molecule organic semiconductors are known to be of considerable interest for use in organic field effect transistors (OFETs).[91] The use of organic molecules for low-dimension nanostructures, like nanowires, is driven by their low cost, solution processability and the opportunity for facile large-scale manufacturability.

There has been other previous work on low-dimensional C_{60} nanowires on surfaces other than pentacene. They have generally been created on metals by taking advantage of step-edges[92–94] or anisotropic surface reconstructions.[95] On organic materials other than pentacene, there have been findings of ordered low-dimensional C_{60} arrangements, such as may be assembled on trans-BCaTBPP,[96] graphene,[97] and α-sexithiophene.[98] However, in all these cases, the C_{60} molecules were spaced relatively far apart, held in place by the geometry of a suitably accommodating organic substrate, but too far apart to optimize charge transport.

1.3.3 Experimental studies of the inverse junction: pentacene on C_{60}

Although the focus of this thesis is C_{60} growth on pentacene (and not the reverse) it is worth pointing out the differences with the inverse systems. Wang *et al.*[18] compared the C_{60}/pentacene heterojunction to the inverse heterojunction, pentacene on C_{60}, finding much lower charge carrier mobilities in the C_{60}/pentacene case than for pentacene/C_{60}. They speculated that this is due to the difference in molecular orientation of the molecules at the interface. There is some discrepancy in the literature about how pentacene grows on C_{60}. Al-Mahboob *et al.* found that the first layer of pentacene lies flat at the C_{60} surface, while subsequent layers adopt the upright orientation. This is similar to behavior found of pentacene grown on some metals.[56,74] On the other hand, Dougherty *et al.* found an initial upright phase of pentacene on C_{60}/Ag(111). Experimental preparation is likely to play a large role on the molecular organization at the interface, but there is still a lack of fundamental understanding of what drives the morphology of the C_{60}/pentacene interface.

1.3.4 Static and dynamic simulations of C_{60} thin film growth

In addition to the experimental work mentioned previously, there has been a handful of very interesting theoretical and simulation work performed on the C_{60}/pentacene interface. As mentioned in Section 1.2.3, there has been some quantum mechanical work done on the impact of pentacene orientation on the interface electrostatics. Linares *et al.* used quantum mechanics and microelectrostatic calculations of molecular aggregates of C_{60} on recumbent pentacene,

and found that the interfacial dipole moment is very sensitive to lateral molecular positioning (*i.e.*, where the C_{60} is positioned over the recumbent pentacene molecule).[99] Similarly, Yi *et al.* used quantum mechanics methods to study charge carrier behavior at C_{60}-recumbent and C_{60}-upright pentacene interfaces; they found that there is significant charge recombination for C_{60}-recumbent pentacene interfaces.[77] Verlaak *et al.* confirmed this with microelectrostatic computations, showing that C_{60} at recumbent pentacene interfaces is more electrostatically "reactive".[78] In light of this information, one might think that C_{60} on recumbent pentacene devices would give poor performance due to charge recombination; however, if such devices are fabricated at very small length scales, where charge carriers only have to travel small distances to their respective electrodes, the charge recombination effect would be reduced.

Simulations of C_{60} thin film growth on pentacene at a larger scale have not been performed outside of this work. However, there have been a couple of larger-scale dynamic simulations of C_{60} growth on other materials. A recent paper by Liu *et al.*[3] combined STM experiments, coarse-grained Molecular Dynamics, and kinetic Monte Carlo (KMC) simulations to investigate the fractal growth process of C_{60} on C_{60} on graphite. Richter *et al.* used Molecular Dynamics to study C_{60} film growth on Si{100}(2×1) at shorter time scales (than would be achievable by KMC) and found that the C_{60} molecules diffuse freely when they are alone, and they become significantly less mobile in the presence of other C_{60} molecules.[100] This effect is similar to some of the results of C_{60} on pentacene that we will describe in Section 4.1.

1.4 Thesis objective

Understanding the interfacial properties of the C_{60}/pentacene heterojunction and acquiring the ability to grow ordered thin films is important for improving the performance of OPVs. Even small changes in film morphology can affect charge separation at the donor/acceptor interface, hole and electron mobility, and hence overall device performance. Interactions at the buried heterojunction depend sensitively on the atomic-level structure of the materials, and are difficult to probe experimentally. This provides the motivation for a molecular-scale computational study of the properties of organic heterojunctions, of which C_{60}/pentacene is an exemplar. In this thesis, molecular simulation is used to explore the nature of the intermolecular interactions between C_{60} and pentacene in a variety of different configurations at a mesoscopic scale.

Despite the growing number of experimental publications on the electronic properties of organic materials in general (*e.g.*, charge carrier mobilities), there has been relatively little simulation work on organic electronic materials compared to inorganic ones. There are some recent publications that use computational means to study organic electronic materials, some of which involve *ab initio* studies of idealized crystal structures of a handful of molecules (often only two molecules) reflecting interest in the electronic structure of these materials.[101–103] However, resource utilization effectively prohibits *ab initio* simulations from predicting the dynamics of surface diffusion and the structures attainable during film growth. Since film structure plays a large role in determining electronic properties, there is clearly a need to coordinate *ab initio* calculations of very small systems with semi-empirical modeling of much larger systems for which simulation of thin film growth provides a good guess at the structure of

the thin film.

In this work, we focus on C_{60} interactions with a variety of different pentacene surfaces that differ most strikingly in the angles that the short and long axes make with the surface normal. First, we compare two experimentally observed upright pentacene polymorphs, the so-called "bulk" and "thin film" phases, which differ slightly in the angle adopted by pentacene's *long axis* as it stands upright on the underlying *insulating* surfaces (see Figure 1.3(b) and Figure 1.5). C_{60} has a tendency to dewet these surfaces due to the consequences of the stronger C_{60}-C_{60} interactions in comparison to those for C_{60}/pentacene, exemplifying the balance of forces that drives the preferred morphology of thin film growth in many such small-molecule organic semiconductor systems. Chapters 3 and 4 focus on molecular probes of these pentacene phases *via* molecular mechanics and Molecular Dynamics, and Chapter 5 extends this study to consider multiple C_{60} molecules on upright pentacene phases *via* kinetic Monte Carlo and a continuum reaction diffusion model. From these studies, we obtain detailed information about the interface potential energy, diffusion coefficients of C_{60} on upright phases of pentacene, and longer time- and length-scale behavior of C_{60} thin film growth though coarse grained models. Many of these properties are difficult to measure either experimentally or through continuum approaches. Thus, this information provides important insight into the C_{60}/pentacene material combination that may be crucial to device performance.

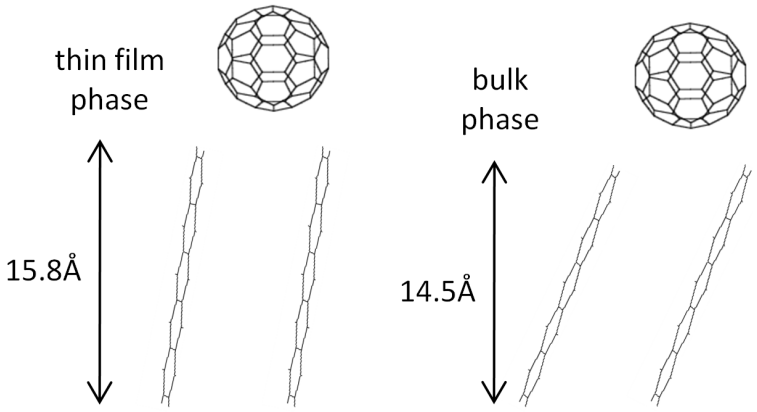

Figure 1.5: Side-view diagram illustrating the orientation and relative heights of the thin film and bulk phases of pentacene.

In addition to the upright bulk and thin film phases of pentacene, a major component of this thesis deals with studies of C_{60} on recumbent pentacene in Chapter 6. The work by Dougherty *et al.* described in Section 1.3 was the first to report a tendency for C_{60} to form nanowires in the crevices formed by the recumbent pentacene rows at sub-monolayer C_{60} coverage.[66] Such nanowire formations could offer a template for ordered C_{60} growth, facilitating a desired directional bias for charge carriers in devices. The observation by Dougherty *et al.* motivated us to ask a more overarching question: How do variations in the short-axis tilt angle affect the interactions of C_{60} with pentacene surfaces and is there a "sweet spot" for the angle made by the short-axis of the pentacene molecules to hold and/or direct the C_{60} molecules to preferred surface orientations that might lead, for example, to nanowire formation? Is there a particular tilt angle (ϕ_1 in Figure 1.3(a)) adopted by the pentacene molecules that would be particularly conducive to forming C_{60} nanowires? In experiments, there is some flexibility to vary the tilt angle of the second (and perhaps one or two more) monolayer(s) by changing the metal substrate under the pentacene, but, as we show in Tables 1.1–1.3, current studies on noble metal surfaces can only explore (off-normal) tilt angles in the ϕ=55°–90° range, depending on the specific pentacene/metal combination and the specific orientation of the pentacene. Pentacene/substrate combinations that give rise to more steeply angled (ϕ<50°) but still recumbent surfaces have yet to be reported.

This situation provides the motivation for the computational study here: Approaching the problem using simulations of an atomically explicit model of the behavior of C_{60} molecules on pentacene affords us the control to create perfectly smooth, step-free, pentacene surfaces in which we systematically vary the tilt of the surface and observe the response of adsorbed C_{60} molecules to organize

on the pentacene surface. Our overarching goal, therefore, is to conduct such a systematic study and determine conditions that are most likely to produce nanowire formation, as opposed to the more compact, fcc-like, motifs that C_{60} molecules adopt in the bulk. We hope that our predictions will spur new experimental studies of C_{60} on surfaces with roughness on the order of 2 Å and tilt angles outside those studied to date.

CHAPTER 2

COMPUTATIONAL METHODS

2.1 Ab initio methods

We give a brief overview of ab initio methods here, to give the reader a sense of their capability in light of the other simulation techniques used more prevalently in this thesis. Ab initio methods involve electronic structure calculations that in general provide extremely accurate information about electronic states, vibrational frequencies, and thermodynamic properties to name a few advantages. These methods are able to so with hardly any empirical data because, as the name suggests, the mathematical models are derived from first principles—solving (usually approximately) the Schrödinger equation $H\Psi = E\Psi$. The simplest wave function-based methods to solve the Schrödinger equation are the Hartree-Fock(HF)-based methods, which ignore electron-electron correlations. The "Møller-Plesset" perturbation theory is an extension to HF, which includes these electron correlations to the second or higher order. Function-based methods such as Density Functional Theory (DFT) are another way to solve the Schrödinger equation. These methods relate the electron density to the total ground state energy through functionals (functions of functions). For both types of ab initio methods, the mathematical approach to these solutions can become very computationally expensive for large sets of atoms. Recent parallelized versions of ab initio softwares have made significant advances in the realizable simulations of large numbers of atoms (~1000 electrons).[104] Although ab initio methods provide a large amount of detail, the use of them in this thesis is limited to verification of potential models that enable larger-scale simulations.

2.2 Choice of potential model

A key component of the Molecular Dynamics simulations that form the majority of the studies in this thesis is the choice of intermolecular potential model. Throughout this thesis we have used the molecular mechanics 3 (MM3) potential model as reported in our previous papers.[105–107] We chose this semi-empirical MM3 force field since it has been shown by its developers (and by us) to accurately describe hydrocarbons, namely three-, four-, five- and six-ringed structures of the type needed here.[108–110] MM3 incorporates stretching, bending and torsional energies as well as the van der Waals interaction energies based on atom-atom parameters related to their chemical environment.[110]

Prior to our simulations, it was necessary to verify that the MM3 model was suitable for pentacene and C_{60}. For pentacene, we had already confirmed that the MM3 potential accurately reproduced ab initio-derived MP2 (second order Møller-Plesset) intermolecular energies and predicted the correct lowest energy herringbone structure as a prelude to extensive studies that showed that the MM3 model reproduces experimental sticking coefficients and other experimentally observed phenomena.[111]

We compared the MM3 model for C_{60}-C_{60} interactions against other known potential models. The Girifalco potential model, one of the most well-known models, is based on the superposition of atom-atom potentials of the Lennard-Jones type.[1] The Pacheco potential model is based on the local density approximation to DFT, together with its extension for excited-state time-dependent DFT.[2] And lastly, the MM3-π model is the same as MM3, except with an additional π-bonding term, adding an extensive π-electron system. Figure 2.1 shows

these three C_{60}-C_{60} potential models as they compare to MM3-derived values. The equilibrium distance apart for all models is within half an angstrom, and the cohesive energies are within 0.05 eV. The software used for all molecular mechanics and Molecular Dynamics simulations in this work, TINKER, is a fully atomistic modeling package with a choice of semi-empirical potentials.[112] Since TINKER is strictly atomistic, including coarsened models for C_{60} such as the Pacheco or Girifalco model was not possible. The MM3-π model seems to match best with the DFT-derived Pacheco model, but implementing this parameter set in TINKER takes about 20 to 100 longer in execution time. Thus, unfortunately, it was not possible to run Molecular Dynamics simulations using MM3-π. Although MM3 appears to slightly overestimate the attractive interaction energy between two C_{60} molecules, it is still within 0.05 eV of the DFT derived value. MM3 has also been shown to reproduce C_{60} unit cell parameters as well as the heat of sublimation, thus we are confident that MM3 parameter set is a close enough approximation to represent C_{60}.[113,114]

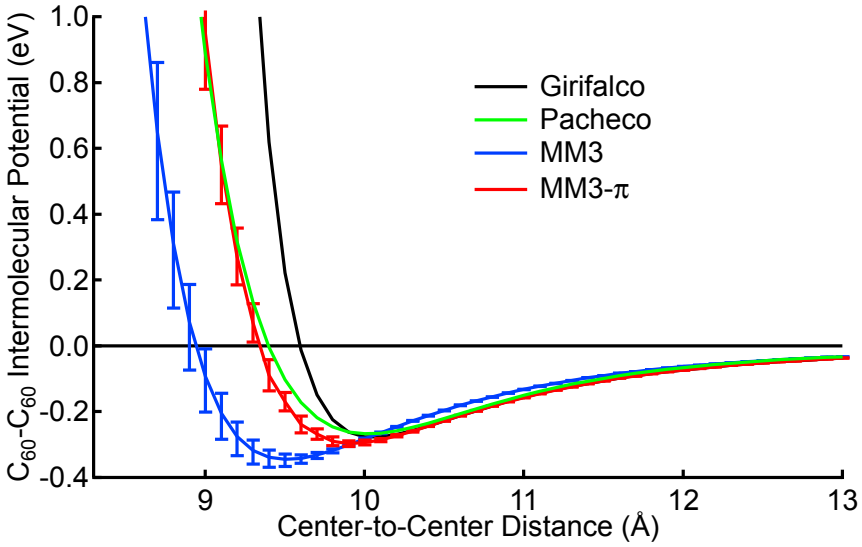

Figure 2.1: Intermolecular energies between two C_{60} molecules, calculated using different models: the Girifalco model,[1] Pacheco model,[2] and molecular mechanics-derived approach using TINKER's MM3 and MM3-π parameter sets.

A further analysis of MM3-derived C_{60}-C_{60} intermolecular potential involved calculating energies for different rotational orientations of C_{60} and then averaging these energies for each center-to-center distance to see if rotational orientation affected the intermolecular energy. Using the geometry-optimized structure of C_{60} for MM3, we calculated C_{60}-C_{60} intermolecular energy values for different orientations as a function of center-to-center distance. Figure 2.2 shows the different energies corresponding to unique configurations. We found that when two C_{60} molecules are oriented such that two apexes face each other, a larger repulsion occurs than when two planar hexagon faces face each other (see Figure 2.3 for schematics). Not surprisingly, the smaller the center-to-center distance, the more the spread in energy between these two orientational extremes, giving larger standard deviations to the average energies at closer distances. For example, at a distance of 8.6 Å, the C_{60}-C_{60} intermolecular potential energy is +1.1±0.3 eV, and at 9.5 Å, it is –0.34±0.02 eV. Overall, orientational effects appear to be small at the distances encountered in the systems considered here, which are typically greater than 9.5 Å.

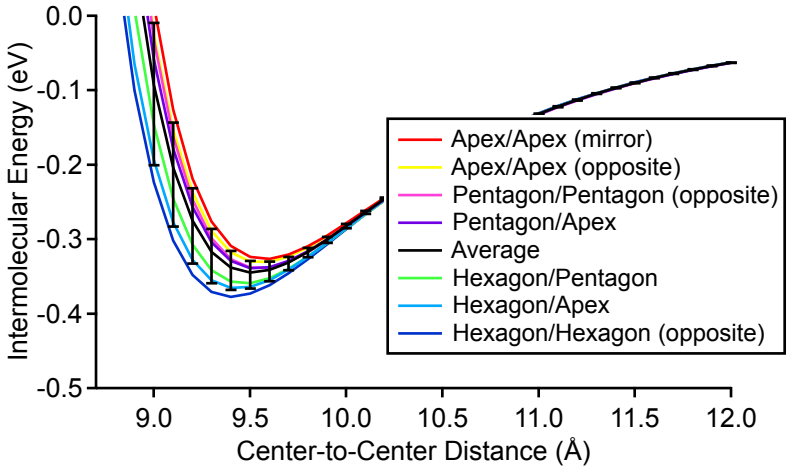

Figure 2.2: Intermolecular energies between two geometry-optimized C_{60} molecules, calculated at different orientations using static energy calculations and the MM3 potential in TINKER. See Figure 2.3 for meanings of "mirror" and "opposite".

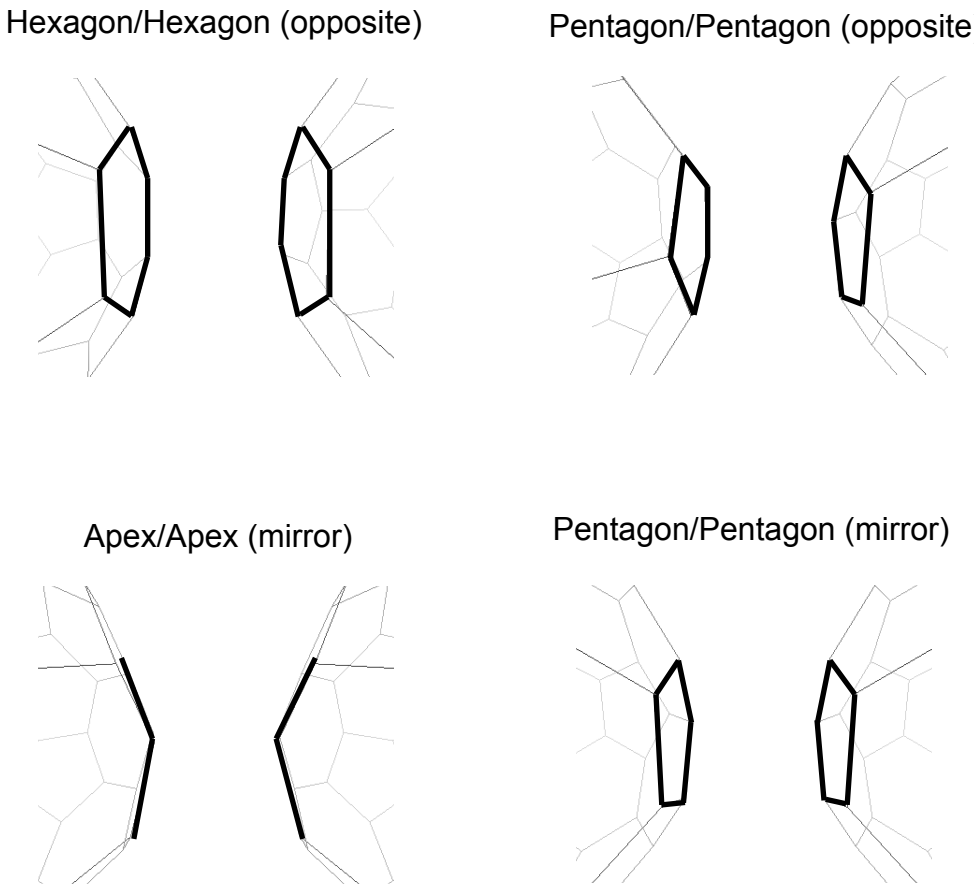

Figure 2.3: Facet-to-facet schematics for C_{60} intermolecular energy calculations in Figure 2.2. "Mirror" means the C_{60} molecules at the interface are mirror images of one another, and "opposite" means the opposite of "mirror".

2.3 Molecular Dynamics (MD) methods

2.3.1 Classical MD

Molecular Dynamics is a classical approach, consisting of numerical, step-by-step, solutions of Newton's equations of motion. The forces at each time step are calculated according to Equation 2.1, where the force on atom is derived from a potential energy $U(r)$. This potential function consists of non-bonding interaction terms (*e.g.*, Lennard-Jones, Coulombic potential) and bonding interaction terms (*e.g.*, intramolecular bonding and bending). The $U(r)$ function for the MM3 potential used in this work is summarized by Equation 2.2, where the form and parameters for each term can be found in references 108–110. There was a later release of MM3 in 2000, which included molecular polarizability, induced dipole moments, and electron correlation in conjugated systems.[115,116] TINKER includes this updated version of MM3. In Equation 2.2, U_s is a bond stretching term, U_θ is an angle bending term, U_ω is a torsion term, $U_{s\theta}$ is a stretch-bend term, $U_{\omega s}$ is a torsion-stretch term, $U_{\theta\theta'}$ is a bend-bend term, and U_{vdw} is a softened van deer Waal's term.

$$f_i = -\frac{\partial}{\partial r_i} U \tag{2.1}$$

$$U = U_s + U_\theta + U_\omega + U_{s\theta} + U_{\omega s} + U_{\theta\theta'} + U_{vdw} \tag{2.2}$$

In TINKER,[112] the MD software package used in this thesis, the Beeman integration method was used to obtain positions, velocities, accelerations and rel-

evant system energies at each integration step (a time step of 0.5 fs). For most simulations, a short thermalization run of 5 ps was performed using a canonical ensemble (NVT), in which a specified equilibrium temperature is achieved and maintained using a Berendsen thermostat. Once the system reached the desired temperature without significant fluctuations (±<3 K), the simulation was continued using a microcanonical ensemble (NVE), which maintains constant energy, for a further few nanoseconds. The average local pressure in the system was 10±210 atm, exhibiting the typical large pressure fluctuations seen in NVE simulations.

Classical MD methods are used for a variety of materials simulations. However, more relevant to this work, there has been some recent computational effort using MD techniques to predict surface phenomena of organic materials for a variety of applications.[117–121] Wang *et al.*[120] used MD to study self-diffusion mechanisms of pentaerythritol tetranitrate (PETN) on the (110) surface of crystalline PETN. They showed that PETN was stable at off-lattice sites, that it diffused along specific directions of the crystal, and that the site-to-site energy barrier was roughly 0.1 eV. As will be seen Section 3.1, these observations of off-lattice site stability and anisotropic diffusion are also seen in the results for the C_{60} on upright pentacene system studied here.

2.3.2 Potential energy surfaces

Potential energy surfaces (PES) are generally obtained by either quantum mechanical or empirical methods to calculate the ground-state electronic energy surfaces to model chemical reactions or physical interactions. In this work, we

obtain potential energy surfaces by means of molecular mechanics in a semi-empirical way, and we are interested in the physical interactions between adsorbents and substrates. It is common to utilize potential energy surfaces for bringing insight into diffusion mechanisms.[122,123] There is a clear relationship between observed diffusion and features of an underlying adsorbent-substrate PES because diffusion occurs by hops between low-energy sites on a PES. From this type of information, energy barriers and diffusion rates can be extracted, which is vital to understanding kinetics of thin film growth.

In several sections throughout this thesis, we calculate the potential energy surfaces that would arise from the adsorption of a C_{60} molecule. These energy surfaces provide insight into the manner in which a C_{60} molecule probes the different pentacene surfaces and any tendency to favor lower energy sites. The potential energies were calculated statically using the TINKER software with the MM3 potential, as described previously.

2.4 Kinetic Monte Carlo (KMC) methods

There are two main variants of Monte Carlo methods: Metropolis Monte Carlo (MC) and kinetic Monte Carlo (KMC). Both are mesoscopic descriptions of systems based on probabilistic data. MC methods are often used to obtain equilibrium properties of multi-particle systems.[124] A Metropolis Monte Carlo move involves performing a trial move and evaluating the subsequent acceptance or rejection based on probabilities and a random number. Each step in MC corresponds to a trial configuration and hence there is no time trajectory through phase space. In contrast, the KMC method (also known as rare event or dy-

namic Monte Carlo Method and the Gillespie algorithm[125]) involves performing a move based on known rates and a random number, where a move is associated with a time increment. In this work, we focus on KMC methods because of our interest in the evolving nature of thin film growth with time.

In order for KMC to be implemented, three things are needed: a representation of the underlying lattice of the system, *i.e.*, a set of allowed locations for particles to occupy, a set of possible event types (*e.g.*, edge diffusion, reaction, deposition, *etc.*), and the rates associated with these defined events. The latter is perhaps the most important part in getting meaningful results; this is why Chapter 5 is devoted largely to cataloguing event rates. The basic algorithm of KMC is shown in Figure 2.4. Essentially, at each "step" in the algorithm, an event is chosen based on a random number targeted at a normalized cumulative sum of all possible event rates. Next, a particle that is able to undergo that chosen event is picked at random and the event is carried out for that particle. The event rates are then recalculated based on the new configuration, and time is updated by $\Delta t = -\ln(u)/\sum R_i$, where R_i is an event rate and u is a random number $\in (0,1]$. The time step is based on the assumption that the probability of one event occurring in the time step with $\sum R_i dt$ occurrences is a Poisson random number.

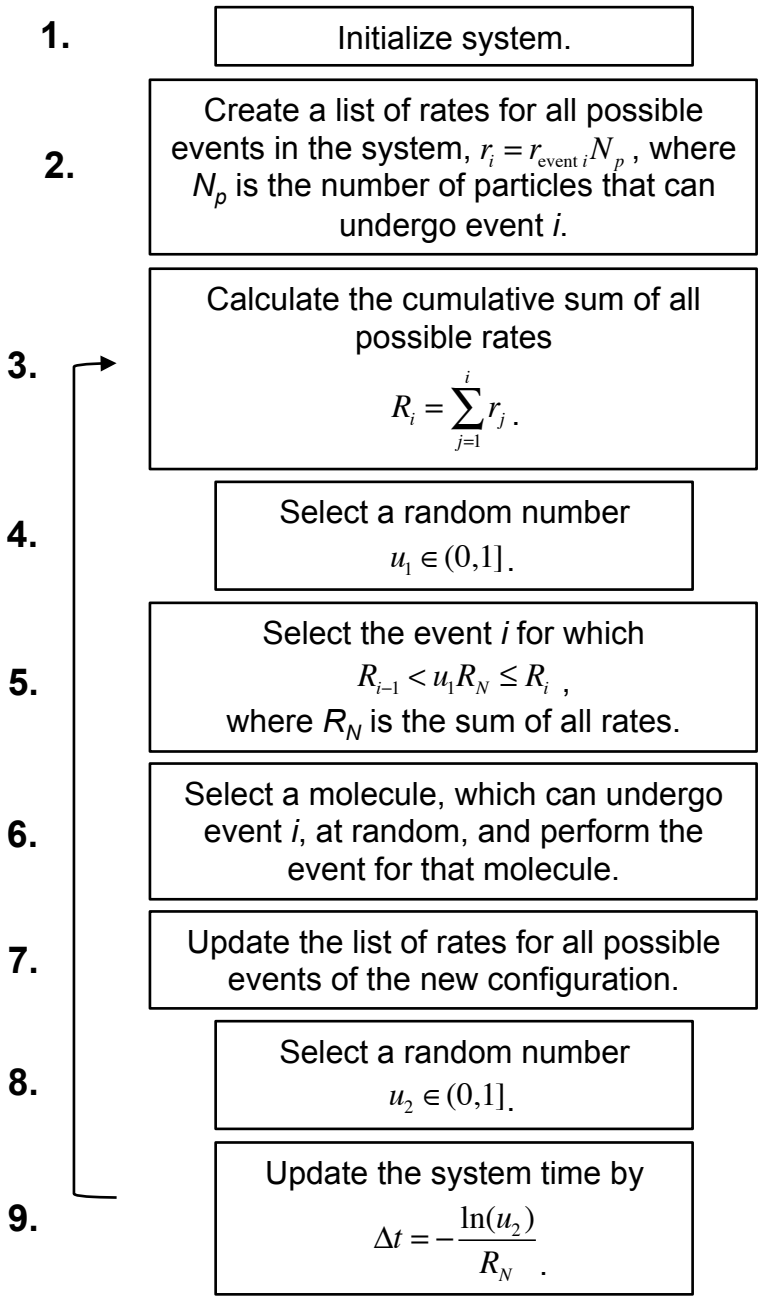

Figure 2.4: Basic algorithm for kinetic Monte Carlo (KMC).

The KMC method is useful for modeling thin film growth because it has the advantage of being able to predict film structure by explicitly accounting for the individual processes that directly shape the film growth. While mean-field theories are very useful for predicting island densities and critical cluster sizes, they generally do not capture the detailed morphology that results from simulating the delicate kinetic balance among the interactions between individual particles. The literature on KMC models of thin film growth is quite expansive, including mainly homo-[126–128] and some heteroepitaxial[129–131] growth, the latter of which is the focus of this work. One of the challenges that comes from simulating heteroepitaxy involves the lattice mismatch between crystalline materials; the general approach then is to assume that the particles adopt the substrate lattice or an otherwise simple lattice,[129–131] so there is only one lattice. There has only been one instance in the literature of a particle-on-substrate KMC simulation which involves multiple lattices.[132] In his dissertation, Hoffmann[132] details a multi-lattice setup where two lattices are defined based on environmental conditions of the CO/Pd(100) system. The KMC algorithm that we developed for heteroepitaxy, described in Section 5.1, also has a multi-lattice setup, which has its own unique rules based on knowledge obtained from Molecular Dynamics as described in Chapter 3.

There has been only one other KMC paper in the literature which simulates C_{60}, a study of thin film growth on itself. Liu *et al.* found fractal-dendritic growth of second-layer C_{60} islands on compact first-layer C_{60} islands deposited on graphite substrate.[3] Their island morphologies agreed very nicely with STM images taken under comparable experimental conditions. We will revisit this work by Liu *et al.* in Section 5.2 to compare C_{60} diffusion rates on C_{60}. However, we are mainly considering submonolayer C_{60} growth on upright pentacene

phases, so a direct comparison of C_{60} island morphologies on C_{60} would be inappropriate.

2.5 Principles of surface diffusion

Surface diffusion describes the general process of particles moving on material surfaces and provides considerable understanding to the kinetics of thin film growth. This topic is extremely important in the field of semiconductors, where control of materials at the microscopic level is increasingly needed. In general, a diffusion process is a series of particle jumps from one site to another in a thermally activated fashion. If the particles indeed exhibit pure diffusive behavior, diffusion coefficients can be extracted from Einstein's equation, $\langle r^2 \rangle = 2dDt$, where $\langle r^2 \rangle$ is the mean squared displacement, d is the dimensionality, D is the diffusion coefficient, and t is time. If these diffusion coefficients are obtained at different temperatures, they should follow the form of an Arrhenius equation, $D = D_0 e^{-E_a/kT}$. From the form of this equation, energy barriers and attempt frequencies can be obtained.

Einstein's equation is based on the assumption that Brownian motion is present in the case where $\langle r^2 \rangle \sim t^n$ with $n = 1$. Anomalous diffusion can also occur, whereby $0 < n < 1$ (subdiffusive behavior) or $n > 1$ (superdiffusive behavior).[133] Subdiffusion occurs when a particle's motion is obstructed due to overcrowding or large potential barriers, or if a particle has not been observed for long enough to uncover normal diffusion. Subdiffusion has been observed for the movement of lipids on cellular membranes.[134] We note here a couple types of superdiffusion: ballistic motion and Lévy flights. If $n = 2$, the motion

is considered ballistic, as in it follows a projectile path. Lévy flights are characterized by having a step size distribution with a long tail, corresponding to large but infrequent steps ("long runs"). Lévy flights have been used to characterize some natural process such as micelle self-diffusion.[135] Much of Chapter 3 is devoted to studying trajectories of single C_{60} particles on various pentacene morphologies, and making sense of their behavior in relation to the observed diffusion coefficients and calculated potential energy surfaces. We will refer back to the diffusion classifications described here.

2.6 Deterministic approaches to thin film growth

In thin film deposition, there is a large interest in understanding the statistical properties of the island arrays. For example, a key interest involves the island density as a function of coverage, deposition rate, and temperature. A primary theoretical approach to solve such a problem is to use mean-field rate equations, which is successful in capturing the behavior of mean island densities,[136] but not island size distributions.[137–139] One of the first detailed theoretical descriptions of epitaxial growth was developed by Burton, Cabrera, and Frank.[140] In their model, the monomer density solution comes from a diffusion equation with an equilibrium boundary condition, and island boundaries moving at a velocity determined from the diffusive flux to the boundary. Modifications to this theory to include deviations from equilibrium include effects such as curvature of the boundary[141] or fast moving steps.[142] These methods still rely on the system being close to equilibrium. The so-called "island dynamics" model is a fully non-equilibrium model developed by Caflisch *et al.*, where the growth is determined by kinetic, rather than equilibrium, assumptions.[143,144] Essentially,

they employ coarse-graining in the lateral directions while retaining atomistic discreteness in the growth direction. The deterministic approach used in this work, described in Section 5.6 is a simplified mean-field approach, which assumes only monomer diffusion and circular islands. The results serve to show, in comparison to the KMC results, how the island densities evolve with coverage.

CHAPTER 3

SINGLE-MOLECULE PROBES OF C_{60} ON UPRIGHT POLYMORPHIC PENTACENE SURFACES

3.1 Effect of admolecule and substrate shape on diffusion

To determine the effect of admolecule and substrate shape on admolecule diffusion properties, we looked at different C_{60}-pentacene adsorbent-substrate combinations because these two molecules have drastically different symmetries. We carried out MD simulations for C_{60} on the surface of pentacene (Figure 3.1(a)), pentacene on the surface of pentacene (Figure 3.1(b)), C_{60} on the surface of C_{60} (Figure 3.1(c)), and pentacene on the surface of C_{60} (Figure 3.1(d)). We began by considering the diffusion of just one adsorbent molecule on a given surface, in essence, using this adsorbed molecule as a single molecular probe of the interactions between depositing molecules and substrate. In subsequent simulations, the diffusion of up to four C_{60} molecules on a pentacene surface would be studied as a means to observe the tendency of C_{60} molecules to prefer to bind to one another rather than to pentacene.

Portions of this chapter are reproduced in part from previous publications in References 105,106

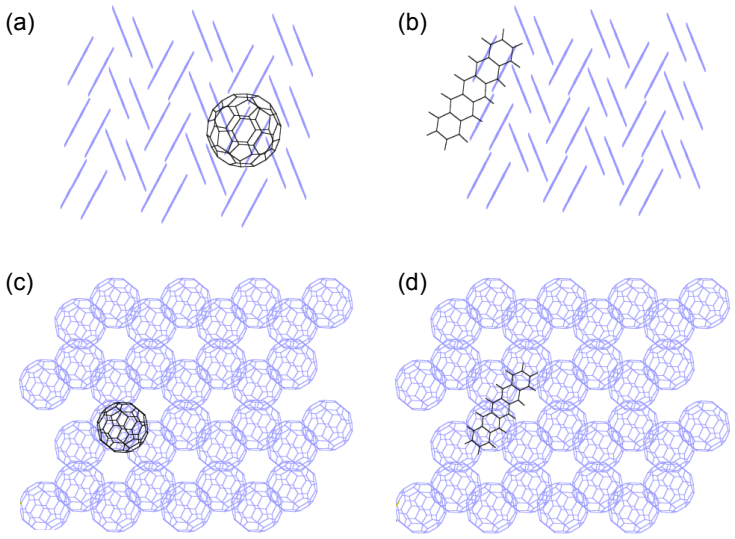

Figure 3.1: Four initial systems considered in the MD simulations: (a) One C_{60} molecule adsorbed on a pentacene surface, (b) pentacene on pentacene, (c) C_{60} on C_{60} and (d) pentacene on C_{60}. The surface molecules are represented in a lighter color for clarity and consist of two layers in each case. Periodic boundary conditions were applied to the simulation cell in the x- and y-directions.

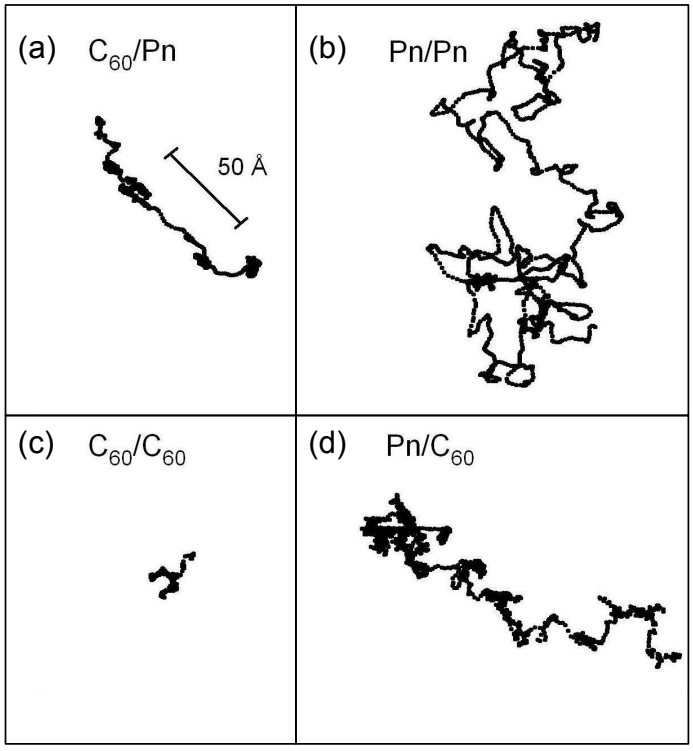

Figure 3.2: Center of mass trajectories of (a) C_{60} moving on a pentacene surface, (b) pentacene moving on a pentacene surface, (c) C_{60} moving on a C_{60} surface, and (d) pentacene moving on a C_{60} surface at 300 K; each trajectory shown is over a time period of 1.5 ns.

In each case, the computational system consisted of two substrate layers with the bottom layer fixed and the top layer free to move. For the C_{60}/pentacene system, system sizes of 3×3 and 4×4 surface unit cells (in the *x*-*y* direction) were considered in order to test the effects of finite system size. A 3×3 system size involves 1,356 total atoms, whereas a 4×4 system has 2,364 atoms—corresponding to a large increase in computational cost. The resulting mean-squared displacements of C_{60} on pentacene showed a negligible difference between the two system sizes, implying that the 3×3 system is sufficient to properly capture the dynamics.

Simulations of all the systems reported here were repeated three times, each simulation followed for 1.5 ns with an integration step of 0.5 fs (*i.e.*, 3,000,000 time steps). The average local pressure in the system was 10±210 atm, exhibiting the typical large pressure fluctuations seen in NVE simulations. Each system of three runs was carried out at eight different temperatures between 225 and 400 K, designed to cover a range of temperatures similar to that used in experimental studies of C_{60} on the surface of pentacene.[14]

Figure 3.3 shows the trajectories of single C_{60} molecules as each traverses the pentacene surface at different temperatures. The diffusion of C_{60} on a pentacene surface displayed considerable anisotropy which is unlike the self-diffusion trajectories of pentacene on a pentacene surface or of C_{60} on C_{60}. Figure 3.2 shows a comparison of the center-of-mass trajectories of C_{60}/pentacene, pentacene/pentacene, C_{60}/C_{60}, and pentacene/C_{60} at room temperature. In cases where pentacene is the substrate, the trajectories appear to follow distinct trends (running along preferred directions), whereas, in the C_{60}-as-substrate cases, there is no clear direction of diffusion. At all the temperatures tested for the

C_{60}/pentacene system, there appear to be preferences for "runs" of the C_{60} admolecule, punctuated by periods of residence at certain clearly identifiable sites on the substrate's lattice; this type of behavior is akin to Lévy flights, which are described in Section 2.5. At and below room temperature, many trajectories tended to follow valleys between the pentacene rows (the $[1\bar{1}0]$ direction that intercepts the $(0,{}^{1}/_{2},0)$ point in the unit cell), which implies that the substrate topography influences the C_{60} molecule's trajectory. The fullerene molecules show a tendency to get trapped in "wells" sited between the hydrogen atoms of the top pentacene molecules, suggesting that there is a site-hopping energy barrier. As expected, the degree of anisotropic diffusion decreases with increasing temperature, as can be seen in Figure 3.3. Once the temperature reaches about 325 K, diffusion across the surface takes on a more random walk-like appearance.

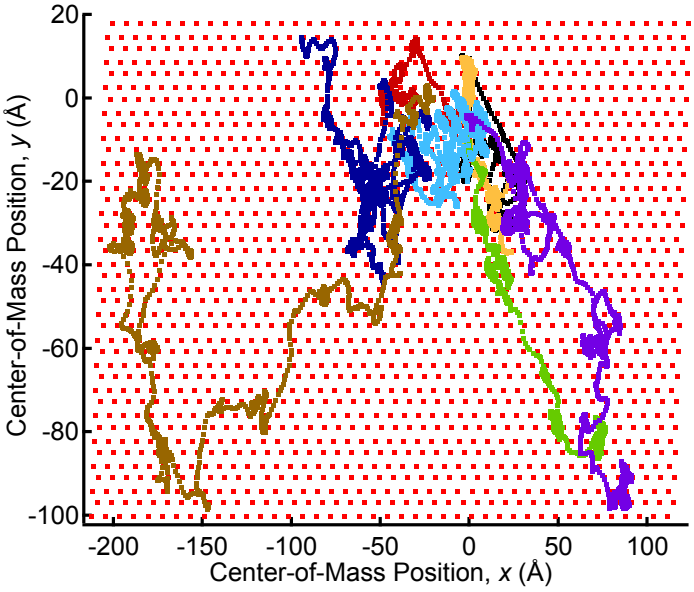

Figure 3.3: Trajectories of a C_{60} molecule over the surface of pentacene taken from 1.5 ns MD simulations at temperatures from 225 to 400 K. The red dots correspond to the time-averaged positions of the top hydrogen atoms on the topmost pentacene layer of the substrate. Trajectories of C_{60} are shown in colors to represent the C_{60} center-of-mass position at 1-ps intervals at a specified temperature. The temperatures represented are 225 K (black), 250 K (maroon), 275 K (orange), 300 K (green), 325 K (light blue), 350 K (dark blue), 375 K (purple), and 400 K (brown).

After realizing this strange behavior of C_{60} on bulk phase pentacene, we compared it to the other main polymorph of upright pentacene, the thin film phase. We performed a similar set of MD simulations of a single C_{60} molecule on the thin film phase, where the computational system consisted of two pentacene layers with the bottom layer fixed and the top layer free to move. We also re-ran some of the MD simulations on bulk phase pentacene so that for both sets, each unique-temperature simulation was repeated 10 times each, and the system size consisted of 5×5 pentacene unit cells (50 molecules). The larger system size was chosen to effectively eliminate spurious system-size effects at the expense of larger computational cost. For simulations of C_{60} on bulk and thin film pentacene, the coordinates of the center of mass of the adsorbed molecule were tracked, as before, to allow us to calculate surface diffusion coefficients, perform an energy barrier analysis, and to undertake an adsorption energy surface mapping of the C_{60}/pentacene systems using a combination of MD and static total-energy calculations.

Comparing the nature of the C_{60} diffusion behavior on the two experimentally observed pentacene phases (thin film and bulk), we found interestingly different behavior. Figures 3.4(a) and (b) shows plan views of their MD-determined trajectories at 300 K for each phase. Each point on the graphs represents the C_{60} center-of-mass point location at 1 ps intervals for a total of 2000 points, or 2 ns. The most obvious difference between these two trajectory images is that there appears to be a strong anisotropic diffusion component for the C_{60} diffusion on bulk-phase pentacene (Figure 3.4(a)), showed before to move in preferred directions over the surface. This is not found on the thin film phase pentacene, Figure 3.4(b), which resembles a typical random walk over the surface. Since the only difference between these two systems is the pentacene

phase, there is something implicit about the nature of the bulk phase pentacene that causes the C_{60} molecule to diffuse anisotropically. To explore this difference, we first consider the physical characteristics of the systems. Based on the unit cell parameters of the bulk and thin film phases of pentacene, the differing angle of the film with the underlying surface gives rise to a vertical distance of a thin film phase layer of 15.8 Å, while that of the bulk phase is only 14.5 Å, as shown in Figure 1.5. In terms of molecules per unit area of the pentacene (001) surface, the surface density of the thin film phase is 7% higher than that for the bulk phase. A higher surface density suggests a less corrugated surface with less prominent places for the C_{60} molecules to get trapped. This suggestion is borne out by the diffusion behavior (Figure 3.4(a)) where there are more locations of extended occupation in the bulk phase than in the thin film (Figure 3.4(b)), suggesting that the former has corrugations that hinder diffusion.

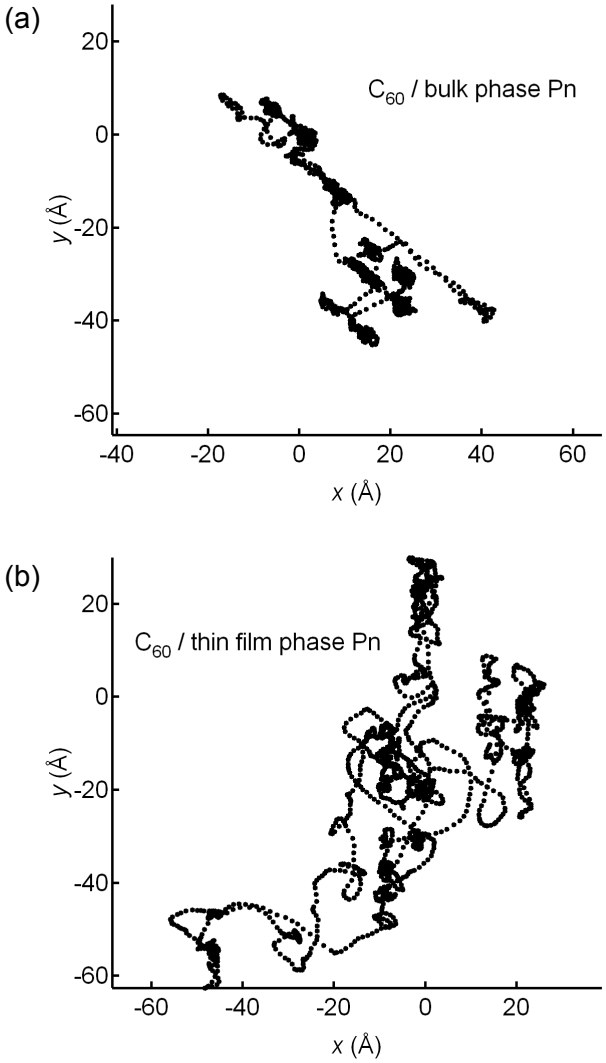

Figure 3.4: MD-generated *xy* trajectories of the center of mass of one C_{60} molecule on (a) bulk phase pentacene and (b) thin film phase pentacene. The black dots represent the location of the molecule at 1 ps increments, for a total of 2 ns each.

3.2 Potential energy surface comparison

Each energy value shown in the contour plots (Figure 3.5, for instance) represents the energy between one C_{60} molecule and the pentacene surface, so as to roughly represent adsorption energy at different points along the surface. The increments in the *x*- and *y*-directions by which the C_{60} scanned the surface were chosen such that there was no increment step greater than 0.4 Å for a given system. Although C_{60} is approximately spherical, it has faceted edges which slightly influence the adsorption energy. Thus, for each point along the surface, the adsorption energy was calculated by averaging over 10 random orientations of the C_{60} molecule to smooth out any contributions from the non-sphericity. We also considered the height of the C_{60} above the surface at different points along the surface. For each set of *x*-*y* points, we determined the height above the surface that gave the minimum energy (chosen to within 0.1 Å in the *z*-direction). The structures of the thin film and bulk pentacene substrates used in these calculations were given by their known triclinic unit cell lattice parameters as described in Section 1.2.2. This method was used to obtain the adsorption energy surfaces of C_{60} on the bulk and thin film pentacene phases discussed here as well as on the recumbent pentacene structures described in Section 6.1.2.

Considering the anisotropic diffusion pattern observed in Figure 3.4, we wanted to see how this related to the bulk phase potential energy surface. Figure 3.5 shows that, per unit cell, there are two distinct minima present (the most intense aqua color) and two maxima (the most intense pink color). The lowest-energy positions were not intuitively obvious; indeed, they were difficult to predict based on the geometric positions of the top hydrogen atoms on the pentacene molecules; thus the potential energy surface provides a convenient way

to determine exactly where the energy minima lie. On this surface energy map, we overlaid the trajectory of C_{60} on pentacene obtained from a typical MD run at 225 K. This confirmed that the observed "traps" for C_{60} molecules on the pentacene surface seen in the MD run correspond to low-energy locations on the surface predicted by potential energy surface and that the anisotropy coincides with patterns in the contours. Depending on the energy well to which the C_{60} would "jump," the saddle point energy barrier ranges from 0.02 eV (~kT at room temperature) to 0.12 eV.

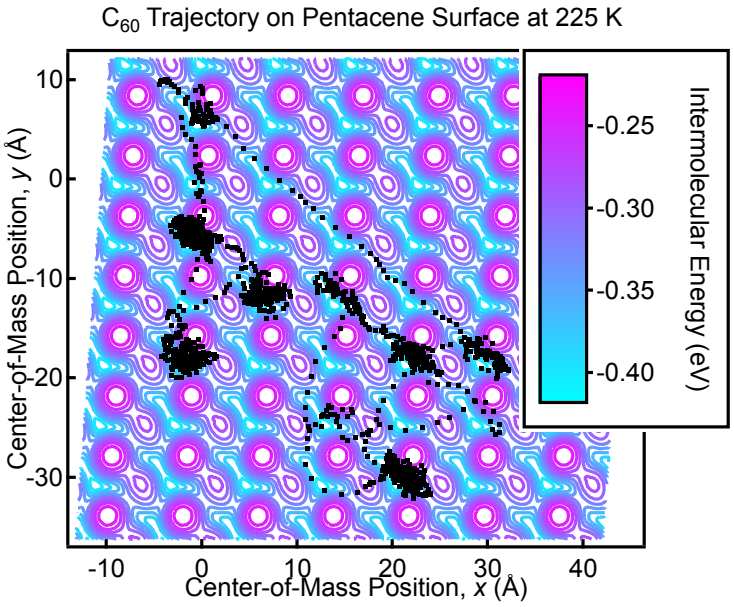

Figure 3.5: Surface interaction energy between a C_{60} molecule and the bulk phase pentacene surface (covering 56 unit cells) to differentiate higher energy (pink) and lower energy (aqua) regions. The energy surface is overlaid with a trajectory from an MD simulation of C_{60} on bulk phase pentacene at 225 K, shown as black dots), demonstrating the close correlation between energy minima and preferred diffusion paths.

In order to determine how often the C_{60} molecule encounters these energy barriers, it is necessary to consider the kinetic energy relative to the energy barriers. For simplicity, we considered this analysis for the bulk phase pentacene only. If the kinetic energy is much larger than the energy barriers, the C_{60} admolecule will exhibit Brownian-like motion; if the kinetic energy is smaller than the energy barriers, the C_{60} admolecule will exhibit activated site-to-site hopping. Figure 3.6(a) shows the total kinetic energy of the C_{60} admolecule at 225 K and 400 K as a function of simulation time. The kinetic energy was calculated post-simulation by the sum of translational and rotational kinetic energies and assumes the C_{60} to be a perfect rigid-body sphere. Figure 3.6(b) shows the four different saddle point energy barriers (black lines) and the largest possible energy barrier (red line) on the surface of pentacene. It should be noted that the fluctuations in the kinetic energy are probably due to an exchange of energy between the C_{60} admolecule and the pentacene substrate. At 225 K, the molecule can invariably overcome the energy barrier along path 1 (shown in Figure 3.6(b)), which resembles a valley. It can often travel along paths 2 and 3, less often along path 4, and rarely over the largest possible energy barrier. Looking at the effect of temperature, the C_{60} molecule at 225 K spends about 70% of its time with kinetic energy below the saddle point barrier 3 (confining it in the valley) whereas, at 400 K, it only spends about 40% of its time confined in the valley. Correspondingly, the 225 K trajectory (black dots in Figures 3.3 and 3.5) exhibits motion akin to what has been described as a "sub-diffusive" process,[145] where the adsorbed molecule seems immobilized in certain sites, occasionally hopping to the next one. In contrast, the 400 K trajectory (brown dots in Figure 3.3) resembles Brownian motion with little or no energy barrier to retard the motion of the adsorbed molecule. It is possible that in the limit of

longer timescales than are accessible by Molecular Dynamics, this sub-diffusive behavior would disappear, replaced by random walk-like diffusion.

To further explore the origin of the hindered diffusion for the bulk phase compared to the thin film phase (as shown in Figure 3.4), we consider now a close comparison of the details of the pentacene surface experienced by a C_{60} molecule through adsorption energy surfaces of C_{60} on bulk (Figure 3.7(a)) and thin film phases (Figure 3.7(b)). It is clear from these contour energy plots that the bulk phase (Figure 3.7(a)) pentacene has deeper energy wells (and higher energy peaks) that a C_{60} molecule can access in comparison to the thin film phase. This is supported by the evidence of trapping shown in the MD trajectories in Figure 3.4(a). In addition, the anisotropy of the adsorption energy surface is manifest in the diagonal low-energy "valleys" (shown in aqua) and the differences between two types of energy peaks that form between the pentacene molecules. These diagonal valleys correspond to the anisotropic "runs" of C_{60} shown in Figure 3.4(a). In contrast, the adsorption energy surface of the thin film phase in Figure 3.7(b) is relatively symmetric, with no clearly preferred direction for a C_{60} molecule to traverse and with a set of roughly equivalent and less steep energy peaks.

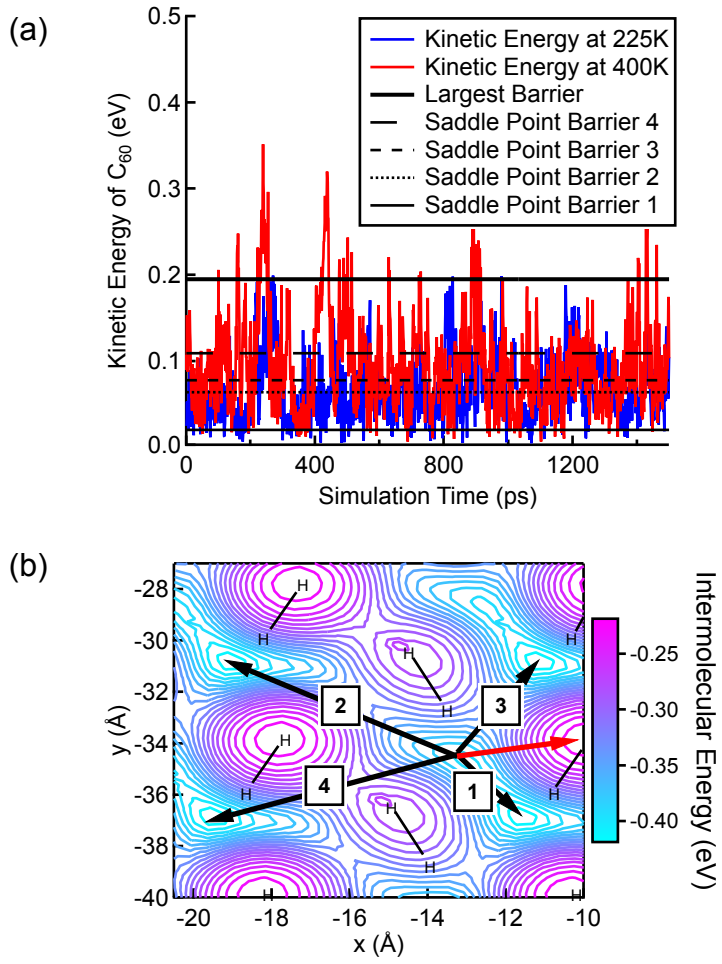

Figure 3.6: (a) Kinetic energies of the C_{60} admolecule while diffusing on bulk phase pentacene at 225 K and 400 K compared to energy barriers along specific directions. (b) Directions of the four saddle point energy barriers (black lines) and the largest energy barrier (red line) overlaid on the potential energy surface of C_{60} on bulk phase pentacene.

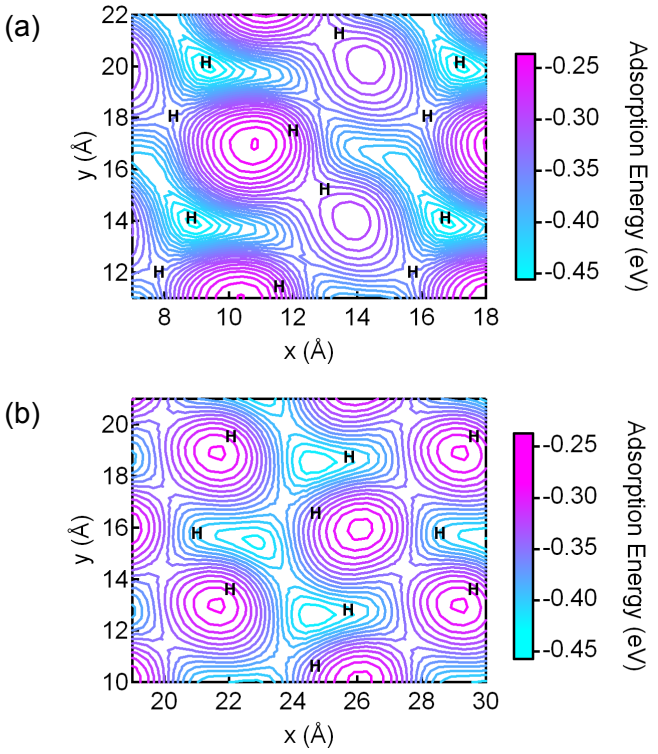

Figure 3.7: Adsorption energy maps of C_{60} on (a) bulk and (b) thin film phases of pentacene. The H letters indicate the location of the top hydrogen positions of the pentacene molecules with which the C_{60} molecules are in contact. Magenta colors signify high-energy areas; aqua colors signify low-energy areas.

3.3 Calculation of diffusion coefficients

So far, we have considered the diffusion of C_{60} on bulk phase pentacene, C_{60} on C_{60}, pentacene on C_{60}, pentacene on pentacene, and lastly C_{60} on thin film phase pentacene. First, we will consider a diffusion coefficient comparison of the first four, the systems of which are represented by Figure 3.1 Second, we will consider a more involved diffusion coefficient comparison of C_{60} on bulk phase pentacene to that of C_{60} on thin film phase pentacene.

Surface diffusion coefficients of molecules or atoms on organic surfaces are not well known. For non-organic substrates, room temperature surface diffusion coefficients of hydrogen on tungsten are on the order of 10^{-7} cm^2/s, while that of propane on silica is on the order of 10^{-3} cm^2/s.[146] As will be shown, the room temperature surface diffusion coefficient of C_{60} on the surface of pentacene falls somewhere in between these two examples. The surface diffusion coefficient, D, was obtained using the Einstein equation (Equation 3.1), where $\langle r^2 \rangle$ is the observed mean-square displacement of the diffusing admolecule, d is the dimension of the range of significant movement (2 in the case of surface diffusion), and t is time. The mean-squared displacement was measured as an ensemble average over varying time intervals (141 time origins at 100-ps intervals). Plotting $\langle r^2 \rangle$ as a function of time, t, the diffusion coefficient is found from the slope (divided by 4) at long times.

$$\langle r^2 \rangle = 2dDt \tag{3.1}$$

Figure 3.8 shows the calculated surface diffusion coefficients as a function of temperature for the four systems shown in Figure 3.1. The general trend

in each case is the expected increase in diffusion coefficient with temperature. Data for the pentacene/pentacene systems appear to display greater variance in surface diffusion coefficients compared to the other systems. This is due to the larger average surface diffusion coefficient values. The coefficients of variation for the pentacene/pentacene system for all data points were less than one, indicating low variance as displayed by the other systems. The most notable trend in Figure 3.8 is the roughly two orders of magnitude difference between diffusion coefficients in the pentacene/pentacene and C_{60}/pentacene systems (see Table 3.1). The magnitude of the diffusion coefficient is highest for pentacene on pentacene (on the order of 10^{-4} cm^2/s), followed by pentacene on C_{60} (a factor of four slower), then C_{60} on pentacene (a factor of five slower still) and, finally, C_{60} on C_{60} (nearly 2 orders of magnitude slower). At these temperatures, the diffusion coefficient for C_{60} on C_{60} is quite small, about 2.5×10^{-6} cm^2/s, which agrees with the relatively immobilized behavior of C_{60} on C_{60} shown in Figure 3.2(c); this seems to imply a strong interaction between C_{60} molecules.

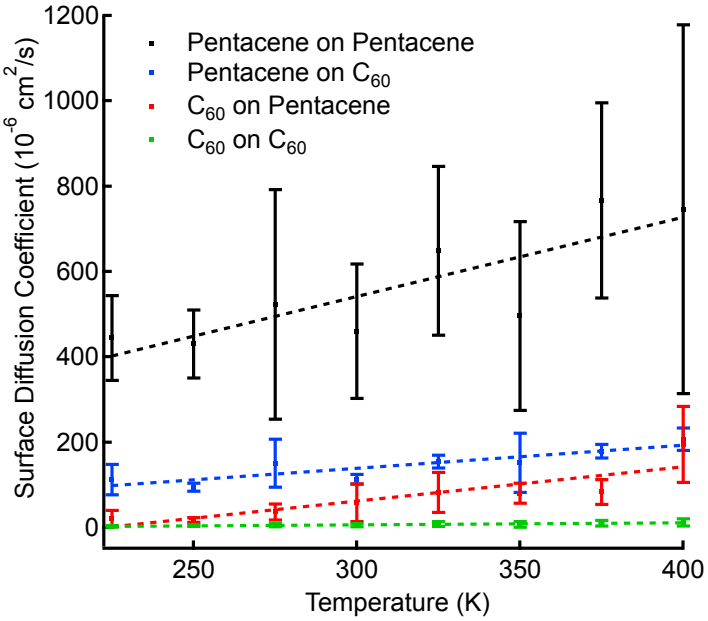

Figure 3.8: Surface diffusion coefficients versus temperature averaged from several 1.5 ns MD simulations. Five pentacene/pentacene simulations were included in the averages shown; the rest were run three times. Dotted straight lines are added to guide the eye.

Table 3.1: Average surface diffusion coefficients for pentacene on pentacene, pentacene on C_{60}, and C_{60} on C_{60} (first three diffusion coefficient columns) compared to that for one, two, and three molecules of C_{60} diffusing over a pentacene surface (last three columns). Pentacene is abbreviated as Pn, and all Pn substrates considered in this data are bulk phase pentacene.

Temperature (K)	Average surface diffusion coefficient ($cm^2/s \times 10^{-6}$)					
	1-Pn/ Pn	1-Pn/ C_{60}	1-C_{60}/ C_{60}	1-C_{60}/ Pn	2-C_{60}/ Pn	3-C_{60}/ Pn
225	445	112	2	22	1	2
250	431	94	5	18	14	4
275	523	151	6	37	11	5
300	461	114	6	58	14	9
325	649	158	9	83	21	16
350	498	152	8	81	36	21
375	767	179	11	84	25	8
400	747	208	12	195	66	38

The scale of differences in diffusion coefficients for the four single-admolecule systems was unexpected, perhaps highlighting the fact that differences in admolecule shape and, ultimately, intermolecular forces strongly influence interfacial dynamics. For each substrate, the pentacene admolecule exhibited larger surface diffusion coefficients than the C_{60} admolecule. This can most likely be attributed to the differing geometry of the two molecules. The admolecule's point of contact with the surface is smaller for C_{60} than for pentacene, making it more likely for C_{60} to get trapped in troughs on the surface and have a lower surface diffusion coefficient. This is further evidenced by the C_{60} trajectories in Figures 3.2(a) and (c) as compared to the pentacene trajectories in Figures 3.2(b) and (d).

Considering the temperature dependence of the observed C_{60}-on-bulk pentacene diffusion, Figure 3.9 shows the average value of the natural logarithm of the diffusion coefficient, $\ln(D)$, taken over three simulation runs. The average value appears to follow Arrhenius-like behavior, but, given fairly substantial error bars, the system cannot be unequivocally identified as such. Nonetheless, if we assume Arrhenius behavior and use a linear fit to the data shown in Figure 3.9, values for the prefactor (D_0) and activation energy (E_a) in the Arrhenius equation (Equation 3.2), were found to be roughly 2×10^{-3} cm^2/s and 0.1 eV, respectively. This energy barrier of ~0.1 eV agrees with that obtained from the static potential energy surface (0.2 eV–0.12 eV). The activation energy has about the same order of magnitude as k_BT at room temperature, thus it can at least be said that the systems do not behave like lattice gases.

$$D = D_0 e^{-E_a/kT} \tag{3.2}$$

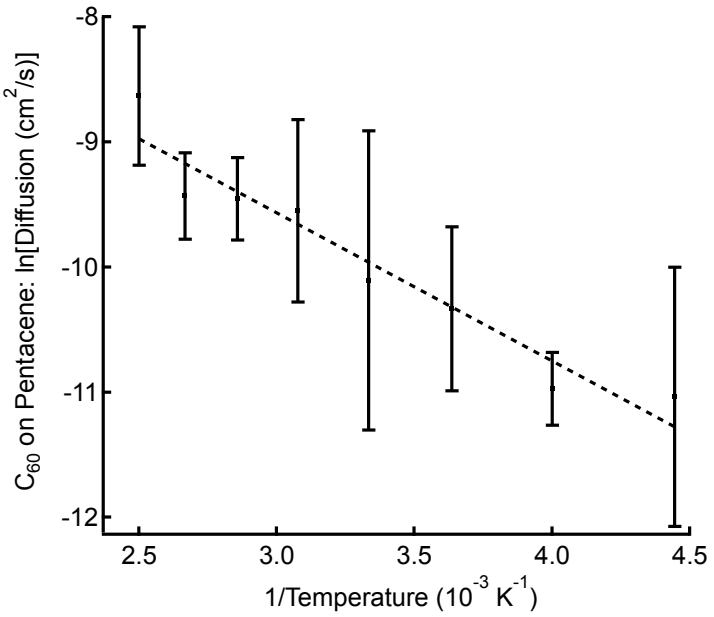

Figure 3.9: Natural logarithm of the diffusion coefficient (averaged over three runs) versus inverse temperature. A linear fit to the data was used to provide estimates of the Arrhenius prefactor, D_0, and the activation energy, E_a. The dotted straight line is added to guide the eye.

At this point, we consider the diffusion coefficient comparison of C_{60} on bulk to C_{60} on thin film phase pentacene. Using the MD trajectory data, an example of which is shown in Figure 3.4, we analyzed the two-dimensional surface diffusion behavior of C_{60} for these two systems in addition to looking at the one-dimensional anisotropic diffusion behavior in the $[1\bar{1}0]$ direction of the pentacene (001) surface. For two-dimensional diffusion, the surface diffusion coefficient, D, was obtained the same way as before, using the Einstein equation. Einstein's equation is based on the assumption that Brownian motion is present in the case where $\langle r^2 \rangle \sim t^n$, with $n = 1$. If $n > 1$, the process is said to be superdiffusive and, if $0 < n < 1$, the process is termed as subdiffusive.[133] In order to confirm which type of diffusional classification represents the motion of C_{60} on pentacene, we determine this power-law coefficient, n, from a log-log plot of the mean-squared displacement vs. time. Figure 3.10 shows the power-law coefficient, n, obtained at different temperatures for both the bulk phase and thin film phases. For both phases at all temperatures, the values for n have error bars that encompass the $n = 1$ value, thus the behavior of the C_{60} on either phase of pentacene is indeed pure diffusion.

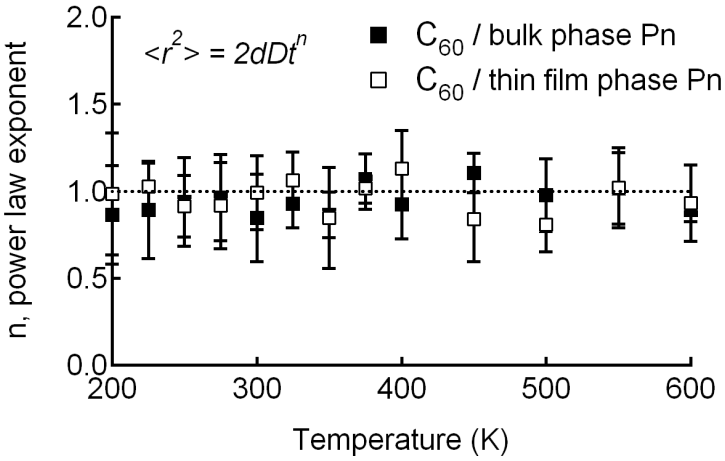

Figure 3.10: Power-law exponent, n, obtained from mean-squared displacement vs. time ($\langle r^2 \rangle$ vs. t) data from MD simulations, as a function of temperature. The exponent n is calculated from $\langle r^2 \rangle = 2dDt^n$, where $n = 1$ yields the Einstein equation and implies typical Brownian motion behavior. In all cases, the MD-derived power-law exponent is close to 1.

As before, the values of the surface diffusion coefficients were found by plotting $\langle r^2 \rangle$ as a function of time, t, and dividing the resulting slope by 4 at long times (following Equation 3.1). Figure 3.11 shows the surface diffusion coefficients of C_{60} on thin film and bulk phase pentacene. At and above a temperature of 500 K, the C_{60} molecule actually desorbed from the surface during some of the MD simulation runs, and the diffusion coefficients for those cases were not included in the averages quoted. With fewer diffusion coefficients in these cases, the average values for temperatures greater than 500 K have less statistical significance, signified by the grey background in Figure 3.11. Disregarding these higher temperatures, the surface diffusion coefficients of C_{60} on thin film phase were, for the most part, higher by about a factor of 2. This is consistent with Figures 3.4 and 3.7, showing the ability of C_{60} to become trapped in low-energy wells on the *bulk* pentacene surface, but not on the *thin film* phase of pentacene.

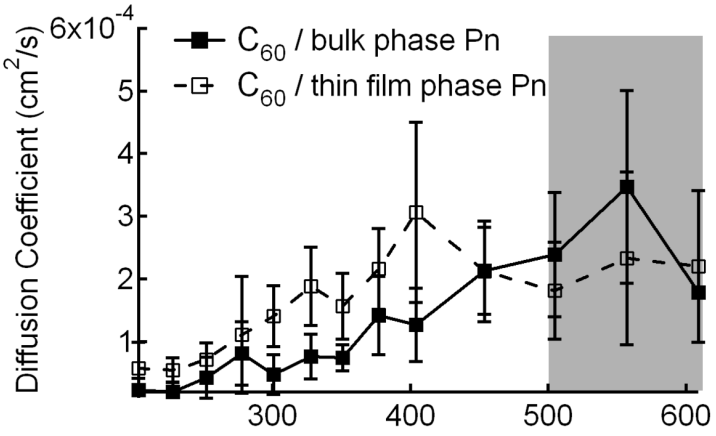

Figure 3.11: Surface diffusion coefficients of C_{60} on bulk phase pentacene (filled squares) and thin film phase pentacene (open squares) as a function of temperature. The grey region signifies a lack of statistically significant data due to desorption of C_{60} molecules from the pentacene substrate.

Again we consider the temperature dependence of the observed diffusion, shown in Figures 3.11, and re-plot the data as ln(D) vs. $1/k_BT$ in Figure 3.12. From this plot, the behavior of C_{60} on pentacene can be assumed to be roughly Arrhenian on *both* thin film and bulk phase pentacene. Assuming a linear fit to the data in Figure 3.12, values for the prefactor (D_0) and activation energy (E_a) in the Arrhenius equation, $D = D_0 e^{-E_a/kT}$, were found to be $D_0 \sim 1.4 \times 10^{-3}$ cm^2/s and $E_a \sim 0.084$ eV for the bulk phase and $D_0 \sim 6.2 \times 10^{-4}$ cm^2/s and $E_a \times 0.045$ eV for the thin film phase. The energy barrier that the C_{60} needs to overcome in order to diffuse on bulk phase pentacene is almost twice as high as that on thin film pentacene, which corresponds well with the energy barrier values indicated from the adsorption energy surfaces in Figure 3.7.

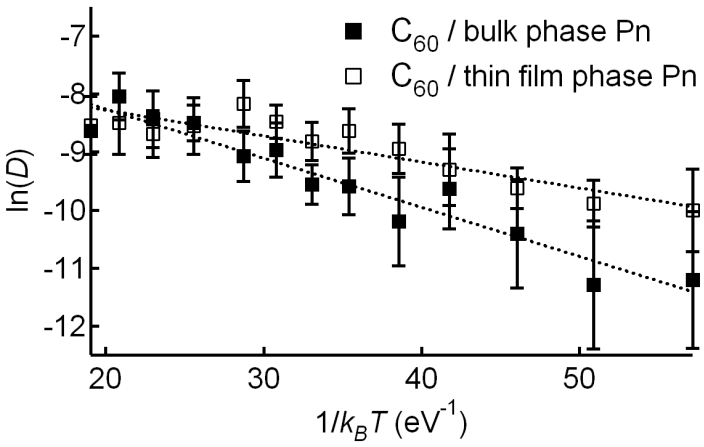

Figure 3.12: The natural logarithm of the surface diffusion coefficient vs. the inverse of k_BT, where k_B is the Boltzmann constant and T is the temperature. The dotted lines guide the eye to the linearity of the data. Following Arrhenius's theory, the steeper slope of the filled square data (bulk phase pentacene) corresponds to a larger energy barrier than the open square data (thin film phase pentacene).

While the anisotropic behavior of C_{60} on the bulk phase pentacene, as shown in Figure 3.4(a), is *qualitatively* apparent by eye, in order to *quantitatively* describe the diffusion of the C_{60} in one dimension, we map the vector displacements onto a particular direction. Here, we compare the diffusion of C_{60} in the $[1\bar{1}0]$ direction to that of the orthogonal [110] direction for both the thin film and bulk pentacene surfaces. We utilize the Green-Kubo relation for diffusion given by Equation 3.3 and the corresponding velocity autocorrelation function given by Equation 3.4.

$$D = \frac{1}{d} \int_0^\infty \langle \mathbf{v}(0) \cdot \mathbf{v}(\tau) \rangle \, d\tau \tag{3.3}$$

$$C_{vv}(\tau) = \langle \mathbf{v}(0) \cdot \mathbf{v}(\tau) \rangle. \tag{3.4}$$

Formally, the Green-Kubo relation is equivalent to the Einstein relation in the sense that it relates the macroscopic phenomenon of diffusion to microscopic transport phenomena. However, we use the Green-Kubo method here with velocity autocorrelation functions to provide a measure of direction relative to the velocity at non-equilibrium time spans. As for the ensemble average, normally this involves an average of values of a large number of particles; however, in this case, we have one particle, so the ensemble average becomes an average over values at different time origins, as shown in Equation 3.5 where $N_{\text{origins}} = N_{\text{steps}} - \tau + 1$.

$$\langle \mathbf{v}(0) \cdot \mathbf{v}(\tau) \rangle = \frac{1}{N_{\text{origins}}} \sum_{k=1}^{N_{\text{origins}}} \mathbf{v}(t_k) \cdot \mathbf{v}(t_k + \tau), \tag{3.5}$$

To obtain the directional diffusion coefficients, $D_{[1\bar{1}0]}$ and $D_{[110]}$, the Green-Kubo equations become Equations 3.6 and 3.7, where the integrations of the autocorrelation functions were performed numerically. Figure 3.13 shows these one-dimensional diffusion coefficients as a function of temperature for both the thin film and bulk phase pentacene. For the thin film phase, there is no significant difference between diffusion of C_{60} in the $[1\bar{1}0]$ and [110] directions, as further evidenced by the lack of anisotropy shown in Figures 3.4(b) and 3.7(b). However, for the bulk phase, diffusion in the $[1\bar{1}0]$ direction is consistently higher than that in the [110] direction, which provides a quantitative assessment of the anisotropy in the diffusion phenomena for this bulk phase polymorph.

$$D_{[1\bar{1}0]} = \frac{1}{d}\int_0^\infty \langle \mathbf{v}_{[\mathbf{1\bar{1}0}]}(0) \cdot \mathbf{v}_{[\mathbf{1\bar{1}0}]}(\tau)\rangle \, d\tau, \tag{3.6}$$

$$D_{[110]} = \frac{1}{d}\int_0^\infty \langle \mathbf{v}_{[\mathbf{110}]}(0) \cdot \mathbf{v}_{[\mathbf{110}]}(\tau)\rangle \, d\tau, \tag{3.7}$$

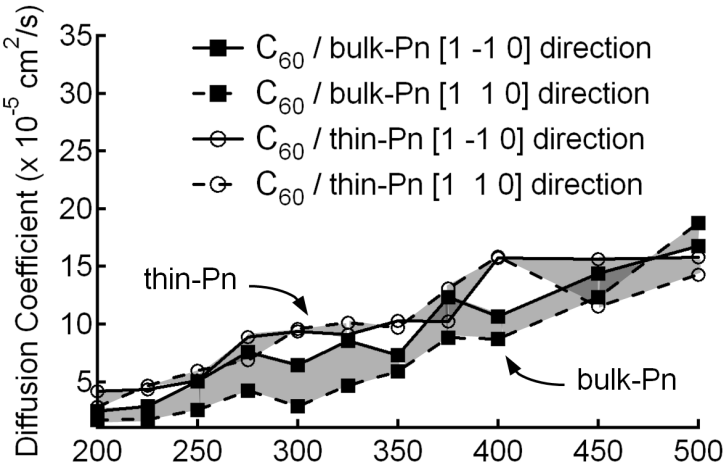

Figure 3.13: One-dimensional diffusion coefficients of C_{60} on pentacene in the [$1\bar{1}0$] direction (solid lines) and the [110] direction (dashed lines). There is a directional bias for diffusion on the bulk phase substrate (filled squares), but not for the thin film phase substrate (open circles). Consistent with Figure 3.11, C_{60} diffusion coefficients for bulk phase pentacene have consistently lower values than for the thin film phase.

CHAPTER 4

GROWTH OF MULTIPLE C_{60} ON UPRIGHT PENTACENE: SEMI-EMPIRICAL STUDIES

4.1 MD studies of small clusters

Consideration of larger systems, involving 1–3 additional admolecules of C_{60}, greatly enlarges the total number of atoms in the system because as the number of admolecules increases, the system size has to be scaled appropriately larger to prevent unwanted interactions between C_{60} molecules and their periodic images. See Table 4.1 for a list of the different system sizes considered for different numbers of C_{60} admolecules. The largest system studied here involved four C_{60} admolecules, leading to a system containing 7,296 atoms. Observation of the C_{60}-C_{60} intermolecular potential energy given by the MM3 model shows that the equilibrium center-to-center distance is 9.5 Å at the potential energy well of –0.34 eV and the range of the potential, the distance beyond which the intermolecular potential is essentially zero, is approximately 12 Å. Thus a system containing two C_{60} molecules adsorbed on pentacene will require a computational cell at least 24 Å in length (twice the range of the potential) on the shortest edge of the *x*-*y* surface of pentacene.

Portions of this chapter are reproduced in part from previous publications in Reference 105

Table 4.1: Pentacene substrate system sizes considered for different numbers of C_{60} admolecules

Number of C_{60} molecules	System size (number of pentacene unit cells in x- and y-direction)	Number of atoms in simulation
1	3×3	1356
2	4×4	2424
3	6×6	5364
4	7×7	7296

The behavior of two, three, and four C_{60} molecules adsorbed on a pentacene surface was considered in order to investigate the tendency of C_{60} to "wet" the pentacene surface at higher coverage conditions. Due to the larger numbers of atoms in these systems, the computational cost increased significantly relative to a single C_{60} admolecule; a single MD simulation of two and three C_{60} molecules on a pentacene surface for 1.5 ns took approximately two and three weeks, respectively, on an AMD Opteron with a 2.6 GHz CPU (or 1.5–2 weeks on an Intel Xeon 2.93 GHz CPU). Simulations containing 2 and 3 adsorbed molecules started out with C_{60} molecules located at random positions on the surface. In all cases, once a C_{60} molecule came within the range of the intermolecular potential of any other C_{60} molecule, they remained in contact. This was true even at the highest temperature tested, 400 K. Two adsorbed molecules formed a dimer, roughly 10 Å apart, once they were in contact with one another. For the 3-admolecule case, the C_{60} molecules formed a roughly equilateral triangle on the surface when they came in close enough contact, and they stayed that way for the remainder of the simulation. We have no evidence of molecules breaking away from the clusters over the relatively limited 1.5-ns timeframe of the simulations.

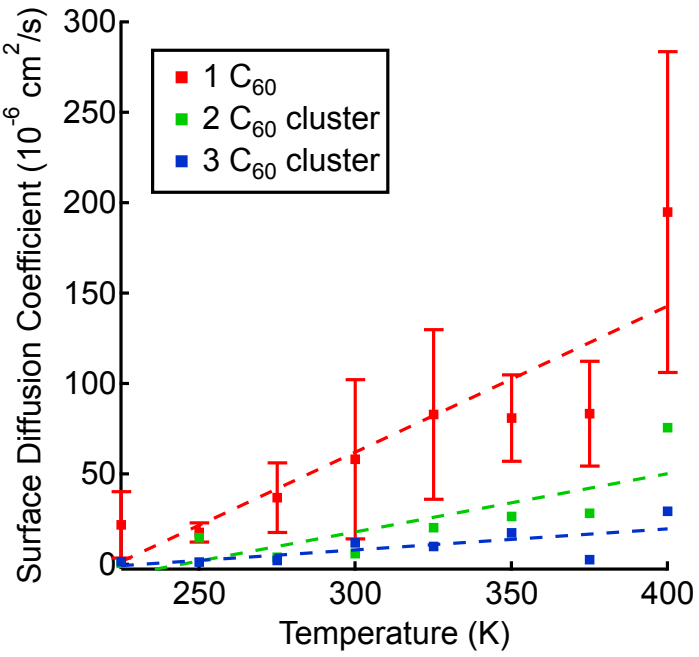

Figure 4.1: Surface diffusion coefficients of multiple C_{60} molecules versus temperature. The system containing one C_{60} molecule was run three times (shown also in Figure 3.8); the two- and three-C_{60} molecule systems were run only once.

Surface diffusion coefficients were calculated for each C_{60} molecule in systems containing one to three adsorbed C_{60} molecules on pentacene as a function of temperature. Figure 4.1 shows that there is a slight increase in the surface diffusion coefficients with temperature for systems containing one to three adsorbed C_{60} molecules. There is a significant decrease in the surface diffusion coefficients when going from one to two adsorbed C_{60} molecules on the surface, with a smaller decrease when a third C_{60} molecule is adsorbed in the vicinity. This evidence, in conjunction with the data shown in Figures 3.2(a) and (c), implies that C_{60}-C_{60} cohesion is stronger than the adhesion of C_{60} on pentacene.

One simulation was performed where a fourth C_{60} molecule was placed on top of three adsorbed C_{60} molecules at the start of the simulation so as to form a pyramid. The goal of this run was to determine the tendency of the fourth C_{60} molecule to roll over the edge of the C_{60} island and adsorb directly on the pentacene surface. For the short length of the simulation, 1.5 ns, the fourth C_{60} molecule showed no tendency to leave its position atop the other C_{60} molecules. Since this simulation took a long time to finish (more than 3 weeks), it was not practical to pursue the simulation of larger systems. But, for comparison, a simulation run of a similar duration for a pentacene molecule on top of a small island of pentacene was long enough for the pentacene molecule on top to jump down onto the terrace below. Clearly then, C_{60} is less likely than pentacene to wet a pentacene surface.

4.2 Geometry optimizations at the planar interface

The preceding simulations have concentrated on using single molecule probes of the pentacene-C_{60} surface. However, bearing in mind the "bigger picture" of looking at heterojunctions between these two dissimilar materials, it was important to begin to look at more extensive scale interactions, in the form of a small multilayer planar interface. To do so, we simulated several layers of a bulk-like fcc-packed C_{60} sample on top of several layers of bulk phase pentacene to observe the morphology of the interface. The orientation of the pentacene molecules at the interface is believed to be critically important in determining how charge carriers behave at the interface with C_{60}.[78] See Section 1.2.3 for a more detailed description of the effect of interface geometry in related planar interfaces.

Our first task was to perform a geometry optimization modeling the system using MM3 semi-empirical models described in Section 2.2. The locations of the molecules on the bottom layer of pentacene were fixed, as were those on the top layer of C_{60} molecules. We did not include periodic boundary conditions in any direction since the unit cells for pentacene and C_{60} are incommensurate. Essentially, we are modeling an "island" consisting of bulk C_{60} on bulk pentacene. Two cases were studied, which differed only in the number of layers of pentacene (three and four layers as shown in Figure 4.2). The reason for considering these two cases was to see how closely correlated the effect observed at the interface was with the proximity to the fixed bottom pentacene layer.

Figure 4.2 shows the behavior of the layers for both cases in both initial and final configurations. The first observation is that the C_{60} molecules hardly move

at all relative to the pentacene molecules in both case studies. This fact can be seen more clearly in Figure 4.3, which shows the initial and final positions of the molecules located at the heterojunction formed by the bottom layer of C_{60} molecules and the top layer of pentacene (positions shown for the top hydrogen atoms) for the case with three pentacene layers. Clearly, energy minimizations causes the top pentacene hydrogen atoms to move much more than the C_{60} molecules; one can hardly distinguish which relaxed H-atom corresponds to which unrelaxed H-atom. In both cases shown in Figure 4.2 (for three and four pentacene layers), it is clear that the pentacene molecules closer to the heterojunction have a greater tendency to stand up essentially straight (perpendicular to the surface) with respect to the regular tilt angle of bulk pentacene (and at an angle distinct from the "thin film" phase). This implies that there is an unusual interfacial configuration for pentacene that occurs within 1–3 molecular layers of the C_{60}/pentacene heterojunction; this could distinctly affect charge carrier mobilities. The persistence, in terms of "depth," of this particular pentacene configuration has yet to be determined.

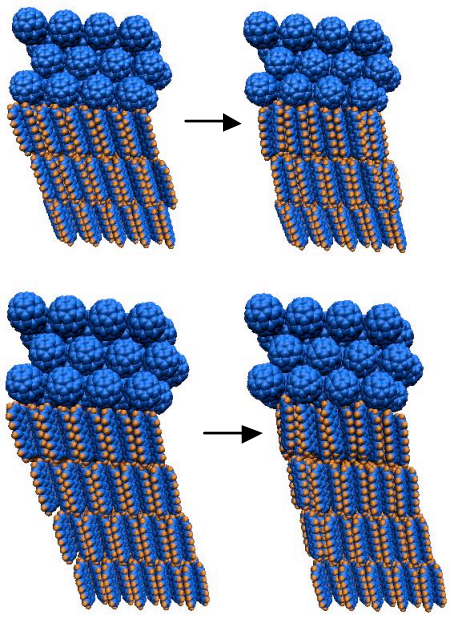

Figure 4.2: Initial (left) and final (right) structures of three layers of C_{60} on top of three (top) and four (bottom) layers of pentacene. The top C_{60} and bottom pentacene layers in both cases were fixed in the MM3 geometry optimization.

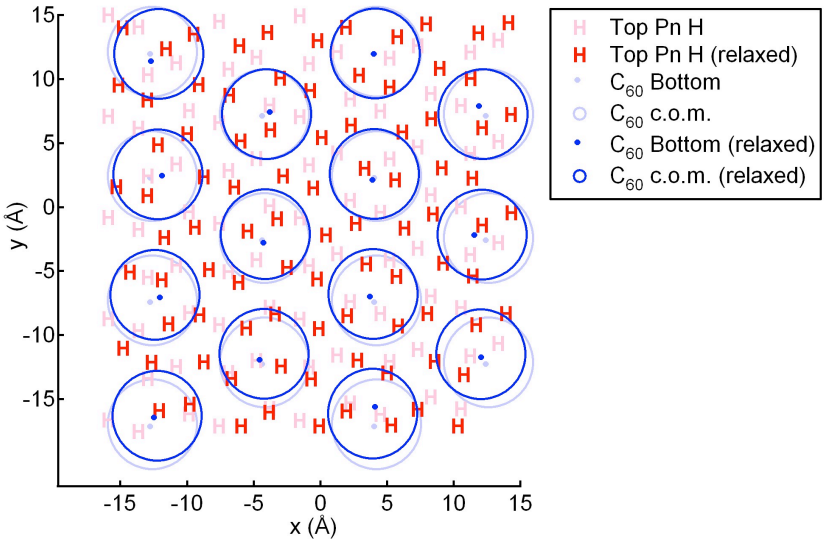

Figure 4.3: Initial and final, *i.e.* relaxed, positions of the C_{60} molecules (blue circles) and top pentacene (Pn) hydrogens (red H's). Significant pentacene rearrangement occurs relative to C_{60} rearrangement.

A quantitative view of the change in structural orientation of the molecules can be found in Figure 4.4, which shows the theta histograms of long- and short-axes of the pentacene molecules with respect to the z-axis and x-axis, respectively, for the case involving three pentacene layers. Pn 1 and Pn 2 refer to the two distinct pentacene molecules in a unit cell. On average, the long axis angle with respect to the z-axis is more upright by nearly 10 degrees when comparing the tilt angle of molecules in the bottom bulk pentacene layer relative to the top pentacene layer at the interface. Even the middle layer is more upright than the normal bulk material by about 5 degrees. This implies that the interfacial pentacene "phase" penetrates the bulk pentacene phase by at least a few monolayers. The short axis angle with respect to the x-axis does not change very much from the bottom to the top pentacene layers, providing evidence that the herringbone structure remains intact for the most part (Note: This is not to say that the short axis does not move; it just does not rotate in the x-y-plane very much).

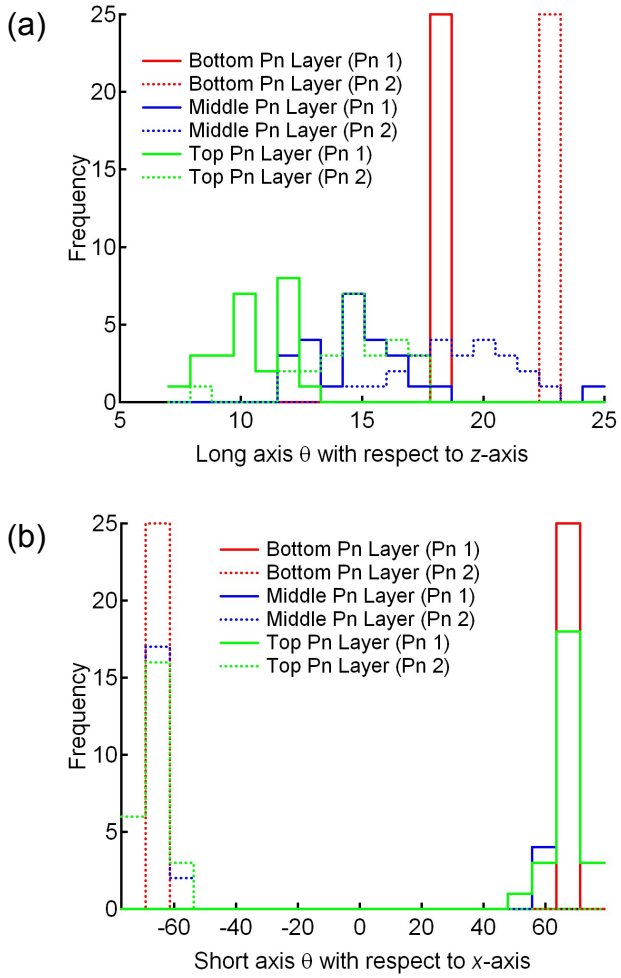

Figure 4.4: Angle distributions of the pentacene (a) long axes with respect to the z-axis and (b) short axes with respect to the x-axis. The solid and dotted lines represent the two different pentacenes present in a unit cell, Pn 1 and Pn 2. The bottom layer of pentacene (red) is fixed and the top pentacene layer (green) is the layer at the C_{60}/pentacene interface.

Since the molecules in the top C_{60} layer are fixed, it is possible that the system is subject to a certain amount of stress at the dissimilar interface of this "island." Accordingly, it would be worthwhile to unfix the molecules in this layer and observe the effect of a stress-free system. It is also possible that, since there are no periodic boundary conditions in our simulations and the system size is quite small, edge effects might be influencing the pentacene behavior at the interface. This project was given to another graduate student in the Clancy research group, Brian Koo. He looked at larger system sizes (9 times larger to be exact) with periodic boundary conditions, which effectively eliminated any edge effects on the interfacial behavior. Even at this scale, the reconfiguration of the pentacene occurred at the interface as it had before with the smaller system sizes. This suggests that stress is not driving this change in the interfacial morphology. Koo also looked at the effect of this distinctive interfacial orientation on the HOMO and LUMO levels, finding the effect of this significant transient orientational disorder to be surprisingly negligible.[147] This result is consistent with recent findings that the effects of thermal fluctuations on the transport parameters of organic semiconducting materials are only prominent in smaller molecular crystals (*e.g.*, naphthalene and anthracene, but not pentacene).[148]

It could be beneficial to perform additional Molecular Dynamics simulations of this system to learn more about this phenomenon (*e.g.*, how deep does this orientational change pervade into the bulk), however the number of atoms would result in a very computationally expensive effort. At this point, we chose instead to move to a new simulation method altogether to study the thin film growth of C_{60} on upright pentacene phases (Chapter 5). What is needed is a way to capture the behavior of many more C_{60} molecules than is realizable with the fully-atomistic Molecular Dynamics approach used here.

CHAPTER 5

GROWTH OF MULTIPLE C_{60} ON UPRIGHT PENTACENE: KINETIC MONTE CARLO STUDIES

We gained a lot of detailed information from our preceding studies of Molecular Dynamics (MD) concerning the behavior of C_{60} molecules as components of the "upright" bulk and thin film phases formed by pentacene, but we were limited in the scope of our investigations by the small system sizes accessible by such atomistic simulations. To simulate monolayers of thin film growth at anything close to experimentally observable length and time scales is clearly beyond the reach of even accelerated Molecular Dynamics techniques; thus Kinetic Monte Carlo (KMC) was chosen to bridge the atomistic length and time scales of MD to more mesoscopic dimensions and hence experimentally accessible regimes. As described in Section 2.4, there has been only one other report of a KMC simulation of heteroepitaxy, in which the environmental conditions of a CO molecule on a Pd(100) surface (*e.g.,* different adsorption site geometries) determine which of two lattices it adopts.[132] In that system, the two lattices are forced to match at the periodic boundary conditions (effectively changing the lattice parameters), which is not an approach used in this work. Our first task is to describe the algorithm used here to capture the C_{60}/pentacene heteroepitaxy.

To create a new algorithm to study heteroepitaxy involves the following major tasks. The first task, described in Section 5.1, is to design a suitable multilattice framework for the KMC simulations, one that allows consideration of five lattices (two for pentacene and three for C_{60}) that an incoming particle has the choice to adopt. Next, Section 5.2 will detail the large collection of energy barriers that are needed to capture all the processes involved in thin film heteroepi-

taxial growth and hence obtain rates for the dynamic simulation. There are, in addition, a few key parameters in the simulation that have to be estimated. In particular, these parameters, discussed in Section 5.3, include prefactors for certain diffusion events and deposition rates.

With the algorithm development completed, the code is then used to study the thin film growth of C_{60} on pentacene. Results from the KMC simulations are categorized by the two main stages of heteroepitaxy: one considering only sub-monolayer coverage (Section 5.4), and one considering the growth of multiple monolayers and inter-layer diffusion. These two stages also reflect major components of the code development since the first monolayer has to be handled quite differently from subsequent monolayers. The reason for this will become evident in the following section.

5.1 Algorithm development

The KMC code was written using the Java SE Development Kit.[149] Multiple hierarchal classes were developed to facilitate the implementation of object-oriented programming. In this section, we describe the construction of a framework of multiple lattices and explain why they were chosen. We also describe the main assumptions built into the code. For reference, Figure 5.1 shows the KMC algorithm implemented in this work. In this section, an event is defined as any action that has an associated rate (*e.g.*, deposition, diffusion, desorption), and diffusion events are referred to as "transitions," where a C_{60} molecule physically transitions from one lattice site to another.

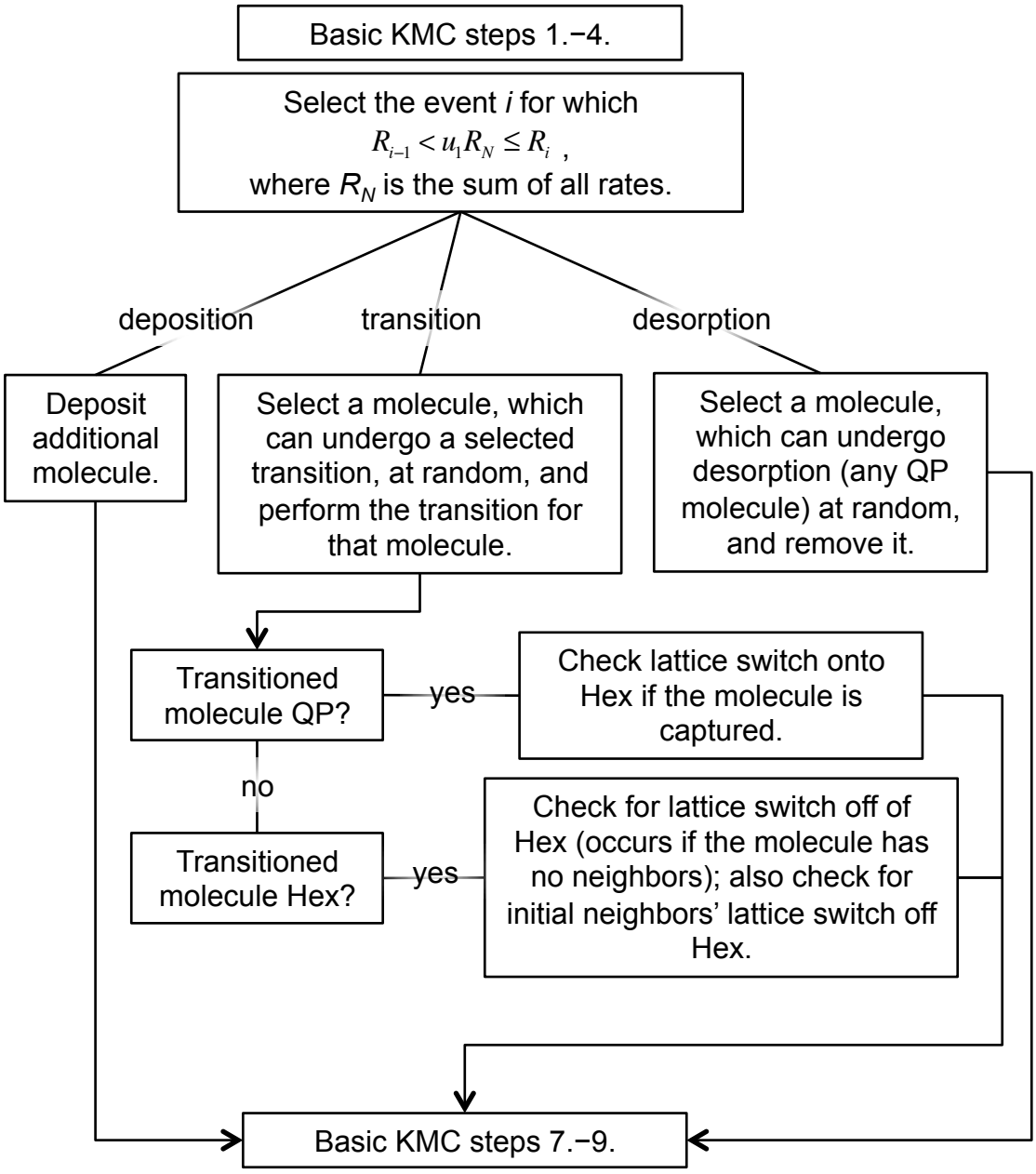

Figure 5.1: KMC algorithm implemented in this work employing a multi-lattice framework. For the basic KMC steps, refer back to Figure 2.4.

5.1.1 Q-P lattice development

The idea for the multiple-lattice structure stemmed from the fact that C_{60} molecules behave differently when they are effectively alone on a pentacene surface (*i.e.,* they have no C_{60} neighbors) in comparison to situations when they are near other C_{60} molecules on a pentacene surface. From the MD simulations described in Sections 3.1–3.2, it was clear that a single C_{60} molecule (with only one molecule present on the pentacene surface) prefers to reside at certain locations relative to the pentacene positions, especially on the bulk phase pentacene. The potential energy surface of one C_{60} on the bulk and thin film phases we obtained earlier (Figure 3.7) provided the basis for a KMC lattice for the first monolayer of growth, where lattice point locations correspond to energy minima on the pentacene surface in the *x-y* plane. Since the upright pentacene phases form a herringbone configuration, the corresponding potential energy surface (although periodic) is not a simple rectangular or hexagonal pattern. In fact, there are some saddle points which cannot be ignored since they are low energy sites (*i.e.*, points of C_{60} residence). Thus, we developed a periodic lattice pattern incorporating the energy well locations as functions of the uppermost hydrogen positions of the upright pentacene molecules. There are four such hydrogen atoms, whose positions define one of the energy minima; we call this a "Q" site, with "Q" standing for "quadrilateral," the geometry of the energy minimum. There are five uppermost hydrogen atoms whose positions define the other energy minimum (the saddle point). We call this a "P" site, reflecting the pentagonal geometry of the enegy minimum. Together, the Q and P sites cover the majority of the pentacene surface. In other words, the surface of pentacene has been defined as being represented as a set of P and Q sites, as shown in Figure 5.2.

A C_{60} molecule at a Q site can move in 12 different directions (six to other Q sites and six to P sites); a C_{60} molecule at a P site can move in 12 different directions (six to Q sites and six to other P sites) as shown in Figure 5.2. Adoption of these Q and P lattices might seem overly complicated, but it was necessary in order to capture the pronounced anisotropy observed in the MD simulations of C_{60} diffusion on a bulk phase of pentacene (refer back to Figure 3.4). The goal of the KMC study, then, is to see, at longer length and time scales, if this anisotropy affects the shapes of C_{60} islands that form during thin film growth. This will be addressed in Section 5.4.

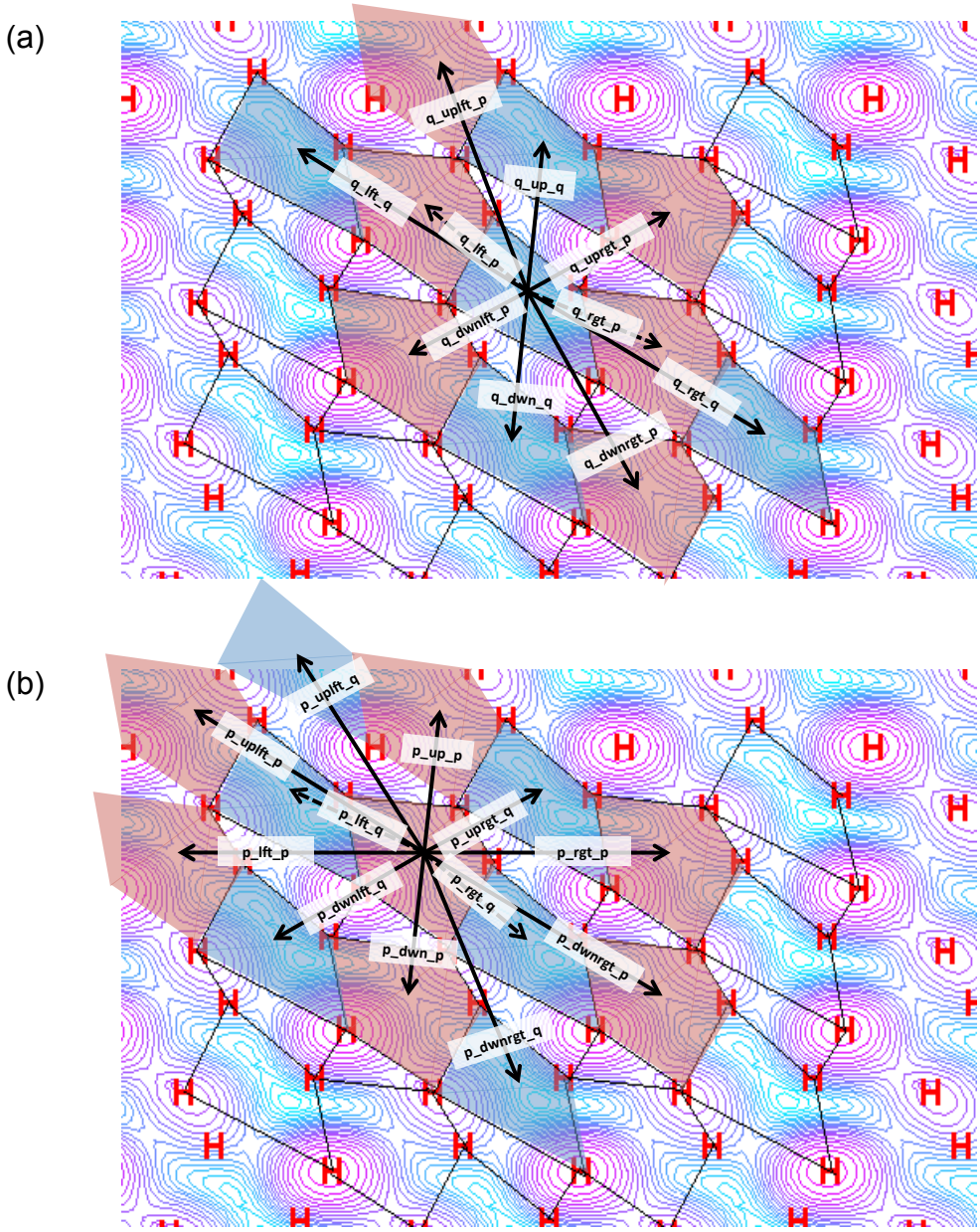

Figure 5.2: Q-P lattice system overlaid on a C_{60} / bulk pentacene potential energy surface. Blue quadrilateral shapes (Q sites) are defined by four specific uppermost pentacene hydrogen locations, and pink pentagon shapes (P sites) are defined by five uppermost pentacene hydrogen locations. Possible transitions from Q-to-P and Q-to-Q sites are labeled in (a), and possible transitions from P-to-Q and P-to-P sites are labeled in (b).

5.1.2 "Hex" lattice development

In addition to the Q and P lattices, another type of sub-monolayer lattice was chosen in order to capture the behavior of C_{60} molecules when they are in the vicinity of other C_{60} molecules as they diffuse over a pentacene surface. As shown in Section 4.1, C_{60} molecules behave quite differently near other C_{60} molecules than they do when they are by themselves on the pentacene surface. C_{60} molecules tend to remain an equilibrium distance (~1 nm) apart from other C_{60} molecules consistently throughout MD simulations of two and three C_{60} molecules. In essence, they are oblivious to where they reside with respect to the pentacene surface. The main reason for this is the considerably stronger C_{60}-C_{60} interaction compared to the interaction between C_{60} and the upright pentacene surface. Such clustering of spherical-like molecules leads to a close-packed type lattice, indeed, that is the preferred crystal packing habit for C_{60}. To capture this in the KMC algorithm, we developed an additional lattice type representative of a hexagonal shape (a "Hex" lattice). During sub-monolayer growth, a C_{60} molecule on a Hex lattice can move in six possible directions, which we have designated as: up-left, up-right, right, down-right, down-left, and left. Figure 5.3 shows the sub-monolayer lattices—Q, P, and Hex—and example diffusion events.

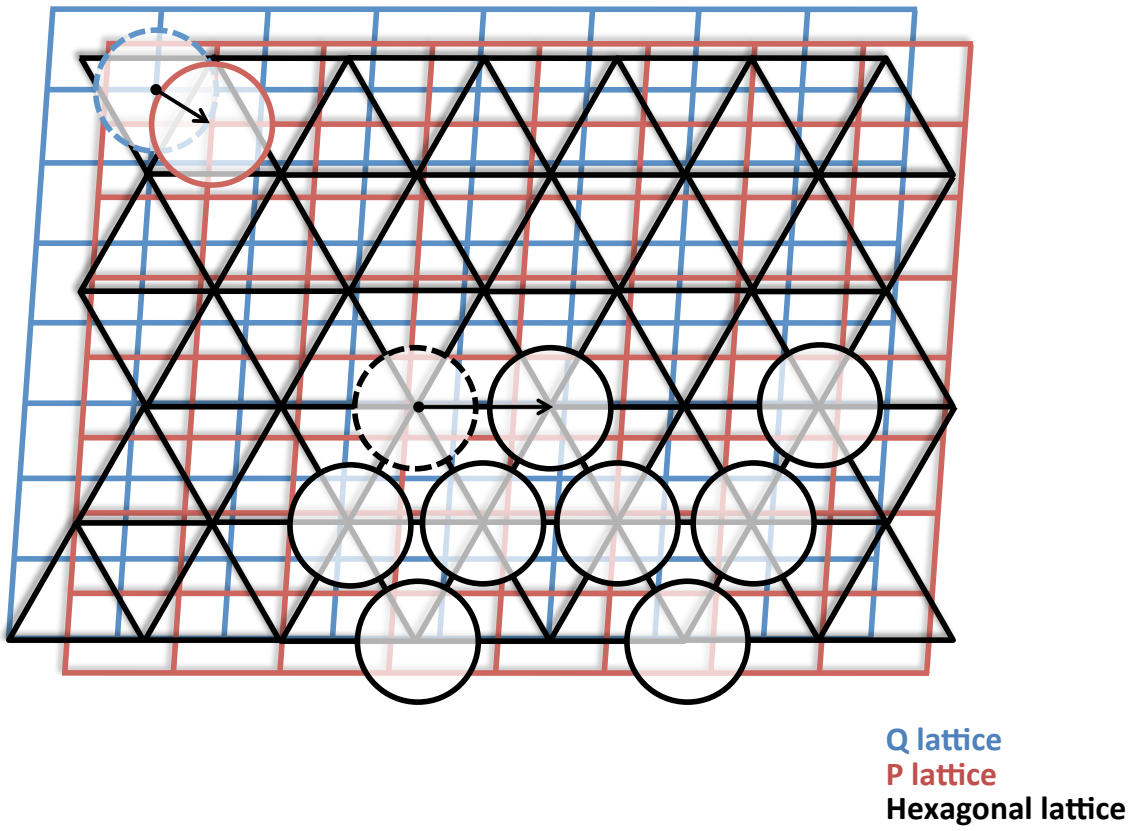

Figure 5.3: Multi-lattice system used in the KMC algorithm to capture sub-monolayer diffusion of C_{60} on an upright pentacene phase. The Q (blue) and P (pink) lattices correspond to sites of possible C_{60} residence when a C_{60} molecule is not in the vicinity of another C_{60} molecule. Figure 5.2 shows all of the possible Q-P lattice transitions, or diffusion events. The Hex lattice (black) corresponds to sites of possible C_{60} residence when a C_{60} molecule *is* in the vicinity of at least one other C_{60} molecule.

The multi-lattice system considered for growth beyond the first monolayer of C_{60} molecules is exactly the same as the sub-monolayer Hex lattice, except that a C_{60} molecule in this situation can now only move in three possible directions, depending on whether it resides on top of an upright C_{60} triangle (possible directions: up-left, up-right, or down) or a downward C_{60} triangle (possible directions: up, down-right, or down-left) as shown in Figure 5.4(a). Since C_{60} prefers to pack in an fcc lattice structure, there are three hexagonally close-packed planes, denoted as A, B, and C. The C_{60} plane (A, B, or C), on top of which another C_{60} is diffusing, determines its own designation (A, B, or C). Figure 5.4(b) shows a schematic example of the movements (or "jumps") of C_{60} molecules beyond the first monolayer. Sub-monolayer C_{60} molecules on a Hex lattice can also either be of type A, B, or C; for simplicity, this was not shown in Figure 5.3.

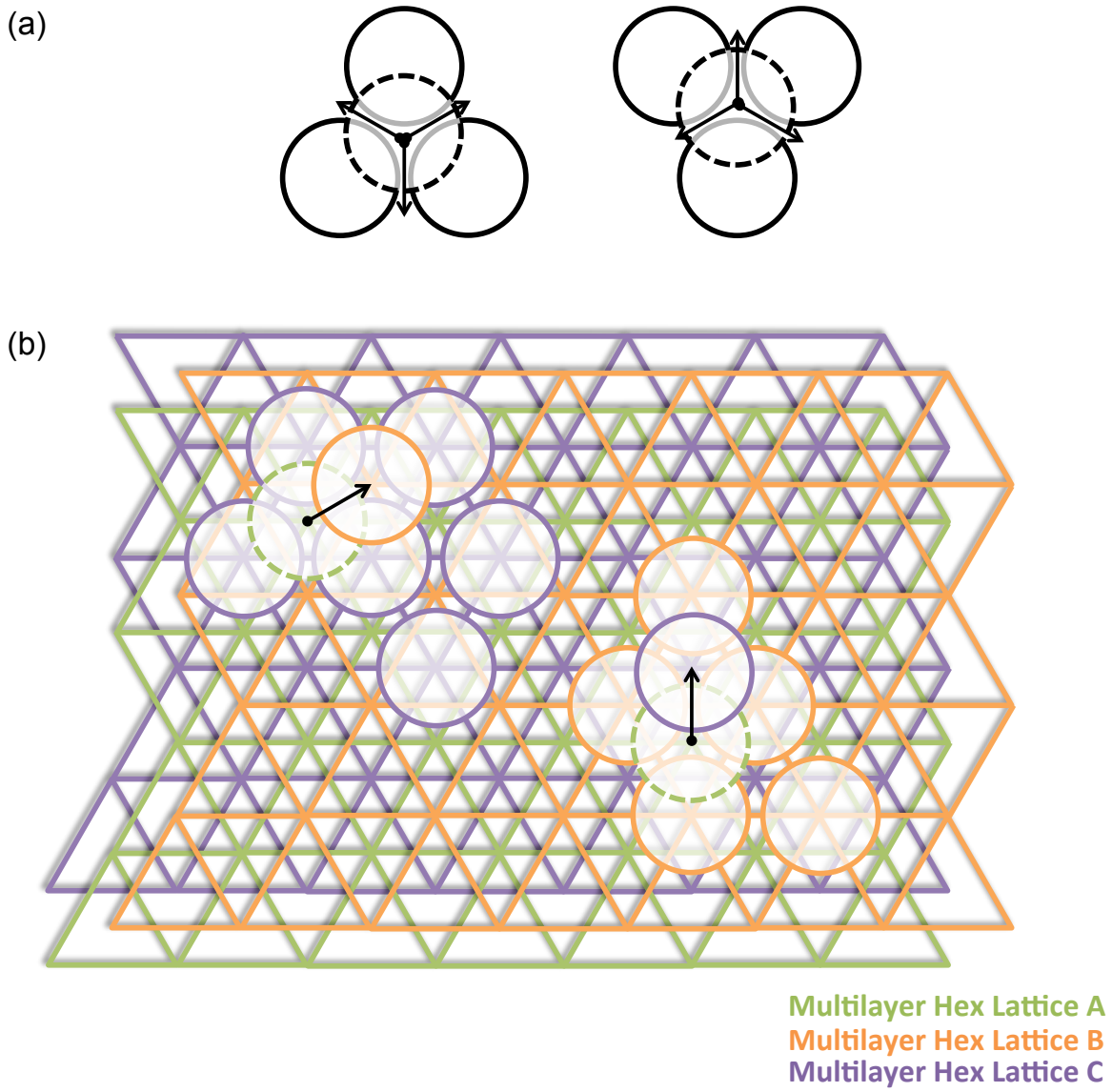

Figure 5.4: (a) Possible jump directions for C_{60} on C_{60}. (b) Multi-lattice system used in KMC for beyond monolayer diffusion of C_{60} on C_{60} with example diffusion events.

Given this multi-lattice framework, considering how to implement periodic boundary conditions in the simulation was not trivial. Due to the oblique QP lattice and the hexagonal Hex lattice, matching at the boundary conditions could not, in practice, be achieved exactly, but the boundary mismatch can be minimized. Figure 5.5 shows this incommensurability more clearly. Since using an infinitely large system size to accommodate the intrinsic lattice mismatch between C_{60} and pentacene was not an option, we had to define a tolerance level of an allowable mismatch at the edges. This "boundary mismatch" was defined as the sum of the distances between the bottom left corner (where a lattice point resides at the origin) and the three other periodic lattice point images. The criterion for this mismatch ($\sum d_i$) is mainly that it needed to be reasonably low ($<\sim$ 10Å). We also wanted a system size with a reasonable aspect ratio (> 0.5 and < 2) in order to minimize the amount of periodic boundary-crossing in the simulation. Lastly, the system size and hence number of molecules in the system had to be taken into account because the speed of the code depends sensitively on the number of particles, roughly as $O(N)$. We wanted to minimize the system size without losing any significance of the accuracy of the results, so as a "target" number of C_{60} molecules, we chose the number of molecules that would fit on 80×80 units cells of bulk pentacene: that is, 3,528 C_{60} molecules.

Using the criteria described above (lattice mismatch, aspect ratio, and system size), we narrowed possible choices of system dimensions down to a set of 15 for each of the bulk and thin film phase pentacene systems. Figure 5.6 shows the normalized values of these parameters for the bulk and thin film phase pentacene systems. The system size chosen for the bulk phase was 71×89 pentacene unit cells for which the $\sum d_i$ = 3Å, the maximum number of C_{60} molecules = 3,483, and the aspect ratio of the system = 1.04. Similarly, the system size cho-

sen for the thin film phase was 52×130 pentacene unit cells for which the $\sum d_i$ = 6Å, the maximum number of C_{60} molecules = 3,499, and the aspect ratio = 0.51. Finding an appropriate system size for the thin film phase was more difficult because the angle γ between lattice parameters a and b is almost 90°, making commensurate periodic system sizes harder to attain. The smaller aspect ratio for the thin film phase systems explains why subsequent KMC snapshots of this system are taller than their bulk phase counterparts.

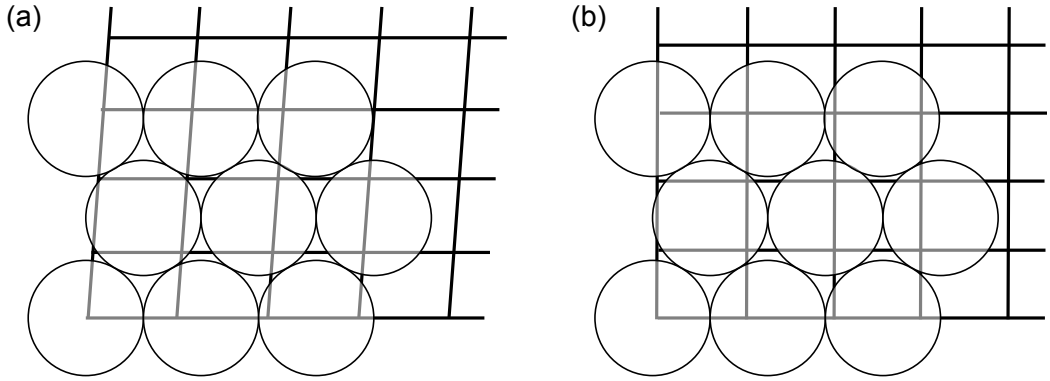

Figure 5.5: Diagram showing the incommensurability of the C_{60} Hex lattice the oblique (a) bulk pentacene lattice and (b) thin film phase pentacene lattice.

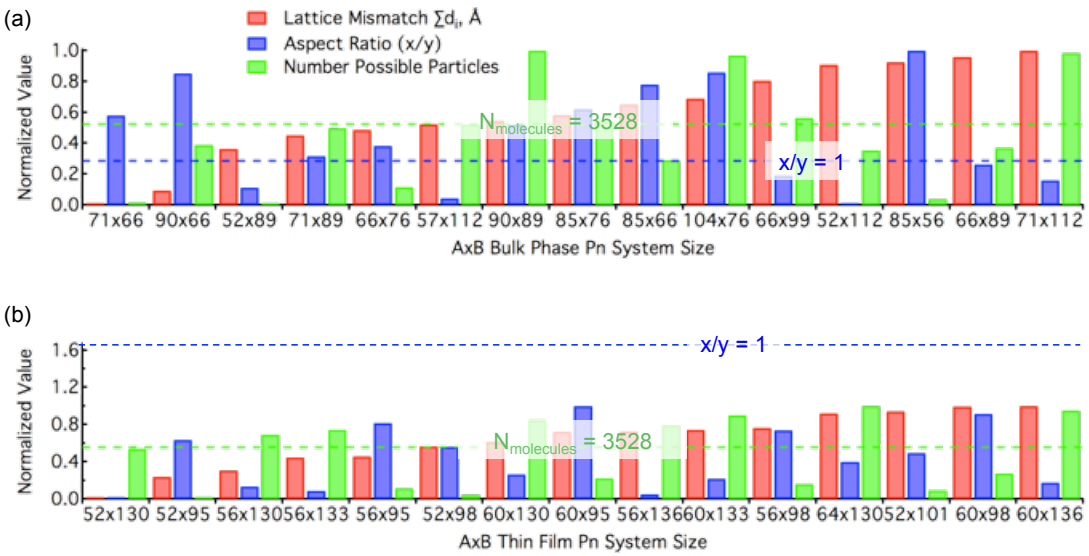

Figure 5.6: System size parameters: lattice mismatch ($\sum d_i$ = sum of the distances between the bottom left corner—where a lattice point resides at the origin—and the three other periodic lattice point images), system aspect ratio, and maximum number of possible particles. The target lattice mismatch is zero, and the normalized target values for the other parameters are shown by the dotted green and blue lines for (a) bulk phase pentacene and (b) thin film phase pentacene.

5.1.3 KMC algorithm details and assumptions

A few assumptions have been made in the KMC code that are either inherent in the discrete nature of such codes or a result of practicality. These assumptions are listed here before proceeding further.

Firstly, all diffusion event rates depend only on temperature, that is, they are activated events. The rates for Q-P jumps are obtained from counting frequencies of events from many MD simulations (as described in the next section), but since this method was infeasible for Hex lattice jumps (both sub-monolayer and beyond monolayer growth), the energy barriers were calculated statically and the attempt frequency, or Arrhenius prefactor, was assumed to be the average of the obtained prefactors from the Q-P jumps. The sensitivity of changing this prefactor for Hex lattice jumps is discussed in Section 5.3.

A "capture radius" was built into the KMC code as a function of temperature. The capture radius is defined as the distance within which a C_{60} molecule will inevitably be captured by another C_{60} molecule, resulting in either the captured C_{60} molecule joining an existing C_{60} cluster or forming a new cluster with another lone C_{60} molecule. The capture radius is calculated based on the inverse of the Pacheco intermolecular potential function between two C_{60} molecules.[2] See Figure 2.1 for a plot of the Pacheco potential function. At 0 K, the capture radius is equal to the distance at which this potential energy function is minimized (r at E_{min}). At higher temperatures, the capture radius is equal to the distance ($> r$ at E_{min}) at which the function is equal to E_{min}+k_BT. Figure 5.7 plots the capture radius as a function of temperature, showing that the dependence is relatively weak: Increasing the temperature from 0 K to 1000 K, increases the capture radius by only 0.7 Å. The method by which C_{60} molecules join the Hex

lattice (A, B, or C) from the Q-P lattice and *vice versa* is implemented in detail in the KMC code.

The range of deposition rates tested is much higher (10^4 ML/s–10^6 ML/s) than is generally experimentally feasible (~1 ML/s). These high deposition rates are essentially dictated by the speed of KMC codes, so that the simulation does not take an impractically long time. For example, a simulation of C_{60} growth on 71×89 pentacene unit cells takes approximately two weeks for a deposition rate of 10^5 ML/s on a single core AMD Opteron at 2.6 GHz CPU (or ~1.5 weeks on an Intel Xeon core operating at 2.93 GHz). Increasing deposition rates for the sake of computational efficiency is often done in KMC because the rate of diffusion is much faster than deposition.[150,151] Thus, in order to follow the simulation of film growth progress as a function of time at a tractable elapsed "wall clock" time, the deposition rate had to be set high. Section 5.3 will describe the sensitivity of the results to deposition rate.

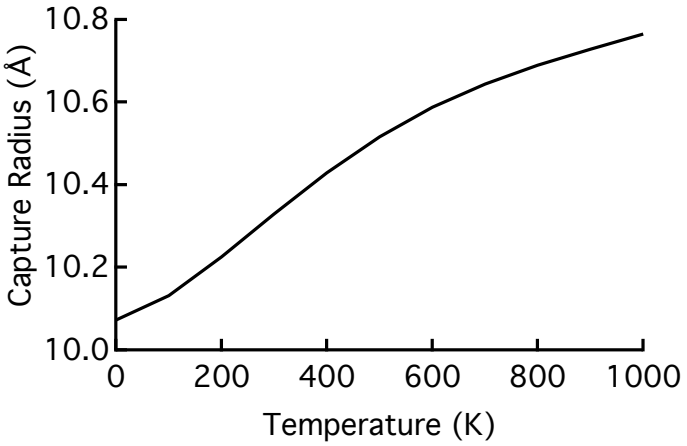

Figure 5.7: Dependence of capture radius on temperature in the KMC simulations.

In addition to the deposition rate itself, there are some other assumptions describing the act of deposition in the KMC code. If C_{60} deposition occurs on the pentacene surface, it joins the Q-P lattice first by default; if the deposition occurs very close to other C_{60} molecules, the deposited molecule either rolls off the edge or initiates a new monolayer. One exception to this deposition protocol is the rare case when there is no appropriate lattice position for a deposited molecule, in which case the randomly located deposition is re-tried. An example of such a rare case would be a deposition at a grain boundary, where the molecule can neither roll off an edge nor be added to the monolayer. Another example would be a deposition at a lattice-mismatched corner where the slight lattice shift confuses the placement of the deposited particle. It should also be noted that, in the code, a deposition event involves the instantaneous appearance of a randomly placed molecule in the vacuum above the surface, as if it had just floated down like a leaf. In reality, this would be most analogous to a vapor phase deposition method, where the incident molecules do not carry any significant incident energy.

Desorption was also considered to be a possible event in the KMC code, but it was only allowed for singleton C_{60} molecules on the Q-P lattice for several reasons. First, if a C_{60} molecule is connected to another C_{60} molecule on a Hex lattice, the admolecule-system interaction strength (> 0.3 eV; 0.3 eV is the C_{60}-C_{60} interaction strength, which is roughly $10kT$) is likely to be too large to cause desorption to occur at any experimentally relevant temperatures. Second, desorption events for single-C_{60} molecules (as would be represented on the Q-P lattice) were seen in Molecular Dynamics simulations at high temperatures. Desorption events for C_{60} molecules in the presence of other C_{60} molecules are unlikely rare events, which would have taken an enormously long time to ob-

serve in MD. For single-C_{60} desorption events, there were very few data points available for desorption rate as a function of temperature, so a linear dependence was chosen for simplicity. Desorption does not occur for C_{60} until ~500 K for bulk phase pentacene, and until ~525 K for thin film phase pentacene, as extrapolated from the MD data. The higher desorption temperature for C_{60} from the thin film phase is reasonable, considering that the average adsorption energy for C_{60} on bulk phase pentacene is about 0.02 eV higher (*i.e.*, less attractive) than that on thin film phase.

5.2 Determination of energy barriers

The determination and cataloguing of energy barriers is one of the most important components in a KMC simulation. In this section, the compilation of energy barriers and other related information are described in detail for the multi-lattice diffusion events. As a convention, for site-to-site hops, we refer to C_{60} diffusion events on pentacene on the Q-P lattice as "QP jumps." Analogously, C_{60} diffusion events on pentacene on a Hex lattice will be referred to as "Hex-sub jumps" (referring to jumps at the submonolayer level), and C_{60} diffusion events on C_{60} will be referred to as "Hex-bulk jumps" (referring to jumps beyond the first monolayer, where C_{60} follows its bulk lattice structure). It should be noted here that both Hex-sub jumps and Hex-bulk jumps can be of type A, B, or C as depicted in Figure 5.4(b).

5.2.1 QP jump rates

For the QP jumps, jump rates were obtained by calculating the frequencies of many different diffusion events during MD simulations of a single C_{60} molecule diffusing on pentacene at different temperatures; all the possible QP jumps are shown in Figure 5.2. The temperatures tested ranged from 200 to 600 K, in increments of 25 K, and each MD simulation was run for 2 ns. These sets of MD simulations were run for both the bulk and thin film phases of pentacene. The frequency *vs.* temperature data were fitted to an Arrhenius equation of similar form to Equation 3.2, but shown in Equation 5.1 in terms of frequencies (ν). In the cases where an Arrhenian fit was not appropriate, a second-order polynomial was fitted to the frequencies as a function of temperature. Figure 5.8 shows the bulk phase frequency *vs.* temperature data (left column) and the corresponding Arrhenian plot of the ln(frequency) vs. $1/k_BT$ (right column). Figure 5.9 shows the same data for the thin film phase. For the linear Arrhenian plots with negative slope, energy barriers (slope) and prefactors (y-intercept) were extracted. Non-linear Arrhenian data suggests the particular diffusion event is not Arrhenian. For such cases, the frequency was taken as the polynomial function of temperature. All of this data combined gives temperature-dependent rates necessary for the QP jumps in the KMC simulation.

$$\nu = \nu_0 e^{-E_a/kT} \tag{5.1}$$

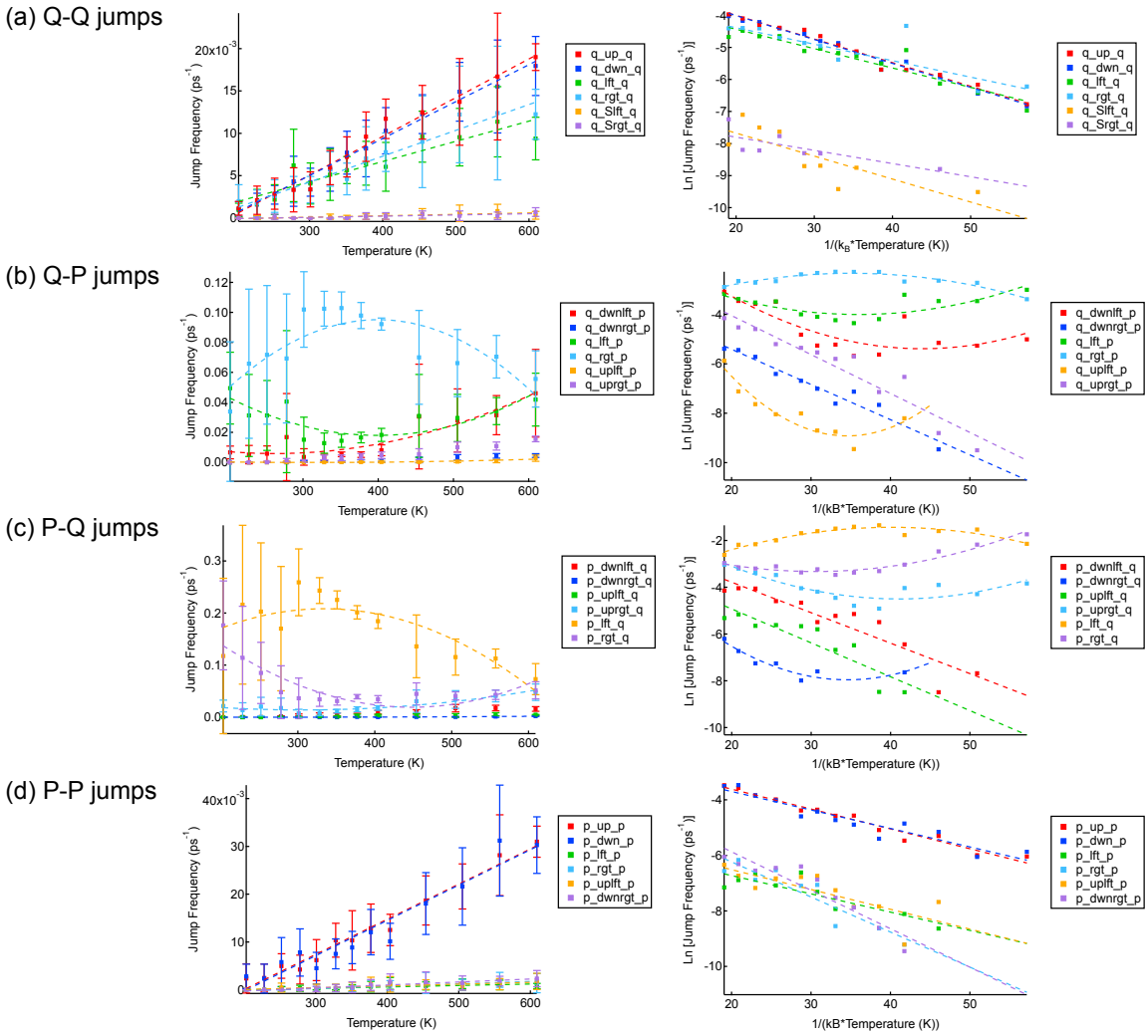

Figure 5.8: C_{60} jump frequencies on bulk phase pentacene: Plots of jump frequency *vs.* temperature (left column) and ln(frequency) *vs.* $1/k_BT$ (right column) for (a) Q-to-Q jumps, (b) Q-to-P jumps, (c) P-to-Q jumps, and (d) P-to-P jumps. Dotted lines are shown to guide the eye; however, the straight lines with negative slopes in the right column set of graphs correspond to specific jumps that are Arrhenian. See Figure 5.2 for the schematic of all possible jumps.

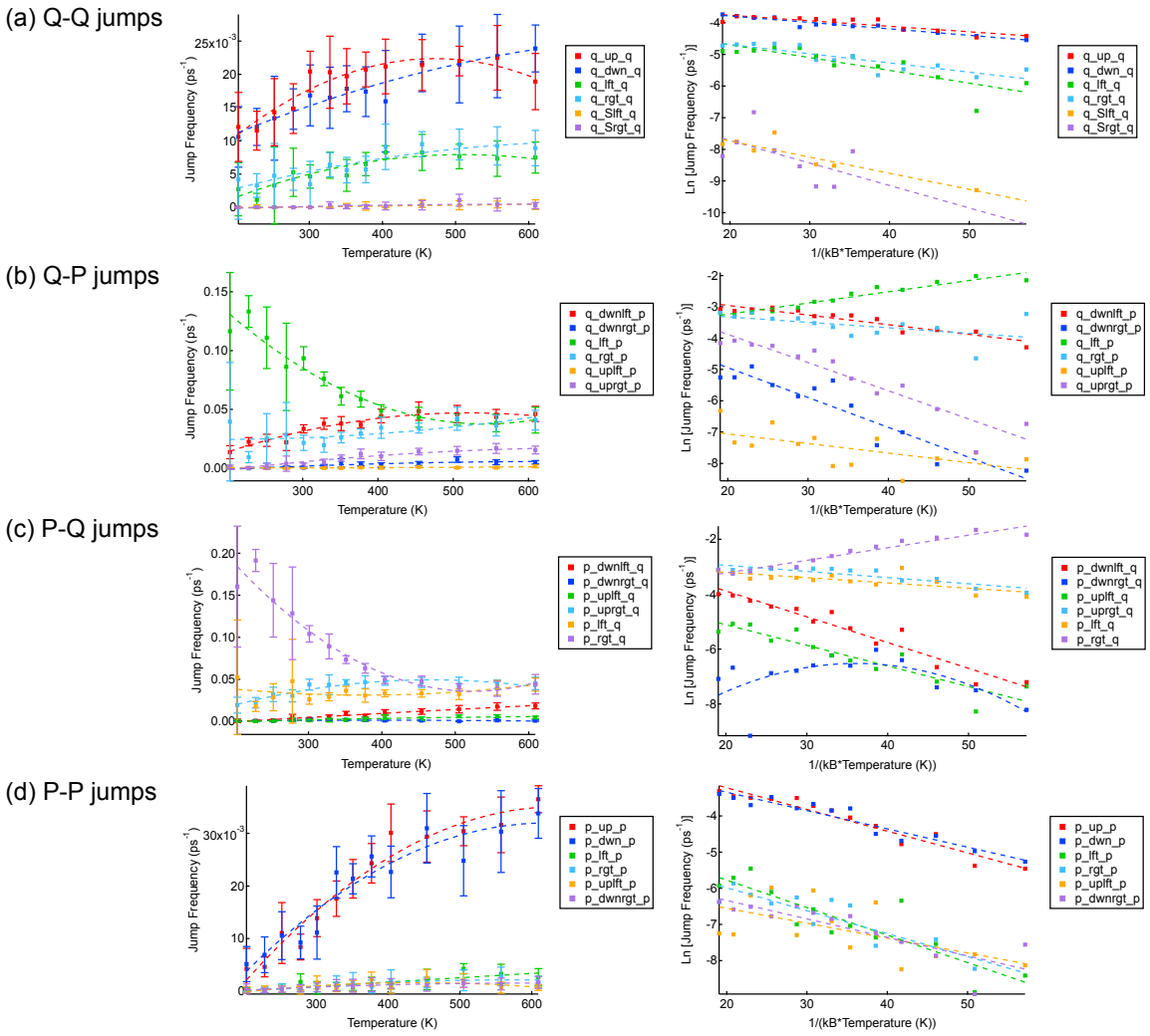

Figure 5.9: C_{60} jump frequencies on thin film phase pentacene. Key as in Figure 5.8.

To verify the KMC model developed so far, the results of KMC-predicted diffusion were compared to those from an MD simulation of a single C_{60} molecule diffusing over bulk phase pentacene. Figure 5.10 compares the trajectories of one C_{60} molecule diffusing on a bulk phase pentacene surface using MD and KMC, each for 1 ns at 300 K. From the figure, it is evident that the KMC code captures the anisotropy of the C_{60} molecule on bulk phase pentacene as well as the lateral extent of diffusion that occurs in 1 ns. For a more quantitative comparison, we calculated the diffusion coefficient of C_{60} on bulk phase pentacene using KMC and compared it to that already obtained using MD. In Figure 5.11 one can see that the KMC simulations reproduce the MD-derived diffusion coefficients within a factor of about five or less; results within an order of magnitude can be regarded as satisfactory. The KMC simulation overestimates the diffusion coefficient at very high temperatures because it does not take into account the effect of the enhanced movement of the pentacene surface disrupting the C_{60} diffusion, a phenomenon we have seen in MD, but which is too complex and stochastic to capture in the KMC code. Overall, however, the Q-P lattice system in the KMC simulations correctly predicts the behavior of solitary diffusing C_{60} molecules, both qualitatively and quantitatively.

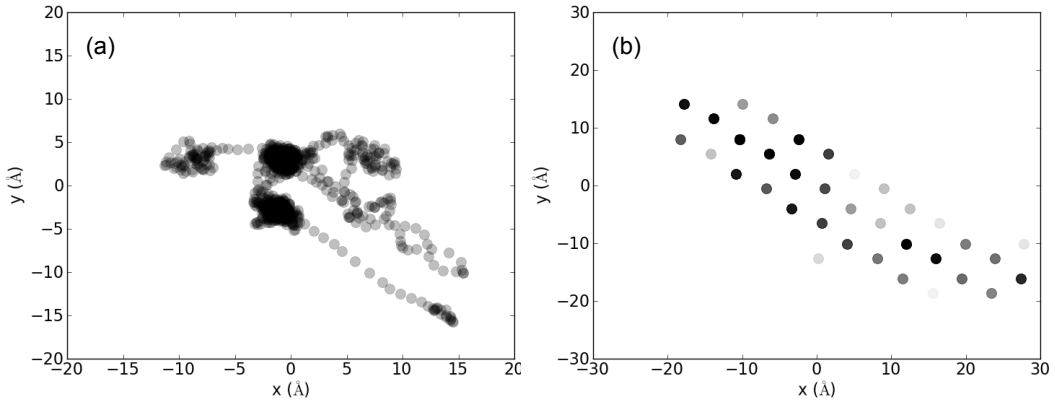

Figure 5.10: C_{60} center-of-mass trajectories on bulk phase pentacene using (a) Molecular Dynamics and (b) Kinetic Monte Carlo. Darker areas show longer periods of residence. Each simulation was performed for 1 ns at 300 K.

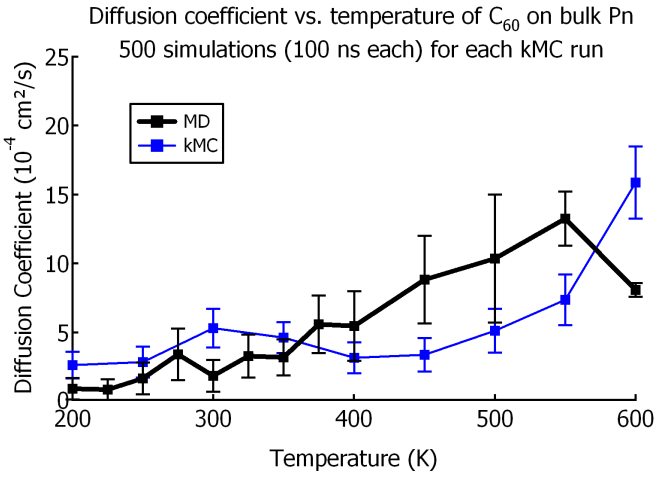

Figure 5.11: C_{60} diffusion coefficients on bulk phase pentacene vs. temperature using MD and KMC.

5.2.2 Hex-sub jump rates

To obtain rates for Hex-sub jumps, it was infeasible to perform multiple MD simulations at different temperatures as it had been for the QP jump rates. This is mainly because additional C_{60} molecules add significantly to computational expense. Instead, we investigated calculating energy barriers statically by means of molecular mechanics. Only "near" neighbors (defined as neighbors exactly one C_{60} van der Waals distance apart) of the initial and final position were considered for simplicity. In calculating the energy barriers, we averaged the effect of rotational degrees of freedom. Figure 5.12 shows schematics of all the unique arrangements of (near) C_{60} molecules on a Hex lattice along with their corresponding energy barriers. In the end, we categorized these arrangements by three factors that determined the energy barrier: the number of initial neighbors, the number of final neighbors, and how many shared neighbors exist between the initial and final jump sites (this can be zero, one, or two).

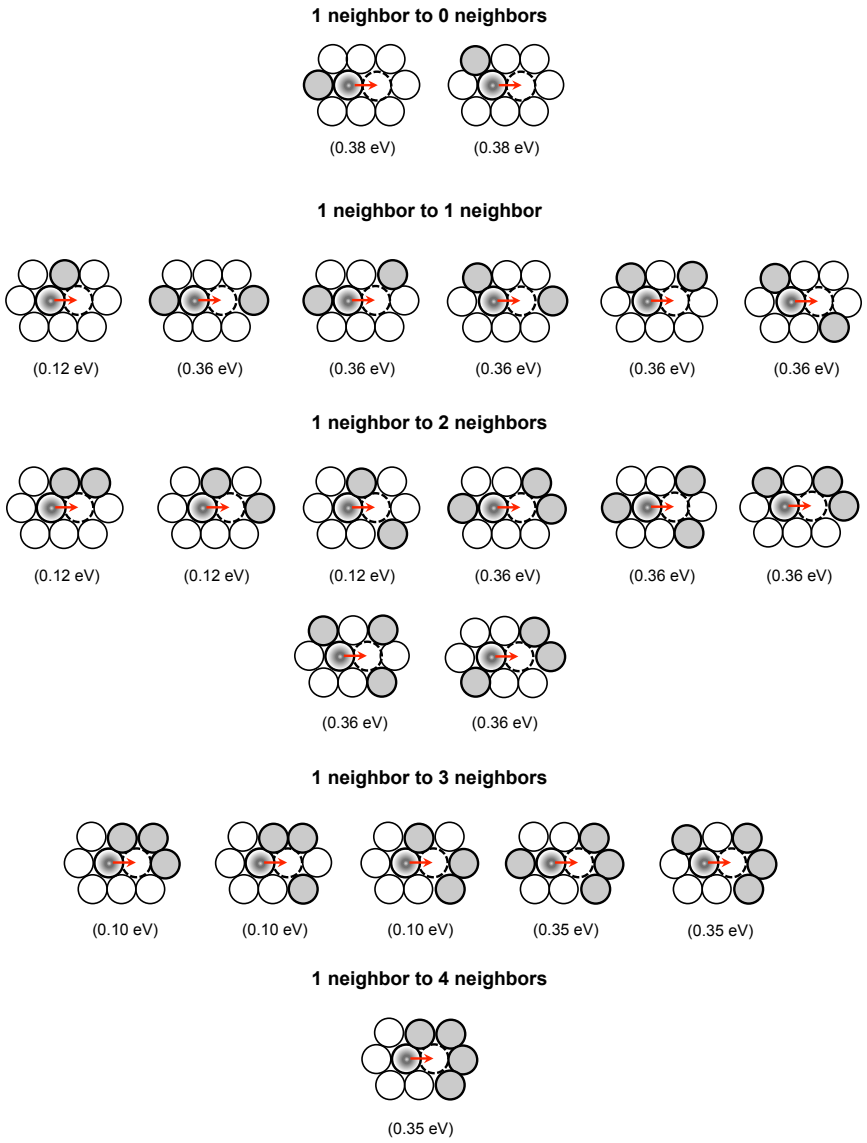

Figure 5.12: Unique C_{60} arrangements for calculating energy barriers that depend on the number of initial and final neighbors as well as the number of shared neighbors that exist between the initial and final jump sites. Gray circles represent C_{60}-occupied sites, empty circles represent empty sites, gradient-filled circles represent the jumping C_{60} molecule, and the red arrow to the dotted, outlined white circle indicates the jump direction.

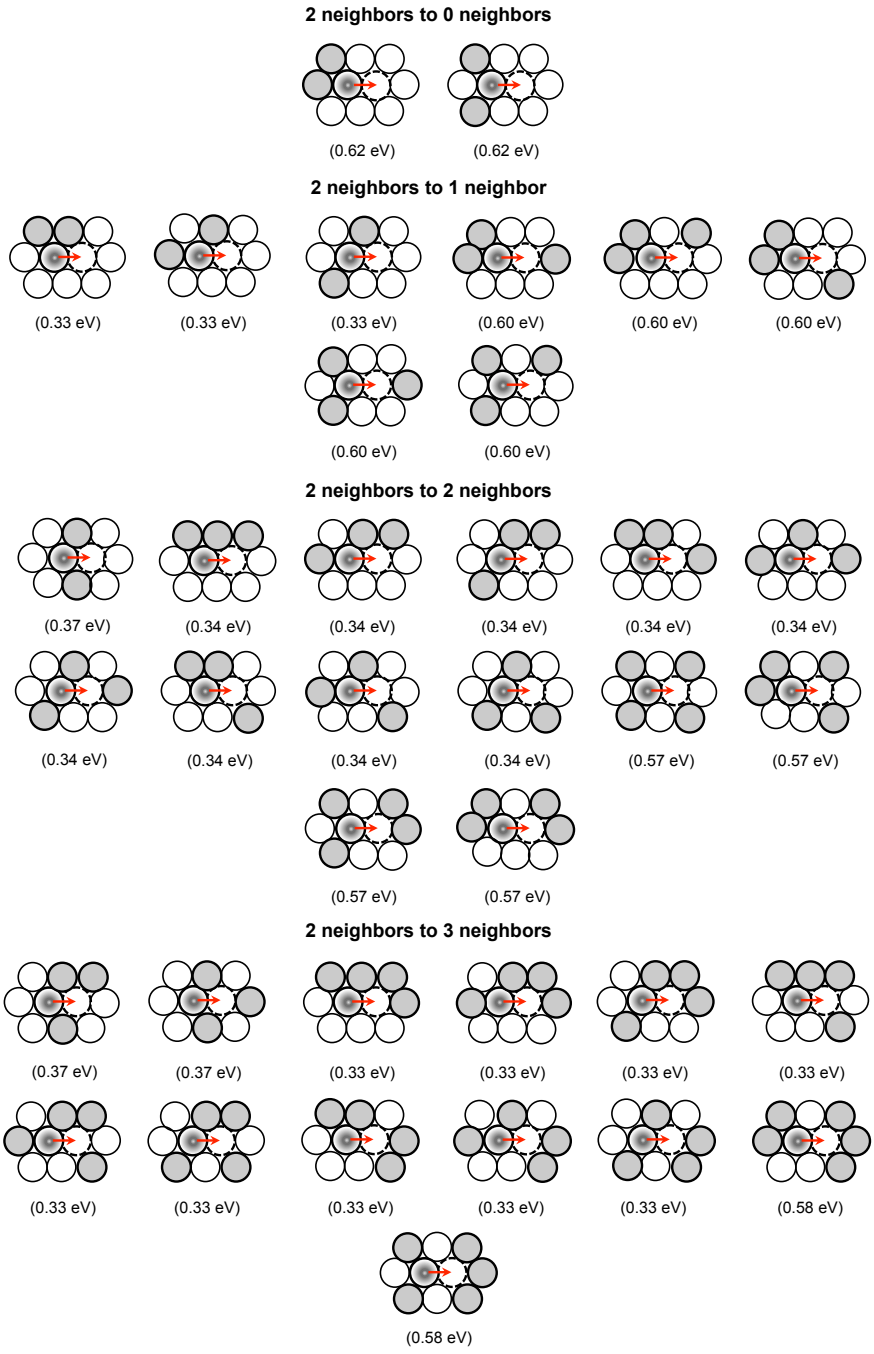

Figure 5.12: Continued. Key as in Figure 5.12.

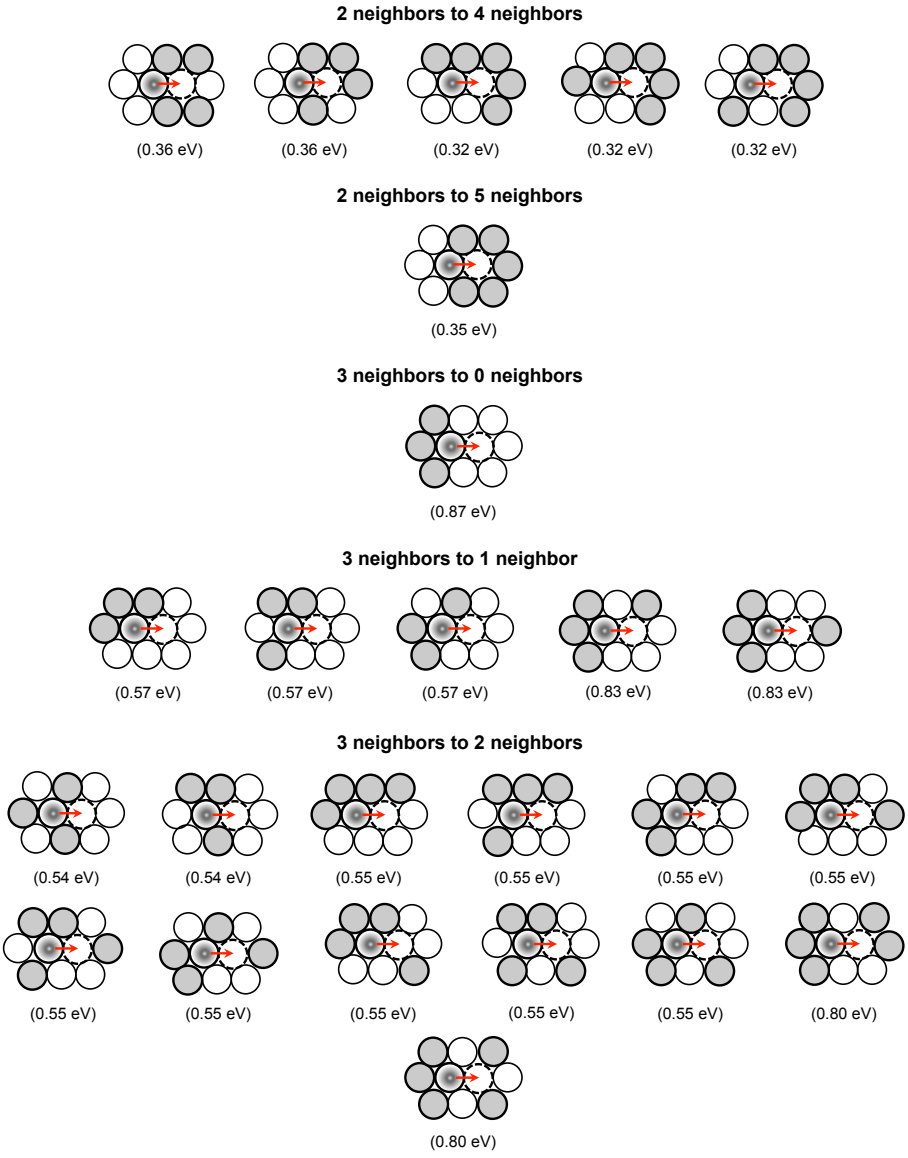

Figure 5.12: Continued. Key as in Figure 5.12.

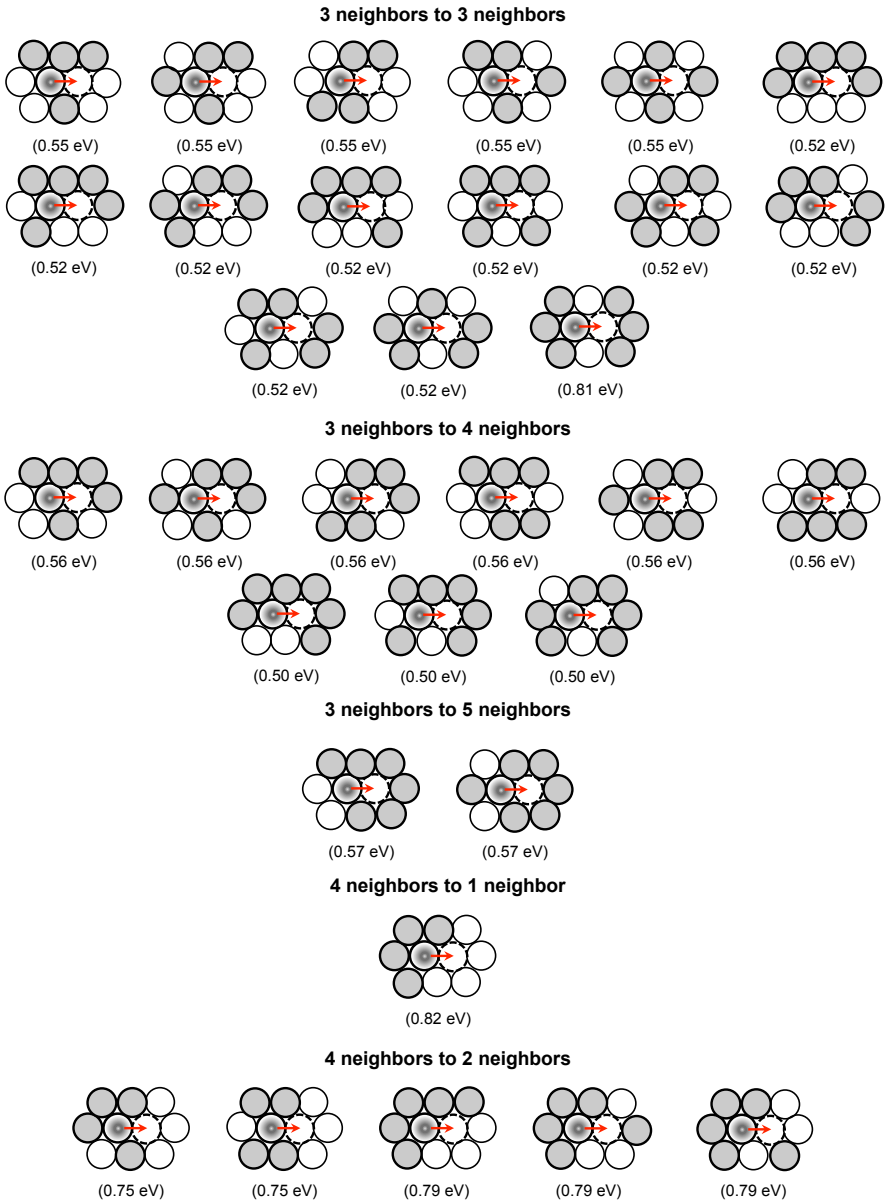

Figure 5.12: Continued. Key as in Figure 5.12.

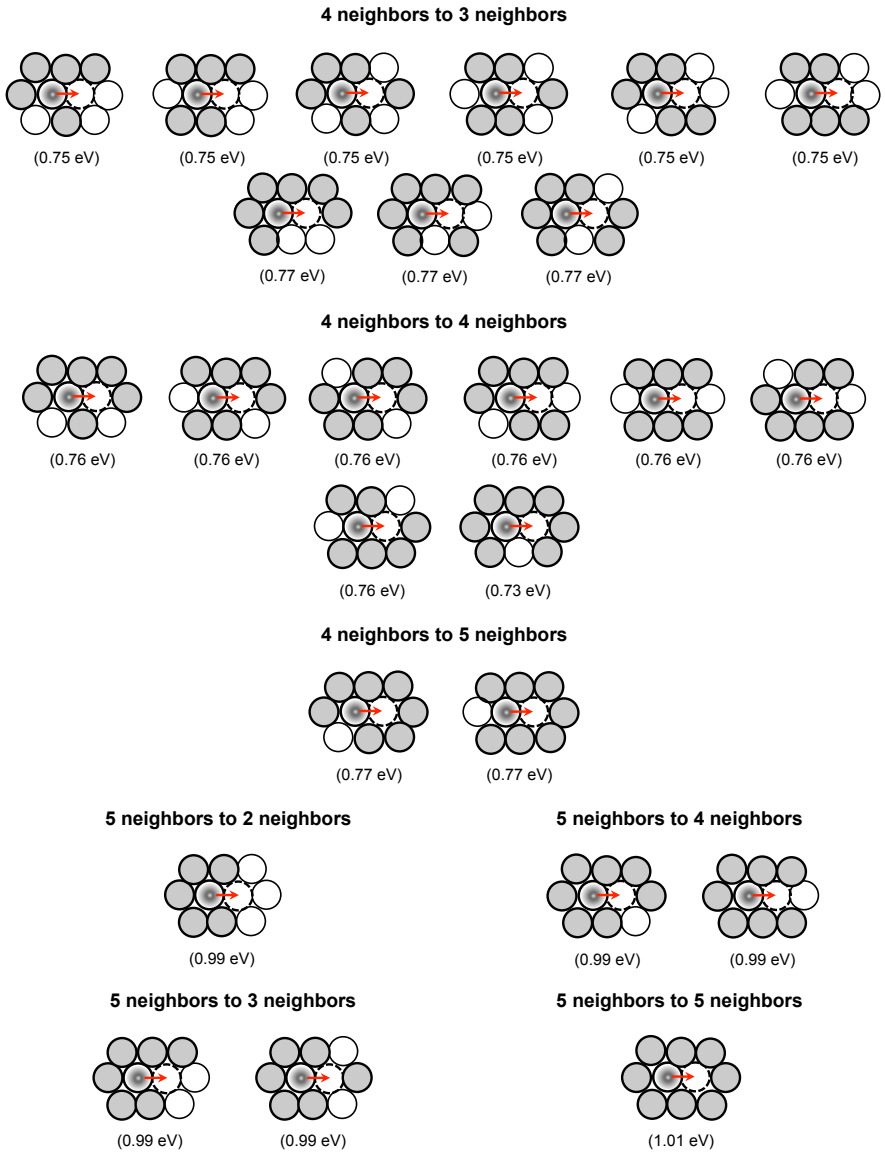

Figure 5.12: Continued. Key as in Figure 5.12.

5.2.3 Hex-bulk jump rates

The energy barriers for Hex-bulk jumps depend not only on the number of initial and final neighbors (as in the case for the Hex-sub jumps described previously), but also on the C_{60} island configuration below it (see Figure 5.13(b)). One of the first questions to be answered was how big does a C_{60} island have to be for the energy barrier of a C_{60} jump not to change (assuming no neighbors in this case). In other words, how close to an island edge does a diffusion molecule atop need to be to have its diffusion energy barriers affected. After testing energy barriers of different island sizes, it was determined that C_{60} jumps starting from positions beyond the second C_{60} row from the edge were essentially identical to those in the middle of a terrace (no proximity to a step). Figure 5.13(a) shows the different types of sites considered near edges. A "T" site refers to a jump starting from a terrace (a site away from, uninfluenced by, a C_{60} island edge), and "A" and "B" sites refer to jumps starting *at* a C_{60} island edge where only "B" jumps can result in C_{60} molecules falling over the edge of the island, surmounting a Schwoebel barrier.

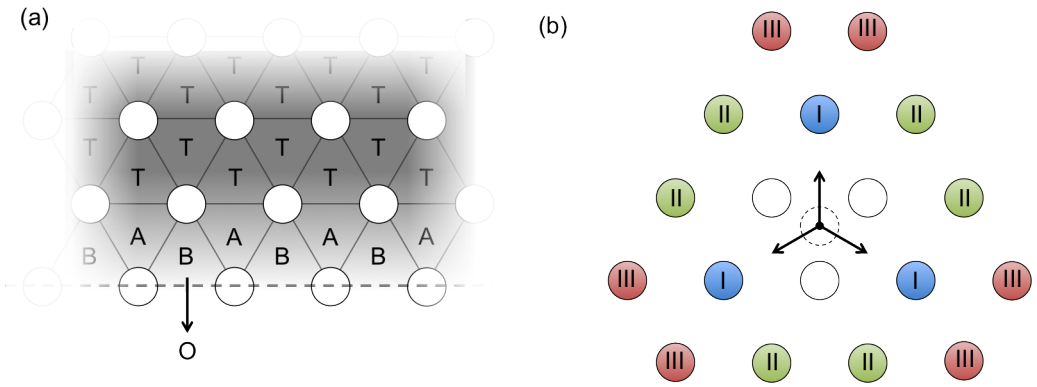

Figure 5.13: Schematics to describe C_{60} islands and near-edge sites. In both (a) and (b), circles represent possible positions of C_{60} molecules in a C_{60} island (diameters are under-represented for clarity); circles outlined in solid black represent molecules in one plane (*i.e.*, within the same monolayer), and the dotted circle in (b) is a molecule atop that monolayer. (a) The three different site types (A, B, T) designate the proximity of a site to an island edge (dotted line), and the O site designates that a molecule has fallen over the edge of an island. (b) C_{60} occupation at sites labeled I (blue), II (green), and III (red) is used to determine how close the jumping molecule (dotted circle) is to the edge of an island.

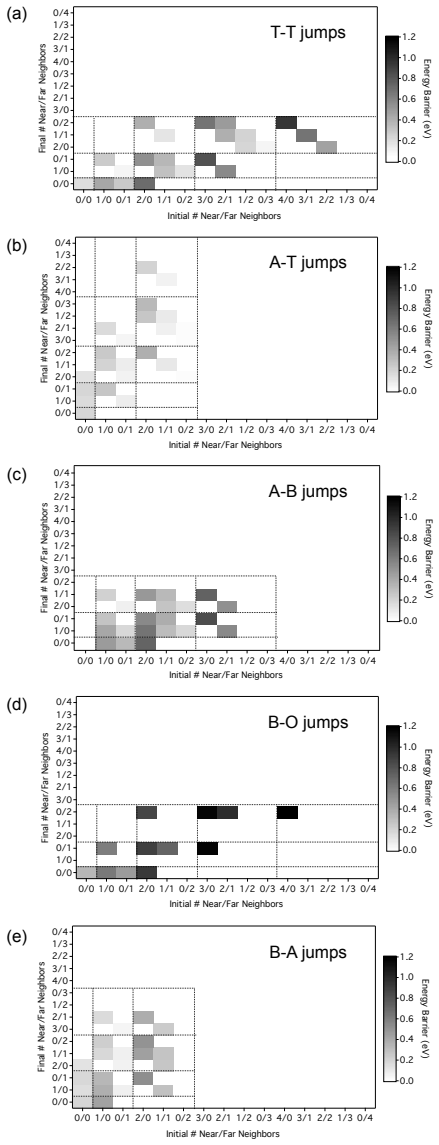

Figure 5.14: A catalogue of energy barriers for C_{60} jumps on a C_{60} lattice (HexML jumps) for (a) T-T site jumps, (b) A-T site jumps, (c) A-B site jumps, (d) B-O site jumps, and (e) B-A site jumps. Refer to Figure 5.13(a) for site type definitions. The darker the gray color, the higher the energy barrier. Blank spots correspond either to impossible arrangements or unnecessary calculations.

In general, C_{60} jumps toward (but not necessarily off) the edge of a C_{60} island have a higher energy barrier than C_{60} jumps far from an edge, showing the existence of the Schwoebel barrier. In the KMC code, this distinction was taken into consideration in detail. Figure 5.13(b) shows the types of sites considered in determining what the energy barrier of a particular jump would be. The presence of type-I sites (blue) determines whether or not the molecule starts out at a "B" site and, if so, whether the jump would result in the molecule going over the edge (referred to as an "O" event to designate "over"); the presence of type-II sites (green) determine whether or not the molecule starts out at an "A" site and/or ends up at a "B" site. The presence of type-III sites (red) determine whether a jump results in an "A" site or a "T" (terrace) site. Thus, a Hex-bulk jump will take place either as T-to-T (or A), A-to-T, A-to-B, B-to-O, or B-to-A, each of which has a unique set of energy barriers depending on the number of initial and final neighbors. Figure 5.14 catalogues each of these energy barriers for reference. Of these energy barriers, the B-to-O are highest (shown as the darkest) because these correspond to Schwoebel barriers to surmount a C_{60} step edge. The A-to-T and B-to-A energy barriers are the lowest because these are jumps away from the C_{60} edge.

At this point, it is appropriate to compare the library of energy barriers generated in this study to those quoted in the Liu *et al.* paper,[3] because this is the only other occurrence in the literature where a KMC simulation of C_{60} growth on C_{60} has been performed. Figures 5.15 and 5.16 show a comparison of the Liu *et al.* energy barriers with those reported here. It should be noted that Liu *et al.* has many fewer values than obtained here and shown in Figure 5.14. A few of the energy barriers, like those shown in Figures 5.15(a) and (b) are very close, but overall the energy barriers they obtained are consistently lower than in this

study, by about 0.1 eV (approximately 4 $k_B T$ at room temparature), which is significant. In the Liu *et al.* paper, some jump types with "far" neighbors (distanced by $^2/_3\sqrt{3}$ times the van der Waals diameter), like those shown in Figures 5.15(c) and (f), are reported as probabilities in lieu of quoting energy barriers. Their rationale is that the initial configuration in these situations is a metastable state (*i.e.*, the jump rate is higher than that of the a jump with no neighbors), so if this situation presents itself, a jump will automatically be performed with a certain probability. While this is reasonable in general, we believe that there are some cases where this logic may not hold. For example, in Figure 5.15(h), we calculate an energy barrier for jump I of 0.34 eV, which is higher than that of a basic neighborless jump (0.21 eV as shown in Figure 5.15(a)); Liu *et al.* categorize this initial state as "metastable," having a 99.86% probability of jumping. There are also some situations where they provide an infinite energy barrier, yet we find that there is only a moderate (potentially surmountable) energy barrier. Jump I in Figure 5.15(g) is an example of this, where we calculate an energy barrier of 0.34 eV and Liu *et al.* describe this barrier as infinite. However, as described in Section 2.4, Liu *et al.* studied C_{60} growth on perfectly compact first-layer C_{60} islands, whereas we are studying C_{60} growth on pentacene with multi-layer C_{60} island formation. This difference makes comparing morphological results inappropriate, but it is still worth noting the differences in rates and energy barriers.

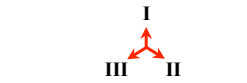

		Molecular Mechanics-derived using MM3	MD-derived from Liu *et al.* paper
(a)	I	E_a = 0.205 ± 0.022 eV	E_a = 0.178 ± 0.004 eV $v_0 = 2\times10^{11}$ s^{-1}
	II	" "	" "
	III	" "	" "
(b)	I	E_a = 0.448 ± 0.025 eV	E_a = 0.429 ± 0.057 eV $v_0 = 6.5\times10^{11}$ s^{-1}
	II	E_a = 0.289 ± 0.029 eV	E_a = 0.185 ± 0.006 eV $v_0 = 2.5\times10^{11}$ s^{-1}
	III	N/A	N/A
(c)	I	E_a = 0.295 ± 0.024 eV	P=0%
	II	E_a = 0.111 ± 0.021 eV	P=50%
	III	" "	P=50%
(d)	I	E_a = 0.717 ± 0.029 eV	$E_a = \infty$
	II	N/A	N/A
	III	N/A	N/A
(e)	I	E_a = 0.556 ± 0.028 eV	E_a = 0.354 ± 0.063 eV $v_0 = 6\times10^{10}$ s^{-1}
	II	" "	" "
	III	N/A	N/A
(f)	I	E_a = 0.054 ± 0.023 eV	P=98.24%
	II	E_a = 0.189 ± 0.024 eV	P=0.88%
	III	" "	" "

Figure 5.15: Comparison of terrace energy barriers (E_a) of C_{60} on C_{60} obtained by the method described in this work (molecular mechanics) and the method of Liu *et al.* (Molecular Dynamics).[3] Liu *et al.* also provided attempt frequencies (ν_0) for certain jump types. They provide probabilities (P) for jump types where they quote the initial configuration as a metastable state.

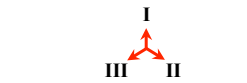

			Molecular Mechanics-derived using MM3	MD-derived from Liu *et al.* paper
(g)	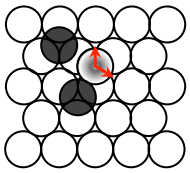	I	E_a = 0.337 ± 0.025 eV	E_a = ∞
		II	E_a = 0.385 ± 0.031 eV	E_a = ∞
		III	N/A	E_a = ∞
(h)	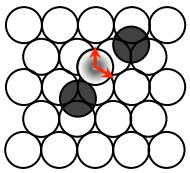	I	E_a = 0.344 ± 0.028 eV	P=99.86%
		II	E_a = 0.180 ± 0.026 eV	P=0.14%
		III	N/A	N/A
(i)	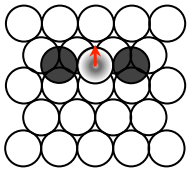	I	E_a = 0.418 ± 0.036 eV	E_a = ∞
		II	N/A	N/A
		III	N/A	N/A

Figure 5.15: Continued. Key as in Figure 5.15

		Molecular Mechanics-derived using MM3	MD-derived from Liu *et al.* paper
(a) 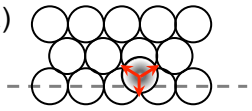	I	E_a = 0.191 ± 0.024 eV	P=45%
	II	" "	" "
	III	E_a = 0.334 ± 0.020 eV	P=10%
(b) 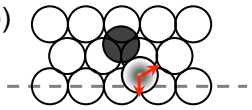	I	N/A	N/A
	II	E_a = 0.258 ± 0.033 eV	P=99.97%
	III	E_a = 0.630 ± 0.021 eV	P=0.03%
(c) 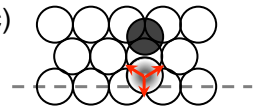	I	E_a = 0.078 ± 0.025 eV	P=50%
	II	" "	" "
	III	E_a = 0.449 ± 0.021 eV	P=0%
(d) 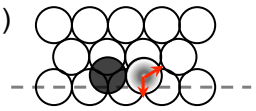	I	N/A	N/A
	II	E_a = 0.441 ± 0.034 eV	E_a = 0.207 ± 0.004 eV $v_0 = 2.9\times10^{11}$ s^{-1}
	III	E_a = 0.596 ± 0.021 eV	E_a = 0.354 ± 0.053 eV $v_0 = 3\times10^{11}$ s^{-1}

Figure 5.16: Comparison of energy barriers at a C_{60} step edge. Key as in Figure 5.15

All Hex-sub and Hex-bulk jumps were considered to be Arrhenian in nature, so the jump rates were calculated as a function of the appropriate energy barrier, temperature, and prefactor. Since we could not obtain frequency *vs.* temperature data for the Hex jumps, as we could the QP jumps, the prefactor was assumed initially to be the average of all the prefactors obtained by analyzing the QP frequency data. This average prefactor, or attempt frequency, was 1.2×10^{11} s^{-1}. The following section describes the sensitivity of the results to the Hex prefactor.

5.3 Sensitivity analysis of key parameters

In our sub-monolayer studies, we consider the sensitivity of the system behavior to changing the Hex prefactor and deposition rate, since the choice of these two parameters strongly affects how long the simulation takes to execute. The lower the deposition rate, the greater the disparity between the deposition rate and the rate of diffusion events, and the more rate-limiting these diffusion events become. The larger the Hex prefactor, the faster the diffusion events become and the more rate-limiting they become. Thus, the combination of a small Hex prefactor and a high deposition rate gives the fastest completion. Figure 5.17 shows the CPU time taken in days for different combinations of Hex prefactor and deposition rate.

The deposition rate was varied from 10^4–10^6 ML/s, and the Hex prefactor was varied from 10^7–10^{11} s^{-1}. For our 71×89 unit cell bulk pentacene system size, 10^4 ML/s corresponds to a deposition rate of $\sim10^7$ s^{-1} (depositions per second), 10^5 ML/s to $\sim10^8$ s^{-1}, and 10^6 ML/s to $\sim10^9$ s^{-1}. A "realistic"

deposition rate would be about 1 ML/s (~10^3 s^{-1}); but, because this rate is much slower than the rate of diffusion events (~10^{10} s^{-1}), the simulation would evolve in time extremely slowly. The range of Hex prefactors chosen overlaps the range of previously reported values for attempt frequencies of the diffusion of large molecules, 10^{10}–10^{14} s^{-1}, such as 4-*trans*-2-(pyrid-4-yl-vynyl) benzoic acid (PVBA), decacyclene (DC), hexa-*tert*-butyl-decacyclene (HtBDC), and C_{60}.[3,152–154] In particular, C_{60} on Pd(110) with surface traps has a reported prefactor of 10^{14} s^{-1} (found experimentally),[154] and C_{60} on C_{60} has a reported prefactor of 6×10^{10}–6.5×10^{11} s^{-1} (found from MD simulations).[3] Lastly, for comparison, the average of the QP jump prefactors obtained here from MD simulations of a single C_{60} molecule diffusing over a pentacene surface was 1.18×10^{11}. From this information, we can assume that the Hex prefactor should be in the range of $O(10^{10})$ – $O(10^{11})$ s^{-1}.

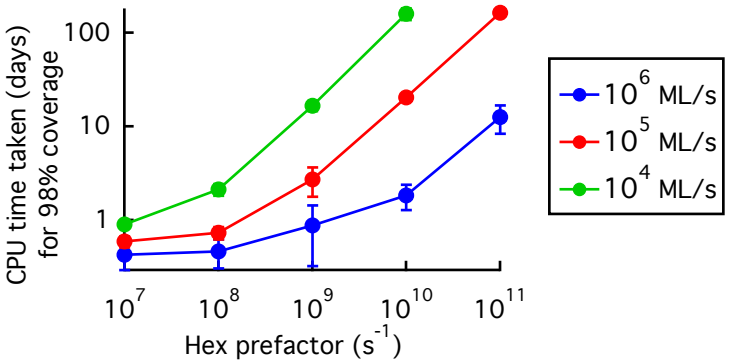

Figure 5.17: CPU time taken in days for monolayer coverage to reach 95% as a function of Hex prefactor and deposition rate.

Before picking the smallest Hex prefactor and the highest deposition rate for convenience, we must determine the sensitivity of the system's properties to choices of these parameters. We chose as a metric for system behavior the cluster size distribution at 10% coverage. Figure 5.18 shows both the average and dominant cluster sizes at 10% coverage for different Hex prefactors and deposition rates. The deposition rate curves converge around Hex prefactors of 10^{10}–10^{11} s^{-1}. Hex prefactors lower than this show significantly different behavior for different deposition rates. Thus, if we stay within the Hex prefactor range of 10^{10}–10^{11} s^{-1}, raising the deposition rate at most to 10^6 ML/s will not significantly alter the system behavior.

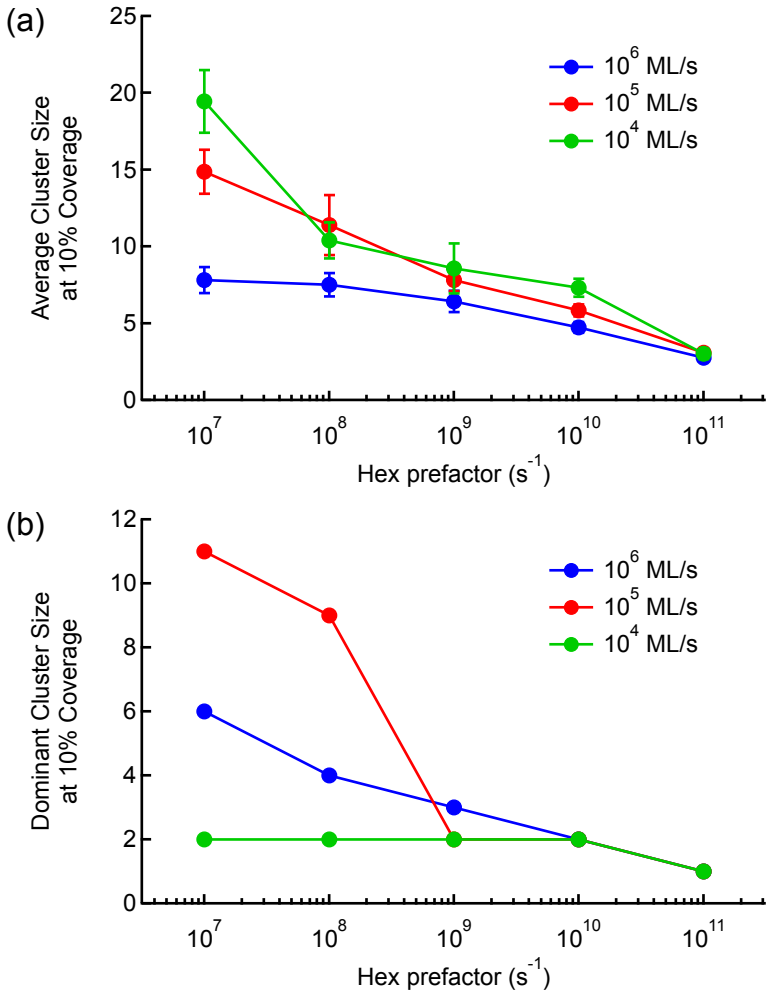

Figure 5.18: (a) Average cluster sizes and (b) dominant cluster sizes at 10% coverage as a function of Hex prefactor and deposition rate. These values were taken from histogram distributions, each containing the statistics of 10 different simulations.

We also considered a second metric regarding the sensitivity analysis, namely the evolution of sub-monolayer and beyond monolayer coverage as a function of simulation time. Figure 5.19 shows the first and n^{th} monolayer coverage as a function of simulation time and deposition rate. This figure plots curves for the different Hex prefactors as well, but they overlap each other within each set of deposition rate data, and cannot be seen. Thus, there is a negligible effect of the Hex prefactor on the rate of coverage. One might think that since a lower Hex prefactor might yield fewer, larger clusters, that sub-monolayer growth would be slower due to the higher tendency of a molecule to land on top of an already clustered island. Zooming into this graph, you can see that this is the case, but the effect is negligible. Note that for 10^4 ML/s, near 100% coverage occurs at ~0.1 milliseconds.

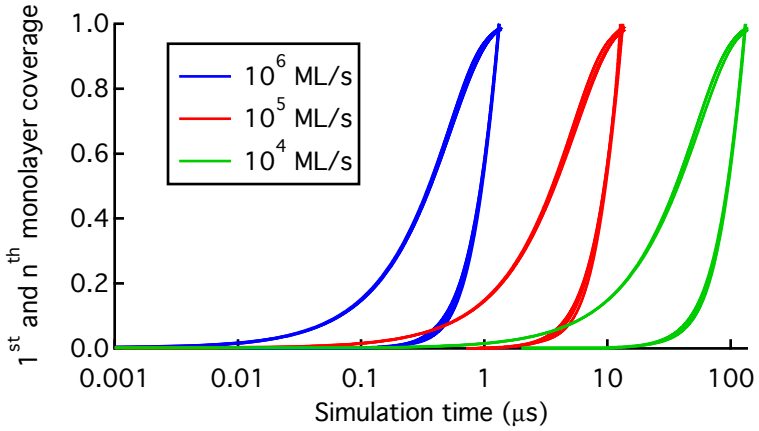

Figure 5.19: First (left side) and n^{th} (right side) fractional monolayer coverage as a function of simulation time for different deposition rates. The different Hex prefactors are also plotted here, but they overlap within each set of deposition rate data, so they cannot be seen.

The reason that the n^{th} monolayer curves in Figure 5.19 (right side within each deposition rate data set) do not reach a plateau like the sub-monolayer curves is that this n^{th} monolayer curve represents the sum of the 2^{nd} ML, 3^{rd} ML, *etc.*, which would each plateau like the first. These data were taken from the first version of the KMC code, where there is no interlayer diffusion and 2^{nd} and 3^{rd} monolayer molecules can occupy the same space upon deposition (obviously impossible). This is the main motivation for incorporating interlayer diffusion into the KMC simulation method, explored in Section 5.5. However, the bottom of the n^{th} layer curves should still accurately represent the system behavior, before interlayer diffusion can play any significant role. For each deposition rate tested, when the second monolayer reaches 5% coverage, the first monolayer has already completed ~50% coverage. Regarding the sensitivity of coverage to Hex prefactor and deposition rate, we conclude that the choice of Hex prefactor does not significantly affect the coverage evolution, and that the deposition rate merely affects the rate of coverage, as would be expected.

5.4 KMC simulations of sub- and multilayer growth of C_{60}

All the analysis in the previous Section 5.3 was performed for sub-monolayer C_{60} growth. Taking a closer look at some of the cluster distributions (used in calculating the values in Figure 5.18) gives a greater understanding of the cluster size evolution for sub-monolayer growth. Figure 5.20 shows cluster distribution histograms for a variety of the deposition rate-prefactor combinations tested. From this figure, it is clear (and expected) that more smaller clusters result from larger deposition rates. Also, smaller average cluster sizes result from higher Hex prefactors. This effect can also be seen clearly in Figure 5.18. For very low

Hex prefactors, there is very little detachment from clusters, emulating almost irreversible growth.

The sub-monolayer C_{60} growth is perhaps best represented by a physical picture of the thin film, showing island shapes as well as sizes. Figure 5.21 shows snapshots of 10, 20, 30, 40, and 50% coverage for C_{60} growth on both thin film and bulk phase pentacene. Both simulations were performed at 300 K, 10^6 ML/s, and a Hex prefactor of 10^{10} s^{-1}. Here, there appears to be a tendency for islands to grow diagonally in the [110] direction on the bulk phase, however we believe this to be an artifact of slightly unequal jump rates in opposite directions, which occurs from averaging out the stochastic nature of MD-derived jump rates (see Figures 5.8 and 5.9). This detail is important over long times because it leads to the constraint of "detailed balance" not being satisfied. This issue is addressed further in Section 5.5. Nonetheless, this artifact of anisotropic island shapes is much less pronounced on the thin film phase, where the nature of the jump rates were inherently more isotropic.

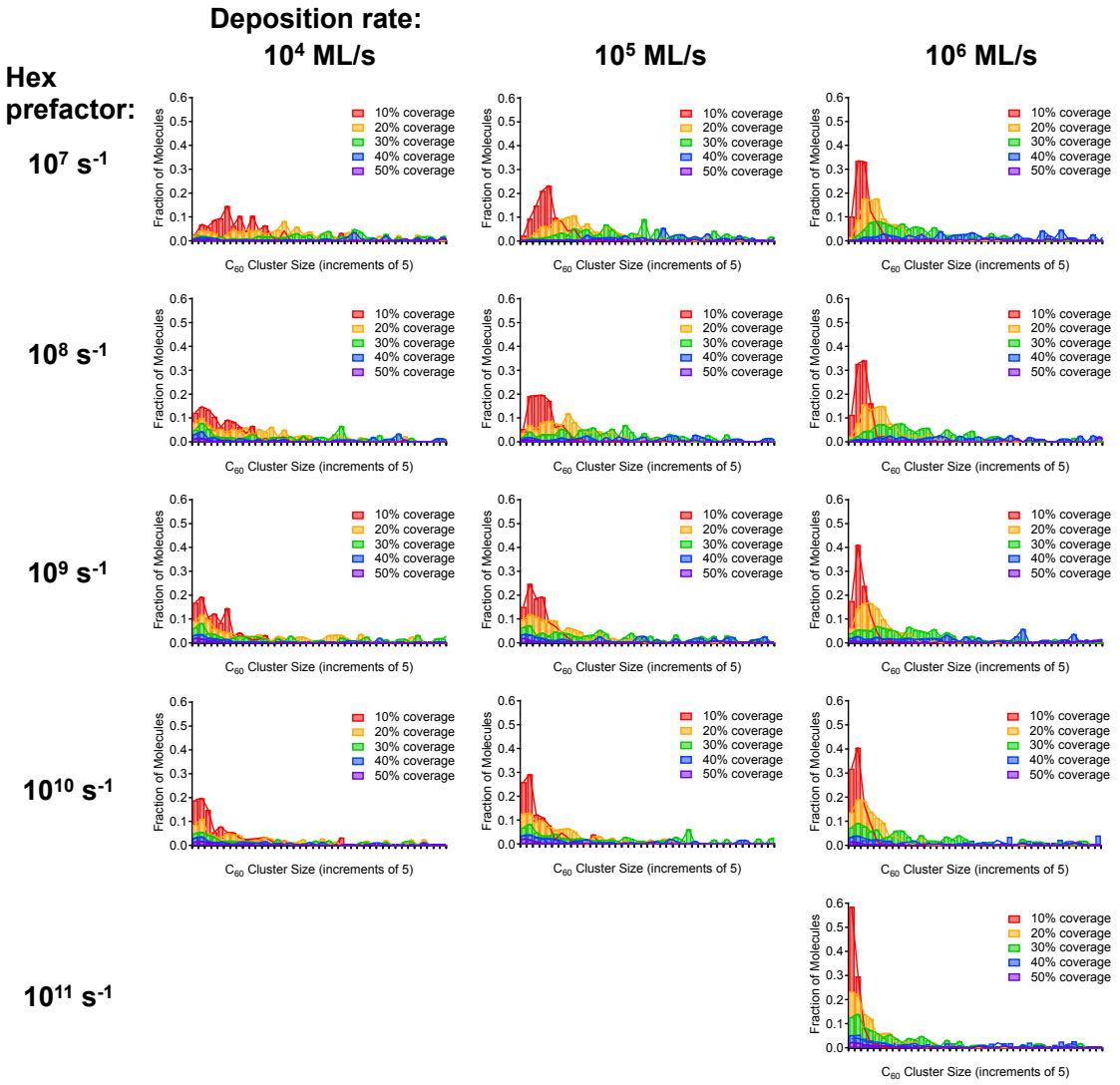

Figure 5.20: Cluster size distribution histograms for different deposition rate-prefactor combinations. The x-axis bins represent clusters of size $5n$ to $5n + 4$, where $n = 0, 1, 2, ..., 39$.

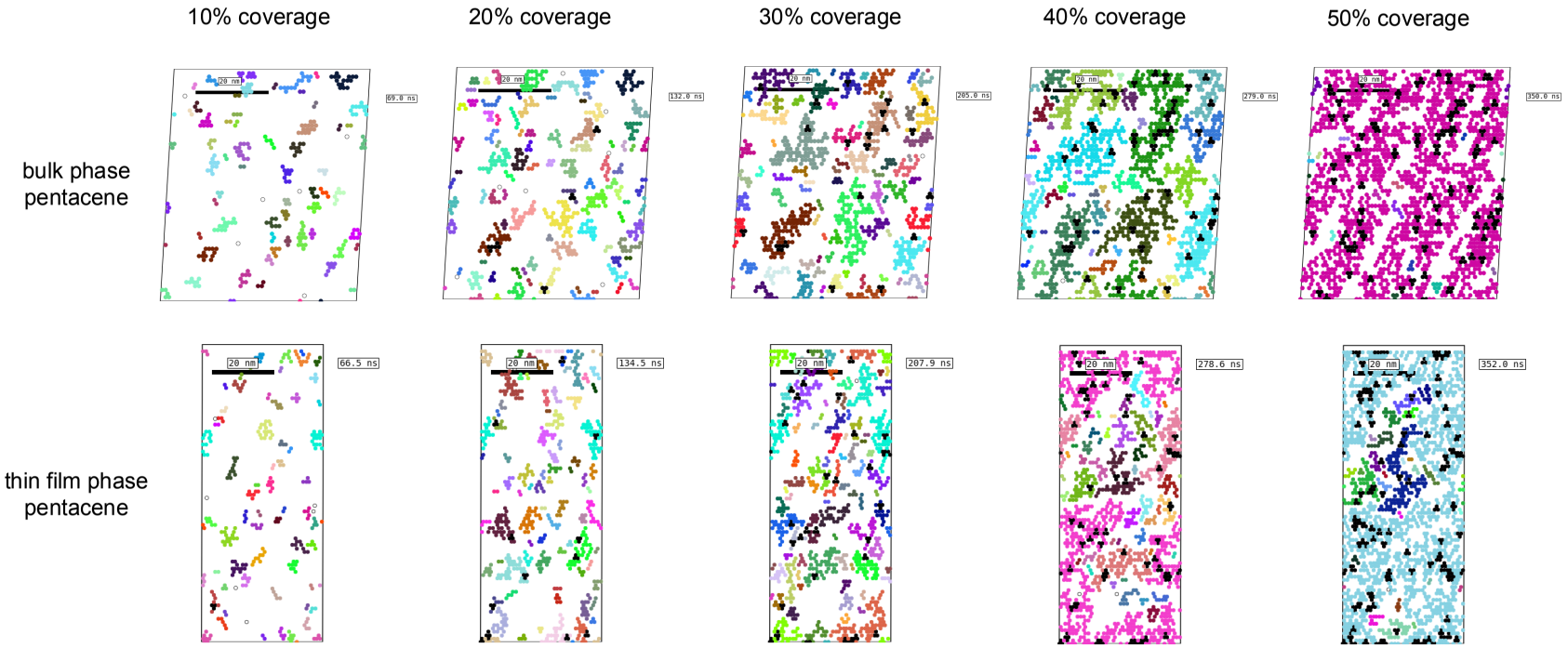

Figure 5.21: Snapshots of C_{60} sub-monolayer growth on bulk phase (top) and thin film phase (bottom) upright pentacene phases. Both simulations were performed at 300 K, 10^6 ML/s, and with a Hex prefactor of 10^{10} s^{-1}. The different colors represent separate clusters, and the black colors represent C_{60} molecules that have been landed upon during a subsequent deposition event and are then deemed to be "frozen" in place. The black bar represents a length scale of 20 nm.

5.5 KMC simulations of multilayer growth of C_{60} on pentacene

The addition of multiple layers in the KMC code introduced more possible events and necessitated a more complicated method of handling deposition. The additional events for multiple layers are referred to as Hex-bulk jumps, as described in Section 5.2.3, and the jump rates for C_{60} on or off of C_{60} islands are generally much higher. The deposition method for the multiple-layer code involves determining whether a C_{60} molecule is deposited onto a C_{60} triangle or not (see Figure 5.4(a)). Previously, we had assumed that if a molecule was deposited on such a triangle, those triangle molecules were not allowed to move (shown as black particles in Figure 5.21), and the deposited molecule was ignored. In the multiple layer version of the KMC code, no molecule is ignored.

Because of the strange artifact of [110]-shaped islands seen in Figure 5.21, caused presumably because of the non-symmetric jump rates, we set the jump rates in opposite directions to be equal in the multiple layer version of the code. After doing this, from the preliminary results so far, we do not observe strange anisotropic island shapes for the bulk phase. Figure 5.22 shows snapshots of the C_{60} growth on bulk phase pentacene with the multiple-layer version of the code. The color scheme for these snapshots is different than that shown in Figure 5.21; the different colors in Figure 5.22 do not represent unique clusters, but instead reflected whether the molecule is on the A, B, or C lattice as shown in Figure 5.4(b). It can be imagined that because C_{60} molecules on bulk phase pentacene travel with ease in the $[1\bar{1}0]$ direction, island shapes might be elongated in that direction. We had hoped to see such island shapes reflecting the potential energy surfaces described in Section 3.2 and shown in Figure 3.7, but the connection was not clear. Further investigation of these simulations is currently

underway, and due to time constraints caused by the extremely slow simulations, the results could not be presented herein. Effects of temperature, deposition rate, pentacene phase on the multilayer evolution of C_{60} on pentacene will be the topic of a future publication.

In the absence of experimental references to C_{60} growth on thin film or bulk phase pentacene at these high deposition rates, at this point we turn to an alternate method of characterizing the C_{60} cluster evolution using a reaction-diffusion continuum model. With the same knowledge obtained from MD (Chapter 3) and molecular mechanics (Section 5.2), we chose to pursue an independent route that used a mathematical model of the evolution of clusters of size j (*i.e.*, clusters consisting of j=1,2,3,... C_{60} molecules) and compare the results to those obtained by KMC. This two-dimensional reaction-diffusion model has the benefit of reaching experimentally feasible deposition rates (~1 monolayer per second as opposed to 10^4–10^6 monolayers per second); however it is not able to give details of the cluster microstructures. The following Section 5.6 describes this method in more detail, and finally, compares the C_{60} cluster evolution to that obtained by KMC for both the thin film and bulk phases.

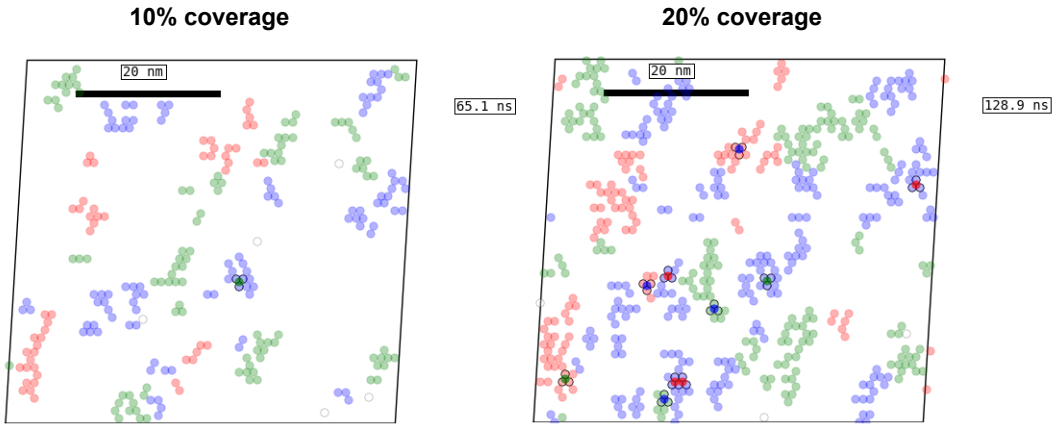

Figure 5.22: Snapshots of 10 and 20 percent coverage of C_{60} growth on bulk phase pentacene from the multilayer version of the KMC code. The simulations were performed at 300 K, 10^6 ML/s, and with a Hex prefactor of 10^{10} s^{-1}. The different colors represent which lattice the molecule is a part of: A (blue), B (pink), C (green), or Q/P (hollow gray circle). Molecules delineated with a black circle are not allowed to move because they are immobilized by other molecule(s).

5.6 Continuum model of cluster evolution in submonolayer growth of C_{60} on pentacene

Viewing the submonolayer C_{60}-on-pentacene system as a two-dimensional reaction-diffusion problem can provide insight into the kinetics behind cluster nucleation and growth. The situation posed is one in which the diffusing species (C_{60} monomers) diffuse in spaces between immobile clusters of size R_j as shown in Figure 5.23. The subscript j denotes the number of monomers in cluster j. These clusters can grow and shrink by monomer addition and subtraction, and the number density of monomers around a cluster j evolves with time as the reaction, diffusion, and deposition rates compete. Solving a set of rate equations for the number density of monomers around cluster j gives insight into the relative island densities. This type of model is valid for submonolayer coverages $<\sim$50%, above which the assumption of diffuse monomers breaks down and in practice multi-layer growth begins to evolve.

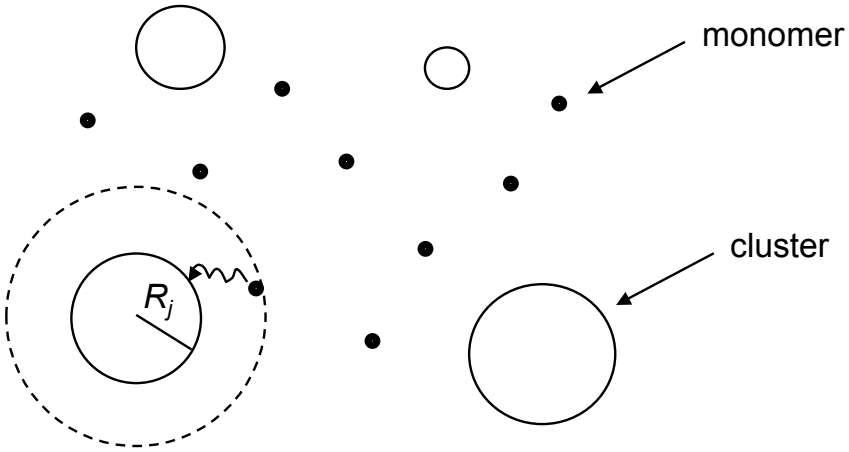

Figure 5.23: Schematic diagram showing the situation posed for solving the two-dimensional reaction-diffusion problem, where only monomers diffuse. The dotted line shows the screening area defined by parameter ξ, outside of which there is no net source or sink of monomers.

At equilibrium, the conservation equation for the number density of monomers around clusters of size j—n_j—is given as Equation 5.2, where D is the diffusion coefficient for monomers and k_j is the rate of all monomer attachment per unit area.

$$-D\nabla^2 n_j = -kn_j \tag{5.2}$$

In Equation 5.2, the right hand side represents the sink of monomer consumption by the surrounding medium of cluster j, and is what allows us to have a finite boundary condition at infinite distances away from the cluster. Otherwise the two-dimensional Laplace equation varies as the logarithm of r, which is not finite as $r \to \infty$. The rate constant k is a pseudo first-order reaction rate constant that represents the sum of the consumption rates due to all other cluster sizes ($k = \sum_{m=1}^{\infty} k_{m1} n_m$ where k_{m1} is the second-order rate constant representing the rate of consumption of monomers by cluster m). The solution to Equation 5.2 with boundary conditions $n_j(r \to \infty)$=finite and $n_j(r = R_j)$=0, gives the solution shown in Equation 5.3.

$$\begin{gathered} n_j = n_1\left(1 - \frac{K_0(r/\xi_j)}{K_0(R_j/\xi_j)}\right) \\ \xi = \left(\frac{D}{k}\right)^{1/2} \end{gathered} \tag{5.3}$$

K_0 and K_1 are the modified Bessel functions of order zero and one, and ξ represents a screening length around a cluster j. The screening length serves to give no net source or sink of monomers outside the circle defined by radius ξ, and the bulk number density of monomers outside this area is given by n_1. The definition of the flux of monomers to a two-dimensional surface of cluster size R_j (assumed circular) is defined by Equation 5.4, where k_{j1} is the second-order

rate constant of monomer consumption by cluster j.

$$J_j = -2\pi R_j D \left(\frac{\partial n_j}{\partial r} \right)_{r=R_j} = -k_{j1} n_1 \tag{5.4}$$

Thus, substituting Equation 5.3 into Equation 5.4 yields Equation 5.5, where $X_j = R_j/\xi$. This gives a solution to the second-order rate constants as long as the first-order rate constant k (and thus ξ and X_j) is known.

$$k_{j1} = 2\pi D X_j \frac{K_1(X_j)}{K_0(X_j)} \tag{5.5}$$

Each set of second-order rate constants given by Equation 5.5 is valid as long as there is no change in the number densities of monomers (n_j) because the n_j values determine k, which determines ξ and the X_j values. Thus, in solving a set of rate equations, the second-order rate constants need to be defined at each time step due to the evolving monomer number densities. The rate equations are shown in Equation 5.6, where R_{dep} is the deposition rate of monomers and $k_{det}(j)$ is the detachment rate of monomers from clusters as a function of cluster size j. These rate equations are based on all the possible events (deposition, attachment, and detachment) that would effect the number densities of n_1 and n_j.

$$\begin{aligned} \tfrac{dn_1}{dt} &= R_{dep} - \textstyle\sum_{j=1}^{\infty} k_{j1} n_j n_1 + \sum_{j=2}^{\infty} k_{det}(j) n_j \\ \tfrac{dn_j}{dt} &= k_{j-1,1} n_{j-1} n_1 - k_{j1} n_j n_1 - k_{det}(j) n_j + k_{det}(j+1) n_{j+1} \end{aligned} \tag{5.6}$$

The detachment rate of monomers, $k_{det}(j)$, depends on the number of edge monomers in a cluster, which depends on the cluster size, and whether those edge monomers have 1, 2, or 3 neighbors (each has a different detachment rate).

To determine this, we wrote a script to place a close-packed lattice on a circle of radius R_j, and picked out the molecules inside the circle that only had 1, 2, or 3 neighbors (molecules with more than three neighbors cannot detach completely from the cluster). See Figure 5.24(a) for a diagram illustrating this. For a given cluster of radius R_j centered about the origin, we placed the lattice in random translational positions, and averaged the number of edge molecules with one, two, and three neighbors. Since we know the detachment energy barriers of monomers having 1, 2, and 3 neighbors (see Figure 5.12), for a given cluster size j, we could calculate the total detachment rate by Equation 5.7, where $\langle N_i \rangle$ is the average number of edge molecules with i neighbors and $k_{det,i}$ is the detachment rate of a monomer from i neighbors.

$$k_{det}(j) = \langle N_1 \rangle_j k_{det,1} + \langle N_2 \rangle_j k_{det,2} + \langle N_3 \rangle_j k_{det,3} \tag{5.7}$$

For $k_{det,1}$, $k_{det,2}$, and $k_{det,3}$, the temperature is assumed to be 300 K and the Hex prefactor is assumed to be 1.1×10^{11} s^{-1}, so following the Arrhenius equation, the values are 4.9×10^4 s^{-1}, 4.6 s^{-1}, and 2.9×10^{-4} s^{-1}, respectively. The total detachment rate as a function of cluster size j was then fit to a power law, and the result is shown in Figure 5.24(b). This function is used for determining $k_{det}(j)$ in Equation 5.6.

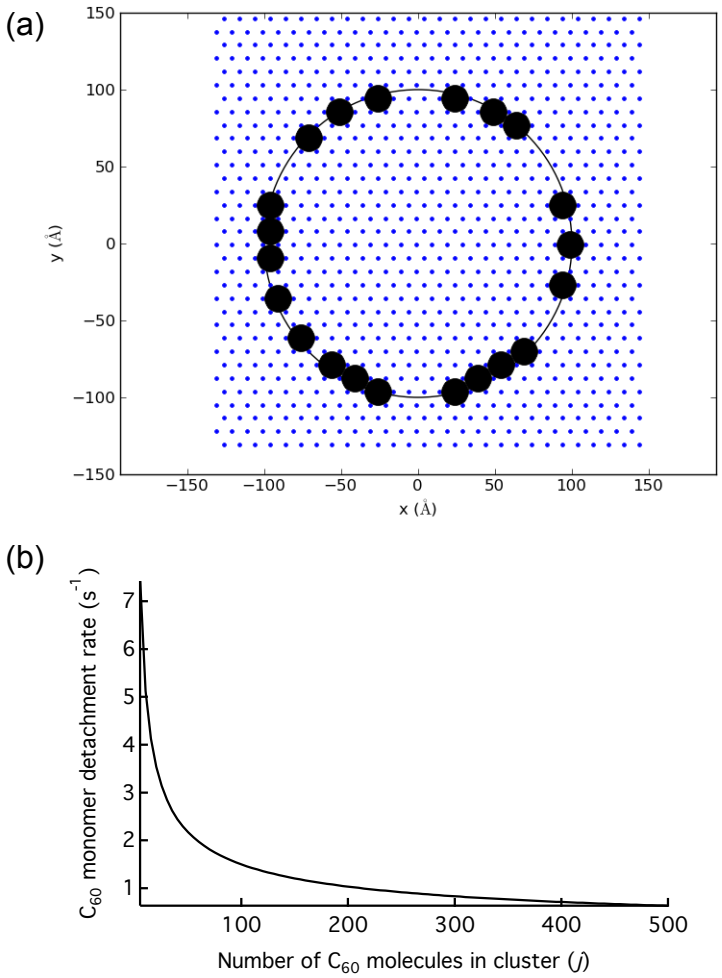

Figure 5.24: (a) Schematic showing how the number of edge molecules were determined for a given cluster of radius R_j; edge molecules (solid black circles) are those capable of detaching and are defined as one having 1, 2, or 3 direct neighbors. The number of edge molecules were averaged over different translational shifts of the lattice (blue dots) relative to the cluster circle of radius R_j centered about the origin. (b) Detachment rate as a function of cluster size j.

The initial number density of monomers was chosen to be very small, corresponding to an initial area fraction (coverage) of $O(10^{-6})$. This value was somewhat arbitrary, but it needed to be low enough to represent a dilute monomer system while still allowing a solution to Equation 5.5. At $t = 0$, n_1 is known and $n_{j>1} = 0$, so $k = k_{11}n_1$ and Equation 5.5 could be solved to get the initial set of all second-order rate constants. The numerical integration loop consists of the following tasks: the rate equation derivatives are calculated, the time step is changed if necessary, the n_j's are updated, and the k_{j1}'s are re-calculated. The rate of monomer detachment ($k_{det} \sim O(10^{-12})$ ps) is much slower than the rate of monomer attachment ($k \sim O(10^{-2} - 10^{-1})$ ps^{-1}), but detachment still plays an important role as it still faster than typical monomer deposition rates. Due to these disparate rate constants, a variable time step was added in the numerical integration in order to evolve the system in time efficiently. The code for this model is given in Appendix B.

We plotted the resulting number density of monomers, n_j, as a function of coverage (and thus simulation time) for different deposition rates for bulk phase pentacene (Figure 5.25) and thin film phase pentacene (Figure 5.26). As expected, the slower the deposition rate, the larger the clusters are at a given coverage. The main difference observed in Figure 5.26 with the thin film phase pentacene as compared to the bulk phase is the larger clusters for a given coverage and deposition rate. The only difference between these two systems in the model is the C_{60} diffusion coefficient—0.5 Å^2/ps for the bulk phase and 1.4 Å^2/ps for the thin film phase. Thus, it makes sense for the system with higher monomer diffusion to have the larger cluster sizes, and reiterates the fact that C_{60} growth on thin film phase pentacene might have more desirable growth patterns for electronic devices.

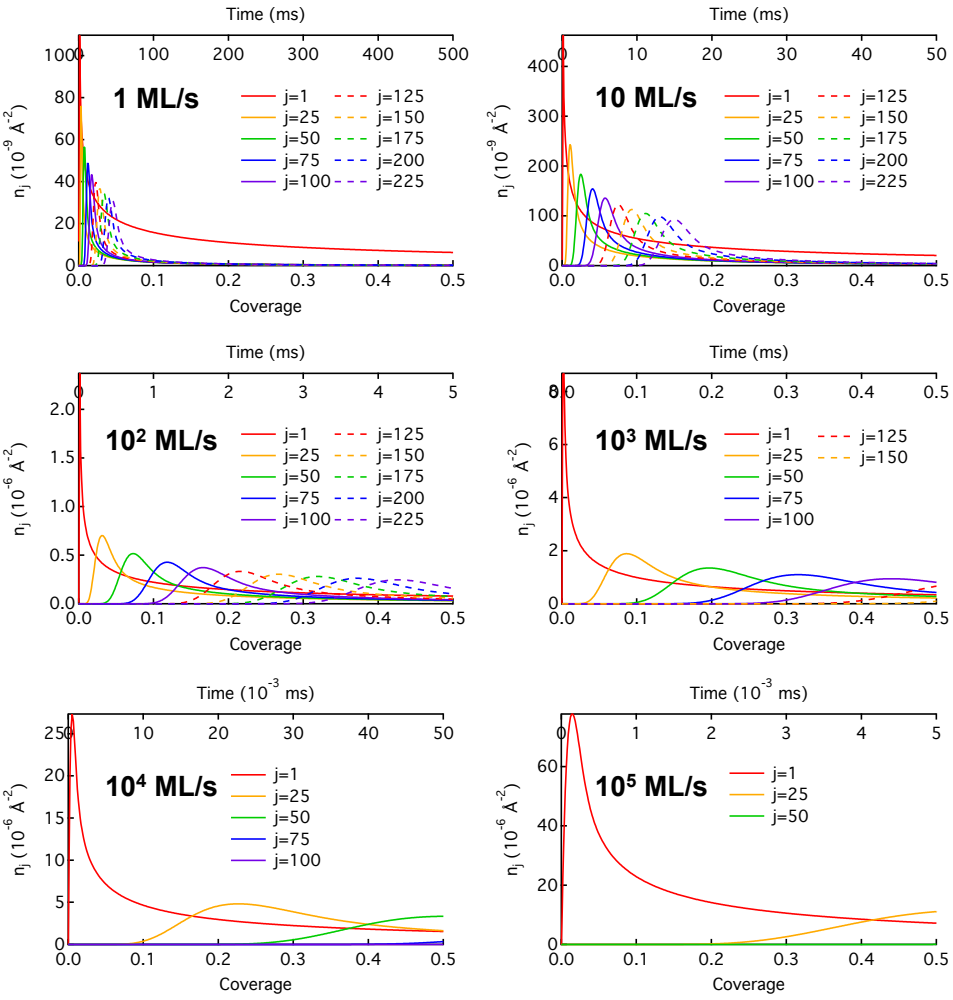

Figure 5.25: Number density of monomers around clusters of size j as a function of coverage and simulation time for C_{60} growth on bulk phase pentacene. Deposition rates are varied from 10^0–10^5 monolayers (ML) per second. Only j's in increments of 25 are shown for simplicity.

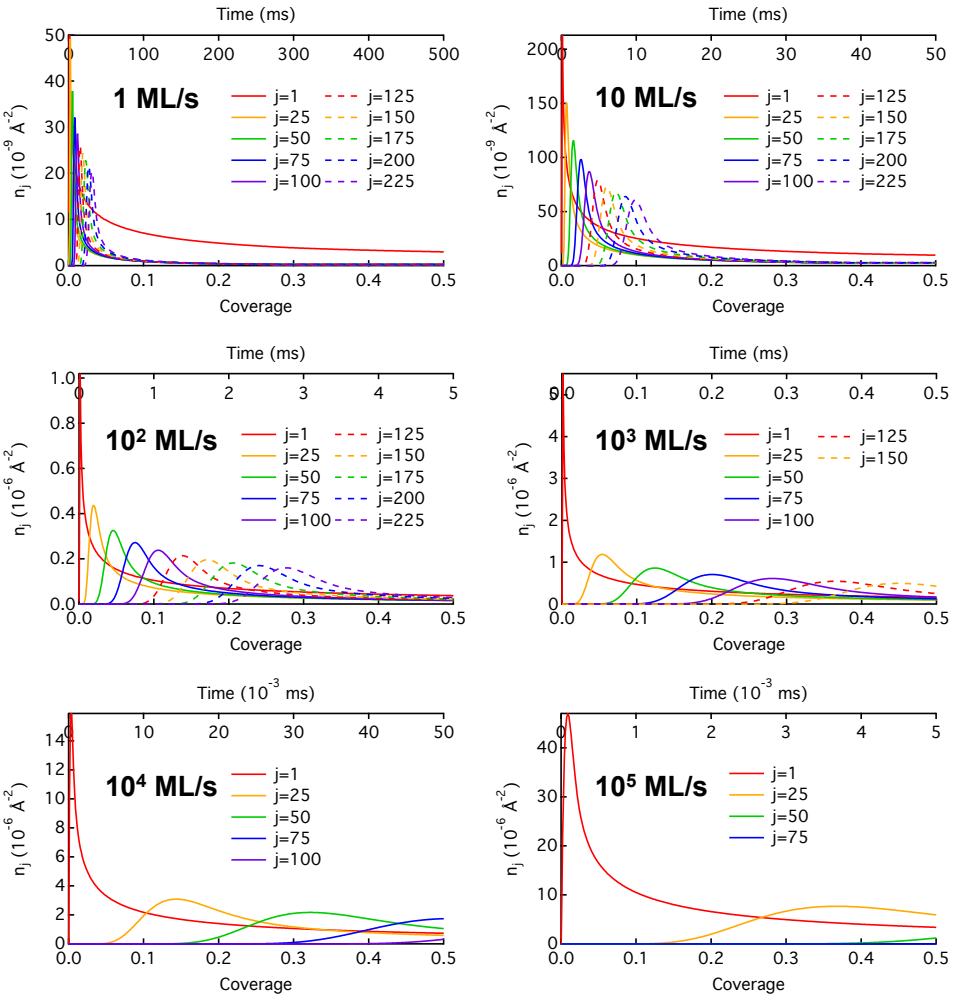

Figure 5.26: Number density of monomers around clusters of size j as a function of coverage and simulation time for C_{60} growth on thin film phase pentacene. Deposition rates are varied from 10^0–10^5 monolayers (ML) per second. Only j's in increments of 25 are shown for simplicity.

Lastly, we compared the cluster distributions obtained using this reaction-diffusion model to those obtained by KMC at high deposition rates. As shown in Figure 5.27, the values match up fairly well. However, KMC consistently predicts a higher number of smaller clusters than the continuum model. There could be several reasons for this, but mainly we attribute this to the fact that KMC allows cluster dissociations in more than one way. For example, the KMC code allows situations where a cluster of size 5 can break up into clusters of size 2, 2, and 1 in one step; in the continuum model, only monomers can split away from clusters.

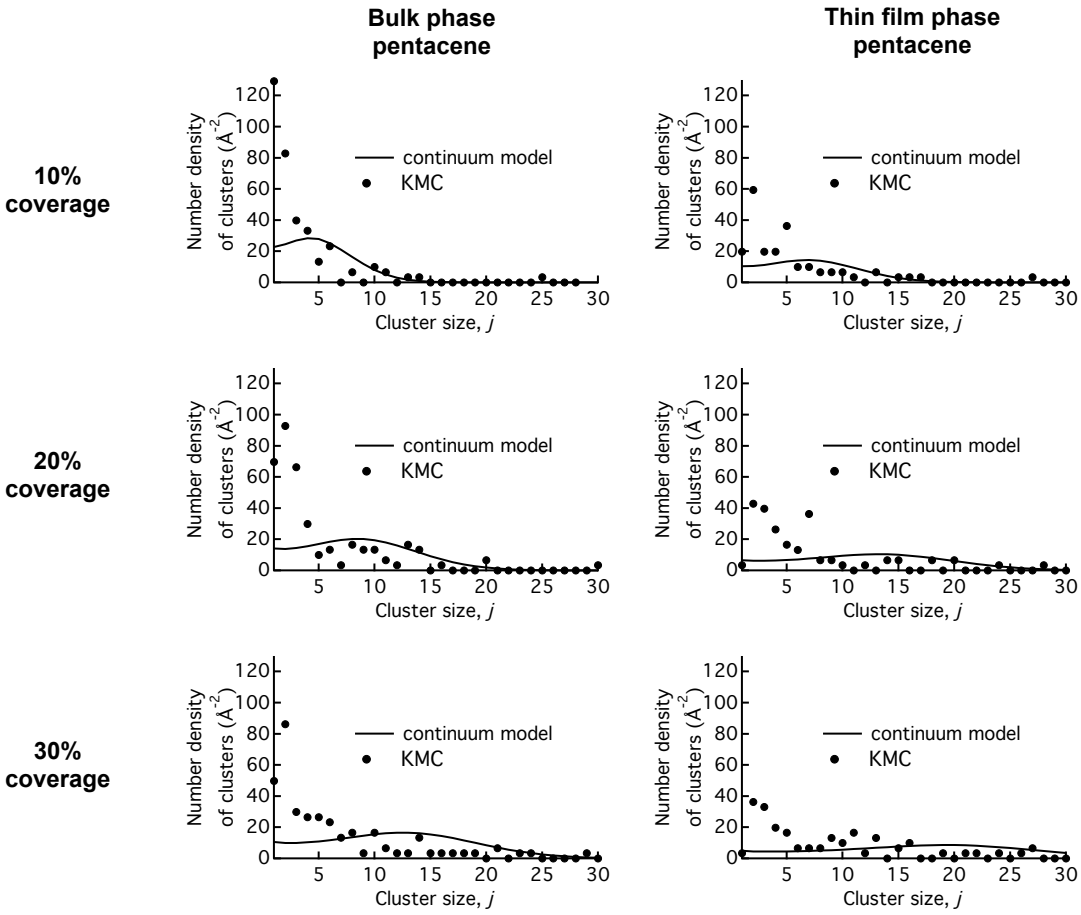

Figure 5.27: Number density of clusters of size j as a function of cluster size j for different coverages and pentacene phases: continuum reaction-diffusion model *vs.* KMC model. For all simulations here, the temperature was 300 K and the deposition rate was 10^5 monolayers per second.

Results from the KMC and continuum model match fairly well considering the completely different approaches taken. Both methods used solely, as inputs, the atomistic information obtained by Molecular Dynamics and molecular mechanics, and arrived at very similar results in terms of island size distributions, for example. The continuum model provides the benefit of being able to simulate slow deposition rates (*e.g.*, 1 monolayer per second), which are not accessible by the KMC code. However, this continuum method is valid only for two-dimensional, sub-monolayer growth, where the clusters are assumed not to impinge upon one another. In future work, it would be beneficial to explore the limits of applicability of the KMC and determine the best way to simulate low deposition rates while also capturing sufficiently descriptive microstructural details and the maintenance of three-dimensional growth. Some further studies along these lines that we have considered for the KMC code in the future are discussed in detail in Section 7.2.

We gained useful information about the growth of C_{60} on pentacene surfaces, not only from the direct results of the KMC and continuum methods, but also from the large set of energy barriers obtained in process of creating the models. The energy barriers shown in Figures 5.12 and 5.14 are the most comprehensive set that exist for C_{60} on pentacene and C_{60} on C_{60}, respectively, and compare well with the energy barriers that already exist in the literature. The C_{60}-on-C_{60} energy barriers from the Liu *et al.* paper[3] overlap quite well with the ones we obtained. Our studies also confirmed the result by Goose *et al.*, who found the minimum value for the Erhlich-Schwoebel barrier for C_{60}-on-C_{60} to be ~0.31 eV,[155] which is very close to the value determined here (0.33 eV).

From the results of the KMC and continuum models, we find that the thin

film phase of pentacene will be a more effective surface for producing larger (and ordered) C_{60} clusters than the bulk phase of pentacene. This is intuitively reasonable due to the larger C_{60} diffusion coefficient on the thin film pentacene surface compared to that on the bulk phase. We believe that the larger grain sizes on the thin film phase might have the undesirable side effect of initiating an earlier onset of a second C_{60} layer due to the lower step edge density, but this has yet to be confirmed. This implication awaits the conclusion of currently ongoing multi-layer simulations using this KMC code. Overall, we conclude that devices of C_{60}/pentacene fabricated using the thin film phase of pentacene would lead to better performance than those on the bulk phase of pentacene (assuming everything else to be constant) due to the desirable larger grain sizes at the C_{60}/pentacene interface.

CHAPTER 6

STUDIES OF C_{60} ON RECUMBENT PENTACENE SURFACES

In contrast to the bulk and thin film structures adopted by pentacene on most insulating surfaces, such as thermal oxides, the first monolayer or so of the pentacene molecules is known to lie essentially flat on some substrates, typically metals,[43–46] but also silicon.[47,48] Refer to Tables 1.1–1.3 for a summary of experimental results of recumbent pentacene grown on different metals. Dougherty *et al.*[66] deposited C_{60} on two layers of pentacene on Ag(111) and found that, at low C_{60} coverage, C_{60} nanowires form between the pentacene rows. This phenomenon is exciting because it suggests that when pentacene is angled close to the underlying surface, it might serve as a "templating" material for more ordered, and directionally biased, growth of C_{60}. Dougherty *et al.* found the first monolayer of pentacene on Ag(111) to lie flat on the substrate, but, in the second layer of pentacene, the molecules' short axis is oriented approximately 28°–34° off the surface (*i.e.* a surface normal angle, ϕ_1, of 62°–56° in the convention we adopt, described in Section 1.2.2). Since C_{60} nanowire formation on pentacene has not been observed elsewhere in the literature, this specific pentacene orientation on Ag(111) found by Dougherty *et al.* could be just right to allow the formation of C_{60} nanowires in the crevices between the pentacene rows. Investigating whether there is indeed a "sweet spot" for the angle of the pentacene molecules to hold or orient the C_{60} molecules provided additional motivation for us to study this system in detail.

In Section 6.1, we begin by describing the method used to obtain lattice parameters for a set of variably-angled recumbent pentacene structures. We

Portions of this chapter are reproduced in part from previous publications in References 106,107

then analyze these structures by investigating the potential energy surfaces and single-C_{60} diffusion behavior. In Section 6.2 we discuss some quite unexpected behavior that is seen upon the addition of many C_{60} molecules to the recumbent pentacene systems. Lastly, in Section 6.3 we present different simulation experiments, which lead to predictions of conditions under which C_{60} nanowires will form on recumbent pentacene.

6.1 Single-molecule C_{60} probes of recumbent pentacene surfaces

Since the recumbent pentacene film in Dougherty *et al.*'s work is the only one in the literature that shown nanowire formation of C_{60} on pentacene,[66] our aim was to emulate Dougherty *et al.*'s recumbent pentacene system by also using two layers of pentacene. However, we also wanted to vary the short-axis angle ϕ_1 that controlled the pentacene film's degree of "flatness" on the surface (see Figure 1.3(a) for reference). Section 6.1.1 describes our method of obtaining this set of structures, Section 6.1.2 reports how these different structures affect the adsorption energy surfaces, and Section 6.1.3 shows how these different structures affect the dynamics of single C_{60} molecules.

6.1.1 Determining lattice structure of recumbent pentacene

There is no commonly accepted crystalline structure for recumbent pentacene because its structure is generally influenced by the underlying substrate and a variety of experimental parameters. Given that we do not know the characteris-

tic unit cell parameters for these hypothetical variably angled pentacene structures, we devised a method to determine a set of parameters (shown schematically in Figure 6.1). We describe a recumbent pentacene unit cell as having two pentacene molecules: one, denoted with the number 1 as Pn_1, lies on the bottom directly above some unspecified substrate material. The other, denoted with the number 2 as Pn_2, lies on top and slightly askew of Pn_1 making a total of two pentacene layers per unit cell (see Figure 6.1). With ϕ_1 being the independent variable, $\phi_1 = 10^\circ$ corresponds to the short axis of pentacene standing nearly upright, and $\phi_1 = 90^\circ$ corresponds to the pentacene lying on its face, flat on the surface. The method used to determine the other lattice parameters is summarized as a flow chart in Figure 6.2. It involves a series of potential energy minimizations using MM3, as a means to provide realistic tilted pentacene structures.

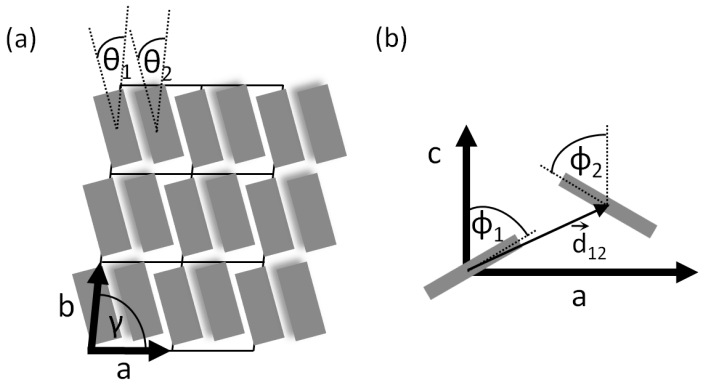

Figure 6.1: Schematic diagrams of the variably angled pentacene systems from (a) a plan and (b) a side view, illustrating the definitions of the parameters a, b, c, γ, θ_1, θ_2, ϕ_1, ϕ_2 and $\mathbf{d}_{12}$, which are listed in Table 6.1. Pentacene molecules are represented as grey rectangles for simplicity.

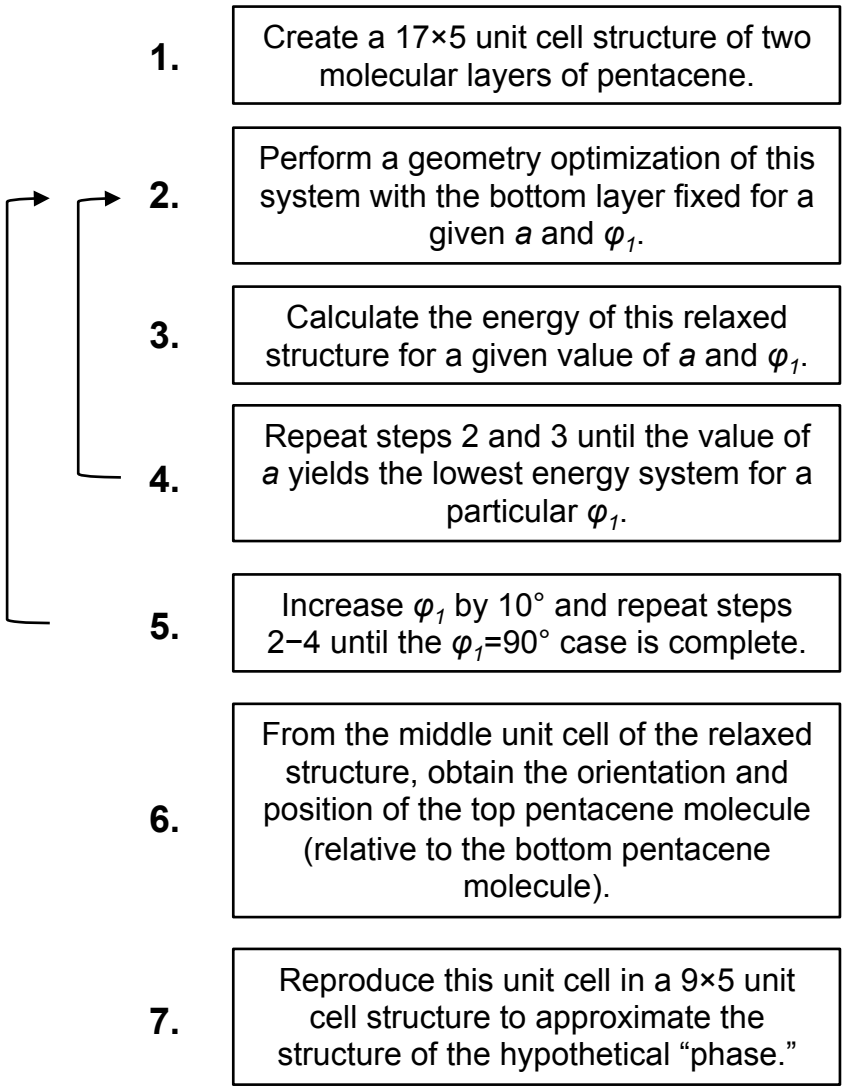

Figure 6.2: Procedure used to determine the approximate structure for the variably-angled recumbent pentacene polymorphs. Refer to Table 6.1 for parameter values used.

The unit cell parameters found from the procedure described in Figure 6.2 are summarized in Table 6.1. Since Pn_1 and Pn_2 comprise a one unit cell thick layer, the unit cell parameters c, α and β are irrelevant. The independent variable is the angle ϕ_1 made by Pn_1's short axis with the surface normal (see Figure 6.1(b)), assuming that Pn_1's long axis is parallel to the substrate. The lattice parameter, a, depends on the value chosen for ϕ_1, with larger a values corresponding to larger ϕ_1 values. The lattice parameters, b and γ, which are assumed not to vary with ϕ_1, were obtained by MD snapshots similar to the one shown in Figure 6.3. The angles θ_1 and θ_2 are the counterclockwise angles that the long axes of Pn_1 and Pn_2, respectively, make with the b unit cell vector (see Figure 6.1(a)). The θ_2 values were also extracted from MD snapshots, and we assumed that $\theta_1 = \theta_2$ initially in the geometry optimizations.

Table 6.1: Summary of unit cell parameters considered in the formation of the hypothetical, variably angled, pentacene structures.

Parameter	Value	Obtained from/by	Fixed in geometry optimization?
a	5 Å (initial guess)	Recursive minimization	Yes
b	15.6 Å	MD snapshot	Yes
c	N/A	N/A	N/A
α	N/A	N/A	N/A
β	N/A	N/A	N/A
γ	86.5°, 76.5°	MD snapshot	Yes
θ_1, θ_2	10.1°	MD snapshot	θ_1 Yes, θ_2 No
ϕ_1, ϕ_2	10°–90°	Independent variable	ϕ_1 Yes, ϕ_2 No
$\mathbf{d}_{12}$	$\langle a/2, b, 5$ Å$\rangle$ (initial guess)	Guess	No

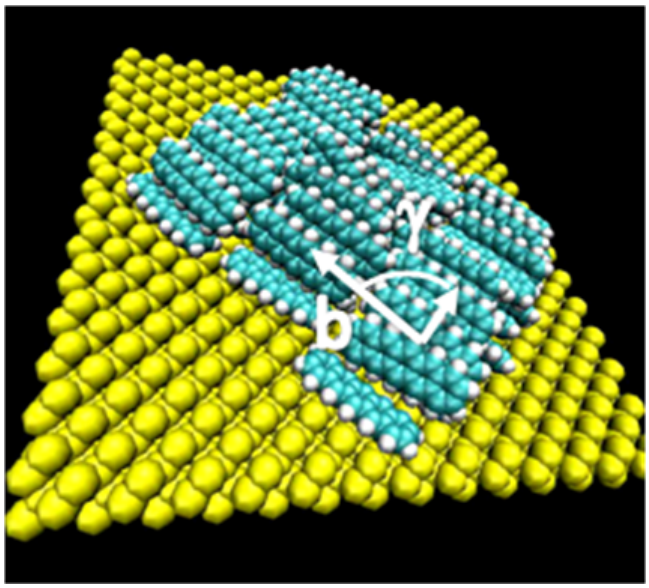

Figure 6.3: MD snapshot of two layers of 24 pentacene molecules (48 total molecules) on three atomic layers of a Si(001) surface. Aqua-colored carbon atoms and white hydrogen atoms make up the pentacene molecules; yellow-colored silicon atoms make up the Si(001) surface.

An MD simulation of pentacene on a silicon substrate (see snapshot in Figure 6.3) was used to obtain the parameters b, γ and θ_2 described above. Although MM3 potential parameters for silicon have not been optimized for this system, we knew from earlier work that it was sufficiently realistic to cause the pentacene to lie face down on the substrate, the only necessary prerequisite. The MD simulation was performed with 48 pentacene molecules on a Si(001) surface, which was three atomic layers thick. Periodic boundary conditions were applied in the x- and y-directions to allow the face-down pentacene cluster to move freely. The simulation was thermalized at 300 K in the constant-temperature NVT ensemble for 50 ps and then run in the NVE ensemble for 2 ns.

Taking five different snapshots, each 300 ps apart, we extracted values for b and γ (excluding the molecules on the edges) by calculating the center-to-center distances of the top layer pentacene molecules. For both b and γ, there were 10 values to extract in each snapshot, making a total of 50 values of b and γ. These values are shown as histograms in Figures 6.4(a) and (b). As illustrated in Figures 6.4(a) and (b), the average value for the lattice parameter b is 15.6 Å and that for γ is 86.5°. The distribution for γ is skewed in the positive direction, so the most probable value is less than the exact average value. We speculate that this is due to our capturing some shearing event of the unit cell rows with respect to one another.

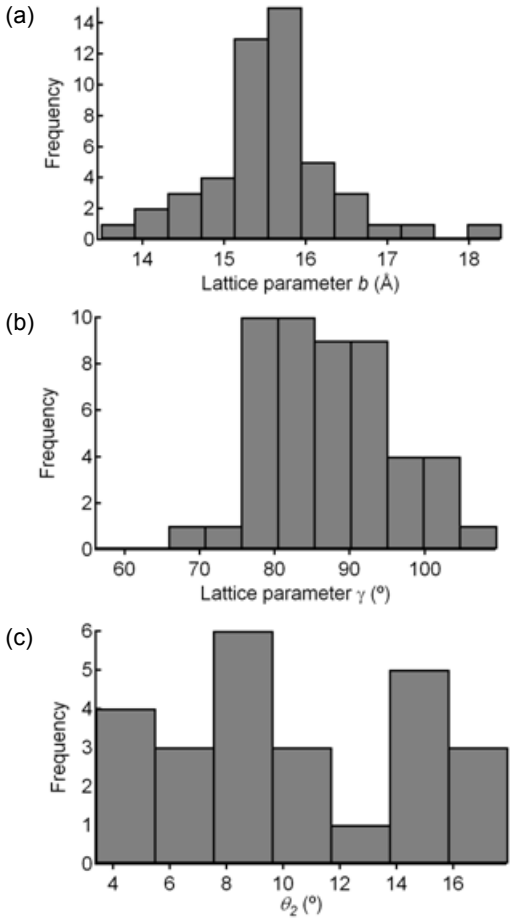

Figure 6.4: Histograms of extracted values of parameters (a) b, (b) γ and (c) θ_2 from five MD snapshots. Histograms of b and γ are based on 50 values, that for θ_2 is based on 25 values.

We also considered the case where $\gamma = 76.5°$, to see the effect of a 10° change in γ on the energy properties of the surface. This change represents our uncertainty in γ and allows us to gauge the sensitivity of the results to our choice of γ. The values for θ_2 were also extracted from these MD snapshots, but, in this case, both the edge molecules and the top and bottom row molecules were excluded to ignore any edge effects. There were five values of θ_2 to extract in each snapshot, making a total of 25 values of θ_2. These values are shown as a histogram in Figure 6.4(c). The distribution of θ_2 values appears to be reasonably uniform, with an average value of 10.1°.

Once the values for b, γ and θ_2 were obtained from the MD snapshots, we could begin to create a 17×5 unit cell layer of the flat pentacene without a substrate. As an initial configuration, we assume that $\theta_1 = \theta_2$, $\phi_1 = \phi_2$ and that the distance vector between Pn_1 and Pn_2, denoted as $\mathbf{d}_{12}$, is $\langle a/2, b, 5\ \text{Å}\rangle$. The next step is to determine appropriate values for a based on a given value of ϕ_1. We varied ϕ_1 from 10° to 90°, in increments of 10°, and for each value of ϕ_1, different values of a were tested. For each a-ϕ_1 combination tested, we fixed the bottom pentacene layer and allowed the top pentacene layer to relax in a geometry minimization. For a particular value of ϕ_1, we choose the value of a (to within a tenth of an angstrom) for which the geometry-minimized structure had the lowest energy; the other non-minimizing a values are not considered. The values of a that gave minimum energy configurations for different values of ϕ_1 are shown in Figure 6.5 for two cases of $\gamma = 76.5°$ and 86.5°. There is no significant difference between the lattice parameter a values for $\gamma = 76.5°$ and 86.5°, but each a-γ-ϕ_1 combination, as shown in Figure 6.5, is treated as a unique system for subsequent calculations.

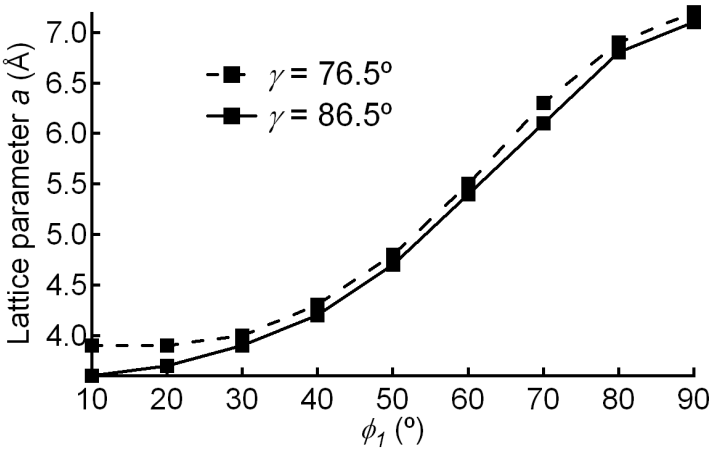

Figure 6.5: Lattice parameter, a, as a function of ϕ_1, the degree of recumbancy of the pentacene molecules on the substrate for both γ = 76.5° (dashed line) and γ = 86.5° (solid line).

At this point, it is beneficial to double-check some of the values obtained so far against those in the literature. We compared the lattice parameters used here to previous experimental lattice parameters for different ordered recumbent pentacene structures. For each of the experimental systems quoted in Tables 1.1–1.3, we considered only those that had reached at least one saturated pentacene monolayer. Our recumbent pentacene lattice parameters matched closely with those found on gold[53,54,58,59] and copper.[73] For example, in reference 58, the authors grew recumbent pentacene films using molecular beam epitaxy at room temperature and quote values of a=6.6±0.5 Å, b=15.5±1 Å, and γ=75±2° for the first monolayer of pentacene on Au(111)-(22× $\sqrt{3}$). Dougherty *et al.*[66] grew two layers of pentacene lying flat on Ag(111) at room temperature and calculated b to be 16 Å through high-resolution STM imaging. These values compare well with our values used in simulation—a=3.9–7.2 Å, b=15.6 Å, and γ=76.5°. There was a variety of other lattice parameters given in experiments, which we attribute to differing conditions shown in Tables 1.1–1.3.

To create the recumbent pentacene surfaces for the adsorption energy calculations, we extract the middle unit cell from the geometry-minimized 17×5 unit cell structure for each γ-ϕ_1 combination as the exemplar for the system. But to make sure that the 17×5 unit cell structures were large enough that the middle unit cell has a converged structure, we calculated the vector components of the long axis for the top pentacene molecules for all of the top pentacene molecules in the middle row (see Figure 6.6(a)). We also checked the $\mathbf{d}_{12}$ vector components to make sure that they converged (see Figure 6.6(b)). Unlike in most convergence graphs, the convergence seen in Figure 6.6 occurs towards the center (x = 0, where x refers to the n^{th} pentacene in the middle row). Each top pentacene molecule in the middle row of the 17×5 structure corresponds to one of

the 17 points on the x-axis. Thus, according to Figure 6.6, the overall structure of the middle unit cell does indeed converge towards the center.

In addition to determining the sufficiency of convergence of the structure of the middle unit cell, it is important to point out how much ϕ_2 and θ_2 changed from their initial values, set equal to ϕ_1 and θ_1, respectively. As shown in Figure 6.7(a), for the ϕ_2 values, there is only significant divergence from the initial value at low ϕ_1 values. Low ϕ_1 values also correspond to low lattice parameter a values. Low values of a correspond to a more compact unit cell, explaining why ϕ_2 values are higher at lower ϕ_1. As shown in Figure 6.7(b) for θ_2 values, there is only significant divergence from the initial value at higher ϕ_1 values, especially for the $\gamma = 86.5^\circ$ case.

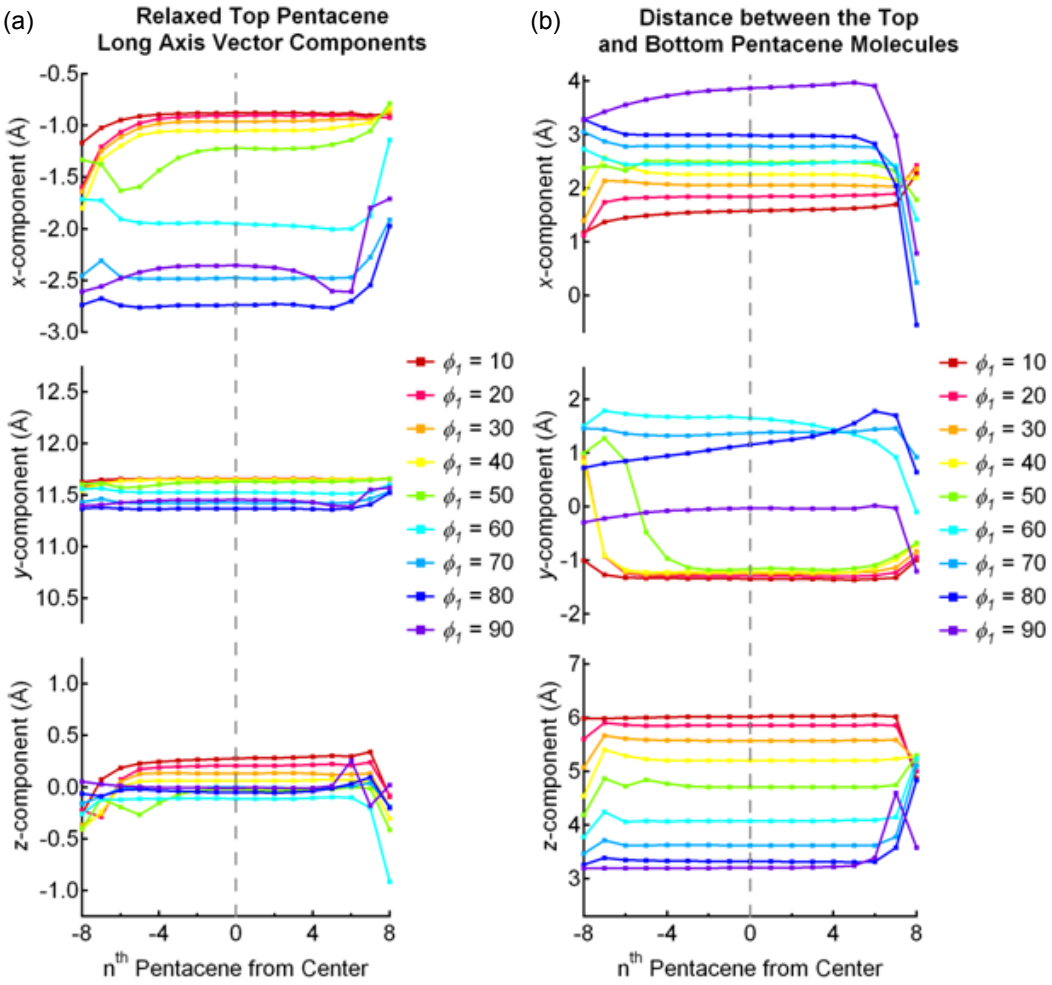

Figure 6.6: Convergence of the middle row of 17×5 pentacene molecules in the geometry-minimized variably angled pentacene structures. The convergence is measured by (a) the vector components of the top pentacene molecule in each unit cell and (b) the distance between the top and bottom pentacene molecules in each unit cell.

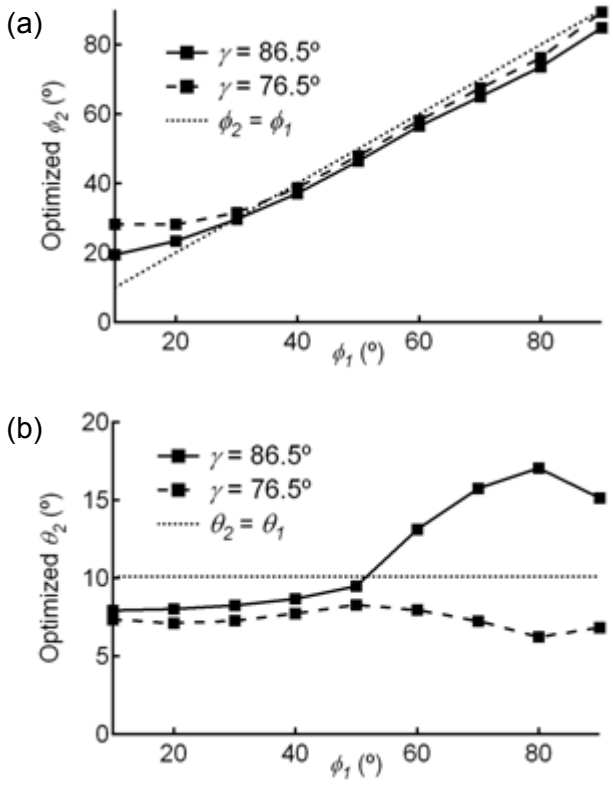

Figure 6.7: For each ϕ_1, deviations of the (a) optimized ϕ_2 and (b) optimized θ_2 *via* geometry optimization as compared to their initial values, ϕ_1 and θ_1, respectively.

After achieving sufficient convergence of the structure of the middle unit cell in each case, as shown in Figure 6.6, we repeated these unit cells in a 9×5 array for each γ-ϕ_1 combination. We choose a 9×5 array because it is large enough to avoid any edge effects of the adsorption energy calculations and it is small enough that the calculations do not take too long. These 9×5 arrays for each γ-ϕ_1 combination are the structures used for the C_{60} surface adsorption energy calculations shown in Figure 6.8 and described in Section 6.1.2.

To summarize, the angle γ is the angle between lattice vectors **a** and **b**, as shown in Figure 6.1(a). Values for γ were obtained by different MD snapshots, and they ranged from about 60° to 110°, with an average of 86.5°. The spread of these values is not symmetric (see Figure 6.4(b)), with the most probable value for γ being less than the average. To determine the sensitivity of our results to the choices made for angles such as γ, we chose an additional angle to test, γ = 76.5°, because it is within the range of most probable values and is, conveniently, exactly 10° less in value. In summary, for the adsorption energy surfaces for variably angled pentacene, we studied two cases of γ = 76.5° and 86.5°, and for each, we vary ϕ_1 from 10° to 90° in increments of 10°.

6.1.2 Single-molecule static analysis of recumbent pentacene polymorphs

In this section, the potential energy surfaces of the variably-angled recumbent pentacene systems are studied in detail. These potential energies were calculated statically using the TINKER software code in conjunction with the MM3 potential. The details of this procedure are the same as those described in Sec-

tion 3.2. From the optimized recumbent pentacene structures for ϕ_1=10–90°, obtained in Section 6.1.1, we performed these potential energy surface calculations. Figure 6.8 show adsorption energy surfaces for γ = 76.5° as we vary ϕ_1 (shown for 10°, 50° and 90°). The angle γ is the angle between lattice vectors **a** and **b**, as shown in Figure 6.1(a), and the γ = 76.5° choice is discussed in Section 6.1.1. Although more data for the contour energy plots were taken at intermediate values of ϕ_1, this set of contour plots in Figure 6.8 shows the general trend. The contour plots for γ = 86.5° (left out in Figure 6.8) look qualitatively very similar to those of γ = 76.5°, implying that the adsorption energy patterns are not overly sensitive to the choice of γ. From Figure 6.8, one can see the interesting observation of the position shift of the dominant energy minima from *between* the rows (at low values of ϕ_1) to *within* the rows (at high values of ϕ_1). This shift implies that the likelihood of forming "east-west" (x-direction) C_{60} nanowires on pentacene is more likely at extreme values for ϕ_1 (e.g. 10° or 90°) where there would be a clear preference for C_{60} to be located between a row or within a row. For intermediate values of ϕ_1, there is no such clear preference for horizontal C_{60} nanowires.

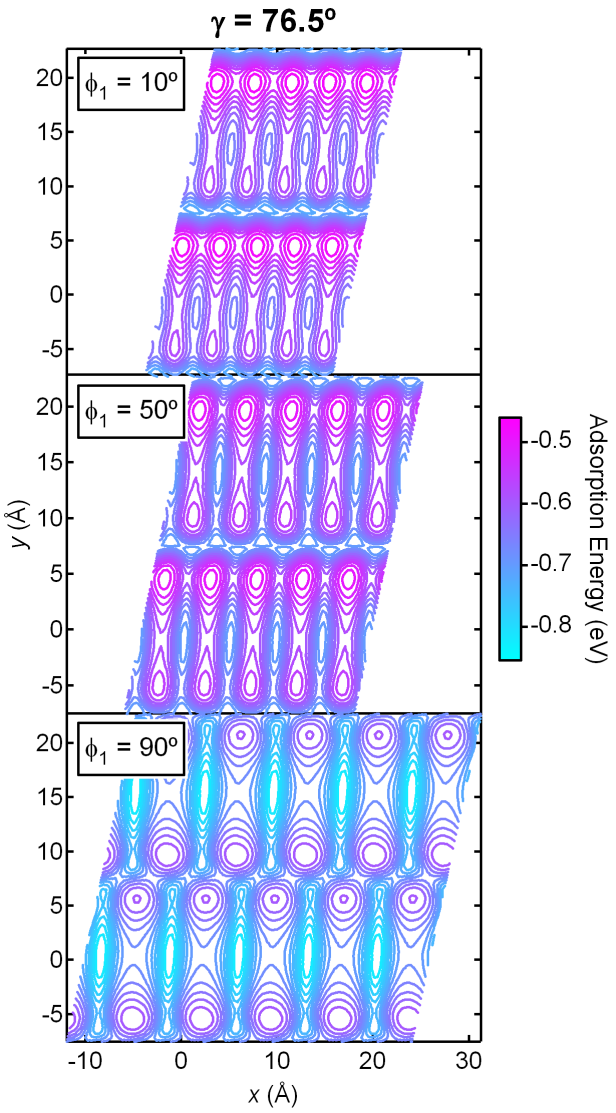

Figure 6.8: Contour adsorption energy plots of variably angled pentacene, at $\phi_1 = 10°$, $50°$ and $90°$, for the $\gamma = 76.5°$ case, with the key as in Figure 3.7. A stretch occurs in the x-direction for higher values of ϕ_1 in order to physically accommodate the pentacene molecules.

Figure 6.9(a) shows data taken from the surface energy plots that allow one to see more clearly where the dominant minimum energy transition occurs. Figure 6.9(a) shows the values of the energy minima both within and between the rows as we vary the angle made by the pentacene with the underlying substrate. The energy minimum transitions from being *between* pentacene rows to *within* the pentacene rows are at an angle of about $\phi_1 = 50°$.

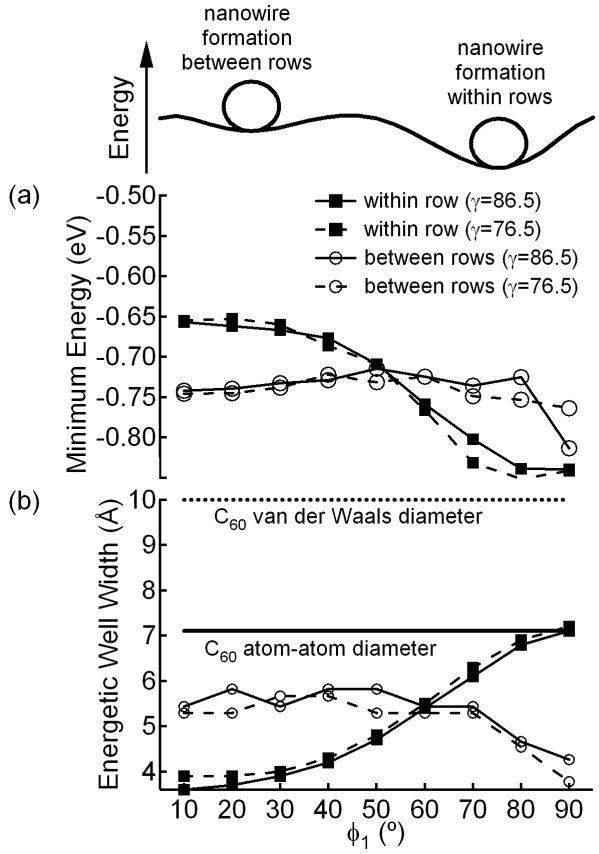

Figure 6.9: (a) Minimum energy and (b) width of the energy wells extracted from adsorption energy maps as a function of angle ϕ_1. Solid lines correspond to the $\gamma = 86.5°$ case; dashed lines to $\gamma = 76.5°$; filled squares correspond to energy wells between molecules within the pentacene rows, open circles correspond to those between the pentacene rows. The schematic diagram above both (a) and (b) illustrates the concept that higher values of ϕ_1 could be expected to yield more stable C_{60} nanowires.

In addition to the minimum energy values of the energy wells, the *width* of the energy wells is also very important for determining the likelihood of C_{60} to reside in a particular site. See Figure 6.10(b) for the shapes of the energy wells referenced herein. If the C_{60} molecule cannot fit in a potential energy well, it is unlikely to reside there no matter how deep the well is. The wells occurring within the rows are ellipsoidal in shape, but the length in the x-direction (from saddle point to saddle point) was chosen to represent the "width" of the well because it is the limiting dimension. The width of energy wells between rows was taken to be the width of the valley, specifically the maximum-to-maximum distance in the y-direction across the valley. Figure 6.9(b) shows the trend of these widths with the angle adopted by the pentacene (or its degree of recumbency to the surface). At $\phi_1 = 60°$, a transition occurs from a dominating between-row well width at low ϕ_1 values to a dominating within-row well width at high ϕ_1 values. This result corresponds approximately to the same transition shown in Figure 6.9(a); thus, the wider the energy well, the lower its energy.

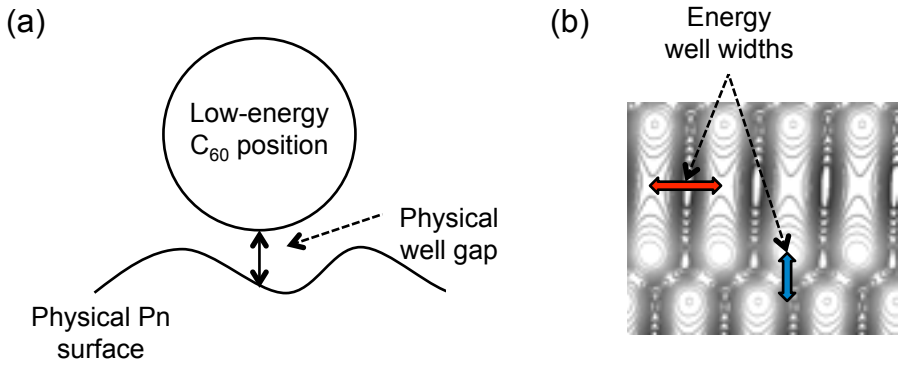

Figure 6.10: Diagram showing what is meant by the energy well (a) gap and (b) width. The direction of the well width depends on the location of the energy well and what limits the size; the East-West direction is considered for wells within pentacene rows, and the North-South direction is considered for wells between pentacene rows.

We can ascertain the ability of an energy well to "swallow" a C_{60} molecule into the surface by comparing the well widths on the pentacene surface to the diameter of C_{60} molecules; horizontal lines are shown in Figure 6.9(b) for the atom-atom and van der Waals diameters. Although both of these diameters are greater than any of the well widths obtainable by varying the angle that the pentacene molecule adopts on the surface, clearly the greater the width of the well, the more likely a C_{60} molecule will reside there. For C_{60} nanowires to form, it is probably unnecessary for the surface to engulf the C_{60} molecule; it only needs to "cradle" it sufficiently well to be structure-directing. Summarizing the results for the energy wells *between rows*: they are lower in energy and wider in width at low values of ϕ_1 (with the width reaching about 80% of the C_{60} atom-atom diameter and 55% of the van der Waals diameter) compared to high values of ϕ_1. The energy wells *within rows* are lower in energy and wider in width at high values of ϕ_1 (with the width reaching roughly 100% of the atom-atom diameter and 70% of the van der Waals diameter) as compared to low values of ϕ_1.

If one considers the *lowest overall* energy in Figure 6.9(a), the most stable configuration for the C_{60} occurs within a row of the flattest pentacene configuration, at ϕ_1 around 90° (as illustrated in the schematic energy diagram "cartoon" in Figure 6.9). However, the extreme $\phi_1 = 90°$ configuration appears unlikely because it minimizes overlap with the neighboring pentacene molecules' π-orbitals. We will see in Section 6.2 that this is indeed the case. At very low values of ϕ_1, we predict that metastable configurations of C_{60} might exist between the rows. Although one may not be able to control where the C_{60} ends up on the surface at thermal deposition conditions, these results suggest that by altering the short-axis tilt angle (long axis flat), one could create a surface that

encourages oriented growth of C_{60} nanowires.

Before moving forward, we take a moment at this point to further analyze the relationship between adsorption energy and the well geometry, both physical and energetic. To determine the physical structure encompassing the energy wells, we interpolated the atomic positions to form a pseudo continuous surface. The pentacene backbone is defined by specific atom locations, so to obtain a continuous surface in three dimensions, we extrapolated the height based on the height and distance away from known atom positions. This extrapolation can be written as Equation 6.1, where the points (x_i, y_i, z_i) are known atom positions and d_i is the distance in the x-y plane between atom i and the point of interest on the pentacene surface. This equation satisfies the limits that $z_{\text{Pn surface}}$=z_i at $d_i = 0$ and $z_{\text{Pn surface}}$=average(z_i) if all d_i values are equal.

$$\frac{\prod_{i=1,i\neq 1}^{N} d_i}{\sum_{j=1}^{N}\left(\prod_{i=1,i\neq j}^{N} d_i\right)} z_1 + \frac{\prod_{i=1,i\neq 2}^{N} d_i}{\sum_{j=1}^{N}\left(\prod_{i=1,i\neq j}^{N} d_i\right)} z_2 + \frac{\prod_{i=1,i\neq 3}^{N} d_i}{\sum_{j=1}^{N}\left(\prod_{i=1,i\neq j}^{N} d_i\right)} z_3 + \cdots \tag{6.1}$$

The physical gap between the C_{60} molecule and the pentacene surface is defined as the difference in height between the bottom (lowest z-value) of the low-energy C_{60} position and the pentacene surface, as suggested by Figure 6.10(a). The width of the wells are also considered, but we considered two types of well widths: physical and energetic. The energetic width is quite easy to picture in relation to the adsorption energy surfaces, as shown in Figure 6.10(b). The physical width is defined by the diameter of the closest points of contact between the C_{60} and the physical well on the pentacene surface. To determine this "diameter," we find the variation of the Δz distances between the C_{60} surface in a low-energy well and the pentacene surface as shown in Figure 6.11 and Equa-

tion Set 6.2. The radius of the well is given to be the distance at which there is a minimum of the averaged Δz values. There are two equivalent well sites between the pentacene rows, so the radial increments at the minimum Δz values are averaged between those two. Figures A.1–A.9 in Appendix A show all the values obtained for the height, gap, and adsorption energy for ϕ_1=10–90°.

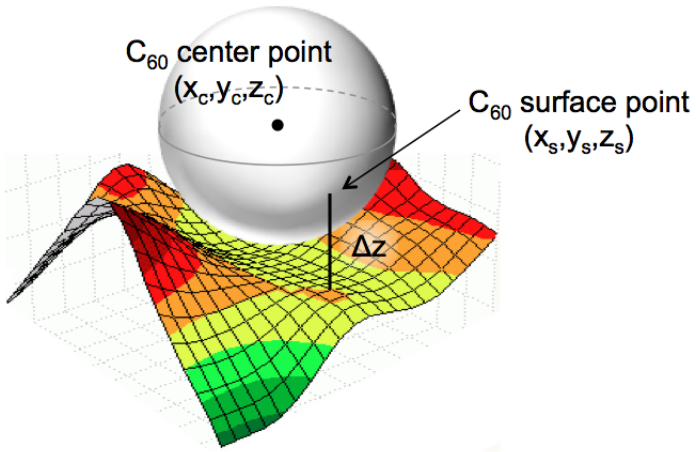

Figure 6.11: Schematic of a C_{60} on an arbitrary contour surface (representing the physical pentacene surface). Δz is a function of the pentacene surface positions and the C_{60} center position as shown by the Equation Set 6.2. Minimized values of Δz (closest points of contact) are used to determine the physical well width.

$$
\begin{aligned}
x_s &= x_{Pn} \\
y_s &= y_{Pn} \\
z_s &= z_c - \sqrt{r^2 - (x_s - x_c)^2 - (y_s - y_c)^2} \\
\Delta z &= z_s - z_{Pn}
\end{aligned}
\tag{6.2}
$$

There are four sets of well-site data, between which we determined correlations: tilt angle ϕ_1, well width (both physical and energetic), well gap, and adsorption energy. Figure 6.12 explores these correlations clearly by representing all possible trends with the independent variable ϕ_1. A distinction is also made between well sites within the pentacene rows (black squares in Figure 6.12) and between the pentacene rows (hollow circles in Figure 6.12). Refer back to Section 6.1.2 for the description of "within" and "between" well sites. Note that the energetic well widths in Figure 6.9(b) are reproduced in Figure 6.12. According to Figure 6.12, the energy wells *within* the pentacene rows exhibit a direct relationship between well width (both physical and energetic) and well gap; however, the energy wells *between* the pentacene rows do not have a clear correlation between well width and well gap. This can be understood because the width of the physical wells between the rows does not really change; the gap does change because the height of the C_{60} above the pentacene surface is greater at lower ϕ_1 values due to the higher adsorption energy. In other words, for well sites *within* rows, the ϕ_1 value is directly related to the well width (both physical and energetic), well gap, and adsorption energy; but for well sites *between* rows, the ϕ_1 value is directly related to the well gap and adsorption energy (but not well width). It can be concluded then, that for all low-energy well sites, it is the vertical length of the gap (see Figure 6.10(a)), not the well width, which influences the adsorption energy.

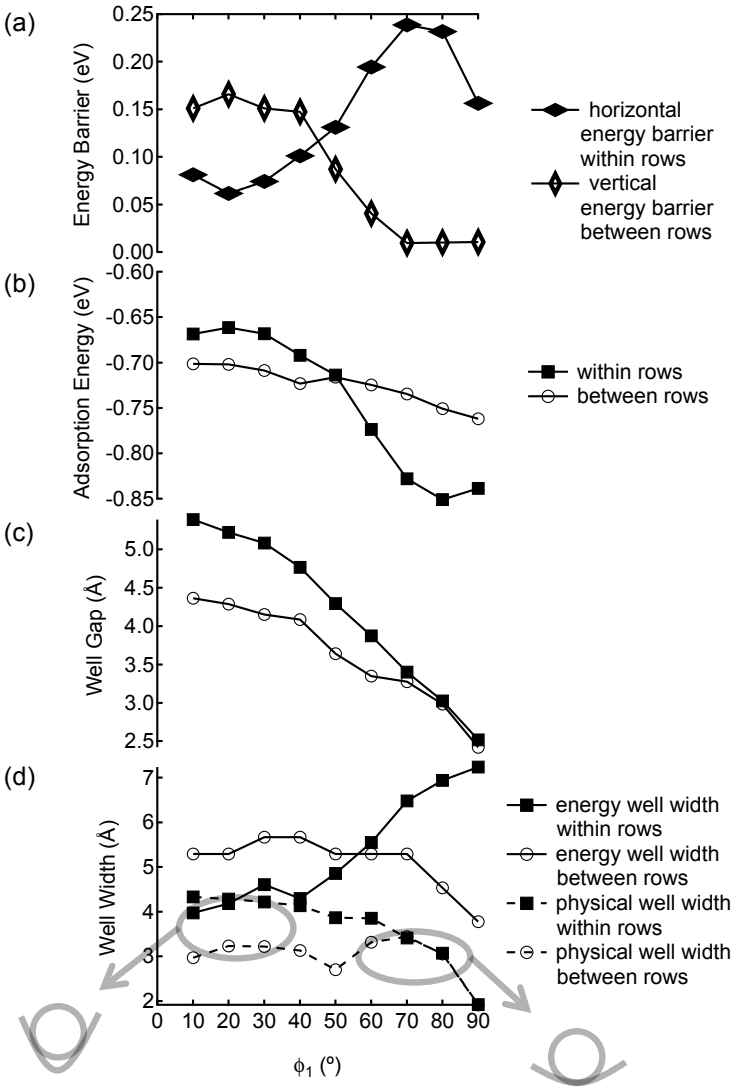

Figure 6.12: Physical and energetic well data as a function of the independent variable ϕ_1 for the $\gamma = 76.5°$ systems. (a) Energy barriers in the N-S direction are considered for wells between rows and in the E-W direction for wells within rows. (b) Minimum adsorption energy of well sites within and between rows (replotted from Figure 6.9). (c) Physical well gap between the C_{60} and the physical pentacene surface. (d) Energy well width (solid lines) and physical well width (dashed lines) for both wells within and between rows.

6.1.3 Single-molecule dynamic analysis of recumbent pentacene polymorphs

We performed MD simulations of the motion of one C_{60} molecule over the nine different pentacene surfaces with a short-axis tilt angle, ϕ_1 varying from 10° to 90°. The goal of these simulations was to qualitatively observe the behavior of a C_{60} molecule at an experimentally accessible temperature (300 K) as a complement to the static (0 K) energy landscapes studied in Section 6.1.2. Periodic boundary conditions were maintained in the x- and y-directions, while a vacuum was assumed in the z-direction. For each system, there were four rows of pentacene unit cells in the y-direction; in the x-direction, the number of pentacene unit cells was chosen such that the dimensions in the x-direction were roughly the same for all choices of tilt angle. For example, for ϕ_1 = 10°, there were 16 pentacene unit cells in the x-direction (62.4 Å), and for ϕ_1 = 90°, there were 8 (57.6 Å). The top (surface) layer of pentacene molecules was allowed to move. To maintain the structural integrity of the variably-angled structures to emulate the experimental set-up, we fixed the two bottom layers of pentacene molecules in place. Though this adds one extra pentacene layer to the MD simulations compared to the two-layer experimental system, the bottom pentacene layer essentially serves in lieu of the metal, acting as an attractive force for the top dynamic pentacene layer. A metal substrate might be more attractive than a pentacene layer, but the top dynamic pentacene layer is far enough away from the bottom pentacene layer (~15 Å) that any such difference in attraction will be negligible, given the relatively short range of influence of the pentacene intermolecular potential.

All simulations were run at 300 K for 2 ns. Figure 6.13 shows the C_{60} center-

of-mass trajectories at 1-ps intervals for ϕ_1 values of 20°, 40°, 60°, and 80°. For systems of all ϕ_1 values, see Figures A.1–A.9 in Appendix A. The data in Figure 6.13 show that, at lower ϕ_1 values (Figure 6.13(a-b)), there is a predominant preference for east-west (E-W) motion *between* the pentacene rows (in the white space), confirming the static energetic predictions in Figures 6.8 and 6.9. As ϕ_1 approaches intermediate values (50°–60°), Figure 6.13(c), there is E-W motion both within the rows (across the gray rectangles) and between the rows (along the white space), again confirming the predictions indicated by the cross-over of lines in Figure 6.9(a). Furthermore, beginning with these intermediate values of ϕ_1, north-south (N-S) motion is also visible (see Figure 6.13(c)), which was *not* predicted by the static calculations above. The prevalence of N-S motion increases at the expense of E-W motion as ϕ_1 increases above about 60°. This is due to the fact that, at higher ϕ_1 values, there is a much stronger energy barrier to travel E-W within rows ($\geq$ 0.20 eV) compared to the small energy barrier to travel N-S between rows ($\leq$ 0.10 eV). If C_{60} molecules are energetically confined to N-S valleys at higher values of ϕ_1, this raises the possibility of N-S-oriented nanowire formation, not considered in our previously with just the static energy calculations in Section 6.1.2. The last important trend to take away from Figure 6.13 is the decreased diffusion for ϕ_1 values of 70° and higher. This is due primarily to the greater adsorption strength for larger values of ϕ_1, as shown in Figure 6.9(a). Thus, if maximizing the extent of diffusion of the C_{60} molecule on a pentacene surface is desired (to improve wetting, say) without the need to direct a specific orientation of nanowires, it would be preferable to tilt the surface to a ϕ_1 value of about 60°.

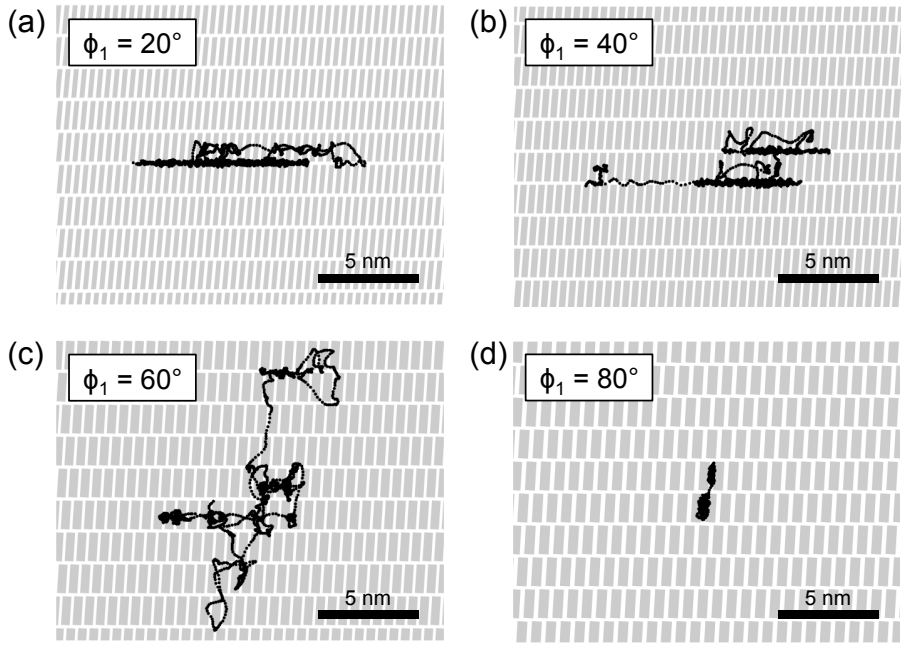

Figure 6.13: 2-ns MD trajectories of C_{60} on one unfixed layer of pentacene on two layers of fixed pentacene at 300 K. The black dots represent the center-of-mass positions of the C_{60} molecule at 1-ps intervals. The recumbent pentacene systems represented here have ϕ_1 values of 20°, 40°, 60° and 80°. Pentacene molecules are represented as pale gray rectangles for simplicity.

6.2 Multiple-molecule C_{60} interactions with pentacene surfaces

In this section, we consider the dynamics of more than one C_{60} molecule on the admolecule surface. The pentacene unit cell structures used in this study are the same as those derived in Section 6.1.1. However, instead of fixing two molecular pentacene layers with the top free to move, we chose to have a silicon substrate underneath a fixed pentacene layer, which is underneath the free-to-move pentacene layer. Ideally, we would have explicitly simulated the presence of a noble metal underneath the recumbent pentacene layers to emulate the experiments. Since there are no TINKER-based models for metals we used a passivated Si(111) structure, Si(111):H, as a substrate beneath two pentacene layers, which MM3 can handle quite well. Like metals, silicon is known to induce the creation of a recumbent pentacene overlayer.[47] The ability of MM3 to model Si(111):H accurately is not particularly important, however, because we fixed the first pentacene layer in place once they had found "equilibrium" (and recumbent) positions on top of the silicon surface. Only molecules in the second pentacene layer are free to move in response to the intermolecular forces. In other words, the first pentacene monolayer acts as a screening layer for any major interactions between the second layer and the Si(111):H surface. By fixing the first pentacene layer, we are emulating the possible positions of pentacene monolayers that might occur on a metal, and seeing how certain orientations (ϕ_1=10°–90°) affect the freely moving top pentacene layer, which, in turn, affect the disposition of the C_{60} admolecules.

Pentacene prefers to share its π-electrons with neighboring pentacene molecules, so there is a natural balance of interactions between neighboring pentacene molecules, both above and adjacent (in the **a** and **b** directions shown

in Figure 1.3(a)). This balance leads to the adoption of a herringbone structure for upright phases of pentacene, shown in Figure 1.3(b). In recumbent pentacene systems, in which we induce pentacene molecules to lie flush against the substrate (ϕ_1=90°), the neighboring pentacene molecules in the first layer are inhibited from sharing their π-electrons. This destabilizes the second layer of pentacene molecules, which want to share their π-electrons with the first layer as well as with one another. Despite this fact, simulations of two pentacene layers on Si(111):H in the absence of C_{60} retain good order (*i.e.*, the arrangement of the top pentacene layer does not vary significantly from its original placement). However, adding C_{60} molecules to the system causes the pentacene molecules in the second layer to behave quite differently at higher ϕ_1 values.

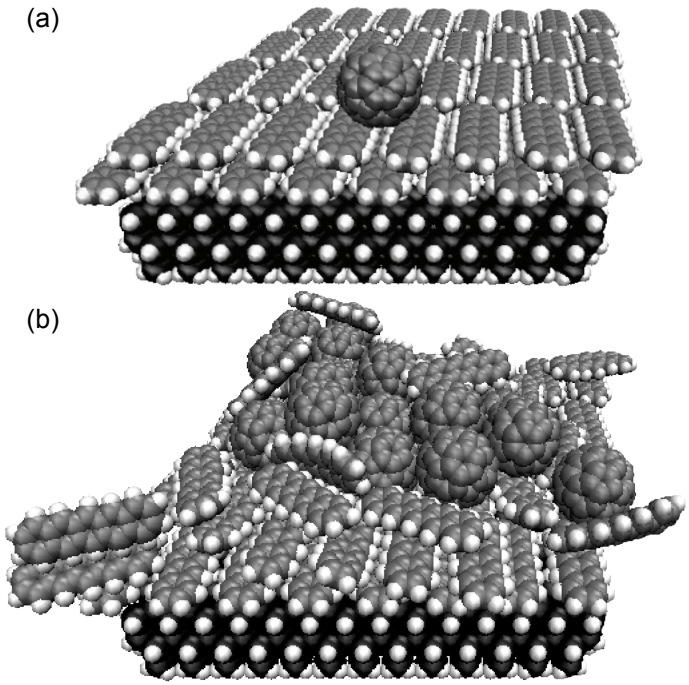

Figure 6.14: Molecular Dynamics snapshots after 2 ns of simulation of recumbent pentacene (gray and white) on a Si:H (black and white) surface with (a) only one C_{60} molecule on top of the pentacene surface and (b) 15 C_{60} molecules on the surface showing the disorder that ensues.

At high ϕ_1 values, where the pentacene molecules are already destabilized by the lack of π-electron sharing, the extra disturbance caused by the presence of C_{60} molecules causes even further disruption to the order of the surface. The presence of a single C_{60} molecule does not have a big impact on the pentacene surface (see Figure 6.14(a)), but adding multiple C_{60} molecules displaces the top pentacene molecules significantly (see Figure 6.14(b)). This behavior is akin to C_{60} "bullying" or burrowing into the pentacene layer to accommodate more desirable positions of the C_{60} molecules. When the recumbent pentacene molecules are arranged such that $\phi_1 \leq \sim 70^\circ$, this "bullying" effect is not observed because the pentacene molecules are now able to more closely resemble their stable herringbone configuration. When $\phi_1 \geq \sim 70^\circ$, however, the burrowing of C_{60} molecules into the pentacene exposes the C_{60} molecules to the fixed pentacene molecules in the first monolayer closest to the metal, a situation that we had not intended to be possible.

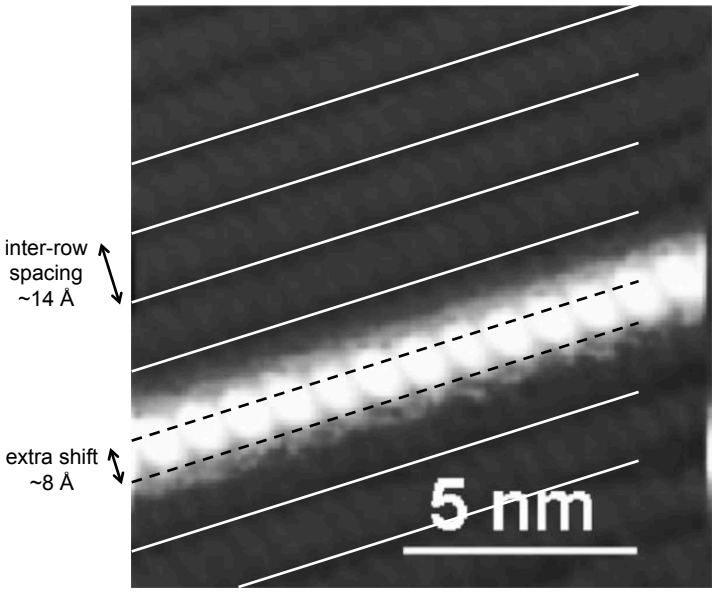

Figure 6.15: Room temperature STM image of a C_{60} nanowire with white lines added to show the location of pentacene rows. Black dotted lines are added to show the location of the extra shift caused by the presence of the C_{60} molecules. [Fig. 2, Phys. Rev. B 77, 073414 (2008) (slightly modified), with permission]

This kind of surface disruption has, in fact, been seen experimentally. The presence of C_{60} can disrupt the positions of gold atoms on a Au(110) surface.[156,157] Of more relevance to this work, we believe that the C_{60} nanowire results achieved by Dougherty *et al.*[66] shows evidence of C_{60} molecules burrowing into the pentacene while retaining its nanowire shape: Figure 6.15 is a copy of Dougherty *et al.*'s STM image of a C_{60} nanowire, in which we have drawn lines to show the location of pentacene rows, regularly spaced 14 Å apart. An extra 8 Å gap can be seen between the pentacene rows where the C_{60} nanowire resides (22 Å apart). Based on the STM image, our interpretation is that the pentacene is being displaced by the presence of the C_{60}. Dougherty cannot conclusively rule out "creep" in the piezo scanner as a cause for this increase in lattice spacing in the vicinity of the nanowire;[158] however, we believe that the regularity in the images suggests this effect, if present, is small.

6.3 Prediction of the propensity to form C_{60} nanowires: Effect of pentacene tilt angle on diffusion behavior

A first attempt to study the tendency for C_{60} to form nanowires on recumbent pentacene involved slowly and incrementally adding C_{60} molecules on top of two layers of recumbent pentacene on Si(111):H. The C_{60} molecules were added one by one (up to seven molecules) to see if they would spontaneously form nanowires. Each addition was placed 10 Å to 20 Å apart from any other C_{60} molecule. After each addition, a canonical ensemble simulation was implemented for 2 ps followed by a microcanonical ensemble for 500 ps. Unfortunately, no nanowires formed spontaneously using this method. The reason for

this, we believe, has to do with the fact that the newly deposited C_{60} molecules were allowed to approach the others from any direction, although, as shown by our own previous MD simulations, the molecules are statistically far more likely to approach from a direction already aligned with the nanowire (see Figure 6.13). Randomly placed molecules led to C_{60} molecules being positioned in high energy locations, and in which the nearest low-energy state for the system was one in which the C_{60} molecules formed compact (fcc-like) structures. See Figure 6.16 for MD snapshots of our unsuccessful attempts at nanowire growth from randomly-positioned C_{60} molecules.

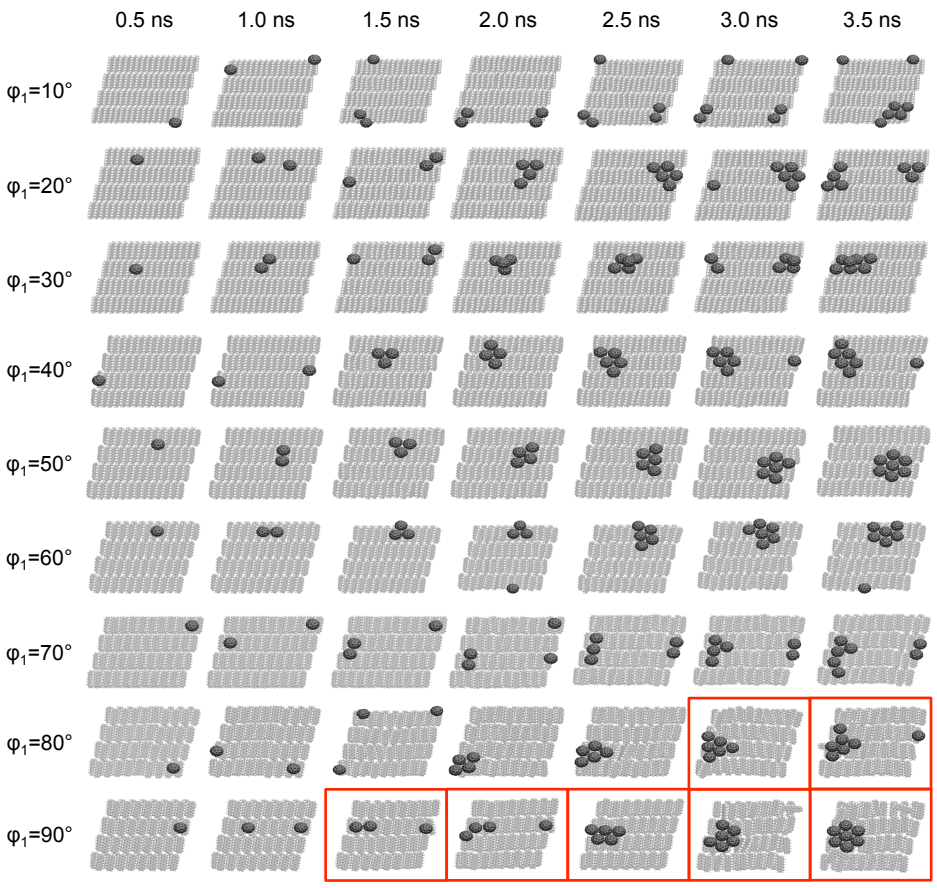

Figure 6.16: Molecular Dynamics snapshots of attempts at spontaneous nanowire growth, through random positioning of new C_{60} molecules. Each column represents a 500-ps advancement in simulation time. Snapshots boxed in red represent cases where the pentacene was significantly disturbed, exposing fixed pentacene molecules, so as to discredit the resulting C_{60} structures.

As an alternative approach, we decided to pre-place the C_{60} molecules in nanowire arrangements and shift our focus to determine the probability that they would remain in place under conditions of thermal equilibrium. We placed the nanowires initially in both an east-west (E-W) orientation (between and within pentacene rows), as well as in a north-south (N-S) fashion, where the nanowire is oriented in the direction of the long axes of the pentacene molecules. See Figure 6.17 for a pictorial description of these arrangements. For each of the three nanowire orientations, nine different pentacene orientations were considered (ϕ_1=10–90°), for a total of 27 simulations. The system size chosen for all simulations had to accommodate both the different periodicity of the pentacene and C_{60} molecules. As a result, there was inevitably some lattice mismatch at the boundaries. The periodic boundary "mismatch" is defined here as the extra distance in Å between C_{60} molecules of neighboring periodic systems (see small arrows in Figure 6.17). The resulting C_{60} arrangements from the nanowire preplacements are shown by MD snapshots in Figure 6.18, but these results can be appreciated more succinctly in the form of a diagram that shows the relationship between tilt angle and the tendency to form nanowires and disordered structures. This diagram, shown in Figure 6.19, captures the resulting structure of the nanowire for given values of ϕ_1 and periodic boundary mismatch. All the simulations depicted in Figures 6.18 and 6.19 were run for 500 ps in a microcanonical ensemble at 300 K.

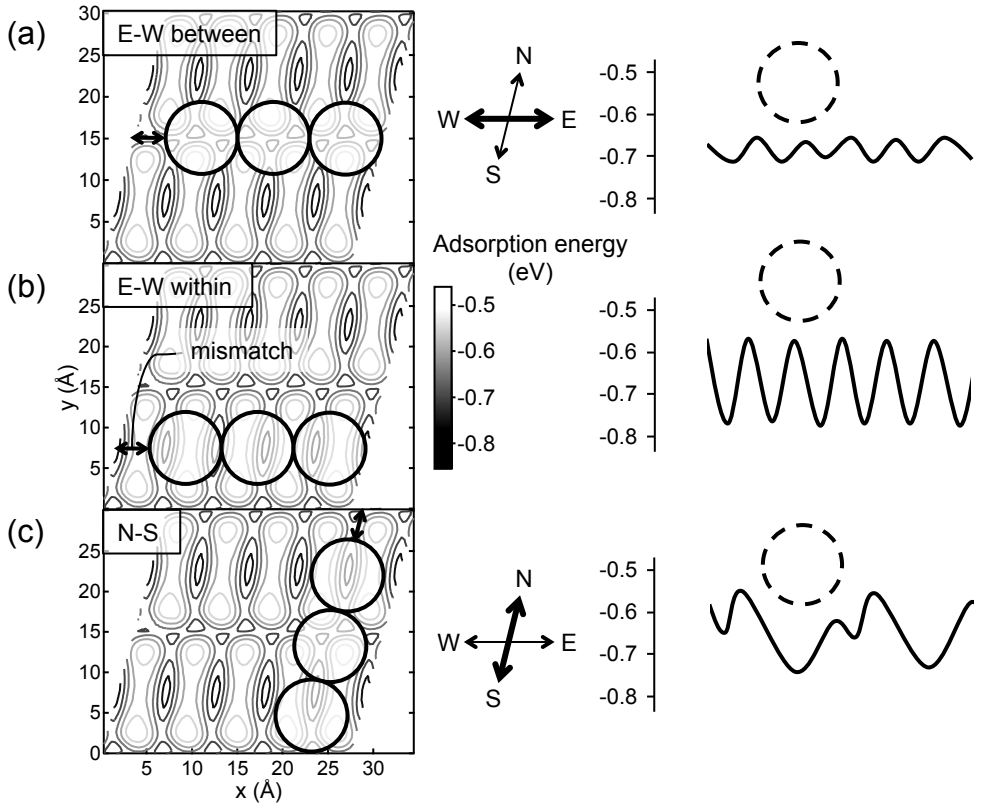

Figure 6.17: Adsorption energy surface (left) and energy corrugation profiles in eV (right) for different nanowire arrangements: (a) east-west (E-W) between pentacene rows, (b) E-W within pentacene rows, and (c) north-south (N-S) along the long axes of the pentacene molecules. This particular adsorption energy surface repeated in (a), (b), and (c) corresponds to ϕ_1=60°. The mismatch distances, shown by the small black arrows, refer to the periodic boundary mismatch due to the incommensurability of the pentacene lattice and C_{60} nanowire.

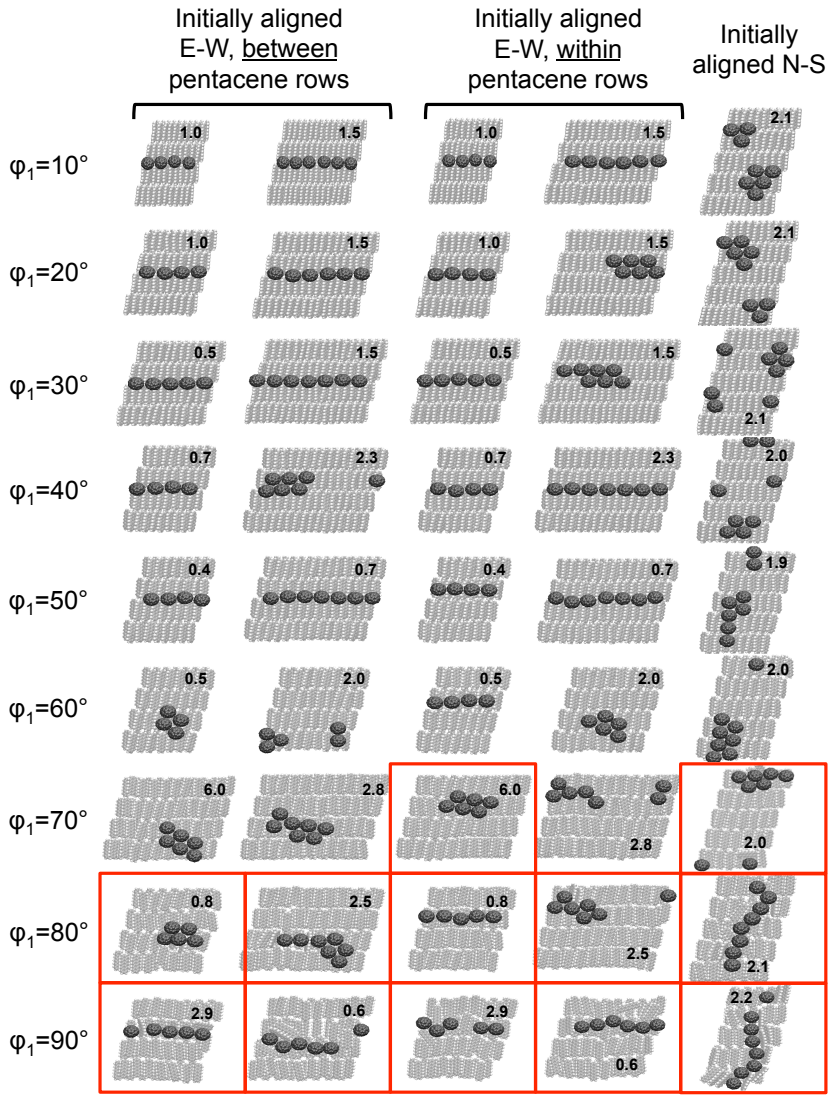

Figure 6.18: Molecular Dynamics snapshots of pre-placed nanowire growth after 500 ps (under no initial strain). Inset numbers are the periodic boundary mismatch (in Å) for the initial nanowire configurations. Snapshots boxed in red represent cases where the pentacene was significantly disturbed, exposing fixed pentacene molecules, which discredits the resulting C_{60} structures.

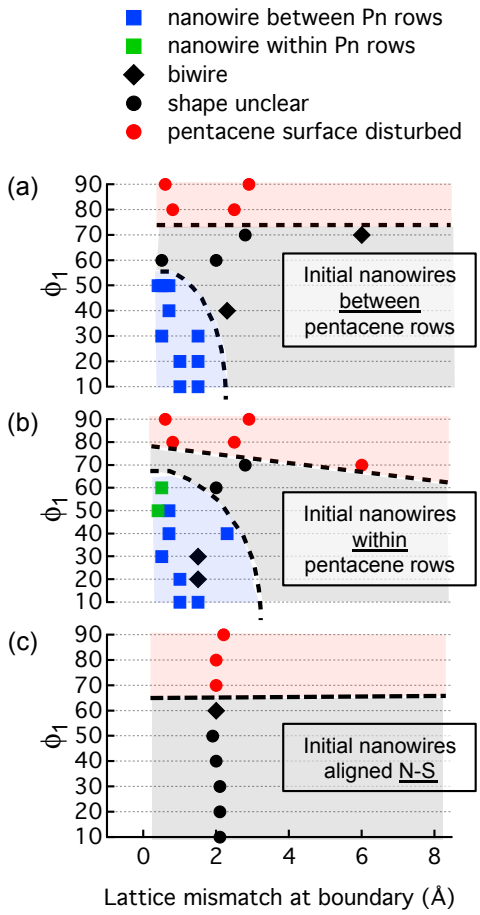

Figure 6.19: Resultant structures of pre-placed nanowires after 500 ps of simulation time for nanowires initially placed in three different locations: (a) between pentacene rows, (b) within pentacene rows and (c) nanowires aligned in a north-south direction. Data points are shown as solid symbols. Boundaries are drawn as hashed lines to guide the eye to distinguish between successful nanowires, unsuccessful nanowires, and systems in which the pentacene was disturbed too badly to report the true behavior of the C_{60} molecules. The shading is also used to reinforce the notion of regions in which nanowires are likely to form (blue and green), the shape of the resulting structure is ambiguous (grey), and the underlying pentacene surface is disordered (pink).

It can be seen in Figures 6.19(a) and 6.19(b) that more successfully persisting nanowires result from very small periodic boundary mismatches as well as for low ϕ_1 values ($\phi_1 \sim \leq 50°$). Generally, the smaller the periodic boundary mismatch, the better the linearity of the nanowire. The low ϕ_1 systems yield more successfully persisting nanowires, especially those residing between pentacene rows, as predicted in Sections 6.1.2 and 6.1.3. It is of particular interest, in Figure 6.19(b), that nanowires starting *within* pentacene rows at lower ϕ_1 values spontaneously transition to positions *between* pentacene rows (see blue squares in Figure 6.19(b), which were originally within pentacene rows). We believe this has to do with the relative energy roughness in the direction of the nanowire. Between the pentacene rows, energy troughs in the E-W direction are more of a continuous valley than that within the rows (see the energy corrugation profiles in Figures 6.17(a) and 6.17(b)), where the pentacene positions create larger energy barriers between minima. Although the energy minima within the pentacene rows can be quite deep (and hence potentially attractive), especially for $\phi_1 \geq 50°$, variations in energy roughness seem to destabilize the nanowire structure within the rows. To a large extent, this has to do with commensurability of the C_{60} diameter and the lattice parameter, a, of the recumbent pentacene structure. The more commensurate these values, the more likely it is to observe a persisting nanowire in which each C_{60} molecule can find its own personal energy trough within the row. The most commensurate recumbent pentacene structure for E-W C_{60} nanowires occurs for $\phi_1 = 50°$, where there are 1.98 C_{60} molecules per lattice parameter (essentially one C_{60} molecule for every two pentacene molecules). Consequently, we see successfully persisting nanowires within pentacene rows for $\phi_1 = 50°$.

For N-S nanowires, Figure 6.19(c) shows that there are no successfully per-

sisting C_{60} nanowires at any ϕ_1 value. Even though there are deep energy minima in the N-S direction and the barriers in the E-W direction are high (as shown in Figure 6.12), we still did not see nanowires in the N-S direction, which was not consistent with our previous predictions. This effect can be explained by the relative roughness of the N-S energy corrugation, as shown in Figure 6.17(c). There is also a low degree of commensurability for C_{60} molecules aligned to the pentacene in the N-S direction (1.64 C_{60} molecules per pentacene), which we believe discourages the nanowires from forming.

For each E-W ϕ_1 system, we ran simulations for different numbers of C_{60} molecules (between five and seven). This study was intended to decouple the effects of the periodic boundary mismatch and the number of C_{60} molecules in the nanowire. In other words, we wanted to ensure that the resultant structures were not an artifact of the specific number of C_{60} molecules in the wire. Figure 6.18 shows the number of C_{60} molecules and the corresponding periodic boundary mismatch (inset numbers) tested for each value of ϕ_1. For the systems in which the C_{60} molecules started at locations between pentacene rows, we tested four different sets for ϕ_1=50° values because the periodic boundary mismatches for four to seven C_{60} molecules were very close in value (±0.1 Å), thus allowing us to decouple the periodic boundary mismatch effect. Figure 6.20 shows the eventual structures of the nanowires plotted against the number of C_{60} molecules in the wire. There is no clear trend of the persistence (or not) of nanowires when plotted against the number of C_{60} molecules; thus, we conclude that there is no artifactual effect due to a given choice of the number of C_{60} molecules included in the nanowire.

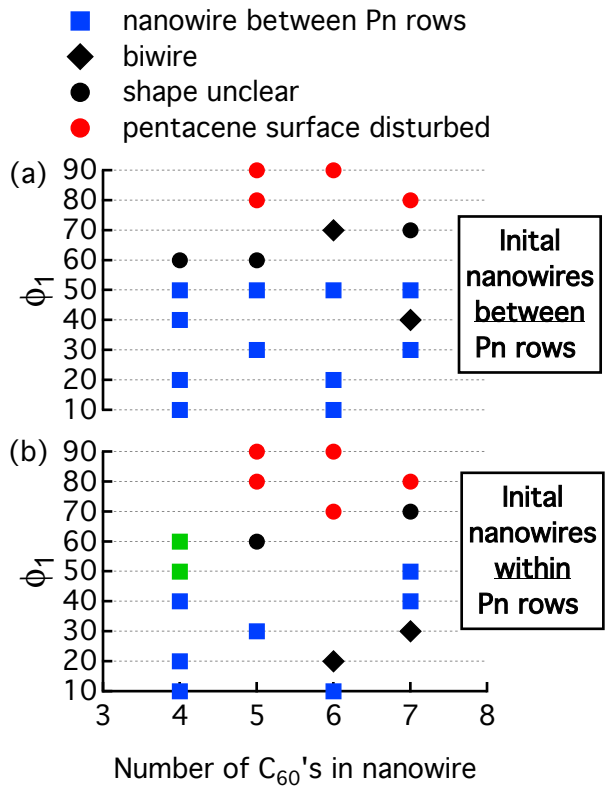

Figure 6.20: Resultant structures of pre-placed C_{60} nanowires after 500 ps of simulation time, as a function of the number of C_{60} molecules in the system. These graphs represent pre-placed nanowires initially in the E-W direction (a) between pentacene rows and (b) within pentacene rows.

To summarize the results so far, pre-placing C_{60} nanowires on variably-angled recumbent pentacene structures allowed us to draw some important conclusions: Firstly, we confirmed our previous prediction that successful nanowires will tend to occur between the pentacene rows at lower angles (see Sections 6.1.2 and 6.1.3). On the other hand, nanowires located within the pentacene rows (which we had predicted from the single C_{60} studies to be more successful at higher angles) were not as persistent as we had predicted, due in part to the disturbance that they caused to the underlying pentacene substrate at higher ϕ_1 values (as confirmed by experiments). Thirdly, nanowires initially oriented along the long-axis of the pentacene molecules (N-S) did not tend to persist due to the lower degree of C_{60}-pentacene commensurability in this direction. Finally, we observed a simulation-related ("housekeeping") issue that the effect of a periodic boundary mismatch between the C_{60} and the pentacene is much more important than the sheer number of C_{60} molecules in the nanowire for obtaining successfully persistent nanowires.

6.3.1 Stability of C_{60} nanowires

The pre-placed C_{60} nanowire simulations described previously were run for 500 ps, and although we gained much information from these relatively short simulations, we also continued the simulations of all the successful nanowires (blue and green squares in Figure 6.19) for a longer time (2 ns) to look for any tendency for the nanowires to break apart. Nanowires starting out between pentacene rows remained in this configuration throughout the 2 ns simulation except for one case at ϕ_1=50°, where the nanowire spontaneously transitioned from between to within the pentacene rows (see Figure 6.21(a)) at the very end

of the simulation. On the other hand, most of the nanowires that started out *within* pentacene rows quickly transition to positions between the pentacene rows for $\phi_1 < 50°$. The systems of $\phi_1 = 50°$ and $\phi_1 = 60°$ were exceptions, in which nanowires within the rows seem more stable (see Figure 6.21(b)). This follows the argument given previously concerning $\phi_1 \sim 50°$ being the most commensurate C_{60}/pentacene system for nanowires within pentacene rows.

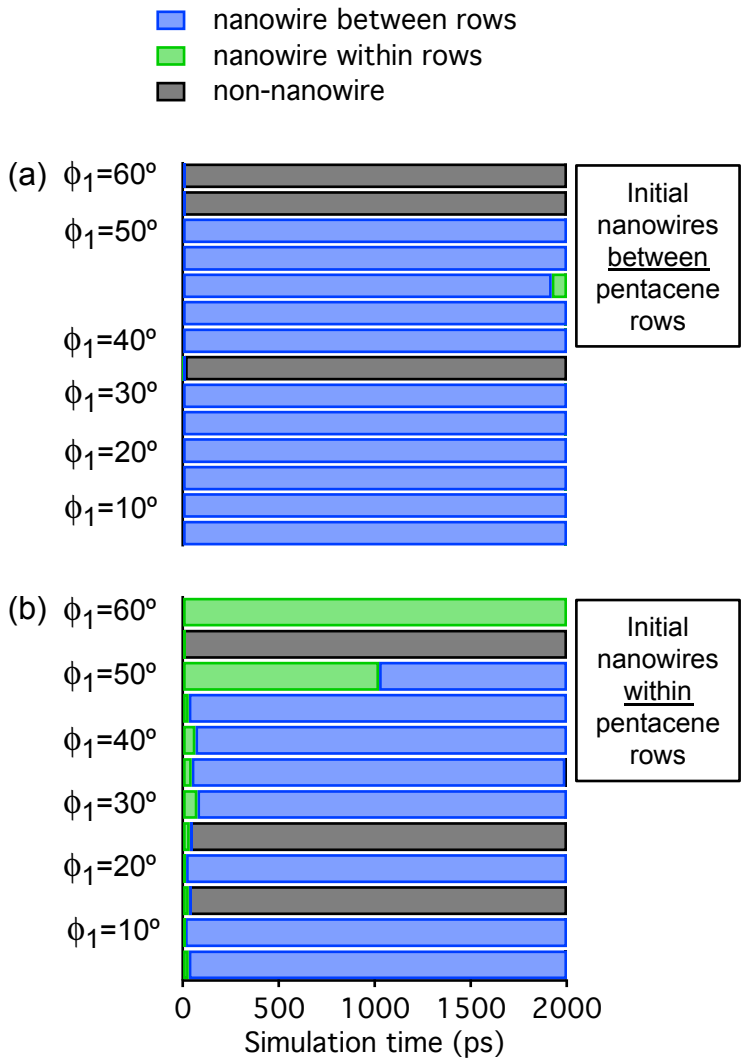

Figure 6.21: Longer-time resulting structures from NVE simulations of pre-placed E-W nanowires initially (a) between pentacene rows and (b) within pentacene rows.

Even the 2 ns simulations described above still describe very short timescales, and since simulations of seconds of elapsed time are unattainable, we looked at another way to test the stability of the successful C_{60} nanowires we had found. We performed simulations in the canonical ensemble (NVT) at three different temperatures—300 K, 350 K, and 400 K—to test the thermal stability of the system. We considered only the pentacene tilted in the range ϕ_1=10–50° because these are the orientations which yielded successful nanowires for the microcanonical (NVE) simulations previously. We limited our temperatures to below 400 K since this is roughly the limit before desorption occurs. Figure 6.22 shows the NVT simulation time evolution of nanowires initially placed between and within pentacene rows at 300 K, 350 K, and 400 K.

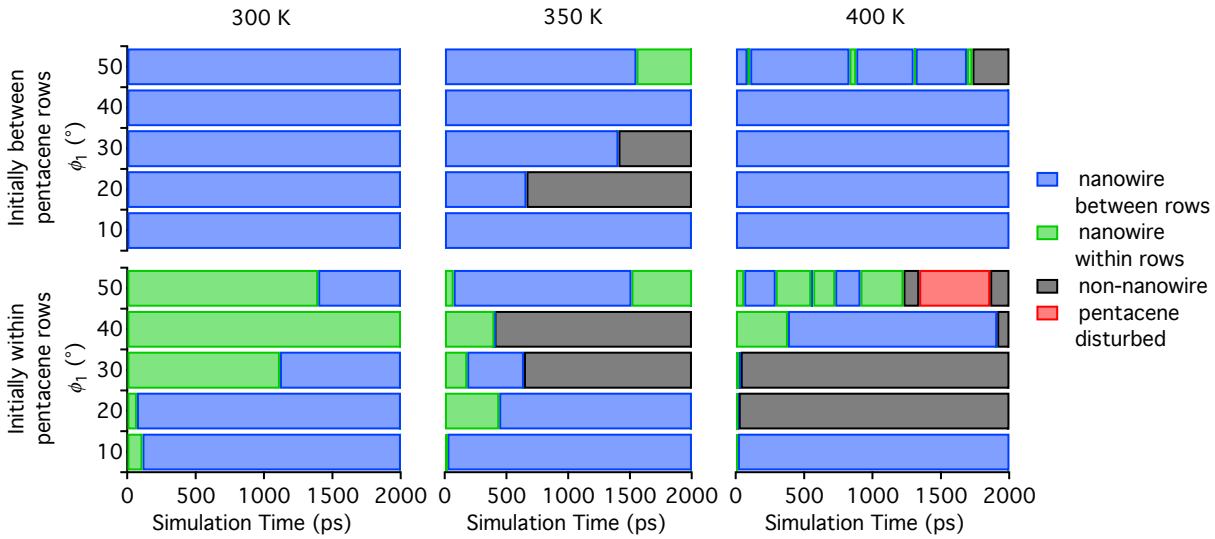

Figure 6.22: Structures resulting from 2 ns of NVT simulation of pre-placed E-W nanowires initially located between pentacene rows (upper) and within pentacene rows (lower) at 300 K, 350 K, and 400 K.

Taken as a group, all the results shown in Figure 6.22 show an encouraging degree of persistence of the nanowires, and a recapitulation of the increased stability of nanowires that are located between pentacene rows over those within rows. Now we discuss some of the other interesting observations. For instance, at ϕ_1=50°, the nanowires tend to switch back and forth between locations within and between the pentacene rows. This switching is most prominent at 400 K, when the molecules have sufficient kinetic energy to cross the barrier between the two locational states (~0.2 eV). The reason why this switching occurs more at ϕ_1=50° than lower tilt angles, 10–40° say, is because the energy wells at this orientation are almost exactly the same for the two different configurations (between and within); see Figure 10 in reference 106 for a comparison of the energy minima. One interesting effect of this switching at ϕ_1=50° at 400 K for a nanowire initially placed within pentacene rows, is that the repeated transitions disrupted the top pentacene layer (to the extent of exposing the fixed bottom pentacene layer) for a period of 500 ps. Surprisingly, in the last 100 ps of that simulation, the pentacene recovered its original structure, and the C_{60} molecules arranged into a compact (non-nanowire) form, as was the case just before the pentacene disruption. In the preceding NVE simulations at 300 K, such a disruption of the pentacene never occurred for orientations as low as ϕ_1=50°; but the higher temperature allows the C_{60} molecules to overcome the energy barriers keeping it from "burrowing". For ϕ_1=10–40°, the switching between locations within and between pentacene rows occurs much less commonly, even at 400 K. For these low tilt angles, the energy wells at the two different configurations (between and within) differ by more than 0.1 eV, making this transition more difficult. There was one case out of the ordinary, at ϕ_1=20° and 350 K, where a nanowire initially located between pentacene rows transitioned to a compact

2D form, but this system had a slightly higher periodic boundary mismatch than the others (1.0 Å). As discussed before, higher periodic boundary mismatches tend to disrupt the nanowire arrangement. Visualizations of the cases where nanowires transition to compact 2D forms show that there is a stochastic element governing individual outcomes, caused by random internal energy fluctuations that lead to the disruption of the linear arrangement. In summary, the NVT simulations at higher temperatures (to 400 K) have shown that the C_{60} nanowires between pentacene rows are surprisingly stable and this goes some way to mitigating the fact that we cannot follow the dynamics of the nanowires over experimental timescales.

6.3.2 Effect of strain on C_{60} nanowire persistence

Since the periodic boundary mismatch at the boundaries appeared to be an important factor in the success of persisting nanowires, it begged the question of whether or not strain applied to the C_{60} nanowire would affect the outcome. We applied an initial tensile strain of about 5% in the direction of the nanowire for the same set of simulations as before, and let the system evolve in time. The strain results from increasing the distance between C_{60} molecules from the preferred equilibrium distance by 1.05 times that distance. The periodic boundary mismatch is not included in what we call the 5% strain, even though it does add to the overall strain. Figure 6.23 shows the Molecular Dynamics snapshots of the resulting C_{60} structures after 500 ps at 300 K, and Figure 6.24 shows the corresponding diagram of results, as before. The first thing of note in Figure 6.24 is that there are far fewer successfully persisting nanowires (blue and green squares) under tensile strain conditions. The initial tensile strain causes

the C_{60} nanowires to attempt to pop back to their equilibrium distance from one another and, in the process, the nanowires become misaligned. The C_{60}-C_{60} interaction is much stronger than the C_{60}-pentacene interaction, resulting in compact or bi-wire C_{60} structures (see the abundance of black markers in Figure 6.24 as compared to Figure 6.19). This shows the impact of the delicate balance of forces between the C_{60}-C_{60}, C_{60}-pentacene, and pentacene-pentacene van der Waals interactions on structural outcomes.

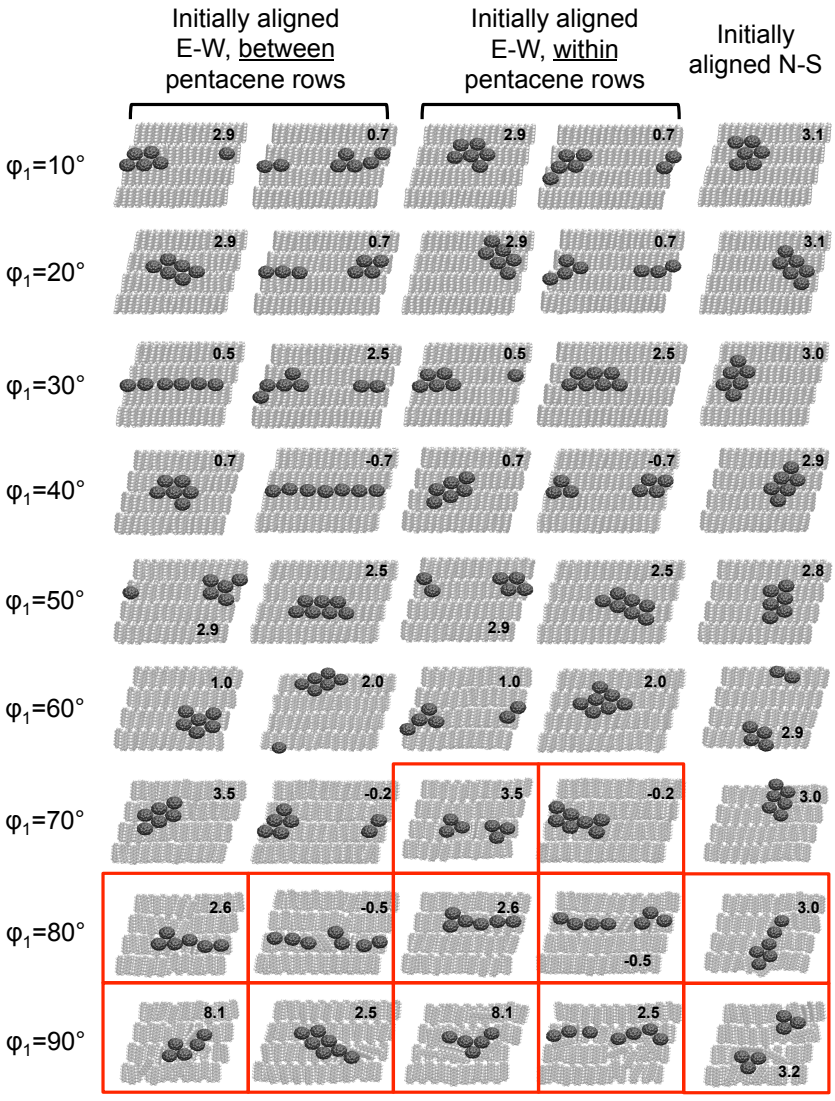

Figure 6.23: Molecular Dynamics snapshots of pre-placed nanowire growth after 500 ps, with an initial applied strain of 5%. Inset numbers are the periodic boundary mismatch (in Å) for the initial nanowire configurations. Snapshots boxed in red represent cases where the pentacene was significantly disturbed, exposing fixed pentacene molecules, which then discredits the resulting C_{60} structures.

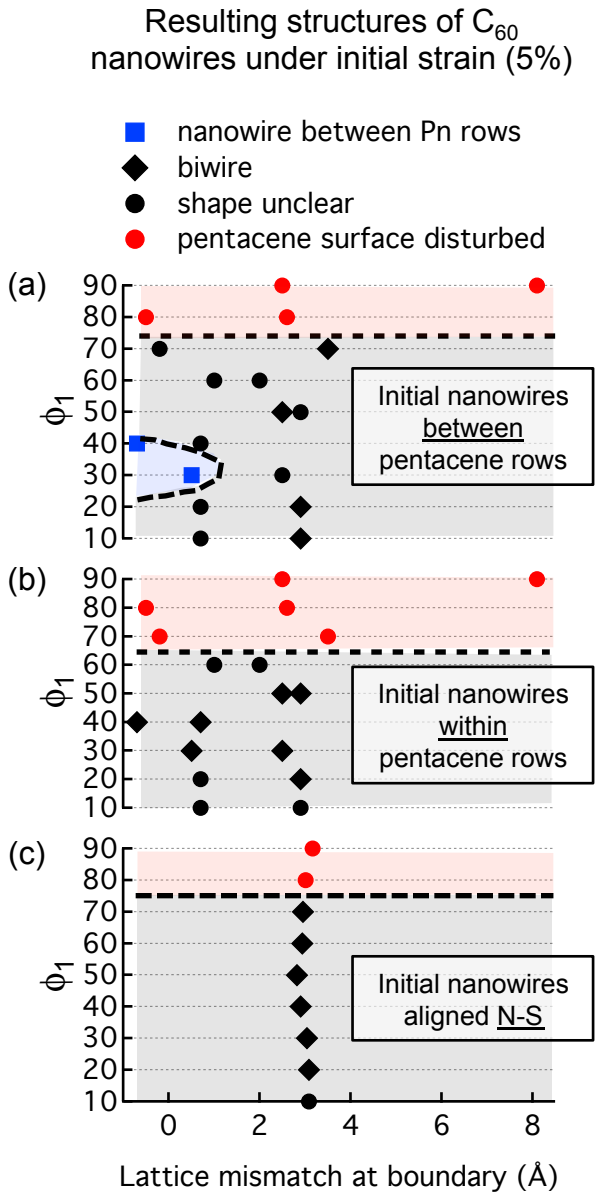

Figure 6.24: Structures formed by initially pre-placed nanowires under a 5% initial strain after 500 ps of simulation time. Key as in Figure 6.19.

6.3.3 Effect of pentacene step edges on nanowire persistence

So far, we have identified a number of factors that disrupt the persistence of nanowires, especially strain-related, and we now looked to an alternative way to create more robust nanowires. We know, from experimental studies, that metallic substrates beneath recumbent pentacene are likely to exhibit a considerable number of step edges.[53,58,62,63,68–70,74] We also know that C_{60} molecules have a strong binding energy to the step edges of upright pentacene polymorphs (which are taller than the diameter of C_{60} molecules);[22] this led us to look at the tendency of C_{60} nanowires to persist at the much lower height step edges of recumbent pentacene molecules (which are smaller than the diameter of C_{60} molecules). The step edges were constructed in both the E-W and N-S directions with a C_{60} nanowire lined alongside them, as shown in Figures 6.25 and 6.26. We suspected that this would greatly improve the persistence of nanowires, so we also placed an initial strain (5% as before) on the nanowire to test its ability to retain a 1D structure in unfavorable circumstances. Each simulation was run for 500 ps, and the resulting Molecular Dynamics snapshots are shown in Figure 6.26. A few of the systems in which the C_{60} nanowires were successful were run for a total of 2 ns to confirm their persistence.

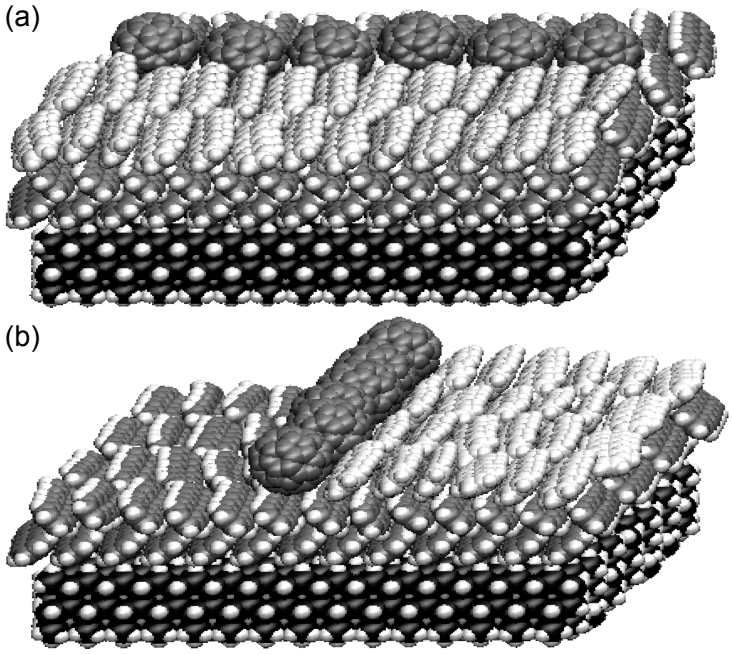

Figure 6.25: Molecular Dynamics snapshots of configurations of C_{60} nanowires in (a) E-W and (b) N-S orientations placed along the corresponding E-W and N-S step edges of recumbent pentacene. ϕ_1=50° for these particular systems. Step edge pentacene molecules in the third molecular layer are colored a lighter shade of gray.

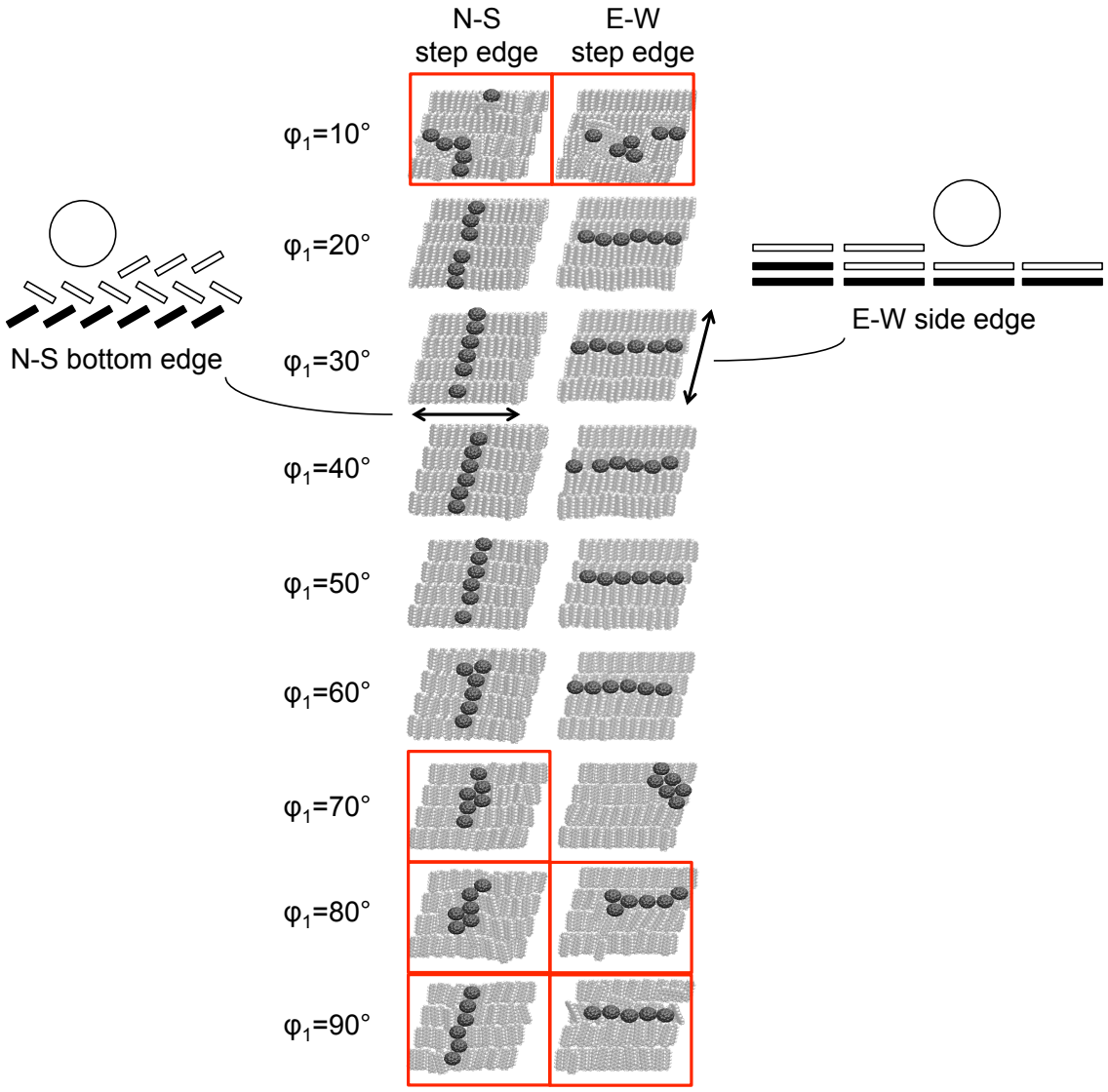

Figure 6.26: Molecular Dynamics snapshots after 500 ps at 300 K of pre-placed C_{60} nanowires on N-S and E-W pentacene step edges. In the schematics to the left and right, the solid rectangles represent pentacene molecules that are held fixed; the hollow rectangles represent pentacene molecules that are free to move. Snapshots boxed in red represent cases where the pentacene was significantly disturbed, exposing fixed pentacene molecules.

The nanowires were much more successful in persisting in the presence of a pentacene step edge, even when a 5% initial strain was applied. In the absence of step edges, there were no successful instances of C_{60} nanowire persistence in the N-S direction, even with no strain applied. Yet with a N-S pentacene step edge, C_{60} nanowires persisted successfully for ϕ_1=20°–50°. To test the limits of the success of exploiting step edges, we ran the same N-S simulations with an even lower half-step; this did not change the resulting success for persisting N-S nanowires. With the E-W pentacene step edges, C_{60} nanowires persisted for ϕ_1=20°–60°, which was the case for pre-placed nanowires without any step edges or initial strain. For both N-S and E-W nanowires, the pentacene molecules were disturbed for $\phi_1 \geq$~70° as before. Unlike before, the surface pentacene molecules were also disturbed for ϕ_1=10°. This implies that pentacene molecules in the ϕ_1=10° configuration are unstable at step edges.

CHAPTER 7

CONCLUSIONS AND FUTURE OUTLOOK

7.1 Main accomplishments

Progress in the field of small molecule organic electronic materials has increased dramatically in the last couple of decades. Despite this, an understanding of the nature of the interface between the prototypical organic-organic heterojunction of C_{60}/pentacene is very limited at the molecular level. This thesis has attempted to broaden the understanding of the heterojunction between these two molecules from a molecular perspective. We have quantified the ability of the angular orientation of pentacene, both in terms of stable and metastable polymorphs, within the context of a thin film to alter the diffusional and nanoscale adsorption properties of C_{60}. Below we summarize the main accomplishments described herein.

From fully atomistic MD simulations, we found interesting results for the diffusion of C_{60} molecules on a surface of the upright pentacene polymorphs—the bulk and thin film phase. We showed that C_{60} diffusion coefficients on thin film phase pentacene are approximately twice as high as that on bulk phase pentacene for experimentally realizable temperatures (200–400 K). This implies that C_{60} might have better growth properties on thin film phase pentacene because a higher diffusion coefficient generally leads to a greater tendency to wet the substrate and grow in an ordered fashion. The reasons for the lower diffusion coefficient of C_{60} on bulk phase pentacene were shown to be due to energy traps on the surface. Furthermore, the anisotropic diffusion of C_{60} on bulk phase pentacene was an interesting and unexpected result. Building from the single-C_{60}

studies with the MD to the extent that we could, we simulated small clusters of C_{60} on bulk phase pentacene. With the addition of more C_{60} molecules on the surface of upright pentacene, the average C_{60} diffusion coefficient decreases by a factor of four when just one more C_{60} molecule is nearby. This decrease continues as a third C_{60} molecule is placed near the other two. This clear preference for C_{60} to reside close to other C_{60} molecules shows that C_{60}-C_{60} cohesion is stronger than C_{60}-pentacene adhesion.

The relatively large system sizes and intermolecular complexity of the models used in the MD simulations meant that the system sizes we could realize were very limited and precluded a study of even submonolayer growth. This necessitated consideration of a more coarse-grained simulation technique. Kinetic Monte Carlo provided to necessary benefits to pursue larger length and time scales that are accessible experimentally. A multi-lattice framework was developed to satisfy the unique surface terrain that the herringbone structure of upright pentacene provides. In the cataloguing of rates for the simulation, a large amount of data emerged on environment-specific energy barriers. In the end, microseconds and tens of nanometers were achievable, a scale unattainable by MD methods. Even so, the detailed differences between C_{60}'s behavior on thin film and bulk phase pentacene deterministically described by MD were still able to be captured in KMC.

In our studies to emulate pentacene adsorbed on metal substrates, in which we varied the angle, ϕ_1, adopted by the short axis of the pentacene molecules from 10° to 90°, we were able to make a prediction about the tendency of C_{60} to form nanowires. Static energy calculations to produced the potential energy surface between a *single* C_{60} molecule and a set of variably-angled recumbent

pentacene structures. We followed this with MD simulations of a single C_{60} molecule moving over a recumbent pentacene substrate in which the tilt angle was controlled. Just from the static and dynamic calculations of a single C_{60} molecule, we were able to predict that C_{60} nanowires were most likely to occur in one of three orientations: "east-west" (E-W) between pentacene rows, E-W within pentacene rows, and "north-south" (N-S). Specifically, the results suggested that, at lower ϕ_1 values ($\phi_1 \leq 40^\circ$), E-W-oriented nanowires would show a slight preference to form *between* pentacene rows (adsorption energy = –0.75 eV) as opposed to *within* pentacene rows (adsorption energy = –0.65 eV). Secondly, at higher ϕ_1 values ($\phi_1 \geq 70^\circ$), E-W nanowires showed a small preference to form within pentacene rows (adsorption energy = –0.85 eV) as opposed to locations between pentacene rows (adsorption energy = –0.75 eV).

Lastly, we explored systems in which there are multiple C_{60} molecules present on recumbent pentacene, examining cooperative effects and the balance of C_{60} interactions with itself and with the pentacene substrate. We confirmed our initial hypothesis that there exists some special (short-axis) tilt angles that enhance the existence of nanowires. We showed that the probability of nanowire formation is most likely in a range of ϕ_1 values, from ~10–50°, and in the E-W direction between pentacene rows. The lower this tilt angle, the more persistent the nanowire. This range of angles has not been observed experimentally for recumbent pentacene structures (see Tables 1.1–1.3), and we predict that if such structures were made, C_{60} nanowires would more readily form. Our simulations also showed C_{60} molecules pushing the pentacene molecules out of the way and "burrowing" into the surface, and we believe that this is consistent with the extra inter-layer distance we observed in Dougherty's STM image in Figure 6.15. Ultra-flat pentacene surfaces, characterized by $\phi_1 \geq \sim 70^\circ$, are

unlikely to offer a viable template for C_{60} nanowire growth in any direction due to this burrowing behavior. We also identified one key factor that destabilizes nanowire persistence and one that stabilizes them: A small amount of strain destroys the nanowires, due to the destabilization of the balance of C_{60}-C_{60} versus C_{60}-pentacene van der Waals interactions. In contrast, any appreciable roughness in the surface will act as attractive sites for nanowires to form. For nanowires in the N-S direction, the only way for C_{60} molecules to likely remain in this configuration is with the aid of a pentacene step edge. We hope that our predictions of the favorability of nanowire formation will spur further experimental studies of novel highly tilted ($\phi_1 < 50°$) recumbent small-molecule organic semiconductors.

7.2 Future work

In the short term, a more complete study of comparisons of ab initio-derived results to the MM3 model would strengthen the case for using MM3. For example, it should be confirmed that the MM3-derived C_{60}-pentacene intermolecular energies are close to those derived by, say, restricted Hartree Fock with an MP2 correction. As an extension to this type of ab initio calculation, revisiting the planar interface described in Section 4.2 would be worthwhile. Specifically, we recommend extending the studies performed by Brian Koo to look at the effect of all orientation combinations of C_{60}-pentacene on the density of states.

Also in the short term, there are several enhancements that can be made to the KMC simulations of C_{60} growth on bulk and thin film phases of pentacene. First, in regard to submonolayer growth of C_{60}, we did not consider the effect

on the jump rates of initial and final *far* neighbors (distanced by $^2/_3\sqrt{3}$ times the van der Waals diameter); only initial and final direct neighbors were considered (distanced by the van der Waals diameter). Second, for Hex-bulk jumps (C_{60} jumps for beyond monolayer growth of C_{60}), the presence of final neighbors (whether direct or far) was not considered; only the presence of initial near and far neighbors were considered. The completion of these energy barrier sets would fine-tune the accuracy of the simulation.

Once these enhancements are considered, there are several studies that would be very interesting using this algorithm. First, it would be valuable to compare multi-layer C_{60} island morphologies on a perfectly-compact first-layer to those obtained by Liu *et al.*, who found fractal C_{60} island formation on a C_{60} substrate. Second, simulating defects, vacancies, or substrate step edges would give insight into the behavior of C_{60} growth in non-ideal conditions. In the longer term, implementing an off-lattice KMC approach would be worthwhile because it would facilitate movements at island edges, fine-tuning the microstructural evolution.

Unfortunately, the C_{60} on pentacene jump rates obtained in this work are very system-specific and hence one-of-a-kind, but we can imagine a broader applicability along several avenues. First, with all of the energy barriers for C_{60} on C_{60} jumps, it would be very useful to develop some sort of correlation between the intermolecular potentials and the energy barriers for different neighbor scenarios. The C_{60} on pentacene jump rates are very specific to the C_{60}-pentacene setup, but a correlation for C_{60} on C_{60} energy barriers could be extrapolated to other spherical, close-packable molecules. This correlation would depend on knowing the basic intermolecular potential as well as the number of initial direct

and far neighbors, the number of final direct and far neighbors, and the number of shared direct and far neighbors between the initial and final jump site. Such a framework could allow for predictions of C_{70}, C_{72}, C_{76}, C_{84}, and C_{100} like-on-like growth behavior. Second, the KMC code developed in this work with grid-switching capabilities could be applied to other oblique-hexagonal lattice systems for heteroepitaxial growth. Organic substrates with herringbone-type packing (*e.g.*, anthracene, tetracene, napthalene, rubrene) would be a very easy extension to this code. Only the jump rates would need to be obtained either by molecular mechanics or Molecular Dynamics methods as described in Section 5.2

Finally, there are several ways in which experimental collaborations would strengthen the results in this work. Comparing the 1^{st}, 2^{nd}, 3^{rd}, *etc.* monolayer coverage evolution obtained by our KMC code to experimental results would help evaluate our model's ability to predict the point at which 3D growth begins. As for the predictions we made regarding C_{60} nanowire formation on recumbent pentacene, it would be invaluable to have experimental collaborators test this prediction. We predicted that the lower the ϕ_1 value, the more successful a C_{60} nanowire would be. However, since none of the tilt angles given in the literature for noble metals were less than 55°, the feasibility of creating a 10° tilt angle would require consideration of a completely different substrate and may not be accessible at all.

APPENDIX A

EXTRA STATIC AND DYNAMIC DATA FOR 1-C_{60} ON RECUMBENT PENTACENE SYSTEMS

Table A.1: Key for Figures A.1–A.9.

Subfigure	Description
(a)	The height (in Å out of the plane) of a 2×5 recumbent pentacene surface.
(b)	The gap (in Å out of the plane) resulting between a C_{60} and the pentacene surface, as would result from a C_{60} molecule scanning the pentacene surface. The pentacene molecules correspond to the same structure as in (a).
(c)	The potential energy, or adsorption energy, (in eV) between a C_{60} molecule and the pentacene surface, as would result from a C_{60} molecule scanning the pentacene surface. The pentacene molecules correspond to the same structure as in (a).
(d)	Three plots showing contact for the three different energy wells: one *within* pentacene rows, and two *between*; darker areas are closer points of contact.
(e)	To get an average "well radius", this subplot plots radial averages of 9 different points from the center to the edge.
(f)	An MD trajectory of 1 C_{60} molecule (center-of-mass) diffusing on the recumbent pentacene surface for 2 ns; blue rectangles represent pentacene molecules, with darker ones denoting the molecules at the periodic system edges.

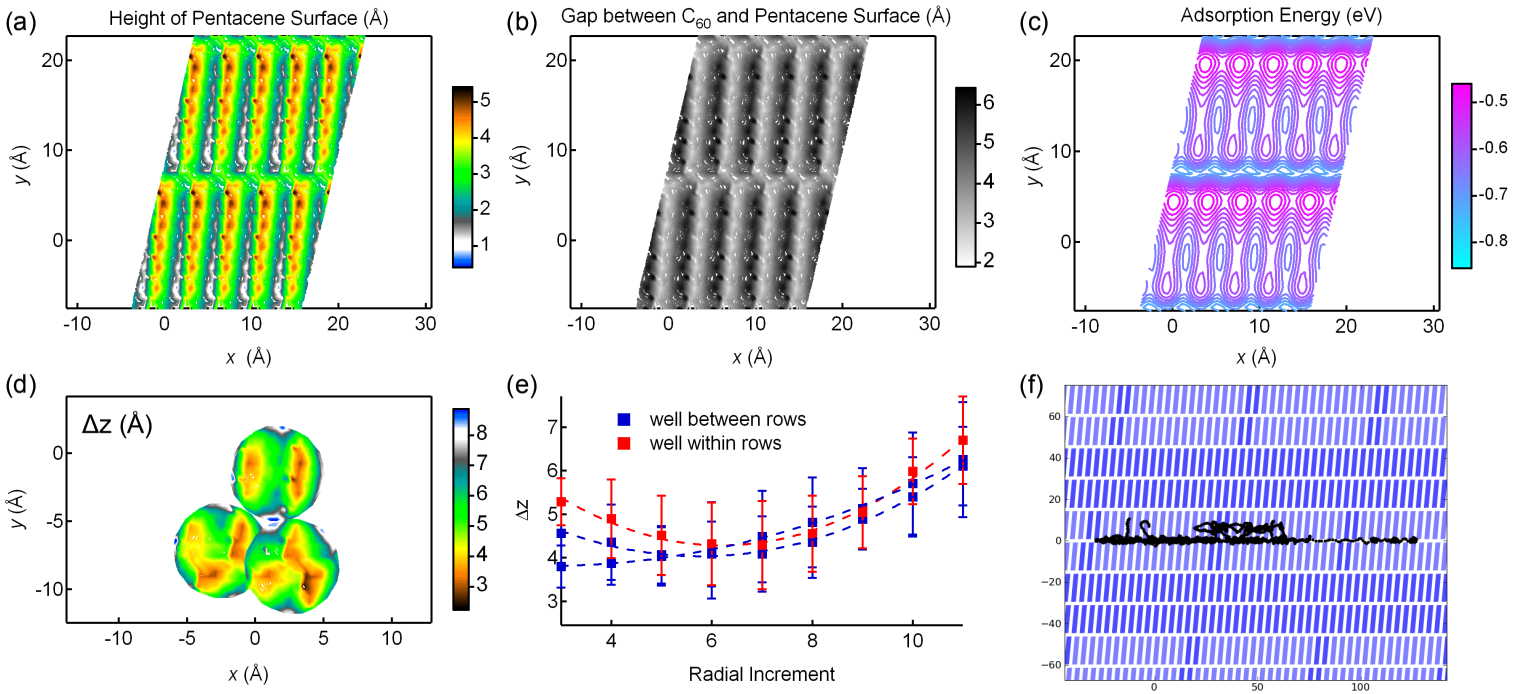

Figure A.1: Static and 1-C_{60} dynamic data for the ϕ_1=10° system. Key as in Table A.1.

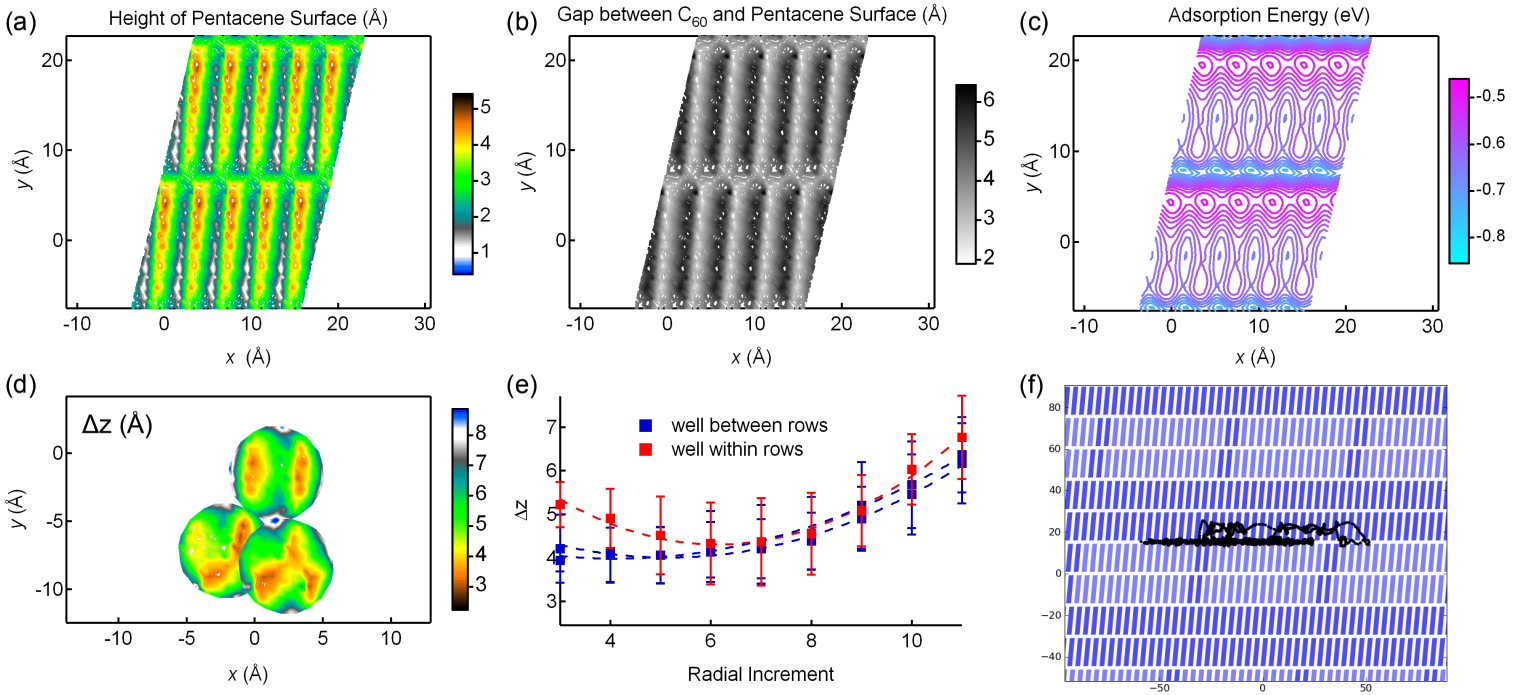

Figure A.2: Static and 1-C_{60} dynamic data for the ϕ_1=20° system. Key as in Table A.1.

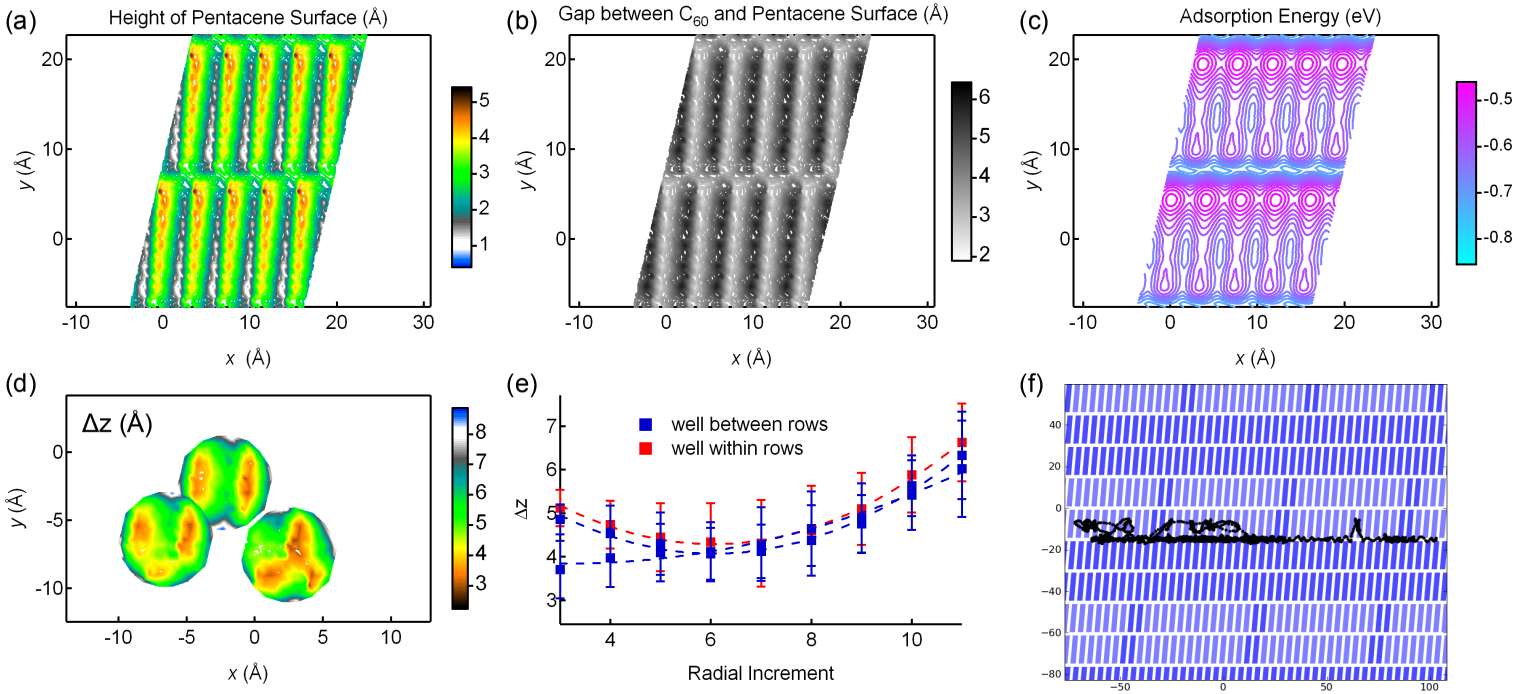

Figure A.3: Static and 1-C_{60} dynamic data for the ϕ_1=30° system. Key as in Table A.1.

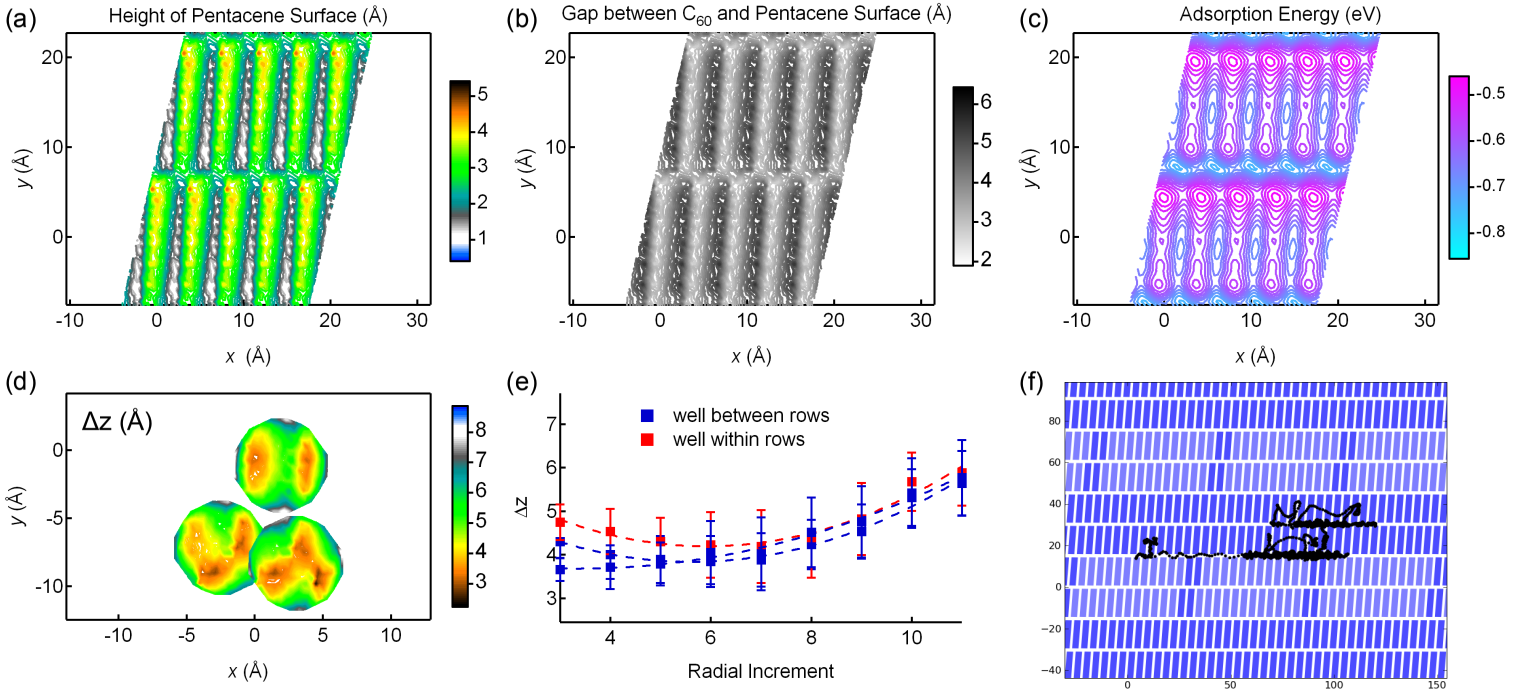

Figure A.4: Static and 1-C_{60} dynamic data for the ϕ_1=40° system. Key as in Table A.1.

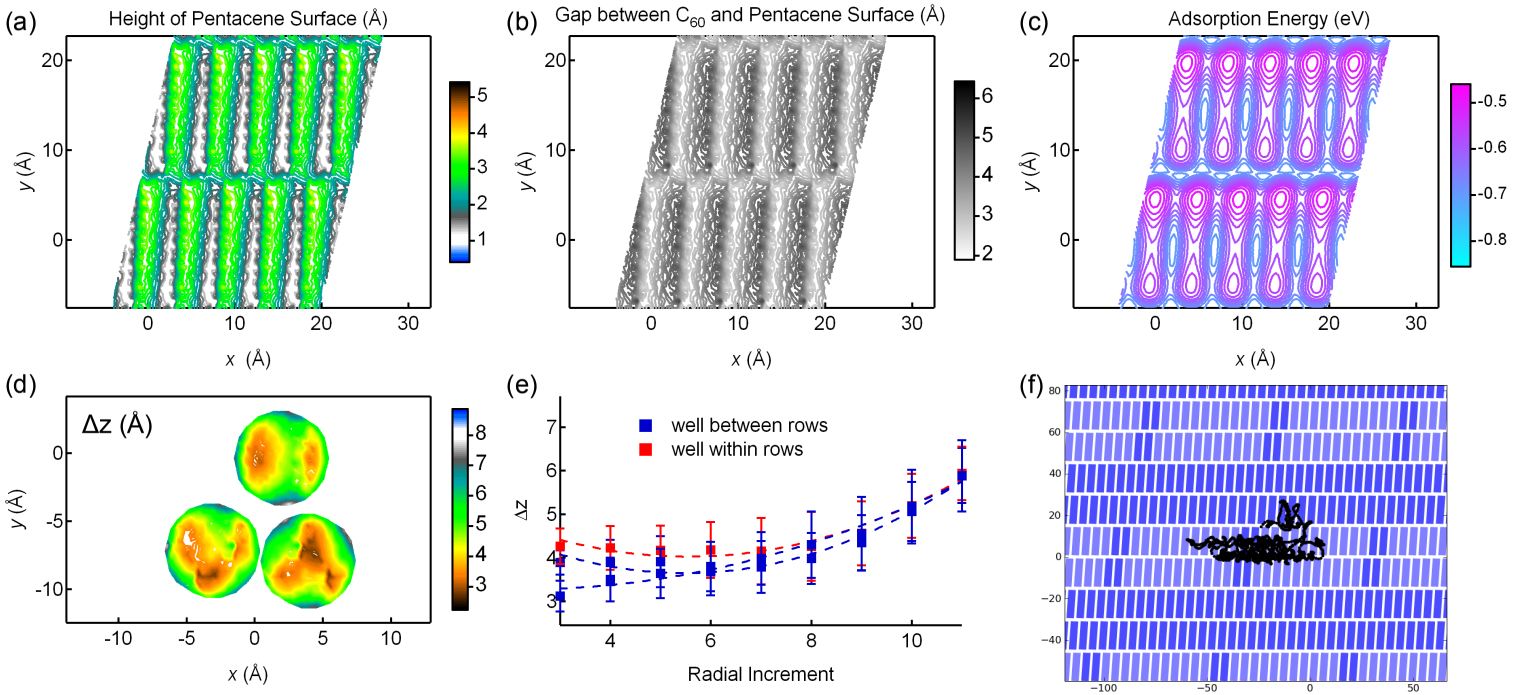

Figure A.5: Static and 1-C_{60} dynamic data for the ϕ_1=50° system. Key as in Table A.1.

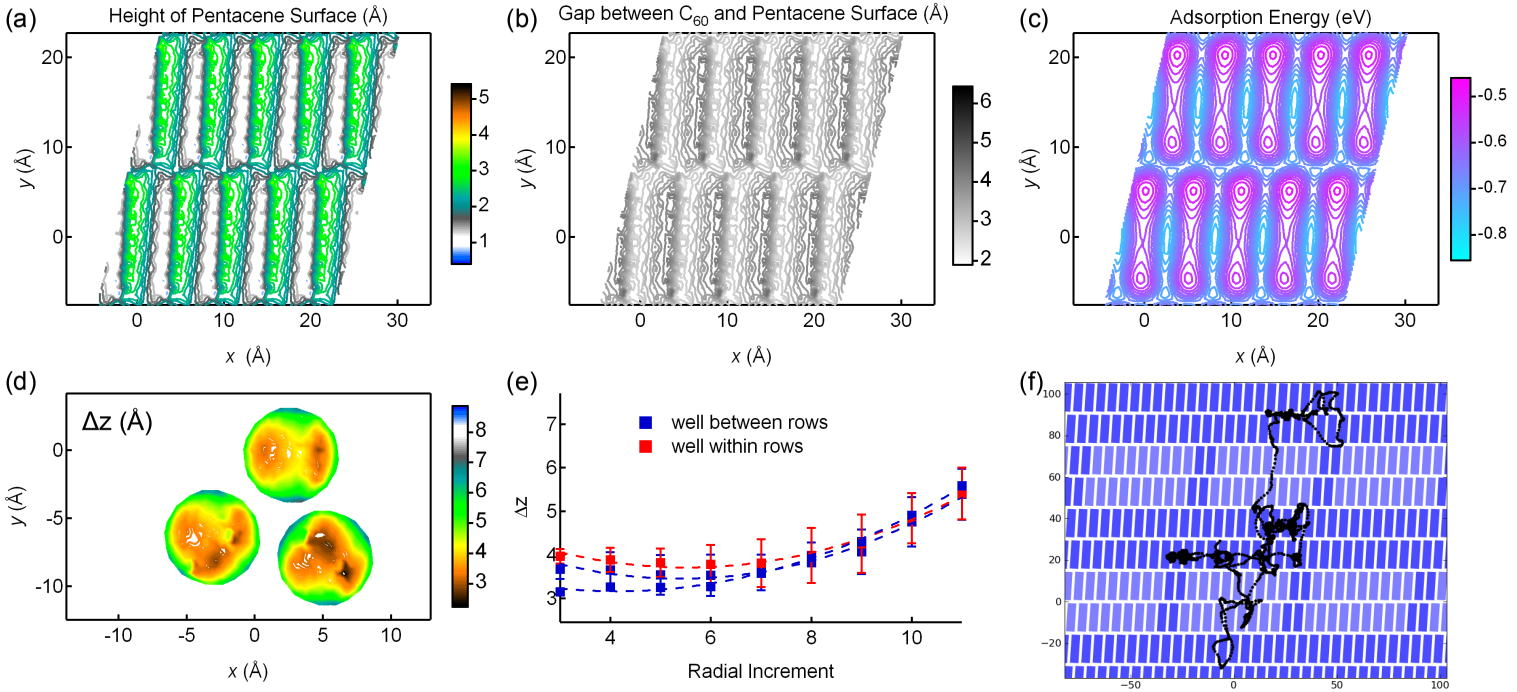

Figure A.6: Static and 1-C_{60} dynamic data for the ϕ_1=60° system. Key as in Table A.1.

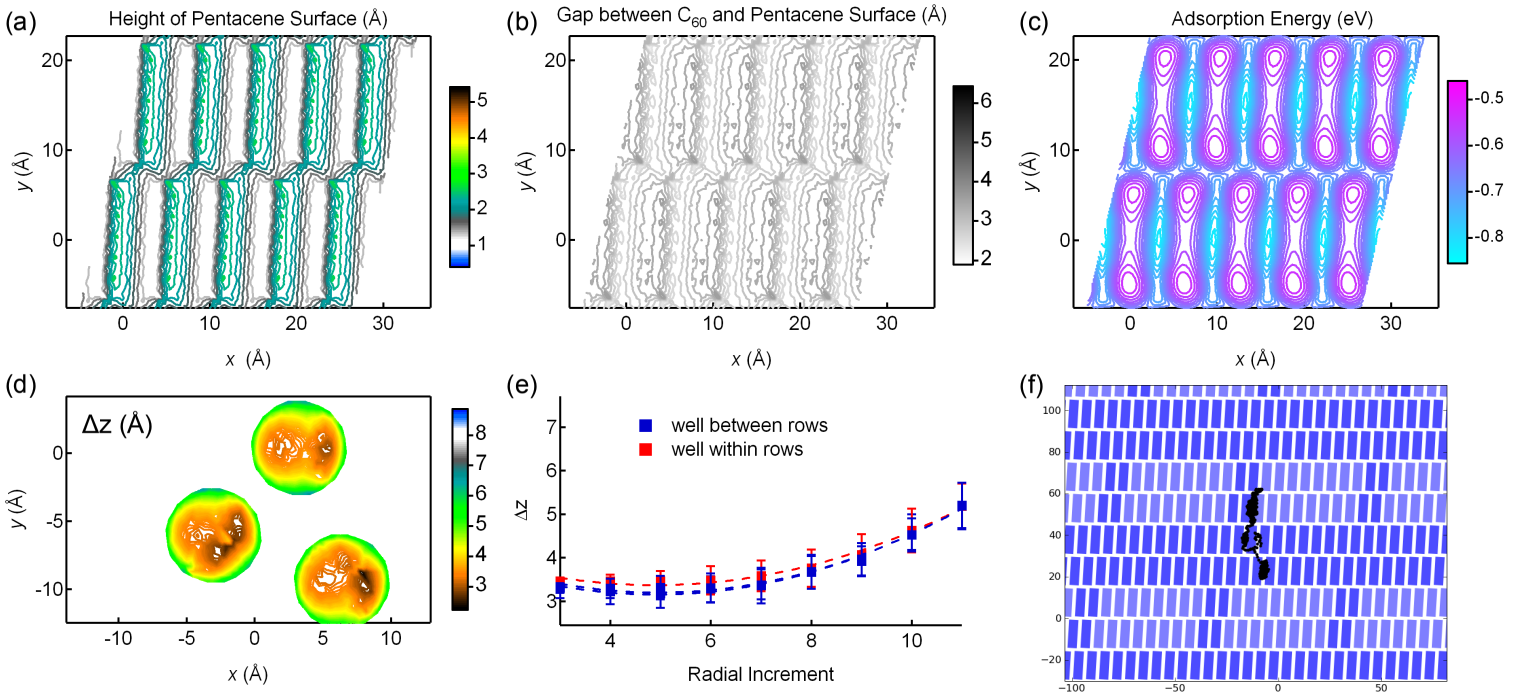

Figure A.7: Static and 1-C_{60} dynamic data for the ϕ_1=70° system. Key as in Table A.1.

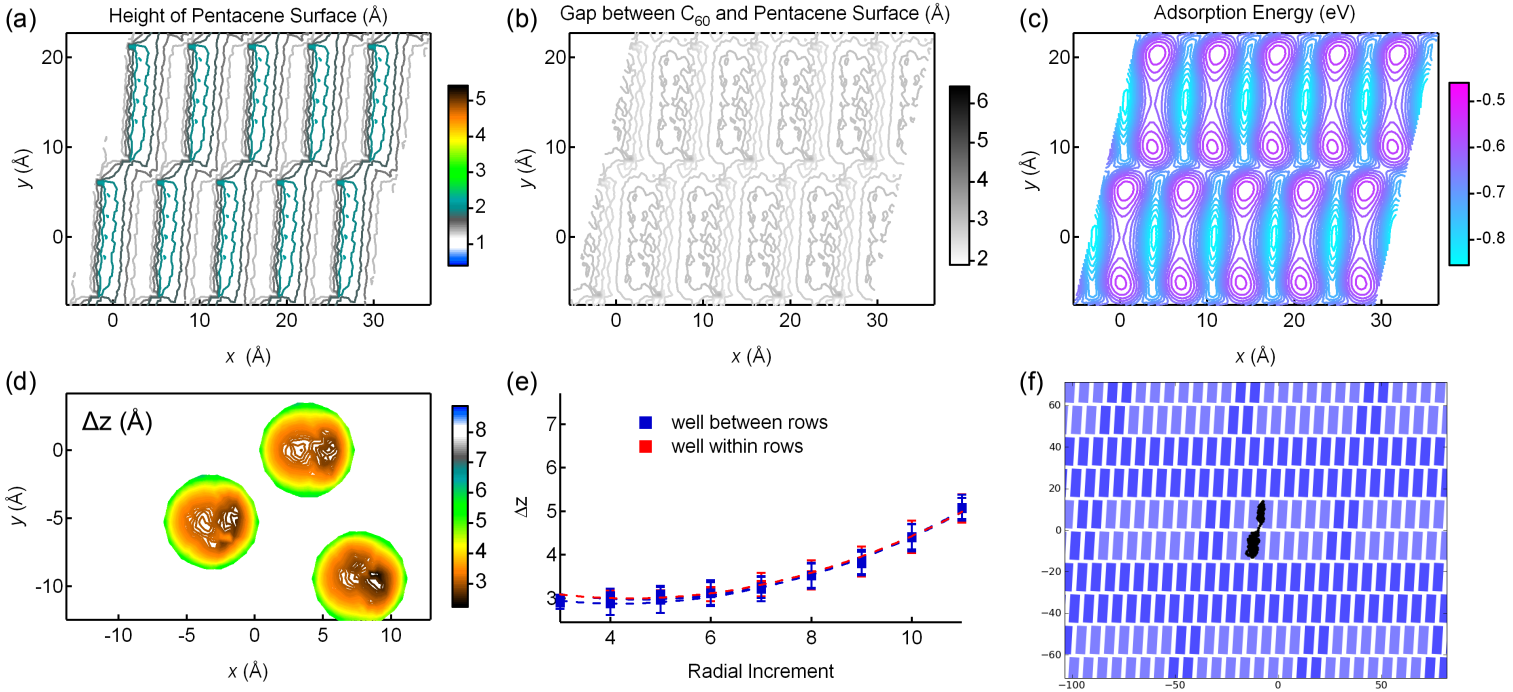

Figure A.8: Static and 1-C_{60} dynamic data for the ϕ_1=80° system. Key as in Table A.1.

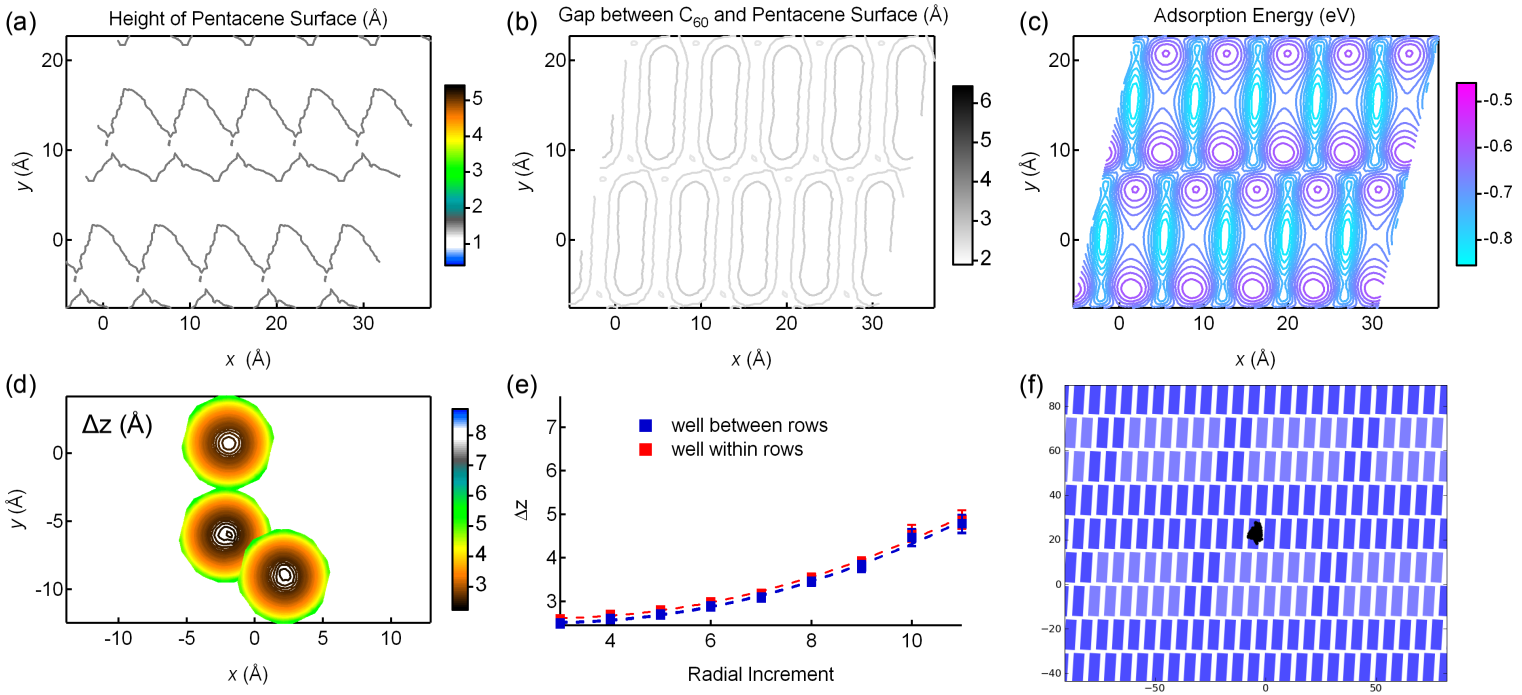

Figure A.9: Static and 1-C_{60} dynamic data for the ϕ_1=90° system. Key as in Table A.1.

APPENDIX B

MATLAB CODE FOR TWO DIMENSIONAL REACTION DIFFUSION MODEL

```
%% Rate equation solver for 2D Laplacian diffusion equation
% Assumptions: 1) clusters are circular, 2) only monomers↵
diffuse
% Rebecca Cantrell
% June 9, 2011

global Rj nj Rdep k_det2 k_det3 k_detNpre k_detNexp

%% Define system parameters
h = 0.01; % initial time step [=] ps
nC = 1000; % initial max cluster size to consider
n0 = 0.0000000115; % initial area fraction = n0*pi*R1^2
phase = 'bulk'; % upright phase of pentacene
diam = 10; % diameter of particles [=] A
k_det2 = 5.0981E-8; % detatchment rate for j=2 [=] 1/(ps)
k_det3 = 5.6146E-9; % detatchment rate for j=3 [=] 1/(ps)
% NOTE: for j>=4, k_det = k_detNpre*j^k_detNexp [=] 1/(ps)
k_detNpre = 1.7520E-11; % detatchment rate prefactor for↵
j>=4 [=] 1/(ps)
k_detNexp = -5.3356E-1; % detatchment rate exponent for j>=4
tolMin = 1E-18; % minimum error, below which a bigger time↵
step should be chosen
tolMax = 1E-6; % maximum error, above which a smaller time↵
step should be chosen

% Parameters that follow...
Rdep = 1.12613E-13; % 1 MLps
timeMS = 0:1E-1:1000; % time array for plotting (in ms)
if strcmp(phase,'bulk')==1
    D = 0.474044; % diffusion rate [=] A^2/ps BULK PHASE
elseif strcmp(phase,'thin')==1
    D = 1.443627; % diffusion rate [=] A^2/ps THIN FILM↵
PHASE
end

%% Define arrays and matrixes
Rj = diam*sqrt(2*(1:nC))*3^(1/4)/(2*sqrt(pi)); % Radii of↵
cluster size j [=] A
nj = zeros(1,nC); % number density of monomers around↵
cluster j [=] 1/A^2
dnj = zeros(1,nC); % first derivative of nj
Xj = zeros(1,nC); % Xj = Rj/xi (used for solving bessel↵
function equation)

%% Initialize variables and arrays (t=0)
nj(1) = n0;
Xj(1)=fsolve(@solveForX_init,1);
xi=Rj(1)/Xj(1); % unique screening length at each time step↵
[=] A
Xj(2:nC)=Rj(2:nC)/xi;
kj1=2*pi*D*Xj.*besselk(1,Xj)./besselk(0,Xj); % monomomer↵
attachment rate to cluster j [=] ps^-1
k=D/(xi^2); % total monomer attachment rate per area [=] 1/↵
(A^2*ps)
```

```
phi=sum(pi*nj.*Rj.*Rj); % area fraction [=] 1/A^2
epsilon=0;

%% Loop in time to solve rate equations
timePS = 0; % system time in picoseconds
iter1 = 1;
iter2 = 1;
while phi<1

    %% Get rate equations
    dnj_old=dnj;
    dnj=get_dnj(kj1,nj,nC);

    %% Calculate time step
    if iter1>1
        % calculate the old nj using runge-kutta
        c1=h*dnj_old;
        c2=h*get_dnj(kj1_old,nj_old+c1/2,nC);
        c3=h*get_dnj(kj1_old,nj_old+c2/2,nC);
        c4=h*get_dnj(kj1_old,nj_old+c3,nC);
        nj_old_RK = nj_old+(c1+2*c2+2*c3+c4)/6.0;
        % compare this to one calculated in previous time
step
        epsilon=norm(nj_old_RK-nj,2);
        if epsilon<tolMin
            h=(3/2)*h; % make time step bigger
        elseif epsilon>tolMax
            h=(1/2)*h; % make time step smaller
        end
    end

    timePS=timePS+h; % current time in ps
    tempTimeMS = timePS*10e-9; % current time in ms


    %% Calculate new nj
    nj_old=nj;
    if iter1==1
        % Forward Euler method
        nj = nj_old + h*dnj;
    else
        % Modified Euler method
        nj = nj_old + (h/2)*(dnj+dnj_old);
    end

    phi=sum(pi*nj.*Rj.*Rj);

    %% Extend arrays if necessary
    if nj(end)>10E-18
        incr=1000;
        nj(end+1:end+incr)=0;
        nj_old(end+1:end+incr)=0;
        kj1(end+1:end+incr)=0;
        dnj(end+1:end+incr)=0;
```

```
        rInd=size(Rj,2);
        Rj(end+1:end+incr) = diam*sqrt(2*(rInd+1:rInd+incr))↙
*3^(1/4)/(2*sqrt(pi));
        nC=nC+incr;
    end

    %% Recalculate rate constants
    k=sum(kj1.*nj);
    xi=sqrt(D/k);
    Xj=Rj/xi;
    bessFrac=besselk(1,Xj)./besselk(0,Xj);
    bessFrac(isnan(bessFrac))=1;
    kj1_old=kj1;
    kj1=2*pi*D*Xj.*bessFrac;

    %% Save values as text files
    if tempTimeMS>timeMS(iter2)
        save timeMS_new.txt tempTimeMS -ASCII
        system('cat timeMS_new.txt >> timeMS.txt; rm↙
timeMS_new.txt');
        save Xj_new.txt Xj -ASCII;
        system('cat Xj_new.txt >> Xj.txt; rm Xj_new.txt');
        save dnj_new.txt dnj -ASCII;
        system('cat dnj_new.txt >> dnj.txt; rm dnj_new.↙
txt');
        save epsilon_new.txt epsilon -ASCII;
        system('cat epsilon_new.txt >> epsilon.txt; rm↙
epsilon_new.txt');
        save k_new.txt k -ASCII;
        system('cat k_new.txt >> k.txt; rm k_new.txt');
        save kj1_new.txt kj1 -ASCII;
        system('cat kj1_new.txt >> kj1.txt; rm kj1_new.↙
txt');
        save nj_new.txt nj -ASCII;
        system('cat nj_new.txt >> nj.txt; rm nj_new.txt');
        save phi_new.txt phi -ASCII;
        system('cat phi_new.txt >> phi.txt; rm phi_new.↙
txt');
        save xi_new.txt xi -ASCII;
        system('cat xi_new.txt >> xi.txt; rm xi_new.txt');
        iter2=iter2+1;
    end

    iter1=iter1+1;
end
```

```
function F1 = solveForX_init(X)

    global Rj nj

    F1 = (2*pi*(Rj(1))^2*nj(1,1))*besselk(1,X)-X*besselk(0,↵
X);

end
```

```
function dnj = get_dnj(kj1,Nj,nC)

    global Rdep k_det2 k_det3 k_detNpre k_detNexp

    dnj = zeros(1,nC);

    % dnj/dt, j==1:
    dnj(1) = Rdep - sum(kj1(:).*Nj(:))*Nj(1) + ...
             (k_det2*Nj(2)+k_det3*Nj(3)+k_detNpre*sum(((4:nC).^k_detNexp).*Nj(4:nC)));

    % dnj/dt, j==2:
    dnj(2) = kj1(1).*Nj(1)*Nj(1)+... % consumption of monomers by cluster size j-1
        -kj1(2).*Nj(2)*Nj(1)+... % consumption of monomers by cluster size j
        -(k_det2*Nj(2))+... % detatchment of monomers from cluster size j
        (k_det3*Nj(3)); % detatchment of monomers from cluster size j+1

    % dnj/dt, j==3:
    dnj(3) = kj1(2).*Nj(2)*Nj(1)+... % consumption of monomers by cluster size j-1
        -kj1(3).*Nj(3)*Nj(1)+... % consumption of monomers by cluster size j
        -(k_det3*Nj(3))+... % detatchment of monomers from cluster size j
        (k_detNpre*(4^k_detNexp)*Nj(4)); % detatchment of monomers from cluster size j+1

    % dnj/dt, j>=4:
    dnj(4:nC-1) = kj1(3:nC-2).*Nj(3:nC-2)*Nj(1)+... %consumption of monomers by cluster size j-1 ...
        -kj1(4:nC-1).*Nj(4:nC-1)*Nj(1)+... % consumption of monomers by cluster size j
        -(k_detNpre*((4:nC-1).^k_detNexp).*Nj(4:nC-1))+... %detatchment of monomers from cluster size j
        (k_detNpre*((5:nC).^k_detNexp).*Nj(5:nC)); %detatchment of monomers from cluster size j+1

    % dnj/dt, j==nC
    dnj(nC)=kj1(nC-1)*Nj(nC-1)*Nj(1)+... % consumption of monomers by cluster size j-1
        -kj1(nC)*Nj(nC)*Nj(1)+... % consumption of monomers by cluster size j=nC
        -k_detNpre*(nC^k_detNexp)*Nj(nC); % detatchment of monomers from cluster size j=nC

end
```

BIBLIOGRAPHY

[1] Girifalco, L. A. *J. Phys. Chem.* **1992**, *96*, 858–861.

[2] Pacheco, J. M.; Ramalho, J. P. P. *Phys. Rev. Lett.* **1997**, *79*, 3873.

[3] Liu, H.; Lin, Z.; Zhigilei, L. V.; Reinke, P. *J. Phys. Chem. C* **2008**, *112*, 4687–4695.

[4] Brabec, C. J. *Sol. Energ. Mat. Sol. C.* **2004**, *83*, 273–292.

[5] Kippelen, B.; Brédas, J.-L. *Energy Environ. Sci.* **2009**, *2*, 251–261.

[6] Nelson, J. *Curr. Opin. Solid St. M.* **2002**, *6*, 87–95.

[7] Jurchescu, O. D.; Baas, J.; Palstra, T. T. M. *Appl. Phys. Lett.* **2004**, *84*, 3061–3063.

[8] Podzorov, V.; Pudalov, V. M.; Gershenson, M. E. *Appl. Phys. Lett.* **2003**, *82*, 1739–1741.

[9] Haddock, J. N.; Zhang, X.; Domercq, B.; Kippelen, B. *Org. Electron.* **2005**, *6*, 182–187.

[10] Cheyns, D.; Gommans, H.; Odijk, M.; Poortmans, J.; Heremans, P. *Sol. Energ. Mat. Sol. C.* **2007**, *91*, 399–404.

[11] Nanditha, D. M.; Dissanayake, M.; Hatton, R. A.; Curry, R. J.; Silva, S. R. P. *Appl. Phys. Lett.* **2007**, *90*, 113505.

[12] Dissanayake, D. M. N. M.; Adikaari, A. A. D. T.; Curry, R. J.; Hatton, R. A.; Silva, S. R. P. *Appl. Phys. Lett.* **2007**, *90*, 253502.

[13] Kang, S.; Yi, Y.; Kim, C.; Cho, S.; Noh, M.; Jeong, K.; Whang, C. *Synthetic Metals* **2006**, *156*, 32–37.

[14] Kuwahara, E.; Kubozono, Y.; Hosokawa, T.; Nagano, T.; Masunari, K.; Fujiwara, A. *Appl. Phys. Lett.* **2004**, *85*, 4765–4767.

[15] Mayer, A. C.; Lloyd, M. T.; Herman, D. J.; Kasen, T. G.; Malliaras, G. G. *Appl. Phys. Lett.* **2004**, *85*, 6272–6274.

[16] Pandey, A. K.; Nunzi, J.-M. *Appl. Phys. Lett.* **2006**, *89*, 213506.

[17] Salzmann, I.; Duhm, S.; Opitz, R.; Johnson, R. L.; Rabe, J. P.; Koch, N. *J. Appl. Phys.* **2008**, *104*, 114518.

[18] Wang, S.; Kanai, K.; Ouchi, Y.; Seki, K. *Org. Electron.* **2006**, *7*, 457–464.

[19] Yoo, S.; Potscavage, W. J.; Domercq, B.; Han, S.-H.; Li, T.-D.; Jones, S. C.; Szoszkiewicz, R.; Levi, D.; Riedo, E.; Marder, S. R.; Kippelen, B. *Solid State Electron.* **2007**, *51*, 1367–1375.

[20] Zheng, Y.; Pregler, S. K.; Myers, J. D.; Ouyang, J.; Sinnott, S. B.; Xue, J. *J. Vac. Sci. Technol. B* **2009**, *27*, 169–179.

[21] Al-Mahboob, A.; Sadowski, J.; Fujikawa, Y.; Sakurai, T. *Surface Science* **2009**, *603*, L53–L56.

[22] Conrad, B. R.; Tosado, J.; Dutton, G.; Dougherty, D. B.; Jin, W.; Bonnen, T.; Schuldenfrei, A.; Cullen, W. G.; Williams, E. D.; Reutt-Robey, J. E.; Robey, S. W. *Appl. Phys. Lett.* **2009**, *95*, 213302.

[23] Dougherty, D. B.; Jin, W.; Cullen, W. G.; Reutt-Robey, J. E.; Robey, S. W. *Appl. Phys. Lett.* **2009**, *94*, 023103.

[24] Heiney, P. A.; Fischer, J. E.; McGhie, A. R.; Romanow, W. J.; Denenstein, A. M.; McCauley, J. P.; Smith, A. B.; Cox, D. E. *Phys. Rev. Lett.* **1991**, *66*, 2911–2914.

[25] Pugachev, A. T.; Churakova, N. P.; Gorbenko, N. I.; Saadly, H.; Solodovnik, A. A. *Low Temp. Phys.* **1999**, *25*, 220–224.

[26] Tanigaki, K.; Kuroshima, S.; Ebbesen, T. W. *Thin Solid Films* **1995**, *257*, 154–165.

[27] Luengo, G.; Campbell, S. E.; Srdanov, V. I.; Wudl, F.; Israelachvili, J. N. *Chem. Mater.* **1997**, *9*, 1166–1171.

[28] Hara, M.; Sasabe, H.; Yamada, A.; Garito, A. F. *Jpn. J. Appl. Phys.* **1989**, *28*, L306–L308.

[29] Tanigaki, K.; Kuroshima, S.; Ebbesen, T. W.; Ichihashi, T. *J. Cryst. Growth* **1991**, *114*, 3–6.

[30] Tada, H.; Saiki, K.; Koma, A. *Jpn. J. Appl. Phys.* **1991**, *30*, L306–L308.

[31] Mattheus, C. C.; Dros, A. B.; Baas, J.; Meetsma, A.; de Boer, J. L.; Palstra, T. T. M. *Acta Cryst.* **2001**, *C57*, 939–941.

[32] Mattheus, C. C.; de Wijs, G. A.; de Groot, R. A.; Palstra, T. T. M. *J. Am. Chem. Soc.* **2003**, *125*, 6323–6330.

[33] Ahn, S. D.; Kang, S. Y.; Lee, Y. E.; Joung, M. J.; Kim, C. A.; Suh, K. S. *Mat. Res. Soc. Symp. Proc.* **2003**, *769*, H6.19.

[34] Knipp, D.; Street, R. A.; Völkel, A.; Ho, J. *J. Appl. Phys.* **2003**, *93*, 347–355.

[35] Bouchoms, I. P. M.; Schoonveld, W. A.; Vrijmoeth, J.; Klapwijk, T. M. *Synthetic Met.* **1999**, *104*, 175–178.

[36] Kakudate, T.; Yoshimoto, N.; Saito, Y. *Mater. Res. Soc. Symp. Proc.* **2007**, *965*, 0965–S12–52.

[37] Goose, J. E.; Wong, K.; Clancy, P.; Thompson, M. O. *Appl. Phys. Lett.* **2008**, *93*, 183306.

[38] Brehmer, L. *Acta Polymerica* **1981**, *32*, 665–665.

[39] Northrup, J.; Tiago, M.; Louie, S. *Phys. Rev. B* **2002**, *66*, 121404.

[40] Ruiz, R.; Choudhary, D.; Nickel, B.; Toccoli, T.; Chang, K.-C.; Mayer, A. C.; Clancy, P.; Blakely, J. M.; Headrick, R. L.; Iannotta, S.; Malliaras, G. G. *Chem. Mater.* **2004**, *16*, 4497–4508.

[41] Campbell, R. B.; Robertson, J. M.; Trotter, J. *Acta Cryst.* **1962**, *15*, 289–290.

[42] Yoshida, H.; Inaba, K.; Sato, N. *Appl. Phys. Lett.* **2007**, *90*, 181930.

[43] Satta, M.; Iacobucci, S.; Larciprete, R. *Phys. Rev. B* **2007**, *75*, 155401.

[44] Wang, Y.; Ji, W.; Shi, D.; Du, S.; Seidel, C.; Ma, Y.; Gao, H.-J.; Chi, L.; Fuchs, H. *Phys. Rev. B* **2004**, *69*, 075408.

[45] Yamane, H.; Yoshimura, D.; Kawabe, E.; Sumii, R.; Kanai, K.; Ouchi, Y.; Ueno, N.; Seki, K. *Phys. Rev. B* **2007**, *76*, 165436.

[46] Kang, J. H.; Zhu, X.-Y. *Appl. Phys. Lett.* **2003**, *82*, 3248–3250.

[47] Choudhary, D.; Clancy, P.; Bowler, D. R. *Surf. Sci.* **2005**, *578*, 20–26.

[48] Weidkamp, K. P.; Hacker, C. A.; Schwartz, M. P.; Cao, X.; Tromp, R. M.; Hamers, R. J. *J. Phys. Chem. B* **2003**, *107*, 11142–11148.

[49] Corradini, V.; Menozzi, C.; Cavallini, M.; Biscarini, F.; Betti, M. G.; Mariani, C. *Surf. Sci.* **2003**, *532-535*, 249–254.

[50] Guaino, P.; Carty, D.; Hughes, G.; McDonald, O.; Cafolla, A. A. *Appl. Phys. Lett.* **2004**, *85*, 2777–2779.

[51] Floreano, L.; Cossaro, A.; Cvetko, D.; Bavdek, G.; Morgante, A. *J. Phys. Chem. B* **2006**, *110*, 4908–4913.

[52] Bavdek, G.; Cossaro, A.; Cvetko, D.; Africh, C.; Blasetti, C.; Esch, F.; Morgante, A.; Floreano, L. *Langmuir* **2008**, *24*, 767–772.

[53] McDonald, O.; Cafolla, A. A.; Carty, D.; Sheerin, G.; Hughes, G. *Surf. Sci.* **2006**, *600*, 3217–3225.

[54] France, C. B.; Schroeder, P. G.; Forsythe, J. C.; Parkinson, B. A. *Langmuir* **2003**, *19*, 1274–1281.

[55] Suzuki, T.; Kurahashi, M.; Ju, X.; Yamauchi, Y. *Appl. Phys. Lett.* **2003**, *83*, 4342–4344.

[56] Beernink, G.; Strunskus, T.; Witte, G.; Wöll, C. *Appl. Phys. Lett.* **2004**, *85*, 398–400.

[57] Hu, W. S.; Tao, Y. T.; Hsu, Y. J.; Wei, D. H.; Wu, Y. S. *Langmuir* **2005**, *21*, 2260–2266.

[58] Kang, J. H.; Zhu, X.-Y. *Chem. Mater.* **2006**, *18*, 1318–1323.

[59] Käfer, D.; Ruppel, L.; Witte, G. *Phys. Rev. B* **2007**, *75*, 085309.

[60] Yang, Y.-C.; Chang, C.-H.; Lee, Y.-L. *Chem. Mater.* **2007**, *19*, 6126–6130.

[61] Pong, I.; Yau, S.; Huang, P.-Y.; Chen, M.-C.; Hu, T.-S.; Yang, Y.; Lee, Y.-L. *Langmuir* **2009**, *25*, 9887–9893.

[62] Danışman, M.; Casalis, L.; Scoles, G. *Phys. Rev. B* **2005**, *72*, 085404.

[63] Eremtchenko, M.; Temirov, R.; Bauer, D.; Schaefer, J.; Tautz, F. *Phys. Rev. B* **2005**, *72*, 115430.

[64] Käfer, D.; Witte, G. *Chem. Phys. Lett.* **2007**, *442*, 376–383.

[65] Pedio, M.; Doyle, B.; Mahne, N.; Giglia, A.; Borgatti, F.; Nannarone, S.; Henze, S.; Temirov, R.; Tautz, F.; Casalis, L.; Hudej, R.; Danışman, M.; Nickel, B. *Applied Surface Science* **2007**, *254*, 103–107.

[66] Dougherty, D.; Jin, W.; Cullen, W.; Dutton, G.; Reutt-Robey, J.; Robey, S. *Phys. Rev. B* **2008**, *77*, 073414.

[67] Mete, E.; Demiroğlu, I.; Danışman, M. F.; Ellialtıoğlu, S. *J. Phys. Chem. C* **2010**, *114*, 2724–2729.

[68] Gavioli, L.; Fanetti, M.; Sancrotti, M.; Betti, M. *Phys. Rev. B* **2005**, *72*, 035458.

[69] Betti, M. G.; Kanjilal, A.; Mariani, C. *J. Phys. Chem. A* **2007**, *111*, 12454–12457.

[70] Baldacchini, C.; Mariani, C.; Betti, M.; Vobornik, I.; Fujii, J.; Annese, E.; Rossi, G.; Ferretti, A.; Calzolari, A.; Felice, R. D.; Ruini, A.; Molinari, E. *Phys. Rev. B* **2007**, *76*, 245430.

[71] Schuerlein, T. J.; Schmidt, A.; Lee, P. A.; Nebesny, K. W.; Armstrong, N. R. *Jpn. J. Appl. Phys.* **1995**, *34*, 3837–3845.

[72] Chen, Q.; McDowall, A. J.; Richardson, N. V. *Langmuir* **2003**, *19*, 10164–10171.

[73] Söhnchen, S.; Lukas, S.; Witte, G. *J. Chem. Phys.* **2004**, *121*, 525–534.

[74] Götzen, J.; Lukas, S.; Birkner, A.; Witte, G. *Surface Science* **2011**, *605*, 577–581.

[75] Dougherty, D. B.; Jin, W.; Cullen, W. G.; Reutt-Robey, J. E.; Robey, S. W. *J. Phys. Chem. C* **2008**, *112*, 20334–20339.

[76] Knupfer, M. *Appl. Phys. A-Mater.* **2003**, *77*, 623–626.

[77] Yi, Y.; Coropceanu, V.; Brédas, J.-L. *J. Am. Chem. Soc.* **2009**, *131*, 15777–15783.

[78] Verlaak, S.; Beljonne, D.; Cheyns, D.; Rolin, C.; Linares, M.; Castet, F.; Cornil, J.; Heremans, P. *Adv. Funct. Mater.* **2009**, *19*, 3809–3814.

[79] Minakata, T.; Imai, H.; Ozaki, M.; Saco, K. *J. Appl. Phys.* **1992**, *72*, 5220–5225.

[80] Casalis, L.; Danisman, M.; Nickel, B.; Bracco, G.; Toccoli, T.; Iannotta, S.; Scoles, G. *Phys. Rev. Lett.* **2003**, *90*, 206101.

[81] Itaka, K.; Yamashiro, M.; Yamaguchi, J.; Haemori, M.; Yaginuma, S.; Matsumoto, Y.; Kondo, M.; Koinuma, H. *Adv. Mater.* **2006**, *18*, 1713–1716.

[82] Wang, Y.; Herron, N. *J. Phys. Chem.* **1991**, *95*, 525–532.

[83] Thostenson, E. T.; Ren, Z.; Chou, T.-W. *Compos. Sci. Technol.* **2001**, *61*, 1899–1912.

[84] Xia, Y.; Yang, P. *Adv. Mater.* **2003**, *15*, 351–352.

[85] Morales, A. M.; Lieber, C. M. *Science* **1998**, *279*, 208–211.

[86] Coleman, N. R. B.; Morris, M. A.; Spalding, T. R.; Holmes, J. D. *J. Am. Chem. Soc.* **2001**, *123*, 187–188.

[87] Schmidt, V.; Wittemann, J. V.; Senz, S.; Gösele, U. *Adv. Mater.* **2009**, *21*, 2681–2702.

[88] Hochbaum, A. I.; Yang, P. *Chem. Rev.* **2010**, *110*, 527–546.

[89] Zhang, Y. F.; Tang, Y. H.; Wang, N.; Lee, C. S.; Bello, I.; Lee, S. T. *Phys. Rev. B* **2000**, *61*, 4518–4521.

[90] Wu, Y.; Yang, P. *Chem. Mater.* **2000**, *12*, 605–607.

[91] Briseno, A. L.; Mannsfeld, S. C. B.; Jenekhe, S. A.; Bao, Z.; Xia, Y. *Mater. Today* **2008**, *11*, 38–47.

[92] Cuberes, M. T.; Schlittler, R. R.; Gimzewski, J. K. *Appl. Phys. Lett.* **1996**, *69*, 3016–3018.

[93] Néel, N.; Kröger, J.; Berndt, R. *Adv. Mater.* **2006**, *18*, 174–177.

[94] Xiao, W.; Ruffieux, P.; Ait-Mansour, K.; Groning, O.; Palotas, K.; Hofer, W. A.; Groning, P.; Fasel, R. *J. Phys. Chem. B* **2006**, *110*, 21394–21398.

[95] Feng, M.; Lee, J.; Zhao, J.; Yates, J. T.; Petek, H. *J. Am. Chem. Soc.* **2007**, *129*, 12394–12395.

[96] Nishiyama, F.; Yokoyama, T.; Kamikado, T.; Yokoyama, S.; Mashiko, S.; Sakaguchi, K.; Kikuchi, K. *Adv. Mater.* **2007**, *19*, 117–120.

[97] Klitgaard, S. K.; Egeblad, K.; Haahr, L. T.; Hansen, M. K.; Hansen, D.; Svagin, J.; Christensen, C. H. *Surf. Sci.* **2007**, *601*, L35–L38.

[98] Chen, L.; Chen, W.; Huang, H.; Zhang, H.; Yuhara, J.; Wee, A. *Adv. Mater.* **2008**, *20*, 484–488.

[99] Linares, M.; Beljonne, D.; rome Cornil, J.; Lancaster, K.; das, J.-L. B.; Verlaak, S.; Mityashin, A.; Heremans, P.; Fuchs, A.; Lennartz, C.; Ide, J.; l Me reau, R.; Aurel, P.; Ducasse, L.; de ric Castet, F. *J. Phys. Chem. C* **2010**, *114*, 3215–3224.

[100] Richter, A.; Smith, R. *Cryst. Res. Technol.* **2003**, *38*, 250–266.

[101] Zhang, X.; He, W.; Zhao, A.; Li, H.; Chen, L.; Pai, W.; Hou, J.; Loy, M.; Yang, J.; Xiao, X. *Phys. Rev. B* **2007**, *75*, 235444.

[102] Liang, G.-C.; Ghosh, A. W. *Phys. Rev. Lett.* **2005**, *95*, 076403.

[103] Lee, J. Y.; Kang, M. H. *Surf. Sci.* **2008**, *602*, 1408–1412.

[104] de Jong, W. A.; Bylaska, E.; Govind, N.; Janssen, C. L.; Kowalski, K.; Muller, T.; Nielsen, I. M. B.; van Dam, H. J. J.; Veryazov, V.; Lindh, R. *Phys. Chem. Chem. Phys.* **2010**, *12*, 6877–7296.

[105] Cantrell, R.; Clancy, P. *Surf. Sci.* **2008**, *602*, 3499–3505.

[106] Cantrell, R.; Cancy, P. *Molec. Sim.* **2010**, *36*, 590–603.

[107] Cantrell, R. A.; Clancy, P. *Mater. Res. Soc. Symp. Proc.* **2010**, *1263*, 1263–Y05–06.

[108] Allinger, N. L.; Yuh, Y. H.; Lii, J.-H. *J. Am. Chem. Soc.* **1989**, *111*, 8551–8565.

[109] Lii, J.-H.; Allinger, N. L. *J. Am. Chem. Soc.* **1989**, *111*, 8566–8575.

[110] Lii, J.-H.; Allinger, N. L. *J. Am. Chem. Soc.* **1989**, *111*, 8576–8582.

[111] Goose, J. E.; Clancy, P. *J. Phys. Chem. C* **2007**, *111*, 15653–15659.

[112] TINKER: Software Tools for Molecular Design. http://dasher.wustl.edu/tinker/ February, 2010.

[113] Nagy, J.; Smith, V. H.; Weaver, D. F. *J. Mol. Struc.-Theochem* **1995**, *358*, 71–77.

[114] Saunders, M. *Science* **1991**, *253*, 330–331.

[115] Tai, J. C.; Allinger, N. L. *J. Comput. Chem.* **1998**, *19*, 475–487.

[116] Ma, B.; Lii, J.-H.; Allinger, N. L. *J. Comput. Chem.* **2000**, *21*, 813–825.

[117] Glosli, J. N.; McClelland, G. M. *Phys. Rev. Lett.* **1993**, *70*, 1960–1963.

[118] Huang, D.; Chen, Y.; Fichthorn, K. A. *J. Chem. Phys.* **1994**, *101*, 11021–11030.

[119] Zeng, Q. H.; Yu, A. B.; Lu, G. Q.; Standish, R. K. *Chem. Mater.* **2003**, *15*, 4732–4738.

[120] Wang, J.; Golfinopoulos, T.; Gee, R. H.; Huang, H. *Appl. Phys. Lett.* **2007**, *90*, 101906.

[121] Connolly, M. J.; Roth, M. W.; Gray, P. A.; Wexler, C. *Langmuir* **2008**, *24*, 3228–3234.

[122] Zhdanov, V. P. *Surf. Sci.* **1989**, *214*, 289–303.

[123] Sanders, D. E.; DePristo, A. E. *Surf. Sci. Lett.* **1992**, *264*, L169–L176.

[124] Frenkel, D. *Computational Soft Matter: From Synthetic Polymers to Proteins* **2004**, *23*, 29–60.

[125] Gillespie, D. T. *J. Comput. Phys.* **1976**, *22*, 403–434.

[126] Itoh, M.; Bell, G.; Joyce, B.; Vvedensky, D. *Surf. Sci.* **2000**, *464*, 200–210.

[127] Bogicevic, A.; Strömquist, J.; Lundqvist, B. I. *Phys. Rev. Lett.* **1998**, *81*, 637–640.

[128] Köhler, U.; Jensen, C.; Wolf, C.; Schindler, A.; Brendel, L.; Wolf, D. *Surf. Sci.* **2000**, *454-456*, 676–680.

[129] Fichthorn, K. A.; Scheffler, M. *Phys. Rev. Lett.* **2000**, *84*, 5371–5374.

[130] Chatterjee, A.; Vlachos, D. G. *Chem. Eng. Sci* **2007**, *62*, 4852–4863.

[131] Baskaran, A.; Devita, J.; Smereka, P. *Continuum Mech. Thermodyn.* **2010**, *22*, 1–26.

[132] Hoffmann, M. J. CO Oxidation on Palladium Using Multi-lattice Kinetic Monte Carlo. Diplomarbeit. Freie Universität Berlin, Berlin, Germany, 2010.

[133] Fa, K.; Lenzi, E. *Phys. Rev. E* **2003**, *67*, 061105.

[134] Schütz, G. J.; Schindler, H.; Schmidt, T. *Biophys. J.* **1997**, *73*, 1073–1080.

[135] Ott, A.; Bouchaud, J. P.; Langevin, D.; Urbach, W. *Phys. Rev. Lett.* **1990**, *65*, 2201–2204.

[136] Bales, G.; Chrzan, D. *Phys. Rev. B* **1994**, *50*, 6057–6067.

[137] Vvedensky, D. D. *Phys. Rev. B* **2000**, *62*, 15435–15438.

[138] Mulheran, P. A. *Europhys. Lett.* **2004**, *65*, 379–385.

[139] Evans, J.; Thiel, P.; Bartelt, M. *Surface Science Reports* **2006**, *61*, 1–128.

[140] Burton, W. K.; Cabrera, N.; Frank, F. C. *Philos. T. Roy. Soc. A* **1951**, *243*, 299–358.

[141] Liu, F.; Metiu, H. *Phys. Rev. E* **1994**, *49*, 2601–2616.

[142] Ghez, R.; Iyer, S. S. *IBM J. Res. Develop.* **1988**, *32*, 804–818.

[143] Caflisch, R. E.; Gyure, M. F.; Merriman, B.; Osher, S. J.; Ratsch, C.; Vvedensky, D. D.; Zinck, J. J. *Appl. Math. Lett.* **1999**, *12*, 13–22.

[144] Caflisch, R. E.; E, W.; Gyure, M. F.; Merriman, B.; Ratsch, C. *Phys. Rev. E* **1999**, *59*, 6879–6887.

[145] Metzler, R.; Klafter, J. *J. Phys. A: Math. Gen.* **2004**, *37*, R161–R208.

[146] Cussler, E. L. *Diffusion: Mass Transfer in Fluid Systems*; Cambridge University Press, 2009.

[147] Private communication with Brian Koo. June, 2011.

[148] Sánchez-Carrera, R. S.; Paramonov, P.; Day, G. M.; Coropceanu, V.; Brédas, J.-L. *J. Am. Chem. Soc.* **2010**, *132*, 14437–14446.

[149] Java SE 6. Santa Clara, California: Sun Microsystems, Inc., 2006.

[150] Yamamoto, M.; Fujinami, A.; Ogata, S.; Shibutani, Y. *J. Comput. Sci. Technol.* **2007**, *1*, 14–21.

[151] Zoontjens, P.; Grochola, G.; Snook, I. K.; Russo, S. P. *J. Phys.: Condens. Matter* **2011**, *23*, 015302.

[152] Schunack, M.; Linderoth, T.; Rosei, F.; Lægsgaard, E.; Stensgaard, I.; Besenbacher, F. *Phys. Rev. Lett.* **2002**, *88*, 156102.

[153] Weckesser, J.; Barth, J. V.; Kern, K. *J. Chem. Phys.* **1999**, *110*, 5351–5354.

[154] Weckesser, J.; Barth, J. V.; Kern, K. *Phys. Rev. B* **2001**, *64*, 161403.

[155] Goose, J. E.; First, E. L.; Clancy, P. *Phys. Rev. B* **2010**, *81*, 205310.

[156] Pedio, M.; Felici, R.; Torrelles, X.; Rudolf, P.; Capozi, M.; Rius, J.; Ferrer, S. *Phys. Rev. Lett.* **2000**, *85*, 1040–1043.

[157] Hinterstein, M.; Torrelles, X.; Felici, R.; Rius, J.; Huang, M.; Fabris, S.; Fuess, H.; Pedio, M. *Phys. Rev. B* **2008**, *77*, 153412.

[158] Private communication with Daniel Dougherty. April, 2011.